

New Transition Metal Complexes of Cobalt(II) and Nickel(II) as Single-Ion Magnets and Spin Equilibrium Molecules

Patrícia da Silva Ferreira

Supervisor: Doctor Pedro Manuel Machado Teixeira Gomes

Co-Supervisors: Doctor Laura Cristina de Jesus Pereira Waerenborgh

Doctor Manuel José Duarte Leite de Almeida

**Thesis approved in public session to obtain the PhD degree in
Chemistry**

Jury final classification: Pass with Distinction and Honour

**New Transition Metal Complexes of Cobalt(II) and Nickel(II) as
Single-Ion Magnets and Spin Equilibrium Molecules**

Patrícia da Silva Ferreira

Supervisor: Doctor Pedro Manuel Machado Teixeira Gomes

Co-Supervisors: Doctor Laura Cristina de Jesus Pereira Waerenborgh
Doctor Manuel José Duarte Leite de Almeida

**Thesis approved in public session to obtain the PhD degree in
Chemistry**

Jury final classification: Pass with Distinction and Honour

Jury

Chairperson: Doctor Maria Teresa Nogueira Leal da Silva Duarte, Instituto Superior Técnico, Universidade de Lisboa

Members of the Committee:

Doctor Maria José Diogo da Silva Calhorda, Faculdade de Ciências, Universidade de Lisboa

Doctor José António de Carvalho Paixão, Faculdade de Ciências e Tecnologia, Universidade de Coimbra

Doctor Pedro Manuel Teixeira Gomes, Instituto Superior Técnico, Universidade de Lisboa

Doctor Clara Sofia Barreiro Gomes, Faculdade de Ciências e Tecnologia, Universidade Nova de Lisboa

Doctor Maria Dulce Jesus Pombo Belo, Instituto Superior Técnico, Universidade de Lisboa

Doctor Tiago Filipe Carpinteiro Cruz, Instituto Superior Técnico, Universidade de Lisboa

Funding Institutions - Fundação para a Ciência e Tecnologia

To my family

ABSTRACT

The PhD work developed throughout these four years aimed at synthesizing and characterizing new transition metal complexes of cobalt(II) and nickel(II) with emphasis on the study of their magnetic properties.

Chapter 1 explores new homoleptic Co(II) complexes bearing two monoanionic *N,N'*-bidentate 2-iminopirrollyl ligands, with different steric and electronic properties, as Single-Ion Magnets (SIMs). The design of the ligand precursors (bulkiness, asymmetry and electron-donor ability) is of great importance, as it determines the geometry in this family of compounds, thus, enabling the control and enhancement of the SIM behavior. The experimental magnetic studies were conducted by static (DC) and dynamic (AC) measurements, High-Frequency and -Field Electronic Paramagnetic Resonance spectroscopy (HFEPFR), and estimated by theoretical *ab initio* calculations. All the complexes displayed slow relaxation of magnetization, most of them at zero DC field, with large negative values for the zero-field splitting parameter D and for the spin-reversal energy barrier U_{eff} . All these studies provided an insight into the correlation between the geometry and the magnetic properties, concluding that changes from a distorted tetrahedral to a distorted trigonal pyramidal geometry enhances this behavior not only by improving the values of D , but also by displaying slow relaxation of the magnetization at zero DC field with very high values of U_{eff} .

Chapter 2 presents a new synthetic route for the new nickel complexes of the type $[\text{Ni}(\eta^5\text{-C}_5\text{Me}_5)(t\text{Bu}_2\text{Im})\text{X}]$ ($X = \text{Cl}, \text{Br}$ and I), in which the neutral $t\text{Bu}_2\text{Im}$ carbene was used instead of the corresponding imidazolium salts. These compounds were fully characterized and their magnetic properties studied in solution, namely the existing spin equilibria processes, by variable-temperature (VT) ^1H Nuclear Magnetic Resonance (NMR) spectroscopy and by the Evans method, and in solid state by DC magnetization measurements. All the complexes showed thermal spin equilibria processes between the diamagnetic singlet ($S = 0$) and paramagnetic triplet states ($S = 1$), in which the triplet state is partially populated at room temperature.

RESUMO

Este trabalho de doutoramento desenvolvido ao longo destes quatro anos visou a síntese e a caracterização completa de novos complexos de metais de transição de cobalto(II) e níquel(II) com ênfase para o estudo das suas propriedades magnéticas.

O Capítulo 1 explorou novos complexos homoléticos de Co(II) bidentados contendo dois ligandos monoaniônicos 2-iminopirrolilo, com diferentes propriedades estereoquímicas e eletrônicas, como magnetos de íão único (*Single-Ion Magnets* ou *SIMs*). O *design* do precursor de ligando (volume estereoquímico, assimetria e capacidade de doação eletrônica) é de grande importância, pois irá determinar a geometria nesta família de compostos e, assim, permitir o controlo e otimização das suas características como SIMs. Os estudos magnéticos foram realizados experimentalmente por medidas estáticas (DC) e dinâmicas (AC), por espectroscopia de ressonância paramagnética eletrônica a alto campo (HFEP) e estimados por cálculos teóricos *ab initio*. Todos os complexos apresentaram relaxação lenta da magnetização, a maioria a campo DC zero, com elevados valores para o parâmetro de anisotropia, D , e para a barreira de energia de reversão de spin U_{eff} . Todos esses estudos forneceram uma visão da correlação entre a geometria e as propriedades magnéticas, concluindo-se que a mudança de uma geometria tetraédrica distorcida para piramidal trigonal distorcida aumenta esse comportamento, não só tornando mais negativos os valores de D , mas também exibindo relaxação lenta da magnetização a campo DC zero com valores elevados de U_{eff} .

O Capítulo 2 apresenta um novo procedimento sintético para os novos complexos de níquel do tipo $[\text{Ni}(\eta^5\text{-C}_5\text{Me}_5)(t\text{Bu}_2\text{Im})\text{X}]$ ($\text{X} = \text{Cl}, \text{Br}$ e I) em que o carbeno $t\text{Bu}_2\text{Im}$ foi utilizado no lugar dos sais de imidazólio correspondentes. Estes compostos foram totalmente caracterizados e as suas propriedades magnéticas, nomeadamente os equilíbrios de spin existentes, foram estudados em solução por espectroscopia de ressonância magnética nuclear (RMN) de ^1H a temperatura variável e pelo método de Evans, e em estado sólido por medidas de magnetização DC. Todos os complexos apresentaram processos térmicos de equilíbrio de spin entre o estado singleto diamagnético ($S = 0$) e o estado tripleto paramagnético ($S = 1$), em que o estado tripleto se encontra parcialmente preenchido à temperatura ambiente.

KEYWORDS

Iminopyrrolyl ligands

Single-Ion Magnets

Pentamethylcyclopentadienyl ligands

N-Heterocyclic carbenes

Spin equilibrium

PALAVRAS-CHAVE

Ligandos iminopirrolilo

Magnetos de íão único

Ligandos pentametilciclopentadienilo

Carbenos N-heterocíclicos

Equilíbrios de spin

Acknowledgments

Throughout this project, many obstacles emerged and were overcome with the support and help of some people that I cannot fail to mention. This dissertation is not entirely mine but also of those who contributed in some way to this work.

I thank the Fundação para a Ciência e a Tecnologia for the financial support of my PhD fellowship (PD/BD/135530/2018– ChemMat PhD Program) and the research project PTDC/QUI-QIN/31585/2017. I also thank Instituto Superior Técnico (IST), Centro de Química Estrutural (CQE), in particular the IOARC group, and Centro de Ciências e Tecnologias Nucleares (C²TN), in particular the Solid-State group, for providing all the facilities required for the development of this work.

To my supervisor Doctor Pedro Teixeira Gomes, I would like to thank this research opportunity, which greatly contributed to the enrichment of my academic, scientific and personal knowledge. I also thank the guidance, patience and availability always manifested both inside and outside the laboratory.

To my co-supervisor Doctor Laura Pereira, I thank all the knowledge transmitted and encouragement during this journey. I also appreciate the patience since initially I was very green in the field of magnetism.

I am grateful to my co-supervisor Doctor Manuel Almeida for guidance and sharing thoughts and critical review of this dissertation.

I would like to thank Doctor Teresa Duarte for the opportunity to learn single crystal X-ray diffraction as well as to Doctor Clara Gomes for teaching me the technique at the beginning when solving my first crystal structures, for guiding me through the lab and for all the knowledge shared.

To Doctor Nuno Bandeira a special thank you for all the theoretical calculations presented in this work, a fundamental piece of work for the complete study of the magnetic properties of these compounds.

To Doctor Joris van Slageren and his PhD students David Hunger and Alexander Allgaier, from the University of Stuttgart, I would like to thank all the HFEPR measurements, which were essential for the complete characterization of the compounds studied. I also thank the hospitality offered during my 3 weeks stay in Stuttgart.

I also would like to thank Doctor José António Paixão and his PhD student José Malta for giving me the opportunity to complete the AC measurements that I needed to finish this work and for the time spent with me. It was a pleasure to be with both of you.

To all my colleagues that became friends Ana Cerdeira, Ana Rodrigues, Carina Fialho, César Reis, Clara Gomes, Cláudia Figueira, Joana Hipólito, Luís Alves, Patrícia Lopes, Rita Ruivo, Tiago Cruz and Vanessa Cacho, a special thank you for the guidance, advice and fun moments shared.

To my friends outside Lisbon a special thank you for the relaxing moments, support and encouragement, despite not understanding what I was working on.

E por último, mas não menos importante, quero agradecer à minha família em especial à minha mãe, irmã e sobrinha/afilhada pelo apoio incondicional, motivação e paciência em todas as fases deste percurso. Um especial agradecimento à minha afilhada pelos fins de semana cheios de diversão e cansaço físico, que tanto precisava para quebrar o ritmo exaustivo de escrita.

Patrícia da Silva Ferreira

1.1.5	Bis(2-iminopyrrolyl) metal complexes.....	34
1.1.6	Objectives of the present work	42
1.2	RESULTS AND DISCUSSION	44
1.2.1	The 5-substituted-2-iminopyrrolyl ligand precursors.....	44
1.2.1.1	Synthesis and characterization.....	44
1.2.2	Homoleptic bis(5-substituted-2-iminopyrrolyl) Co(II) complexes	46
1.2.2.1	Synthesis and characterization.....	46
1.2.2.2	X-ray diffraction studies.....	48
1.2.2.3	Complexes 1.4a-e : influence of sterically bulky ligands and geometrically congested iminopyrrolyl Co(II) complexes on the SIM behavior	54
1.2.2.3.1	Static (DC) magnetic measurements of complexes 1.4a-e	55
1.2.2.3.2	The calculation of ZFS parameters <i>D</i> and <i>E</i>	57
1.2.2.3.2.1	HFEPR spectroscopy of complexes 1.4a-d	59
1.2.2.3.2.2	Theoretical studies of complexes 1.4a-d	61
1.2.2.3.3	Dynamic (AC) magnetic measurements for complexes 1.4a-d	68
1.2.2.3.4	Magnetic studies on complex 1.4e	77
1.2.2.3.4.1	HFEPR measurements for complex 1.4e	78
1.2.2.3.4.2	Theoretical calculations for complex 1.4e	79
1.2.2.3.4.3	Dynamic (AC) magnetic measurements of complex 1.4e	79
1.2.2.4	Complexes 1.4f-i : influence of the ligand asymmetry and electron-donor ability on the SIM behavior	83
1.2.2.4.1	Static (DC) magnetic studies	84
1.2.2.4.2	HFEPR measurements.....	85
1.2.2.4.3	Theoretical calculations.....	87
1.2.2.4.4	Dynamic (AC) magnetic studies	88
1.2.3	Conclusion.....	98
1.3	EXPERIMENTAL SECTION	100
1.3.1	General considerations	100
1.3.2	Characterization techniques and methodologies	100
1.3.2.1	Nuclear Magnetic Resonance (NMR)	100
1.3.2.2	Single crystal X-ray diffraction	101
1.3.2.3	Elemental analysis	102
1.3.2.4	HFEPR spectroscopy	102
1.3.2.5	Computational studies	102

1.3.2.6	Magnetic measurements	103
1.3.3	Synthetic procedures.....	104
1.3.3.1	General procedure for the synthesis of 5-substituted-2-(<i>N</i> -formimino)-1 <i>H</i> -pyrroles (1.3d and 1.3f-i).....	104
1.3.3.1.1	Synthesis of 5-(adamant-1-yl)-2-[<i>N</i> -(adamant-1-yl)formimino]pyrrole (1.3d).....	104
1.3.3.1.2	Synthesis of 5-phenyl-2-[<i>N</i> -(2- <i>t</i> -butylphenyl)formimino]pyrrole (1.3f).....	105
1.3.3.1.3	Synthesis of 5-(3,5-trifluoromethyl)-2-[<i>N</i> -(2- <i>t</i> -butylphenyl)formimino]pyrrole (1.3g)	106
1.3.3.1.4	Synthesis of 5-(2,6-dimethoxyphenyl)-2-[<i>N</i> -(2- <i>t</i> -butylphenyl)formimino]pyrrole (1.3h)	107
1.3.3.1.5	Synthesis of 5-(2,6-dimethylphenyl)-2-[<i>N</i> -(2- <i>t</i> -butylphenyl)formimino]pyrrole (1.3i)	108
1.3.3.2	General procedure for the syntheses of homoleptic bis(5-substituted-2-iminopyrrolyl) Co(II) complexes (1.4d-i).....	109
1.3.3.2.1	Synthesis of [Co{ κ^2N,N' -5-(adamant-1-yl)-NC ₄ H ₂ -2-C(H)=N(adamant-1-yl)}] (1.4d).....	109
1.3.3.2.2	Synthesis of [Co{ κ^2N,N' -5-(2,4,6- <i>i</i> Pr ₃ -C ₆ H ₂)-NC ₄ H ₂ -2-C(H)=N(2,6- <i>i</i> Pr ₂ -C ₆ H ₃)} ₂] (1.4e)	110
1.3.3.2.3	Synthesis of [Co{ κ^2N,N' -5-(C ₆ H ₅)-NC ₄ H ₂ -2-C(H)=N(<i>t</i> Bu-C ₆ H ₄)} ₂] (1.4f)	111
1.3.3.2.4	Synthesis of [Co{ κ^2N,N' -5-(3,5-(CF ₃) ₂ -C ₆ H ₃)-NC ₄ H ₂ -2-C(H)=N(<i>t</i> Bu-C ₆ H ₄)} ₂] (1.4g).....	111
1.3.3.2.5	Synthesis of [Co{ κ^2N,N' -5-(2,6-(OCH ₃) ₂ -C ₆ H ₃)-NC ₄ H ₂ -2-C(H)=N(<i>t</i> Bu-C ₆ H ₄)} ₂] (1.4h).....	112
1.3.3.2.6	Synthesis of [Co{ κ^2N,N' -5-(2,6-(CH ₃) ₂ -C ₆ H ₃)-NC ₄ H ₂ -2-C(H)=N(<i>t</i> Bu-C ₆ H ₄)} ₂] (1.4i).....	113
1.4	REFERENCES	114

**CHAPTER 2: Pentamethylcyclopentadienyl nickel(II)
complexes stabilized by N-heterocyclic carbenes (NHCs) as
spin equilibrium molecules**

2.1	INTRODUCTION	125
2.1.1	Cyclopentadienyl ligand.....	125
2.1.1.1	Coordination to metals	125
2.1.1.2	Types of metal-cyclopentadienyl complexes	129
2.1.1.3	Spin equilibrium	130
2.1.1.4	Dynamic processes	132
2.1.1.5	Reactivity.....	133
2.1.2	Pentamethylcyclopentadienyl ligand.....	135
2.1.3	Carbenes	136
2.1.3.1	Electronic structure and stabilization	136
2.1.3.2	Classification of carbenes.....	138
2.1.3.2.1	N-Heterocyclic carbene ligands	139
2.1.3.2.1.1	Historical overview	139
2.1.3.2.1.2	Coordination of NHCs to metals.....	142
2.1.3.2.1.3	Electronic influence on the M–NHC bond.....	143
2.1.3.2.1.4	Stereochemical influence on the M–NHC bond.....	145
2.1.3.2.1.5	Applications of organometallic complexes stabilized by NHC ligands.....	146
2.1.4	Pentamethylcyclopentadienyl Nickel complexes stabilized by NHC ligands.....	147
2.1.5	Objectives of the present work	152
2.2	RESULTS AND DISCUSSION	153
2.2.1	Pentamethylcyclopentadienyl Nickel complexes	153
2.2.1.1	Synthesis of new $[\text{Ni}(\eta^5\text{-C}_5\text{Me}_5)(\text{NHC})\text{X}]$ compounds.....	153
2.2.1.2	X-ray diffraction studies.....	156
2.2.1.3	Nuclear Magnetic Resonance (NMR) studies	161
2.2.1.4	Spin Equilibrium	165
2.2.1.5	Magnetic properties	168
2.2.2	Conclusions	172

2.3	EXPERIMENTAL SECTION	174
2.3.1	General considerations	174
2.3.2	Characterization techniques.....	174
2.3.2.1	Nuclear Magnetic Resonance	174
2.3.2.2	Single crystal X-ray diffraction	175
2.3.2.3	Elemental analysis	175
2.3.2.4	Magnetic measurements	176
2.3.3	Synthetic procedures.....	176
2.3.3.1	General procedure for the syntheses of $[\text{Ni}(\eta^5\text{-C}_5\text{Me}_5)(\text{tBu}_2\text{Im})\text{X}]$	176
2.3.3.1.1	Synthesis of $[\text{Ni}(\eta^5\text{-C}_5\text{Me}_5)(\text{tBu}_2\text{Im})\text{Cl}]$ (2.4a)	176
2.3.3.1.2	Synthesis of $[\text{Ni}(\eta^5\text{-C}_5\text{Me}_5)(\text{tBu}_2\text{Im})\text{Br}]$ (2.4b).....	177
2.3.3.1.3	Synthesis of $[\text{Ni}(\eta^5\text{-C}_5\text{Me}_5)(\text{tBu}_2\text{Im})\text{I}]$ (2.4c).....	178
2.3.3.2	Synthesis of $[\text{Ni}(\eta^5\text{-C}_5\text{Me}_5)\{\text{a}(\text{tBu}_2\text{Im})\}\text{Cl}]$ (2.5).....	179
2.4	REFERENCES	180

CHAPTER 3: Conclusions and Future Perspectives

3.1	GENERAL CONCLUSIONS	189
3.2	FUTURE PRESPECTIVES	190
	APPENDIX I: Magnetometers	193
	APPENDIX II: Crystallographic data	203
	APPENDIX III: Fitting parameters of the generalized Debye model	209

INDEX OF FIGURES

Figure 1.1	(a) Schematic diagram demonstrating the magnetization and magnetic relaxation processes in a SMM and (b) the slow relaxation of the magnetization in SMMs with an easy axis, results from an energetic preference for the magnetization to be aligned along the predominant axis of magnetic anisotropy 5	5
Figure 1.2	(a) Temperature dependence of the inverse of the magnetic susceptibility, χ^{-1} , in three situations: $\theta = 0$ (ideal paramagnet, red), $\theta > 0$ (paramagnet with ferromagnetic interactions, green) and $\theta < 0$ (paramagnet with antiferromagnetic interactions, blue) and (b) temperature dependence of the χT product (and of μ_{eff}) for the three situations..... 8	8
Figure 1.3	Typical magnetic hysteresis loop of a ferromagnet 10	10
Figure 1.4	Plots of the (a) in-phase (χ') and (b) out-of-phase (χ'') signals in typical AC susceptibility studies vs. temperature in an AC field oscillating at the indicated frequencies..... 12	12
Figure 1.5	A typical Argand diagram or Cole-Cole plot..... 13	13
Figure 1.6	The high and low limits of the in-phase susceptibility corresponding to the isothermal and adiabatic susceptibility, while a relevant feature of the out-phase susceptibility is the possibility of determining the relaxation time τ 13	13
Figure 1.7	Argand or Cole-Cole plot where the solid lines represent the best fits to the experimental data using the generalized Debye model..... 14	14
Figure 1.8	Potential energy diagram for SMM changes as the field is applied 16	16
Figure 1.9	Illustration of the three primary mechanisms for spin–lattice relaxation of magnetization and their temperature dependence 17	17
Figure 1.10	Arrhenius plot constructed from data. Dashed lines represent data fits to the Direct (dark yellow), QTM (dark cyan), Raman (purple), and Orbach (blue) processes. The solid green line represents the best fit to the Equation 1.21 for the four processes simultaneously 19	19

- Figure 1.11** (a) Magnetic structure of the molecule $\text{Mn}_{12}\text{-OAc}$. Orange arrows, green arrows, red spheres, and grey spheres represent Mn(III), Mn(IV), O, and C atoms, respectively. The orientation of the arrows represents the antiferromagnetic coupling between Mn(III) and Mn(IV) ions leading to an overall $S = 10$ ground states, (b) temperature dependence of the real component of the magnetic susceptibility of a powdered sample of $\text{Mn}_{12}\text{-OAc}$; in the inset the imaginary component of the AC susceptibility is displayed at three different frequencies and (c) magnetization vs. magnetic field hysteresis loop of $\text{Mn}_{12}\text{-OAc}$ at 1.77, 2.10 and 2.64 K; the red dotted lines correspond to characteristic applied field values, which enhance the magnetic relaxation through QTM.....20
- Figure 1.12** View of the cluster Fe_8 . The red, yellow, purple and grey circles represent the iron, oxygen, nitrogen and carbon atoms, respectively. The spin structure of the $S = 10$ ground state is schematized by the arrows 22
- Figure 1.13** Dependence of the hysteresis loops of Fe_8 on the field sweeping rate in the pure tunneling regime ($T = 0.3$ K)23
- Figure 1.14** Structure of the trigonal pyramidal complex $[\text{Fe}(\text{tpa}^{\text{Mes}})]^-$ (**L1**) and splitting of the $3d$ orbital energies. Orange, blue, and grey spheres represent Fe, N, and C atoms, respectively. Hydrogen atoms were omitted for clarity25
- Figure 1.15** General structure of four-coordinate trigonal pyramidal Fe(II) complexes, $[\text{Fe}(\text{tpa}^{\text{R}})]^-$ (**L1-L5**)26
- Figure 1.16** Structure of the tetracoordinate $[\text{Co}(\text{SPh})_4]^{2-}$ (**L6**) complex and splitting of the d orbital energies. Purple, yellow, and grey spheres represent Co, S, and C atoms, respectively. Hydrogen atoms were omitted for clarity27
- Figure 1.17** (a) Frequency dependence of the molar out-of-phase AC susceptibility (χ_M'') collected at temperature intervals of 0.1 K between 1.7 and 2.4 K and intervals of 0.2 K between 2.4 and 7.0 K, with no applied DC field and (b) molar out-of-phase AC susceptibility (χ_M'') collected at 2 K under applied DC fields from 0 to 1 kOe in 100 Oe increments. Solid lines are guides for the eye.....28
- Figure 1.18** Molecular structures of compounds **L10**, **L11** and **L12**, respectively.....29

Figure 1.19	Energies of the <i>d</i> orbitals of the D_{2d} symmetrized $[\text{Co}(\text{XPh})_4]^{2-}$ (X = O (L7); X = S (L8); X = Se (L9); X = Te) complexes computed by <i>ab initio</i> LFT	30
Figure 1.20	Molecular structure of compounds L16 (X = Cl), L17 (X = Br) and L18 (X = I).....	30
Figure 1.21	Tetrahedral N_4 -coordinated Co(II) complexes (L20-L24) displaying SIM behavior reported in the literature.....	33
Figure 1.22	(a) 2-iminopyrrolyl and (b) 5-substituted-2-iminopyrrolyl ligands	34
Figure 1.23	Bis(2-iminopyrrolyl) chromium complexes	35
Figure 1.24	Bis(iminopyrrolyl) zirconium complexes	36
Figure 1.25	Bis(iminopyrrolyl) titanium complexes.....	36
Figure 1.26	Hafnium bis(iminopyrrolyl) complexes.....	37
Figure 1.27	Group 5 and 6 metal complexes with 2-iminopyrrolyl ligands	38
Figure 1.28	Homoleptic bis[2-(<i>N</i> -arylimino)pyrrolyl] metal complexes.....	39
Figure 1.29	Iron and cobalt complexes bearing 2-iminopyrrolyl ligands reported by our research group.....	39
Figure 1.30	Homoleptic nickel(II), copper(II) and zinc(II) compounds bearing 2-iminopyrrolyl ligands	40
Figure 1.31	Alkaline-earth metal complexes with 2-iminopyrrolyl ligands	40
Figure 1.32	Rare-earth metal complexes bearing iminopyrrolyl ligands.....	41
Figure 1.33	Synthetic route used to prepare the 5-substituted-2-iminopyrrole ligand precursors 1.3a-i	44
Figure 1.34	Synthetic routes used to prepare the 2-substituted pyrroles 1.1a-i	45
Figure 1.35	Synthesis of 5-substituted-2-formylpyrroles 1.2a-i	45
Figure 1.36	Synthesis of 5-substituted-2-iminopyrrolyl ligand precursors 1.3a-i	46
Figure 1.37	Synthesis of homoleptic Co(II) complexes 1.4d-i	47
Figure 1.38	ORTEP-3 diagrams with ellipsoids drawn at 30% probability level. All hydrogen atoms were omitted for clarity	50
Figure 1.39	ORTEP-3 diagrams with ellipsoids drawn at 30% probability level, showing the geometry of the five-membered coordinating chelates in compounds 1.4d-e , 1.4f and 1.4i . The hydrogen atoms and the remaining ligand carbon atoms were omitted for clarity	51
Figure 1.40	Crystal packing of complex 1.4g , when viewed along <i>b</i> . The interactions mentioned in the text are not shown for clarity	53

Figure 1.41	Crystal packing of complex 1.4h , when viewed along <i>b</i> . The interactions mentioned in the text are not shown for clarity	53
Figure 1.42	Complexes 1.4a-e studied in this work.....	55
Figure 1.43	$\chi_M T$ vs. <i>T</i> plot measured at 500 Oe for complexes 1.4a-d (left) and $\chi_M T$ vs. <i>T</i> plot measured at 500 Oe for complex 1.4e . The red line represents the simulation on the basis of the spin Hamiltonian parameters (right).....	56
Figure 1.44	<i>M</i> vs. <i>B</i> plot measured from 0 to 5 T at different fixed temperatures for complexes 1.4a-e	57
Figure 1.45	HFEPR spectra of a pressed powder pellet of complex 1.4a at <i>T</i> = 5 K and different frequencies (left) and HFEPR spectra of a pressed powder pellet of complex 1.4a at ν = 300 GHz and different temperatures (right). The black lines represent the measurement, red lines the simulation on the basis of the spin Hamiltonian parameters. The strong resonance line at fields higher than 10 T is due to an instrumental artefact.	59
Figure 1.46	HFEPR spectra of a pressed powder pellet of complex 1.4b at ν = 300 GHz and different temperatures. Black lines represent the measurement, red lines the simulation on the basis of the spin Hamiltonian parameters. The strong resonance line at fields higher than 10 T is due to an instrumental artefact.....	60
Figure 1.47	HFEPR spectra of a pressed powder pellet of complexes (a) 1.4c at ν = 320 GHz and different temperatures and (b) 1.4d at <i>T</i> = 50 K and different frequencies (left) and at ν = 320 GHz and different temperatures (right). Black lines represent the measurement, red lines the simulation on the basis of the spin Hamiltonian parameters. The strong resonance line at fields higher than 10 T is due to an instrumental artefact.....	61
Figure 1.48	Calculated zero-field splitting plots with transition moments between each spin-orbit state. The two crystallographic units of complex 1.4a are shown in plot (a), 1.4b in (b), 1.4c in (c) and 1.4d in (d)	62
Figure 1.49	Active space orbitals of complex 1.4a shown in their magnetic axis frame	63
Figure 1.50	AILFT-NEVPT2 3 <i>d</i> orbital splitting of metal complexes 1.4a-d . The green and red arrows correspond to the energy gap between the $3d_{x^2-y^2} \rightarrow 3d_{xy}$ and $3d_{z^2} \rightarrow 3d_{yz}$ orbitals, respectively	63

Figure 1.51	Magnetostructural analysis of the D parameter (a) and E/D (b) as a function of planarization (improper dihedral angle ϕ) of a tetrahedral bis(2-iminopyrrolyl) Co(II) model complex.	65
Figure 1.52	Magnetostructural analysis of the D parameter (a), E/D (b) and ligand field (c) as a function of angle ω , representing the pyramidalization of a tetrahedral bis(2-iminopyrrolyl) Co(II) model complex (at the center of the left plot). In left, the dummy atoms used as a reference for the angle value are shown in pink.....	66
Figure 1.53	Variation of D (a) and E/D (b) with the ligand bite angle θ	67
Figure 1.54	Temperature dependence of the in-phase χ' (left) and out-of-phase χ'' (right) magnetic susceptibilities in the absence of an external magnetic field at different frequencies for complexes (a) 1.4a , (b) 1.4b , (c) 1.4c and (d) 1.4d	69
Figure 1.55	Frequency dependence of the in-phase χ' (left) and out-of-phase χ'' (right) magnetic susceptibilities at different temperatures for complex 1.4c under zero DC field. The solid lines are for guidance	70
Figure 1.56	Frequency dependence of the in-phase χ' (left) and out-of-phase χ'' (right) magnetic susceptibilities at different temperatures for complex 1.4d under zero DC field. The solid lines are for guidance	70
Figure 1.57	Cole-Cole plot for complex 1.4c in the absence of an external magnetic field. The solid lines represent the best fits to the experimental data using the generalized Debye model (left) and $\ln(\tau)$ vs. T^{-1} plot for 1.4c in the absence of an external magnetic field; the red line is the fit for the Orbach process using the Arrhenius law (right)	70
Figure 1.58	Cole-Cole plot for complex 1.4d in the absence of an external magnetic field. The solid lines represent the best fits to the experimental data using the generalized Debye model (left) and $\ln(\tau)$ vs. T^{-1} plot for 1.4d in the absence of an external magnetic field; the red line is the fit for the Orbach process using the Arrhenius law (right)	71
Figure 1.59	Temperature dependence of the in-phase χ' (left) and out-of-phase χ'' (right) magnetic susceptibilities at different frequencies for complexes (a) 1.4a under 3000 Oe, (b) 1.4b under 1000 Oe, (c) 1.4c under 800 Oe and (d) 1.4d under 800 Oe	72

Figure 1.60	Frequency dependence of the in-phase χ' (left) and out-of-phase χ'' (right) magnetic susceptibilities at different temperatures for complexes (a) 1.4a at 3000 Oe, (b) 1.4b at 1000 Oe, (c) 1.4c at 800 Oe and (d) 1.4d at 800 Oe. The solid lines are for guidance.....	73
Figure 1.61	Cole-Cole plots for complexes (a) 1.4a under a DC field of 3000 Oe, (b) 1.4b under a DC field of 1000 Oe, (c) 1.4c under a DC field of 800 Oe and (d) 1.4d under a DC field of 800 Oe. The solid lines represent the best fits to the experimental data using the generalized Debye model	74
Figure 1.62	$\ln(\tau)$ vs. T^{-1} plots, the red lines are the best fits to the sum of Raman and Orbach processes (a) for 1.4a under 3000 Oe, (b) for 1.4b under 1000 Oe, (c) 1.4c under 800 Oe and (d) 1.4d under 800 Oe.....	75
Figure 1.63	HFEPR spectra of a pressed powder pellet of complex 1.4e at $\nu = 320$ GHz and different temperatures, in the range of 4-9 T. Black lines represent the measurement and red lines the simulation on the basis of the spin Hamiltonian parameters	78
Figure 1.64	Kramers doublets and zero-field splitting of complex 1.4e with associated transition magnetic moments between each state	79
Figure 1.65	Temperature dependence of the in-phase χ' (left) and out-of-phase χ'' (right) magnetic susceptibilities for complex 1.4e in the absence of a DC field, at different frequencies.....	80
Figure 1.66	Frequency dependence of the in-phase χ' (left) and out-of-phase χ'' (right) magnetic susceptibilities at different temperatures for complex 1.4e in the absence of a DC field. The solid lines are for guidance.	80
Figure 1.67	Cole-Cole plot for 1.4e in the absence of an external magnetic field. The solid lines represent the best fits to the experimental data using the generalized Debye model (left) and $\ln(\tau)$ vs. T^{-1} plot for 1.4e in the absence of an external magnetic field, the red lines are the best fits to the sum of Raman (green line) and Orbach (blue line) processes (right)	81
Figure 1.68	Superposition of both $\ln(\tau)$ vs. T^{-1} plots under $H_{DC} = 0$ Oe (black) and $H_{DC} = 1200$ Oe (red) for complex 1.4e	82
Figure 1.69	Complexes studied in this work 1.4f-i	83
Figure 1.70	$\chi_M T$ vs. T plot measured at 500 Oe for complexes 1.4f-h (left) and $\chi_M T$ vs. T plot measured at 500 Oe for complex 1.4i . The red line represents the simulation on the basis of the spin Hamiltonian parameters (right).....	84

Figure 1.71	<i>M</i> vs. <i>B</i> plot measured from 0 to 5 T at different fixed temperatures for complexes 1.4f-i	85
Figure 1.72	HFEPR spectra of a pressed powder pellet (a) of complex 1.4f at $\nu = 275$ GHz at different temperatures, (b) of complex 1.4g at $T = 10$ K at different frequencies (left) and at $\nu = 375$ GHz at different temperatures (right) and (c) of complex 1.4i at $\nu = 275$ GHz at different temperatures. Black lines represent the measurement, red lines the simulation on the basis of the spin Hamiltonian parameters	86
Figure 1.73	Calculated zero-field splitting plots with transition moments between each spin-orbit state for (a) complex 1.4f , (b) the two crystallographic units of 1.4g , (c) for 1.4h and (d) for 1.4i	88
Figure 1.74	Temperature dependence of the in-phase χ' (left) and out-of-phase χ'' (right) magnetic susceptibilities in the absence of an external magnetic field at different frequencies for complexes (a) 1.4f , (b) 1.4g , (c) 1.4h and (d) 1.4i	89
Figure 1.75	Frequency dependence of the in-phase χ' (left) and out-of-phase χ'' (right) magnetic susceptibilities at different temperatures for complex 1.4i in the absence of a DC field. The solid lines are for guidance	90
Figure 1.76	Cole-Cole plot for complex 1.4i in the absence of an external magnetic field. The solid lines represent the best fits to the experimental data using the generalized Debye model (left) and $\ln(\tau)$ vs. T^{-1} plot for 1.4i in the absence of an external magnetic field, the red line is the best fit to the sum of Raman and Orbach processes (right).....	91
Figure 1.77	Temperature dependence of the in-phase, χ' (left) and out-of-phase, χ'' (right) magnetic susceptibilities at different frequencies for complexes (a) 1.4f under 2000 Oe, (b) 1.4g under 1000 Oe, (c) 1.4h under 1500 Oe and (d) 1.4i under 1200 Oe.....	92
Figure 1.78	Frequency dependence of the in-phase χ' (left) and out-of-phase χ'' (right) magnetic susceptibilities at different temperatures for complexes (a) 1.4f at 2000 Oe, (b) 1.4g at 1000 Oe, (c) 1.4h at 1500 Oe and (d) 1.4i at 1200 Oe. The solid lines are for guidance	93
Figure 1.79	Cole-Cole plots for complexes (a) 1.4f under a DC field of 2000 Oe, (b) 1.4g under a DC field of 1000 Oe, (c) 1.4h under a DC field of 1500 Oe and (d) 1.4i under a DC field of 1200 Oe. The solid lines	

	represent the best fits to the experimental data using the generalized Debye model	94
Figure 1.80	Ln(τ) vs. T^{-1} plots, the red lines are the best fits to the sum of Raman and Orbach processes (a) for 1.4f under 2000 Oe, (b) for 1.4g under 1000 Oe, (c) 1.4h under 1500 Oe and (d) 1.4i under 1200 Oe	95
Figure 1.81	Experimental and calculated χT vs T curves ($H = 500$ Oe) (left) and magnetization curves ($T = 2$ K) (right) of the 1.4h complex.....	96
Figure 2.1	(a) Cyclopentadiene and (b) cyclopentadienyl anion.....	125
Figure 2.2	Different Cp binding modes to metals	126
Figure 2.3	Cp slippage promoted by the addition of CO by photoinduction	127
Figure 2.4	Synthesis of $[\text{Ni}(\eta^5\text{-C}_5\text{H}_5)(\eta^1\text{-C}_5\text{H}_5)(\text{R}_2\text{Im})]$ compounds L1 and L2	127
Figure 2.5	Molecular orbital diagram of cyclopentadienyl ligand.....	128
Figure 2.6	Ene-allyl, diene and intermediate distortions of the η^5 -Cp ligand. In each case, the L-Ni-X plane is indicated by a dashed line.....	129
Figure 2.7	Structural varieties of Cp based-metal complexes.....	130
Figure 2.8	Chemical structure of $[\text{Ni}(\eta^5\text{-C}_5(\text{CH}_3)_5)(\text{acac})]$	131
Figure 2.9	Schematic representation of singlet ($S = 0$) and triplet ($S = 1$) states	131
Figure 2.10	Fluxional processes of Cp ligands in the L1 complex: ring whizzing of η^1 -Cp and rotation of η^5 -Cp around the metal coordination axis	133
Figure 2.11	Synthesis of compounds L4 and L5	134
Figure 2.12	Synthesis of compounds L7 and L8	134
Figure 2.13	Synthesis of compound L9	135
Figure 2.14	(a) Pentamethylcyclopentadiene and (b) pentamethylcyclopentadienyl anion.....	135
Figure 2.15	Relationship between the carbene bond angle and the nature of the frontier orbitals.....	136
Figure 2.16	Representation of the singlet and triplet states of the carbene.....	137
Figure 2.17	(a) Fisher type carbene and (b) Schrock type carbene.....	138
Figure 2.18	Illustration of the difference in bonding between (a) Fischer carbenes showing donor-acceptor bonding, and (b) Schrock carbenes showing covalent bonding.....	139
Figure 2.19	Synthesis of complexes with imidazol-2-ylidene: (a) by Öfele and (b) by Wanzlick	140
Figure 2.20	NHCs trapped but not isolated by Wanzlick.....	140

Figure 2.21	First isolated stable imidazol-2-ylidene	140
Figure 2.22	Ground-state electronic configuration showing the π -electron-donating and σ -electron-withdrawing effects of the nitrogen atoms in the stabilization of the singlet carbene structure and resonance structures of an NHC ligand.....	141
Figure 2.23	Structures of some of the most important classes of NHCs.....	142
Figure 2.24	π -Backdonation in metallic carbonyls containing the ligand L: (a) a good π -acceptor disfavors M \rightarrow CO backdonation, increasing the frequency of stretching of the C-O bond and (b) a bad π -acceptor favors M \rightarrow CO backdonation, decreasing the frequency of bond stretching C-O.....	144
Figure 2.25	Classification of carbenes in descending order of basicity	145
Figure 2.26	Representation of the dimensions of the sphere for determination of the % V_{bur} parameter in NHC ligands	145
Figure 2.27	Synthesis of compound L12 by Abernethy	147
Figure 2.28	Synthesis of compounds L13-L17	148
Figure 2.29	Synthesis of compounds L20 and L21	148
Figure 2.30	Synthesis of cationic Cp* compounds L22-L24	149
Figure 2.31	Synthesis of compounds L26 from L25 and LiCp*	150
Figure 2.32	Synthesis of compounds L28-L32 with chelating Cp-NHC ligands.....	150
Figure 2.33	Synthesis of compounds L33-L35 with chelating Cp-NHC ligands.....	151
Figure 2.34	Synthetic route of compounds 2.4a-c and 2.5	154
Figure 2.35	Normal NHC with coordination through the C2 carbon to the metal center and abnormal NHC with coordination to the metal through the C4 carbon	155
Figure 2.36	ORTEP-3 diagram for complexes (a) 2.4b (b) 2.4c and (c) 2.5 with ellipsoids drawn at 30 % probability level. All hydrogen atoms were omitted for clarity.....	157
Figure 2.37	Molecular structures of 2.4b (top) and 2.4c (bottom) revealing the diene distortions	160
Figure 2.38	Molecular structure of 2.5 revealing the ene-allyl distortion.....	160
Figure 2.39	Symmetry plane containing the halogen, nickel, NHC carbene carbon atoms and the Cp* _{centroid} (Cg) on compound 2.4b	161
Figure 2.40	Stacking of VT- ¹ H NMR spectra for compound 2.4a , in toluene- <i>d</i> ₈	162

Figure 2.41	^1H NMR spectrum for compound 2.4a at +90 °C	163
Figure 2.42	Stacking of VT- ^1H NMR spectra for compound 2.4b , in toluene- d_8	163
Figure 2.43	^1H NMR spectrum for compound 2.4b at +90 °C.....	164
Figure 2.44	Stacking of VT- ^1H NMR spectra for compound 2.4c , in toluene- d_8	164
Figure 2.45	^1H NMR spectrum for compound 2.4c at +90 °C	165
Figure 2.46	δ vs T plots for the ^1H NMR resonances of compounds 2.4a-c (a) for $t\text{Bu}$ and $\text{C}_5(\text{CH}_3)_5$ and (b) for $\text{HC}=\text{CH}$ resonances. The solid lines represent the best fits to the experimental data using the Equation 2.1.....	166
Figure 2.47	$\chi_M T$ vs. T plot for compound 2.4a-c	170
Figure 2.48	Schematic drawing of the plot $\chi_M T$ vs. T in a molecule exhibiting a spin transition process.....	171
Figure I.1	The direct-current (DC) SQUID consisting of two Josephson junctions arranged on a superconducting ring.....	195
Figure I.2	(a) Schematic setup of a SQUID magnetometer with 2nd order gradiometer (left). The centering SQUID response VSQUID versus sample position (right) and (b) three quarter section view of the standard cryostat and insert.....	196
Figure I.3	SQUID (Cryogenic Ltd.) facility available at C2TN.....	197
Figure I.4	^3He insert.....	197
Figure I.5	MagLab 2000 (Oxford Instruments) facility available at C2TN-IST	198
Figure I.6	Magnetic properties probe of the MagLab 2000 multipurpose characterization system (Oxford Instruments).....	198
Figure I.7	Schematic diagram of a general VSM	199
Figure I.8	VSM (Cryogenic Ltd.) facility available at C2TN-IST	200

INDEX OF TABLES

Table 1.1	Spin Hamiltonian and Orbach relaxation parameters for L7–L928
Table 1.2	A list of four-coordinate Co(II) complexes showing SIM behavior. Some of them are described in the text32
Table 1.3	Effective magnetic moments μ_{eff} (μ_B) measured in toluene- d_8 solution (Evans method) and in solid state (SQUID method), at r.t. for complexes 1.4d-i48
Table 1.4	Selected bond distances (\AA), bond angles ($^\circ$) and parameters τ_4 for complexes 1.4d-i49
Table 1.5	Dihedral angles of <i>N</i> -aryl ring and 5-aryl ring relative to the 2-iminopyrrolyl moiety of complexes 1.4e-i52
Table 1.6	List of intermolecular interactions for complexes 1.4g–h54
Table 1.7	Calculated and experimental (HFEPFR) <i>D</i> , <i>E</i> and <i>g</i> values for complexes 1.4a-d64
Table 1.8	Bite angles θ , dihedral angles ϕ and interligand angles ω for complexes 1.4a-d66
Table 1.9	Orbach and Raman relaxation parameters for complexes 1.4a-d76
Table 1.10	Calculated and experimental <i>D</i> , <i>E</i> and <i>g</i> values for complex 1.4e79
Table 1.11	Bite angles θ , dihedral angle ϕ and interligand angle ω for complex 1.4e83
Table 1.12	Calculated and experimental <i>D</i> , <i>E</i> and <i>g</i> values for complexes 1.4f-i87
Table 1.13	Orbach and Raman relaxation parameters for complexes 1.4f-i95
Table 1.14	Bite angles θ , dihedral angles ϕ and interligand angles ω for complexes 1.4f-i97
Table 2.1	Variation of the reaction conditions in order to obtain compounds 2.4a-c and their abnormal analogues155
Table 2.2	Selected bond distances (\AA) and bond angles ($^\circ$), dihedral angles α and β for complexes 2.4b-c and 2.5158

Table 2.3	Chemical shifts (ppm) of ¹ H NMR resonances of compounds 2.4a-c , at room temperature, in toluene- <i>d</i> ₈	161
Table 2.4	Thermodynamic parameters of the spin transition obtained from the fits of the ¹ H NMR resonances for complexes 2.4a-c	167
Table 2.5	Effective magnetic moments μ_{eff} (μ_B) measured in benzene solution (Evans method) and in solid state (SQUID magnetometry), at r.t. for complexes 2.4a-c	168
Table 2.6	k , ΔG and x_T calculated from the μ_{eff} obtained in solution (Evans method) and in solid state (SQUID magnetometry), at r.t. for complexes 2.4a-c	169
Table II.1	Crystallographic data and refinement details of complexes 1.4d-f	205
Table II.2	Crystallographic data and refinement details of complexes 1.4g-i	206
Table II.2	Crystallographic data and refinement details of complexes 2.4b-c and 2.5	207
Table III.1	Fitting parameters of the generalized Debye model for complex 1.4a , from 5.5 to 14 K, under an applied DC field of 3000 Oe	211
Table III.2	Fitting parameters of the generalized Debye model for complex 1.4b , from 7 to 15 K, under an applied DC field of 1000 Oe	211
Table III.3	Fitting parameters of the generalized Debye model for complex 1.4c , from 5 to 10 K, without the application of a DC field.....	212
Table III.4	Fitting parameters of the generalized Debye model for complex 1.4c , from 5 to 12 K, under an applied DC field of 800 Oe	212
Table III.5	Fitting parameters of the generalized Debye model for complex 1.4d , from 7 to 11 K, without the application of a DC field.....	213
Table III.6	Fitting parameters of the generalized Debye model for complex 1.4d , from 5.5 to 10.5 K, under an applied DC field of 800 Oe	213
Table III.7	Fitting parameters of the generalized Debye model for complex 1.4e , from 6 to 13.5 K, without the application of a DC field.....	214
Table III.8	Fitting parameters of the generalized Debye model for complex 1.4e , from 5.5 to 13.5 K, under an applied DC field of 1200 Oe	215
Table III.9	Fitting parameters of the generalized Debye model for complex 1.4f , from 6 to 12 K, under an applied DC field of 2000 Oe.	216
Table III.10	Fitting parameters of the generalized Debye model for complex 1.4g , from 3.5 to 20 K, under an applied DC field of 1000 Oe.	216

Table III.11	Fitting parameters of the generalized Debye model for complex 1.4h , from 6 to 14 K, under an applied DC field of 1500 Oe.	217
Table III.12	Fitting parameters of the generalized Debye model for complex 1.4i , from 7.5 to 17.5 K, without the application of a DC field.....	218
Table III.13	Fitting parameters of the generalized Debye model for complex 1.4i , from 6 to 17.5 K, under an applied DC field 1200 Oe	219

Abbreviations

χ_S	Adiabatic susceptibility
χ_T	Isothermal susceptibility
τ_0	Relaxation rate
^{13}C NMR	Carbon-13 nuclear magnetic resonance
^1H NMR	<i>Proton nuclear magnetic resonance</i>
Å	<i>Angstrom</i>
AC	Alternating-current
Acac	Acetylacetonate
AILFT	<i>Ab initio</i> Ligand-Field Theory
aNHC	Abnormal N-heterocyclic carbene
br	Broad
C_6D_6	Benzene
<i>ca.</i>	<i>Circa</i> (approximately)
CASSCF	Complete Active Space Self-Consistent Field
Co	Cobalt
Cp	Cyclopentadienyl
Cp*	Pentamethylcyclopentadienyl
C_{Raman}	Raman coefficient
d	Doublet
D	Uniaxial anisotropy parameter or axial zero field splitting parameter
DC	Direct-current
DMSO	Dimethyl sulfoxide
E	Rhombic or transverse zero field splitting parameter
Fe_8	$[\text{Fe}_8\text{O}_2(\text{OH})_{12}(\text{tacn})_6]\text{Br}_8(\text{H}_2\text{O})_9$ cluster
FTIR	Fourier-transform infrared spectroscopy
g	Landé g-factor
H	Magnetic field
HFEPR	High-Frequency Electron Paramagnetic Resonance

HOMO	Highest occupied molecular orbital
<i>i.e.</i>	<i>Id est</i> (that is)
Im	Imidazol-2-ylidene
<i>J</i>	Coupling constants
JT	Jahn-Teller
KD	Kramers doublet
KOtBu	Potassium <i>ter</i> -butoxide
L	Ligand
LiBr	Lithium bromide
LiBu	Butyllithium
LiCl	Lithium chloride
LUMO	Lowest Unoccupied Molecular Orbital
χ_M	Molar magnetic susceptibility
m	Multiplet
$M(B)$	Magnetization in function of the field
MAO	Methylaluminoxane
Mn ₁₂ -OAc	[Mn ₁₂ O ₁₂ (CH ₃ COO) ₁₆ (H ₂ O) ₄] \cdot 2CH ₃ COOH \cdot 4H ₂ O cluster
NaH	Sodium hydride
NaI	Sodium iodide
NHC	N-heterocyclic carbene
Ni	Nickel
NMR	Nuclear magnetic resonance
nNHC	Normal N-heterocyclic carbene
n_{Raman}	Raman relaxation exponent
PEt ₃	Triethylphosphine
Ph	Phenyl
PPh ₃	Triphenylphosphine
ppm	Parts per million
PPMS	Physical Property Measurement System
QD-NEVPT2	Quasi-Degenerate N-Electron Valence Perturbational Theory
QTM	Quantum Tunneling of Magnetization
s	Singlet
SIM	Single-Ion Magnet
SMM	Single Molecule Magnet

SOC	Spin-orbit coupling
SQUID	Superconducting Quantum Interference Device
t	Triplet
T_B	<i>Blocking temperature</i>
tBu	<i>Tert-butyl</i>
tBu ₂ Im	1,3-bis(<i>tert-butyl</i>)imidazol-2-ylidene
T_c	Critical temperature
TEP	Tolman electronic parameter
THF	Tetrahydrofuran
Tol.	Toluene
U_{eff}	Spin-reversal energy barrier
vs.	<i>versus</i>
VSM	Vibrating Sample Magnetometer
VT- ¹ H NMR	Variable-temperature NMR experiments
ZFS	Zero-field splitting
α	Dispersion coefficient
δ	Chemical shift
η^n	Ligand hapticity
μ_{eff}	Effective magnetic moment
τ	Magnetization relaxation time
χ''	Imaginary or out-of-phase component
χ'	Real or in-phase component
$\chi''(T)$	Out-of-phase component in function of the temperature

CHAPTER 1

Single-Ion Magnet (SIM) behavior in new 2-iminopyrrolyl cobalt(II) complexes

The following works resulted from this chapter: (a) Ferreira, P. S.; Cerdeira, A. C.; Cruz, T. F. C.; Bandeira, N. A. G.; Hunger, D.; Allgaier, A.; van Slageren, J.; Almeida, M.; Pereira, L. C. J.; Gomes, P. T. *Inorg. Chem. Front.* **2022**, *9*, 4302-4319; (b) Ferreira, P. S.; Malta, J. F.; Bandeira, N. A. G.; Allgaier, A.; van Slageren, J.; Paixão, J. A.; Almeida, M.; Pereira, L. C. J.; Gomes, P. T. *Chem. Commun.* **2022**, *58*, 9682-9685; (c) Ferreira, P. S.; Malta, J. F.; Bandeira, N. A. G.; Allgaier, A.; van Slageren, J.; Paixão, J. A.; Almeida, M.; Pereira, L. C. J.; Gomes, P. T. **2022**, manuscript in preparation; (d) Ferreira, P. S.; Cerdeira, A. C.; Bandeira, N. A. G.; Hunger, D.; Allgaier, A.; van Slageren, J.; Almeida, M.; Pereira, L. C. J.; Gomes, P. T. **2022**, manuscript in preparation.

1.1 INTRODUCTION

Since the discovery in 1993 of the first molecular material behaving as a Single-Molecule Magnet (SMM), considerable attention has been given to SMMs owing to their remarkable potential applications in several areas such as in data storage and processing, quantum computing and in molecular spintronics.¹

1.1.1 The concept of a Single-Molecule Magnet

Single-Molecule Magnets, a designation employed for the first time by David Hendrickson and George Christou in 1996,² are molecules with slow relaxation of the magnetization of purely molecular origin.³ In these molecules, in response to an external magnetic field, the molecular magnetic moment can be oriented parallel to the field and at sufficiently low temperatures, below a *blocking temperature* (T_B), will retain its value after the field has been removed. This gives rise to a hysteresis loop in a magnetization vs. field cycle (see below Figure 1.3), considered as a consequence of the slow relaxation of the magnetization, and this is one of the requirements for these molecules to function effectively as a means of data storage.

An interesting feature in molecular nanomagnets is the coexistence of classical and quantum scales, since the same molecule can behave as a simple paramagnet and as a magnet. The magnetic hysteresis results from individual non-interacting molecules, where each SMM has a large enough magnetic moment and magnetic anisotropy to behave as a magnet, in a behavior different from that of a large number of magnetic particles cooperatively interacting over large distances in a lattice, as in conventional magnets.⁴⁻⁶

The magnetic behavior of SMMs is governed by the anisotropic zero-field splitting (ZFS) parameters D and E , according to this Hamiltonian:

$$\hat{H} = D \left[\hat{S}_z^2 - \frac{S(S+1)}{3} \right] + E(\hat{S}_x^2 - \hat{S}_y^2) \quad (1.1)$$

where D and E are the axial and rhombic (the latter also called transverse) ZFS parameters, respectively, which reflect the type of symmetry around the magnetic center and \hat{S} is the spin operator that describes the spin projection along a given axis.^{6,7}

Chapter 1

Therefore, the effect of the ZFS is to lift the degeneracy of the $2S+1$ spin states (M_s levels) in the absence of an external magnetic field. For a cubic symmetry D and E are zero and thus the M_s levels are all degenerate. For an axial symmetry $D < 0$ and $E = 0$, the magnetization is preferentially oriented parallel to the z axis, and so the M_s levels are degenerated pairs. The case when $D < 0$ and $E \neq 0$ corresponds to the existence of transverse magnetic anisotropy (in the xy plane), meaning that the degeneracy of the M_s levels is removed.⁶ The sign of D is critical, since it determines the type of magnetic anisotropy associated with the S multiplet, describing the separation of the M_s states within the spin ground state. A positive sign $D > 0$ (easy plane anisotropy) implies that the $M_s = 0$ state (or the $M_s = \pm 1/2$ states for half integer S or Kramer systems) will have the lowest energy. On the other hand, a negative sign $D < 0$ (easy axis anisotropy), with some exceptions, is a characteristic of SMMs, indicates that $M_s = \pm S$ states are those with lower energy (Figure 1.1a). The energy difference between $M_s = 0$ or $\pm 1/2$ and $M_s = \pm S$ is called U_{eff} and represents an energy barrier to thermal inversion of the magnetic moment.⁶⁻⁸

The magnetization and relaxation processes are traditionally described by the double-well potential energy diagram, where the two wells represent the lowest energy $\pm M_s$ levels, and M_s is the summation of individual spin quantum numbers (m_s) of the unpaired electrons (Figure 1.1a). At zero field all $2S+1$ M_s levels are degenerate pairs, considering the $-S$ the “spin down”, or “0” in binary coding, and $+S$ the “spin up”, or “1”.

When an external magnetic field is applied, the unpaired spins of the SMM align along a specific direction, the so-called easy axis (by definition, the z -direction), that normally corresponds to the most energetically favorable direction of spontaneous magnetization in a system (Figure 1.1b). This alignment allows the stabilization of one side of the well, $-M_s$ levels, due to Zeeman effect. The magnetization of the system reaches the saturation point when only the $M_s = -S$ level remains populated. If the thermal energy of the system, $k_B T$, is lower than the energy required to escalate all the M_s states and reach the top of the well overcoming the barrier, this means that the magnetization can be retained in the lowest level for a certain time. Therefore, after the removal of the field, the system will be unable to randomly reorientate its magnetic moment and will thus remain trapped in a potential energy minimum (providing $k_B T$ never becomes greater than U_{eff}).^{6,9,10}

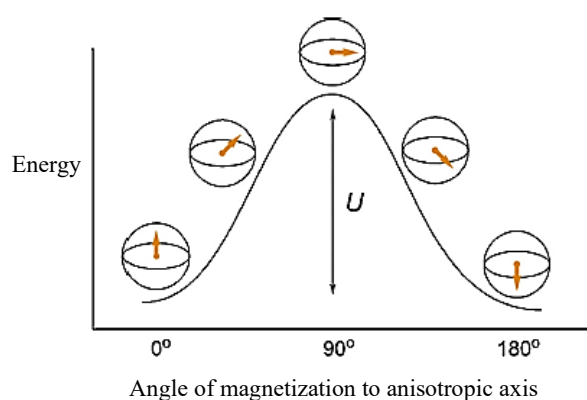
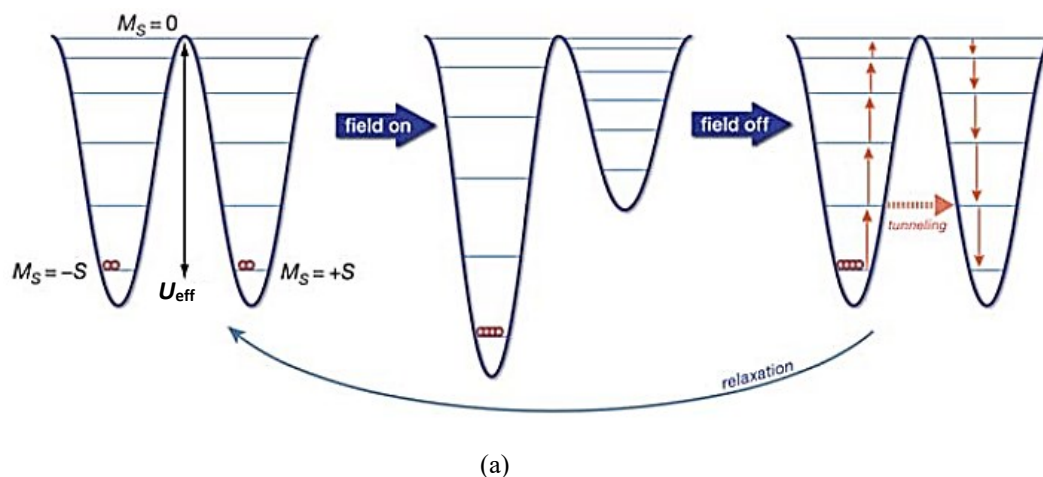


Figure 1.1 (a) Schematic diagram demonstrating the magnetization and magnetic relaxation processes in a SMM (adapted from Ref. 6) and (b) the slow relaxation of the magnetization in SMMs with an easy axis results from an energetic preference for the magnetization to be aligned along the predominant axis of magnetic anisotropy.⁸

Therefore, the higher the barrier the longer the relaxation time will be and, consequently, the longer the magnetization can be retained. The U_{eff} can be estimated, under condition of axial symmetry (x,y equivalent), using the following equations:

$$U_{eff} = S^2 |D| \text{ for integer spin systems} \quad (1.2)$$

$$U_{eff} = \left(S^2 - \frac{1}{4}\right) |D| \text{ for half-integer spin systems} \quad (1.3)$$

In order to obtain higher values of U_{eff} , SMMs need to follow two requirements: a large spin ground state (S) and a large and negative magnetic anisotropy, easy axis type, $D < 0$.⁵ However, efforts to obtain SMMs from polynuclear transition metal complexes, in order to increase S , did not succeed since the energy barrier does not increase proportionally.

Chapter 1

Instead, in most of the cases, it decreased. One of the reasons for such behavior is that S is inversely proportional to D , thus attempts to obtain better SMMs by increasing S have failed.^{6,7} Based on this fact, the strategy is currently focused on enhancing negative D values as a way to achieve higher spin-reversal barriers. Therefore, to reach this purpose there are some intrinsic prerequisites: first, the ground state should be doubly-degenerate and with a large value of M_s in order to maintain a high magnetic moment at temperatures where only the ground state is significantly populated; second, the separation between the bistable ground M_s state and the first excited M_s state should be large.

1.1.2 Magnetism: Basic notions

The physical basis for the magnetic properties of materials results from the electrons, both orbital and spin degrees of freedom, and how electrons interact with each other. So, when a material is placed under a magnetic field it gets magnetized and its magnetic response can be quantified by the magnetic susceptibility χ :

$$\chi = \frac{M}{H} \quad (1.4)$$

where the magnetization M is the sum of all magnetic moments of a given material per unit of volume or mass. The experimental susceptibility consists of the sum of two contributions, the paramagnetic (χ_p) and diamagnetic (χ_D) susceptibilities. Depending on the values of χ , magnetic materials are classified as paramagnetic when $\chi > 0$, where the spin of the unpaired electrons will tend to align parallel to an applied magnetic field, and those with $\chi < 0$ are classified as diamagnetic. Paramagnets placed in a non-homogeneous magnetic field are attracted to the field while the diamagnets are repelled. While the paramagnetic contribution to the magnetic susceptibility is due to the spins of unpaired electrons which tend to align parallel to the magnetic field, the diamagnetic contribution is due to interaction of the magnetic field with the motion of paired electrons in their orbitals, a contribution being present in all molecules.¹¹ It can be calculated using the Pascal's approach,¹² considering it as the sum of the diamagnetic contributions of all atoms, present in the molecules with corrections for the type of chemical bonds, oxidation states of ions and functional groups.¹³

Considering an ideal paramagnetic material, where there are no interactions between the magnetic moments, the paramagnetic susceptibility follows the Curie law:

$$\chi_P = \frac{C}{T} \quad (1.5)$$

where C is the so-called *Curie constant*, being defined for a system with a S spin as:

$$C = \frac{N\mu_B^2 \mu_{eff}}{3k_B} \quad (1.6)$$

where μ_{eff} is the effective magnetic moment, which for a system with spin-only contribution and total spin S is defined as:

$$\mu_{eff} = \sqrt{g^2 S(S + 1)} \quad (1.7)$$

Each atom has a magnetic moment that is randomly oriented as a result of thermal agitation. The application of a magnetic field favors the alignment of these moments increasing the magnetization. However, as the temperature rises the thermal agitation tends to random the orientation of the magnetic moments, decreasing the susceptibility. The Curie law corresponds to a linear relation by plotting χ^{-1} vs. T , at $T = 0$ K (C can be obtained from the slope of the line) (Figure 1.2a) or to a constant value in a plot of χT vs. T (Figure 1.2b).

In real paramagnetic systems, the interactions between magnetic moments often cannot be neglected and deviations from the Curie law are observed, corresponding to deviations to the above mentioned linear plots. Therefore, the Curie law is a special case of the more general Curie-Weiss law, where a new parameter, the *Weiss temperature* θ (which can be positive, negative, or zero) takes into account those interactions:

$$\chi = \frac{C}{T - \theta} \quad (1.8)$$

In a χT vs. T plot, when $\theta = 0$ K, the Curie-Weiss law is equivalent to the Curie law, displaying a horizontal line. When $\theta \neq 0$, interactions between neighboring magnetic

Chapter 1

moments take place, and the material is only paramagnetic above a certain transition temperature, and at lower temperatures magnetic ordering phase transitions can occur, or the system can undergo a transition to a spin glass. Thus, if θ is positive the χT vs. T plot increases upon cooling, suggesting the presence of ferromagnetic interactions, whereas if the θ is negative, a decrease in the plot might reveal the existence of antiferromagnetic interactions (Figure 1.2b).¹⁴

In order to obtain θ and C it is more appropriate to plot χT vs. T rather than χ vs. T since the former is less sensitive.¹⁵

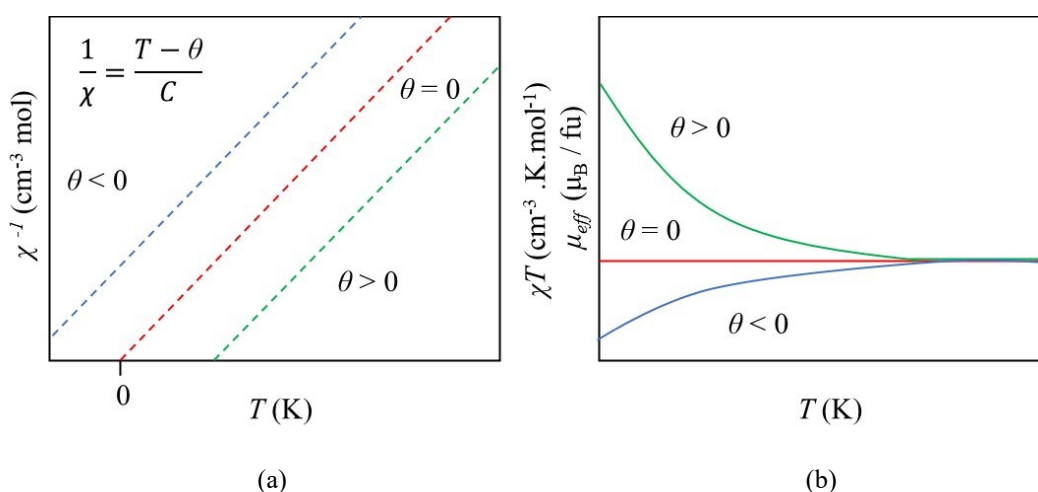


Figure 1.2 (a) Temperature dependence of the inverse of the magnetic susceptibility, χ^{-1} , in three situations: $\theta = 0$ (ideal paramagnet, red), $\theta > 0$ (paramagnet with ferromagnetic interactions, green) and $\theta < 0$ (paramagnet with antiferromagnetic interactions, blue) and (b) temperature dependence of the χT product (and of μ_{eff}) for the three situations.

1.1.2.1 Magnetic characterization of SMMs

As seen throughout the previous subsections it is essential to calculate important parameters such as T_B , D and U_{eff} , not only to identify the SMM behavior in the studied samples, but also to compare the results with other compounds. Static (direct-current DC) and dynamic (alternating-current AC) magnetization susceptibility measurements are two different types of measurements that allow the detection of SMM behavior in a given sample. The static measurements were performed using a 6.5 T S700X Superconducting Quantum Interference Device, SQUID, (Cryogenic Ltd.) magnetometer, under magnetic fields up to 7 T and at temperatures down to 1.7 K, while the dynamic measurements

were performed in the range of frequencies from 10 to 10000 Hz, using a MagLab 2000 (Oxford Instruments) and a Vibrating Sample Magnetometer, VSM, (Cryogenic Ltd.) at the Low Temperature and High Magnetic Field Laboratory of the Solid-State Group of C²TN-IST. In two of the studied samples (as will be mentioned further on) the AC measurements were performed using a PPMS magnetometer (Quantum Design) from the Physics Department, University of Coimbra.

Each equipment has its own operating methods, with different procedures concerning the sample preparation and calibrations. In a SQUID magnetometer, before starting measuring the sample, the same conditions of temperature and magnetic field were applied to the empty sample holder (straw and gelatin capsule), allowing the subtraction of its (diamagnetic) contribution. A diamagnetic correction for the compounds is also taken into account using the Pascal approach.¹²

The centering of the sample and the calibration are previously performed before starting the measurements in the MagLab 2000 and the VSM in both DC and AC modes.¹⁶ It is also crucial to degauss the magnet and then determine the remanent field, in order to compensate it during the magnetic measurements.

The three magnetometers are described in detail in Appendix I.

1.1.2.1.1 Static DC measurements

In a SQUID magnetometer, the magnetic moment of a sample is measured through an induction technique under a static DC magnetic field. The sample is moved vertically through a pickup coil, which detects variations in the flux via induced current. A set of superconducting pickup coils allows the signal to be proportional to the flux rather than being dependent of the sample movement. The detection coil is used to detect the change in magnetic flux due to the presence of the magnetic moment. The sample flux coupled to the detection coil is made to vary by moving the sample.^{17,18} Therefore, the two most useful measurements on studying a SMM behavior in a sample are:

- the magnetization of the sample at a constant field varying the temperature $M(T)$. This measurement gives information about the microstate level structure, and normally is represented by the molar magnetic susceptibility χ_M . In a $\chi_M T$ vs. T plot, the existence of

Chapter 1

ZFS will lead to a depopulation of the excited M_s states, causing the decrease of the $\chi_M T$ values, which is more evident at low temperatures. When this decrease is observed it can be indicative of one (or more) of the following possible contributions: (i) antiferromagnetic interactions between the metallic centers (see Figure 1.2b); (ii) the thermal depopulation reflecting the Boltzmann distribution over the M_s levels; and/or (iii) the presence of significant magnetic anisotropy.¹⁴

- the magnetic field dependence of the magnetization $M(B)$. The sample is magnetized by sweeping the magnetic field at a constant temperature while the magnetic moment of the sample is measured. This measurement gives information about the composition of the ground state, where at low temperatures and high fields only the lowest level is expected to be populated. Also, the appearance or not of a hysteresis in the cycle and its shape is given by this type of measurement (Figure 1.3).

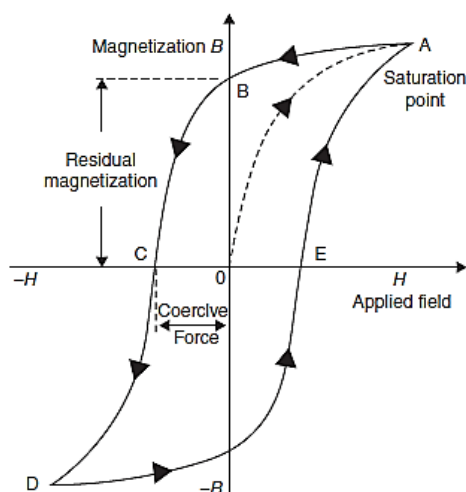


Figure 1.3 Typical magnetic hysteresis loop of a ferromagnet.¹⁵

At $H = 0$ the magnetic moment of a SMM is randomly orientated. When a magnetic field is applied, the magnetic moments tend to align parallel to the field, reaching the saturation, point A. When the field is reduced to zero, the sample magnetization will not relax back to its initial position with zero-magnetization and the amount of magnetization present is known as *remnant*, point B. The external magnetic field required to the complete demagnetization of the sample is known as coercivity field, point C. The cycle repeats itself when a magnetic field is applied in the opposite direction, path D to E.¹⁵ The maximum temperature at which the $M(B)$ hysteresis is observed is called the *blocking*

temperature (T_B). This value can be defined as the temperature below which the relaxation of the magnetization becomes slow compared to the time scale of measurement of a particular experimental cycling technique. T_B is strongly dependent on the scan rate (the faster the scan rate, the wider the loop and the higher the T_B) and on the sweep rate of the magnetic field, so it is only reliable to compare T_B of two compounds when they were both measured under the same sweep rate.¹⁹⁻²¹

Sometimes the hysteresis loop is not observed which can be attributed to either the occurrence of Quantum Tunneling of Magnetization relaxation process (see subsection 1.1.2.2) or by technical limitations of the equipment (in achieving high sweep rates or temperatures low enough).

1.1.2.1.2 Dynamic AC measurements

In an AC susceptometer the sample is generally centered within a detection coil and magnetized by an AC magnetic field. The magnetic moment of the sample follows the applied field cycle. The detection circuitry is generally balanced with a second identical pair of coils, but oppositely wound, empty coil to null out the flux changes related to the AC field. As a result, the AC susceptometer uses a detection coil to detect changes in the magnetic flux as in a DC magnetometer, but these changes are due to the changing moment of the sample as it responds to the AC field (no sample movement is required to produce an output signal) and not to the moment itself as in DC method. Thus, the AC technique consists in the differential response of the magnetization of the sample to an oscillating magnetic field where, in addition to this AC field, also a static field may be applied. This means that this technique detects changes in the magnetization that lead to dM/dH in the limit of small AC fields, and this is why sometimes it is referred to as a differential susceptibility, this being the main difference between the AC and DC measurement techniques.

In a DC experiment, the magnetic moment of the sample is not expected to change with time while in an AC measurement, the moment of the sample is actually changing in response to an applied AC field, allowing the possible dynamics of the magnetic system to be studied (that is why they are called static DC and dynamic AC measurements). So, while in a DC measurement the equilibrium value of the magnetization is determined, in

Chapter 1

an AC experiment a small AC drive magnetic field can be superimposed on a DC field. This causes a time-dependent moment in the sample, and therefore one can access the dynamic processes that might be occurring and that cannot be detected in DC measurements.^{22,23} These differences in the two techniques make them complementary and crucial in the complete study of compounds with SMM behavior.

In an AC measurement, when an AC field is applied depending on the dynamics of the individual magnetic moments, the magnetization of the compound tends to lag behind the driving field as it alternates, in a way that the measured magnetic susceptibility will incorporate a phase shift.²¹ This gives rise to the so-called in-phase and out-of-phase components of the susceptibility:

$$\chi_{AC}(\omega) = \chi'(\omega) + i\chi''(\omega) \quad (1.9)$$

where ω is the angular frequency (the frequency with which the AC field oscillates), χ' is the real (or in-phase) component, related to the reversible magnetization process, which stays in-phase with the applied oscillating field, and χ'' is the imaginary (or out-of-phase) component, related to losses due to the irreversible magnetization process and energy absorbed from the field.^{15,23}

During an AC measurement both χ' and χ'' components can be measured as a function of temperature, at fixed frequencies, and as function of the AC frequency. During a temperature dependence scan, as the temperature decreases a frequency-dependent maximum in the $\chi''(T)$ plot will appear indicating that the reversal of the spin has been blocked (Figure 1.4b).

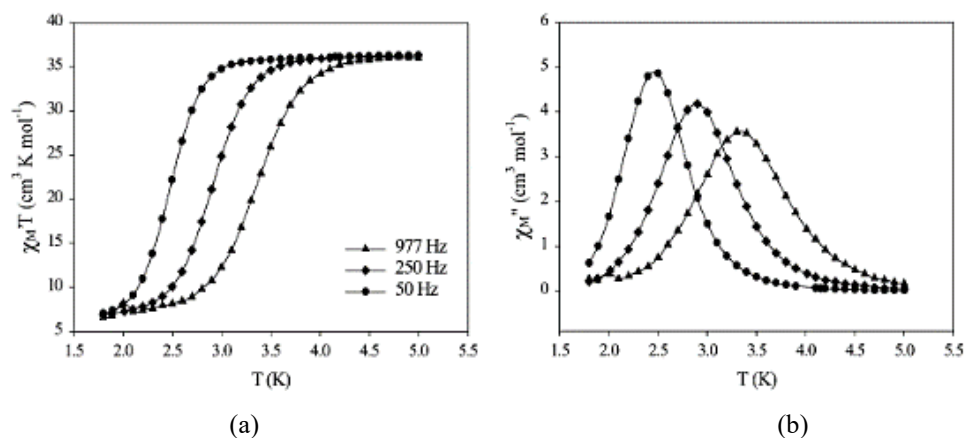


Figure 1.4 Plots of the (a) in-phase (χ') and (b) out-of-phase (χ'') signals in typical AC susceptibility studies vs. temperature in an AC field oscillating at the indicated frequencies.²⁴

The existence of an energy barrier to spin reversal prevents the magnetization to follow the fast field oscillations, causing a decrease of the in-phase component (Figure 1.4a) and an increase of the out-of-phase component as the frequency is increased (Figure 1.4b). The maximum out-of-phase signal is dependent on both frequency of the AC signal and the time of relaxation that is dependent on the temperature. Thus, in the $\chi''(T)$ plot by decreasing the frequency will lead to the shifting of the maximum to lower temperatures, indicating the presence of slow relaxation of the magnetization.^{7,20,21}

The frequency dependence of χ' and χ'' at different temperatures are also important to establish a SMM behavior since the relaxation processes involved as well as the energy barrier for the magnetization reversal can be estimated. By plotting χ'' vs. χ' , which is called Argand diagram or Cole-Cole plot (Figure 1.5), a semi-circular shape diagram can be obtained, where χ_T and χ_S are the limiting values of the diagram.¹⁵ When ω is low, $\omega\tau \ll 1$ (where τ is the magnetization relaxation time), the susceptibility measured is the isothermal one, χ_T , on the other hand, when $\omega\tau \gg 1$, the susceptibility measured is the adiabatic susceptibility χ_S . The maximum is when $\omega\tau = 1$ (Figures 1.5 and 1.6).^{3,15,25}

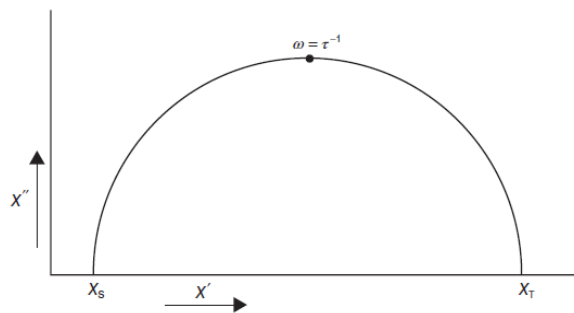


Figure 1.5 A typical Argand diagram or Cole-Cole plot.¹⁵

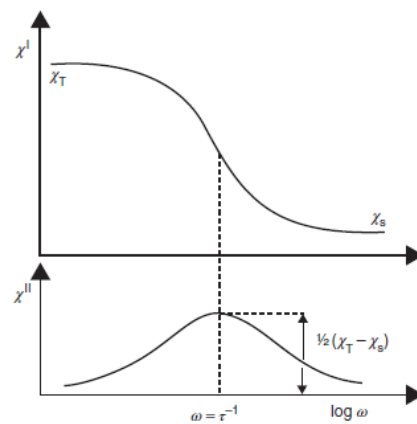


Figure 1.6 The high and low limits of the in-phase susceptibility corresponding to the isothermal and adiabatic susceptibility, while a relevant feature of the out-phase susceptibility is the possibility of determining the relaxation time τ .¹⁵

Chapter 1

The resulting data obtained by the frequency dependence measurements can be fitted using a generalized Debye model for the relaxation (Equations 1.10 to 1.12 and Figure 1.7):

$$\chi_{AC}(\omega) = \chi_S + \frac{(\chi_T - \chi_S)}{1 + (i\omega\tau)^{1-\alpha}} \quad (1.10)$$

$$\chi'(\omega) = \chi_S + (\chi_T - \chi_S) \frac{1 + (\omega\tau)^{1-\alpha} \sin(\frac{\pi\alpha}{2})}{1 + 2(\omega\tau)^{1-\alpha} \sin(\frac{\pi\alpha}{2}) + (\omega\tau)^{2(1-\alpha)}} \quad (1.11)$$

$$\chi''(\omega) = (\chi_T - \chi_S) \frac{1 + (\omega\tau)^{1-\alpha} \sin(\frac{\pi\alpha}{2})}{1 + 2(\omega\tau)^{1-\alpha} \sin(\frac{\pi\alpha}{2}) + (\omega\tau)^{2(1-\alpha)}} \quad (1.12)$$

where α is a parameter related to the distribution of the relaxation times ($0 \leq \alpha \leq 1$). If only a single relaxation process is present, α is near zero, and the shape of the plot approaches to a regular semi-circle. On the contrary, a large distribution gives large α values, and less symmetrical Argand plots. When $\alpha = 0$, Equations 1.10 to 1.12 are reduced to Equations 1.13 to 1.15, describing an ideal single relaxation process.^{3,15,25}

$$\chi_{AC}(\omega) = \chi_S + \frac{(\chi_T - \chi_S)}{1 + i\omega\tau} \quad (1.13)$$

$$\chi'(\omega) = \chi_S + \frac{(\chi_T - \chi_S)}{1 + \omega^2\tau^2} \quad (1.14)$$

$$\chi''(\omega) = \frac{(\chi_T - \chi_S) \omega\tau}{1 + \omega^2\tau^2} \quad (1.15)$$

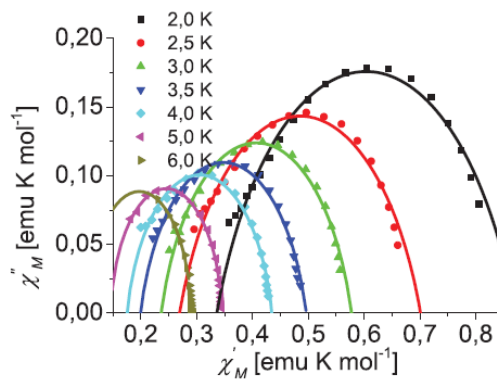


Figure 1.7 Argand or Cole-Cole plot where the solid lines represent the best fits to the experimental data using the generalized Debye model.²⁶

When more than one relaxation process is involved due to extrinsic factors (non-equivalent magnetic centers or effects of intermolecular interactions in the crystal)

or intramolecular origin,²⁷ the data is fitted using a linear combination of two modified Debye models as presented in Equation 1.16, with the β parameter being the weight ratio of both relaxation times:^{28–30}

$$\chi_{AC}(\omega) = \chi_S + (\chi_T - \chi_S) \left[\frac{\beta}{1+(i\omega\tau_1)^{1-\alpha_1}} + \frac{1-\beta}{1+(i\omega\tau_2)^{1-\alpha_2}} \right] \quad (1.16)$$

The AC susceptibility data after being fitted using the previous equations give the values of the aforementioned parameters χ_S , χ_T , α and τ . For a simplified SMM, the spin relaxation would occur through only a thermally activated mechanism called the Orbach process, where U_{eff} and the relaxation rate, τ_0 , can be determined by a linear fit of the $\ln(\tau)$ vs. T^{-1} plot, using the Arrhenius law:

$$\tau = \tau_0 \cdot \exp\left(\frac{U_{\text{eff}}}{k_B T}\right) \quad (1.17)$$

where T is the temperature at which the maximum is observed in the out-of-phase AC susceptibility and k_B is the Boltzmann constant. If the measurement is made at different frequencies, the U_{eff} and τ_0 can be determined from the $\ln(\tau)$ vs. T^{-1} plot.

Deviations from linearity in Arrhenius plots suggest that other relaxation mechanisms can also contribute to the magnetic relaxation, such as Quantum Tunneling of Magnetization (QTM), Direct, and Raman relaxation processes, originating U_{eff} values lower than expected.^{10,31}

Therefore, observation of hysteresis in the $M(B)$ plot and the presence of frequency-dependent signals in the out-of-phase AC susceptibility measurements are generally taken as evidence that a compound can be considered as a Single-Molecule Magnet.

1.1.2.2 Magnetic relaxation processes

Most of the compounds reported in the literature, despite having high values of magnetic anisotropy (D), present values of U_{eff} , obtained from the magnetic measurements far lower than the calculated values. This means that not only the Orbach process is contributing to the magnetic relaxation but also QTM, Direct and/or Raman

Chapter 1

processes may be present. These relaxation pathways were derived within the framework of the theory of spin lattice relaxation, which is concerned with the establishment of thermal equilibrium between a spin system and its surroundings, after a disturbance in the population of the system. In simple terms though, it is helpful to think about SMM systems as being composed of two parts, the spin and the lattice, with interactions between spin and lattice vibrations (phonons) offering additional relaxation pathways to the overall system.¹⁰

At low temperatures, QTM begins to compete with the thermal relaxation processes. This process allows the spin to flip through tunneling from an M_s state on one side of the barrier to a resonant M_s state (Figure 1.1). So, the barrier is completely bypassed without requiring external energy to do so. It is an unwanted mechanism because not only decreases the value of the effective barrier, but also because it is responsible for the lack of (or low) signal in the out-of-phase component at zero DC field and, in many cases, for the lack of hysteresis loop in the $M(B)$ plots. One way to suppress it is by applying an external magnetic field bringing off-resonance the two states. In subsection 1.1.1 we have seen that when $H = 0$ all the M_s sublevels are degenerated pairs and therefore the QTM mechanism can occur between the degenerated ground state or the degenerated excited states. The application of a small DC field will lead to non-degenerated levels resulting in a lower rate of tunnelling, allowing the magnetization to relax predominately through the thermal regime down to lower temperatures (Figure 1.8). For a practical application of SMMs as components in memory devices, QTM needs to be suppressed. Otherwise, it will be impossible to store data without it rapidly being lost. As such, QTM remains a crucial point of investigation in SMM research.

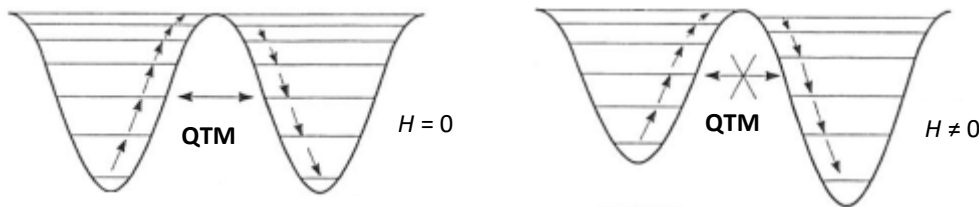


Figure 1.8 Potential energy diagram for SMM changes as the field is applied (adapted from Ref. 9).

This process can arise if there is a transverse anisotropy ($E \neq 0$ see subsection 1.1.1) in the system, which is introduced by distortions from purely axial symmetry. Therefore, the relationship between symmetry and the presence of transverse anisotropy needs to be kept in mind on the design of new SMMs in order to hinder this mechanism.

The tunnelling rate is usually described by Equation 1.18, where B_1 and B_2 are system dependent parameters that can be determined empirically.^{32,33} QTM is responsible for flattening the curve in the Arrhenius plot since it is completely temperature-independent process (see below Figure 1.10).

$$\tau_{\text{QTM}}^{-1} = \frac{B_1}{1+B_2 \times H^2} \quad (1.18)$$

The increase of the temperature allows the appearance of other dominating relaxation mechanisms like phonon-assisted processes such as the Direct, Orbach and Raman which are schematically indicated in Figure 1.9.

The Direct process involves the spin of the molecule to flip from a $-M_s$ state to $+M_s$ state with emission of a single phonon. The relaxation time depends not only on the temperature, but also on the magnetic field strength, H , meaning that at zero magnetic field this pathway should not be considered.

$$\tau_{\text{Direct}}^{-1} = A_{\text{Direct}} \times H^{n_{\text{Direct}}} \times T \quad (1.19)$$

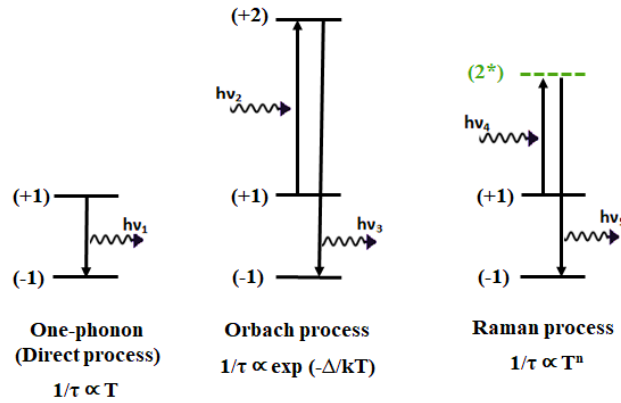


Figure 1.9 Illustration of the three primary mechanisms for spin–lattice relaxation of magnetization and their temperature dependence (adapted from Ref. 33).

The Direct coefficient (A_{Direct}) is empirically determined, and the Direct relaxation exponent (n_{Direct}) varies accordingly with the nature of the system. For Kramers systems $n_{\text{Direct}} = 4$, while for non-Kramers $n_{\text{Direct}} = 2$. This relaxation process becomes more relevant for the so-called field-induced SMMs, where the slow relaxation is observed only under a static DC field.^{32,34}

Chapter 1

The Orbach process is related with the absorption of a phonon followed by phonon emission and relaxation from an excited state. It is the only process that directly depends on the energy gap between M_s levels. As seen in the previous subsection (1.1.2.1.2), the U_{eff} value can be determined by a linear fit of the $\ln(\tau)$ vs. T^{-1} using an Arrhenius law (Equation 1.17).

The Raman process is analogous to the Orbach mechanism, with the exception that the relaxation occurs from a virtual state. While in the Orbach process the phonon energies correspond to the energy separation between real electronic states, in the Raman process it proceeds through absorption and reemission of virtual phonons.

$$\tau_{\text{Raman}}^{-1} = C_{\text{Raman}} \times T^{n_{\text{Raman}}} \quad (1.20)$$

Similarly to the Direct process, the Raman coefficient (C_{Raman}) is also empirical, and the Raman relaxation exponent (n_{Raman}) also varies accordingly with the nature of the system. Ideally, for non-Kramers systems with isolated ground states $n = 7$; for Kramers systems in the same conditions $n = 9$; and for systems with very low-lying states, *i.e.*, thermally populated excited states, $n = 5$.^{32,34}

The combination of all the above relaxation mechanism can be described by Equation 1.21:

$$\tau^{-1} = \underbrace{\frac{B_1}{1 + B_2 H^2}}_{\text{QTM}} + \underbrace{A H^{n_1} T}_{\text{Direct}} + \underbrace{C T^{n_2}}_{\text{Raman}} + \underbrace{\tau_0^{-1} \exp\left(-\frac{U_{\text{eff}}}{k_B T}\right)}_{\text{Orbach}} \quad (1.21)$$

Phonons of all energies are involved in Raman and Orbach processes, their number not changing with the magnetic field, unlike what happens in the Direct mechanism, in which just phonons with a particular frequency are involved. So, at very low temperatures and/or at very high magnetic fields only one-phonon processes can be efficient. Conversely, at higher temperatures the Raman mechanism becomes competitive with the Orbach process.³⁴⁻³⁶

As previously mentioned, deviations from linearity in the Arrhenius plots are a sign that other relaxation mechanisms may be involved. Thus, Direct and Raman mechanisms

will be manifested through a curvature in the $\ln(\tau)$ vs. T^{-1} plot, while QTM is completely temperature-independent (Figure 1.10).

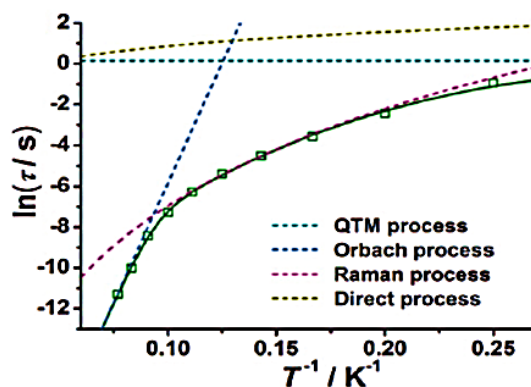


Figure 1.10 Arrhenius plot constructed from data. Dashed lines represent data fits to the Direct (dark yellow), QTM (dark cyan), Raman (purple), and Orbach (blue) processes. The solid green line represents the best fit to the Equation 1.21 for the four processes simultaneously.³⁶

In conclusion for a sample to behave as a strong SMM, a large thermal barrier and not significant QTM are required, so that the *blocking temperature* (T_B) can be as high as possible. For that, it is important to study and understand the correlation between the chemical structure with the magnetic behavior.

1.1.3 Historical overview: the most investigated SMMs

1.1.3.1 $[\text{Mn}_{12}\text{O}_{12}(\text{CH}_3\text{COO})_{16}(\text{H}_2\text{O})_4] \cdot 2\text{CH}_3\text{COOH} \cdot 4\text{H}_2\text{O}$

The first and most thoroughly studied SMM was a dodecanuclear manganese cluster $[\text{Mn}_{12}\text{O}_{12}(\text{CH}_3\text{COO})_{16}(\text{H}_2\text{O})_4] \cdot 2\text{CH}_3\text{COOH} \cdot 4\text{H}_2\text{O}$ (hereafter abbreviated as $\text{Mn}_{12}\text{-OAc}$), synthesized and structurally characterized by Lis in 1980,^{37a} obtained by addition of potassium permanganate to a solution of manganese acetate in acetic acid. The resulting cluster is tetragonal and contains eight manganese(III) centers with $S = 2$ and four manganese(IV) centers with $S = 3/2$, which are octahedrally coordinated (Figure 1.11a). Crystallographic data shows a S_4 symmetry, in which the four Mn(IV) ions are located in the central unit surrounded by the ring of eight Mn(III). The Mn(III) ions display a pronounced Jahn-Teller (JT) distortion by tetragonal elongation which will be

Chapter 1

the main contributor to the unexpected magnetic properties in this compound. In the early 1990s, Gatteschi and co-workers^{37b} established the magnetic properties of this cluster. The use of several techniques, such as High Field Magnetization and High Field EPR (HFEP) showed a spin ground state of $S = 10$ compatible with all Mn(III) spins up and all Mn(IV) spins down. The AC susceptibility was measured at zero applied field, where, in the out-of-phase component, frequency-dependent peaks were shown shifting to higher temperature on increasing the frequency, indicating slow relaxation of the magnetization (Figure 1.11b). However, the major breakthrough was just in 1993 when Sessoli *et al.*^{37c} discovered that the magnetization relaxation time became very long below 4 K, when a magnetic field along the tetragonal z axis is applied, originating a magnetic hysteresis of molecular origin (Figure 1.11c). Three years later, Thomas and co-workers^{37d} demonstrated that in addition to thermal activation, the reversal of the direction of the magnetization also occurs via QTM due to the existence of transverse anisotropy.

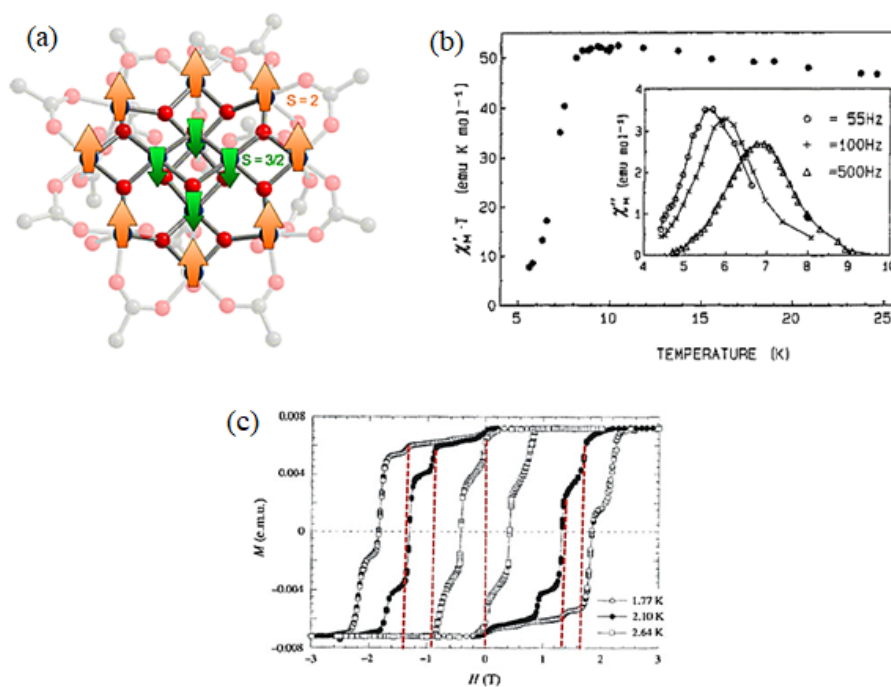


Figure 1.11 (a) Magnetic structure of the molecule Mn₁₂-OAc. Orange arrows, green arrows, red spheres, and grey spheres represent Mn(III), Mn(IV), O, and C atoms, respectively. The orientation of the arrows represents the antiferromagnetic coupling between Mn(III) and Mn(IV) ions leading to an overall $S = 10$ ground state,^{37c} (b) temperature dependence of the real component of the magnetic susceptibility of a powdered sample of Mn₁₂-OAc; in the inset the imaginary component of the AC susceptibility is displayed at three different frequencies^{37b} and (c) magnetization vs. magnetic field hysteresis loop of Mn₁₂-OAc at 1.77, 2.10 and 2.64 K; the red dotted lines correspond to characteristic applied field values, which enhance the magnetic relaxation through QTM.^{37f}

All these studies enable the calculation of the parameters: $T_B = 3$ K, $D = -0.50$ cm⁻¹ and $U_{\text{eff}} = 43$ cm⁻¹ (at *ca.* 61 K). HF-EPR investigations^{37g} established that the JT elongation axis of Mn(III) corresponds to an easy magnetic direction for the $S = 2$ spin and since the eight JT axes are roughly collinear, the local anisotropies sum up resulting in a huge anisotropy in the $S = 10$ ground state of the molecule. The magnetic moment then lies preferably along the tetragonal axis, and much less favorably perpendicular to it.

Unfortunately, its geometrical arrangement and the strong ferromagnetic interactions between spin carriers led to a system with a very low anisotropy.^{37h} So, the existence of a negative value of D induces a splitting of the 21 possible spin states, each level with a spin quantum number, M_s , which can be represented as a double-well potential energy diagram (Figure 1.1). At 2 K, by applying a magnetic field, the relaxation time for the Mn₁₂-OAc was on the order of two months.

The easy synthesis, good crystallinity, high stability in solution and the very interesting magnetic properties of Mn₁₂-OAc stimulated the synthesis and study of new analogous compounds with the goal of obtaining higher magnetic anisotropies and consequently energy barriers, and to preserve this behavior at a more accessible temperature. Thus, the [Mn₁₂O₁₂(RCOO)₁₆(H₂O)₄] (R = Me, Et, Ph, etc.) was the first SMM family studied, providing most of the current knowledge on this field and dominating SMM studies during the first subsequent years. More than a hundred of Mn₁₂-OAc analogous have been synthesized and magnetically characterized in the past decades, being the largest family of SMMs.³⁸⁻⁴⁰

1.1.3.2 [Fe₈O₂(OH)₁₂(tacn)₆]Br₈(H₂O)₉

A second milestone in the development of SMMs was provided by the octanuclear Fe(III) oxo-hydroxo cluster [Fe₈O₂(OH)₁₂(tacn)₆]⁸⁺, where tacn = 1,4,7-triazacyclononane (hereafter abbreviated as Fe₈). Similarly to what happened to the Mn₁₂-OAc complex, the synthesis and isolation of this Fe(III) cluster was reported by Wieghardt in 1984,^{41a} more than a decade before its properties as SMM were discovered. It was prepared by controlled hydrolysis of [Fe(tacn)Cl₃] in a water/pyridine mixture with the addition of sodium bromide. Crystallographic data showed that the internal Fe(III) ions are octahedrally coordinated to two oxides and four hydroxo bridges, the two Fe(III) (Fe3

Chapter 1

and Fe4) are coordinated to three nitrogen atoms, two hydroxides and one oxide ion and the remaining external Fe(III) are coordinated to three nitrogen atoms and three hydroxyl groups. The oxo ligands form μ_3 bridges, while the hydroxy ligands form μ_2 bridges. Fe1, Fe2, Fe3, Fe4 form a structure described as butterfly, which is often found in polynuclear metal complexes.^{41a-c} The temperature dependence of $\chi_M T$ indicates a ferromagnetic behavior with a spin ground state of $S = 10$ due to the eight $S = 5/2$ iron spins, six spins up and two down confirmed also by high-field magnetization measurements (Figure 1.12).^{41d}

HFEPR showed that the ground $S = 10$ state is largely split in zero-field and that the splitting has a large rhombic component, large values of the $|E/D|$ ratio. By defining the orientation of the **D** tensor axes, it revealed that the easy axis makes a small angle, (about 10°) with the perpendicular to the plane of the iron ions, while the hard axis passes through the Fe1 and Fe2 ions, this being the cause of the high values of E . This technique provided an accurate estimate of $D = -0.191 \text{ cm}^{-1}$ and $E = 0.032 \text{ cm}^{-1}$.^{41b,41f} The origin of the magnetic anisotropy responsible for the observed ZFS is presumably a mixture of dipolar and single ion contributions. Just like in $\text{Mn}_{12}\text{-OAc}$, Fe₈ also gives rise to a stepped hysteresis loop and the steps are also attributed to QTM (Figure 1.13).

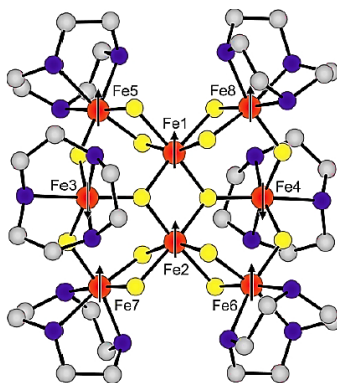


Figure 1.12 View of the cluster Fe₈. The red, yellow, purple and grey circles represent the iron, oxygen, nitrogen and carbon atoms, respectively. The spin structure of the $S = 10$ ground state is schematized by the arrows.^{41e}

The AC susceptibility measurements and Mössbauer spectroscopy showed that the magnetization relaxation of the cluster follows a thermally activated behavior with a U_{eff} of 22.2 K (*ca.* 15 cm^{-1}). For temperatures below 400 mK, the relaxation rate was temperature-independent suggesting that this cluster exhibits QTM, similarly to $\text{Mn}_{12}\text{-OAc}$.

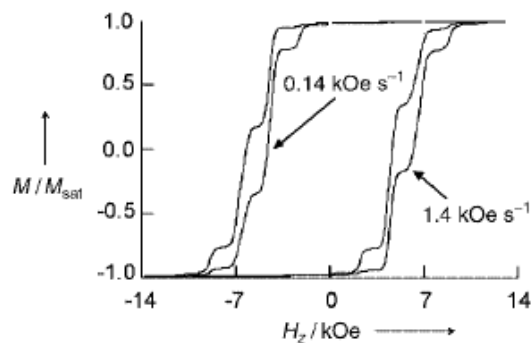


Figure 1.13 Dependence of the hysteresis loops of Fe_8 on the field sweeping rate in the pure tunneling regime ($T = 0.3 \text{ K}$).^{41g}

1.1.4 Single-Ion Magnets (SIMs)

For many years the main focus when synthesizing a compound with SMM behavior was to increase the spin quantum number S in order to proportionately increase the values of the barrier (see Equations 1.2 and 1.3). Driven by this assumption the number of polynuclear transition metal compounds with high values of S increased exponentially, the record being associated to a manganese cluster with an $S = 83/2$, comprising 19 Mn centers.⁴² However, when studying these compounds, a common factor is observed, the values of the ZFS parameter D are low and, consequently, it decreases the values of the barrier. The manganese family is one of the examples. As mentioned before for the $\text{Mn}_{12}\text{-OAc}$, the value of D is only of -0.50 cm^{-1} , while for the Mn_6 ($[\text{Mn}^{\text{III}}_6\text{O}_2(\text{Et-sao})_6(\text{O}_2\text{CPh}(\text{Me})_2)_2(\text{EtOH})_6]$, where $\text{sao} = 2\text{-hydroxybenzaldehyde oxime}$), which until 2013 had the record for the highest energy barrier among the $3d$ metal SMMs, the value is even smaller, -0.43 cm^{-1} .⁴³ Therefore, despite the efforts made to maximizing the S , the achievable barrier is constrained to 46 cm^{-1} and 62 cm^{-1} , respectively for the $\text{Mn}_{12}\text{-OAc}$ and Mn_6 systems. By comparing these values with those usually observed in mononuclear Mn complexes, it revealed that for an axially elongated Mn(III) center D is typically around -4.5 cm^{-1} , ten times greater than the values associated with the clusters mentioned above. The reasons leading to small magnetic anisotropies in polynuclear SMMs are the limited control of the precise symmetry of the compound and, consequently, of the alignment with the easy axis when several metal ions are present and the energy barrier, which essentially is not a function of the total spin S .

Chapter 1

Therefore, nowadays, the research is focused on enhancing the negative D values, to achieve higher spin-reversal barriers. One approach is the design of mononuclear compounds in which the structure is well-controlled in order to favor the magnetic anisotropy. These compounds are called Single-Ion Magnets (SIMs) and represent the smallest possible unit for spin-based electronic devices.

Several methodologies have been explored to control the values of D :

- increasing the covalency of the donor atoms;⁴⁴⁻⁴⁶
- introducing heavier halide ions, which will induce the ground state to mix with the excited state via spin-orbit coupling (SOC);⁴⁷
- varying the substituents on the ligands, their geometry and charge;^{48,49} and
- changing the anion or cation.

These are some of the examples that will be explored in detail in the next pages.

1.1.4.1 3d metal Single-Ion Magnets

Since the beginning of the 2000s, lanthanide ions have been the subject of intensive study in this field due to their large magnetic moment and strong magnetic anisotropy. Compared to them Single-Ion complexes of the first-row transition metals possess smaller magnetic moments, lower SOC constants and strong coupling of the d orbitals to the ligand field that consequently can quench first-order orbital contributions to the magnetic moment. The first-order SOC is preserved by a strict symmetry of the ligand and can provide a large anisotropy, leading to a strong ZFS.

In certain metals, such as tetrahedral Co(II) ions, the ground state electronic configuration does not give rise to first-order orbital angular momentum. In these cases, the origin of magnetic anisotropy is due to the second-order orbital angular momentum. When the ground and the first excited levels of the crystal field splitting are close in energy, the levels can mix through SOC resulting in a larger ZFS. This mixing is totally governed by the geometry. In general, the geometry around the metal in transition metal complexes has a significant influence on both the sign and magnitude of D .^{7,10,50}

The interest in Single-Ion Magnet systems of the d-block began, with the report in 2010 of Long and co-workers⁴⁹ of an Fe(II) system showing slow magnetic relaxation. Since this discovery, the number of 3d systems with SIM behavior has grown steadily.

1.1.4.1.1 The first metal 3d SIM: [Fe(tpa^{Mes})]⁻

The first mononuclear SIM based on a transition metal ion was the [Fe(tpa^{Mes})]⁻, where tpa = tris(pyrrolylmethyl)amine (**L1**). The Fe(II) ion lies in a trigonal pyramid, with an N4 coordination sphere and a spin ground state of $S = 2$ (Figure 1.14).

The fitting of its static magnetic properties allowed the calculation of the parameter $D = -39.6 \text{ cm}^{-1}$, indicating a strong magnetic anisotropy due to the presence of a first-order orbital angular momentum, caused by the unequal occupation of electronically degenerate levels (1e). The rhombic parameter $E = 0.4 \text{ cm}^{-1}$ is due to a slight structural distortion around the Fe(II) ion, which lowers the three-fold symmetry. In the absence of an external magnetic field, no out-of-phase signal was detected, which was attributed to efficient QTM owing to the presence of the transverse anisotropy (E).

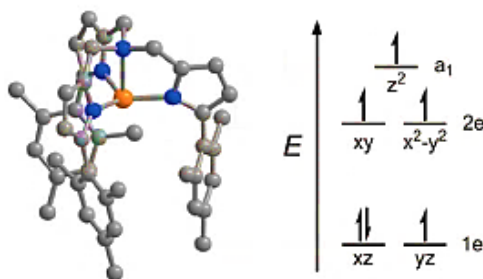


Figure 1.14 Structure of the trigonal pyramidal complex [Fe(tpa^{Mes})]⁻ (**L1**) and splitting of the 3d orbital energies. Orange, blue, and grey spheres represent Fe, N, and C atoms, respectively. Hydrogen atoms were omitted for clarity.⁴⁹

The application of a DC field of 1500 Oe showed temperature-dependent peaks in the χ'' vs. ω plot. The magnitude of the D parameter suggests a very large theoretical value of the barrier ($U = 158 \text{ cm}^{-1}$), predicted by the Equation 1.2. However, the experimental effective barrier $U_{\text{eff}} = 42 \text{ cm}^{-1}$ is much lower, indicating that other relaxation pathways apart from Orbach are involved.

Chapter 1

The study of the SIM behavior in the aforementioned compound was inspirational for the design of the extension of this family of trigonal pyramidal Fe(II) complexes supported by tris(pyrrolyl- α -methyl)amine ligands (**L2-L5**) (Figure 1.15).⁴⁸

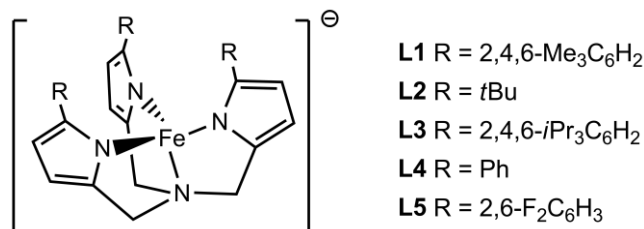


Figure 1.15 General structure of four-coordinate trigonal pyramidal Fe(II) complexes, [Fe(tpa^R)]⁻ (**L1-L5**).⁴⁸

These analogous complexes allowed to study the influence of the ligand field in relation to the static and dynamic magnetic behavior. The extensive study of this family enabled to draw some conclusions about the correlation between the magnetic behavior and the chemical structure. The small structural distortion in the Fe-N bonds, the location of the Fe near the equatorial plane of the three nitrogen atoms of the ligand and the increase in the basicity of the N ligands are the main parameters required to enhance the magnetic anisotropy in this family of complexes, resulting in large D and negligible E values. The magnitude of the axial anisotropy is related to the energy separation between the 1e (d_{xz} and d_{yz}) and 2e (d_{xy} and $d_{x^2-y^2}$) orbitals, as the energy of the 2e orbitals increases with the σ -donating ability of the ligand. For all the complexes, no signal was observed in the absence of an applied DC field probably because of a QTM process that dominates other relaxation pathways. So, from all the studies, it was shown that complex **L2** is the most successful with a $D = -48 \text{ cm}^{-1}$, $E = 0.4 \text{ cm}^{-1}$ and an $U_{\text{eff}} = 65 \text{ cm}^{-1}$. In contrast, the **L5** had the worst results especially due to the presence of the least basic ligand (bearing electron withdrawing fluorine atoms) with a $D = -6.2 \text{ cm}^{-1}$ and an $E = 0.1 \text{ cm}^{-1}$.^{48,51}

This complex was the pioneer in the study of other 3d compounds with SIM behavior. Based on the fact that Co(II) has a large SOC, which could be harnessed under suitable conditions to reveal a new generation of molecular magnets, the interest in this metal ion with different coordination geometries increased in the past years.

1.1.4.1.2 Tetracoordinate Co(II)-based SIMs

Some four-coordinate SIM Co(II) complexes were reported, the majority showing SIM behavior under an applied DC field. One of the first examples that shows slow relaxation of the magnetization at zero field is the distorted tetrahedral Co(II) complex $[\text{Co}(\text{SPh})_4]^{2-}$ (**L6**) with a D_{2d} symmetry, synthesized by Coucouvanis,⁵² and the magnetic characterization being described by Ohya-Nishiguchi and Long (Figure 1.16).^{53,54}

From the results obtained by the combination of EPR spectroscopy and magnetic susceptibility measurements, the high spin Co(II) ion is shown to possess an $S = 3/2$, a large and negative D value of -62.0 cm^{-1} , and a relatively low rhombicity of $E/D < 0.09$. The geometry around the Co(II) brings large magnetic anisotropy on this system due to the close energetic proximity of the filled $3d_{x^2-y^2}$ orbital and the singly occupied $3d_{xy}$ orbital.

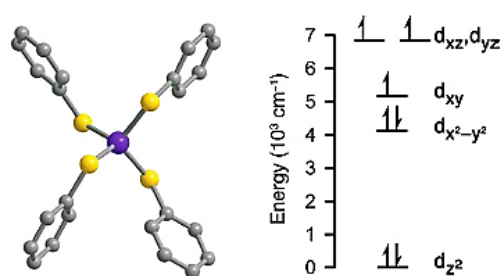


Figure 1.16 Structure of the tetracoordinate $[\text{Co}(\text{SPh})_4]^{2-}$ (**L6**) complex and splitting of the d orbital energies. Purple, yellow, and grey spheres represent Co, S, and C atoms, respectively. Hydrogen atoms were omitted for clarity.⁵⁴

This near degeneracy leads to a mixing of the ground and excited states through SOC to afford a large negative D value (Figure 1.16). The AC susceptibility measurements, in the absence of an applied DC field, reveal a signal in the out-of-phase component (χ_M'') that decreases in height with increasing temperature, with an estimated energy barrier of 21 cm^{-1} (Figure 1.17a). This value is significantly lower than the expected barrier value $2|D|$ of *ca.* 140 cm^{-1} , meaning that other faster relaxation processes of magnetization such as QTM are involved.

To confirm a frequency dependence of χ'' on these processes, a study at different magnetic field values (from 0 to 1 kOe) was performed. It could be observed that as the strength of the field increase, one relaxation process is seen to decrease in intensity at higher frequencies, whilst another one, at lower frequency, appears to gain intensity

Chapter 1

(Figure 1.17b). This indicates a change in the relaxation mechanism from thermally activated, at higher frequencies, to a Quantum Tunneling process, at lower frequencies.

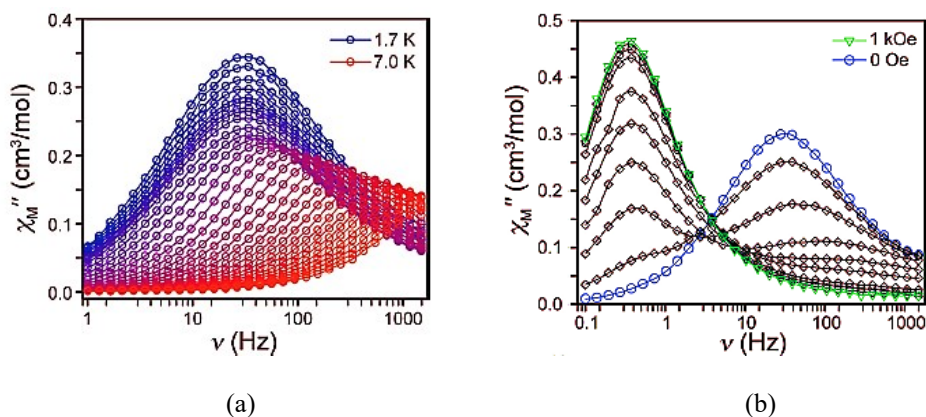


Figure 1.17 (a) Frequency dependence of the molar out-of-phase AC susceptibility (χ_M'') collected at temperature intervals of 0.1 K between 1.7 and 2.4 K and intervals of 0.2 K between 2.4 and 7.0 K, with no applied DC field and (b) molar out-of-phase AC susceptibility (χ_M'') collected at 2 K under applied DC fields from 0 to 1 kOe in 100 Oe increments. Solid lines are guides for the eye.⁵⁴

A series of analogous of the aforementioned complex were reported by the same authors, varying the donor atom.⁴⁵ The homoleptic cobalt(II) complexes with the general formula $[\text{Co}(\text{EPh})_4]^{2-}$ (E = O (**L7**), S (**L8**), Se (**L9**)) were studied in order to understand the relationship between D values and U_{eff} . Magnetic susceptibility data for these complexes indicate a $S = 3/2$ with axial zero-field splitting parameters ranging from $D = -11.1(3) \text{ cm}^{-1}$ to $-83(1) \text{ cm}^{-1}$ (Table 1.1), due to a second order SOC interaction between ground and low-lying excited states. Detailed AC relaxation dynamics revealed that all the complexes show zero-field SIM behavior, with an anisotropic barrier estimated in range of $19\text{--}21 \text{ cm}^{-1}$, indicating that an increase in D does not guarantee an increase in the energy barrier U_{eff} . This demonstrates that apart from the Orbach process, other faster relaxation processes are involved.

Table 1.1 Spin Hamiltonian and Orbach relaxation parameters for **L7–L9**.

Complex	D (cm^{-1})	U_{eff} (cm^{-1})
L7	-11.1(3)	21(1)
L8	-62.0(1)	21(1)
L9	-83(1)	19(1)

Table 1.1 shows that the values of D are highly sensitive to the donor atoms of the ligands. The study of the splitting of the d orbitals in all the complexes highlight the importance of soft ligands in generating weak ligand fields with significant covalency between the metal ion and the donor atom and thus generating larger ZFS parameters.⁵⁵

The concept that soft donors stabilize easy axis anisotropy was further corroborated by the study of Dunbar and Saber in 2014.⁴⁶ They prepared a series of mononuclear distorted tetrahedral Co(II) complexes of general formula $[\text{CoL}_2\text{I}_2]$, where L = quinoline (**L10**), triphenylphosphine (**L11**) and triphenylarsine (**L12**) (Figure 1.18).

The results support the hypothesis that ligands with softer main group donor atoms significantly enhance the global magnetic anisotropy of the metal complexes, as evidenced by the increased ZFS parameters. The D values increased from +9.2 to -36.9 and to -74.7 cm^{-1} for the compounds **L10**, **L11** and **L12**, respectively. However, the energy barrier for spin reversal did not increase as much as the D .

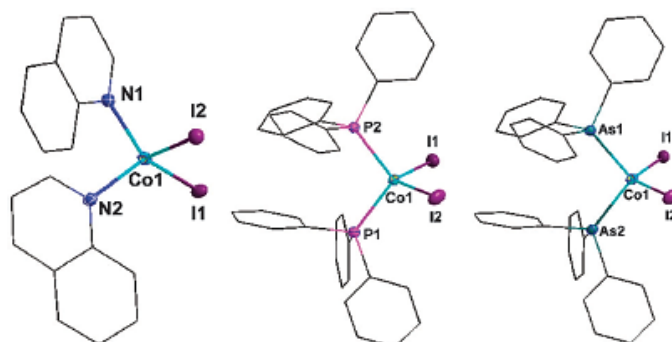


Figure 1.18 Molecular structures of compounds **L10**, **L11** and **L12**, respectively.⁴⁶

In a D_{2d} geometry, the doubly degenerate d_{xz} and d_{yz} have highest energy while the d_{z^2} has the lowest (Figure 1.19). The transitions between the $3d_{xy}$ and $3d_{x^2-y^2}$ orbitals contribute to a $D < 0$ for the overall D -value of the complex, while transitions between $3d_{x^2-y^2}$ and d_{xz} or (d_{yz}) orbitals contributes to a $D > 0$. So, in order to stabilize a large easy axis magnetic anisotropy, the energy between the $3d_{xy}$ and $3d_{x^2-y^2}$ orbitals must be as small as possible and the energy gap between the $3d_{x^2-y^2}$ and d_{xz} (or d_{yz}) must be large. Therefore, by varying the ligand field strength, the energy gap between the $3d_{xy}$ and $3d_{x^2-y^2}$ orbitals is significantly affected. In this direction, the use of soft donor atoms (S, Se, or Te) allows the stabilization of the d_{xy} orbital and increase the energy of the $d_{x^2-y^2}$ orbital (Figure 1.19).⁵⁰

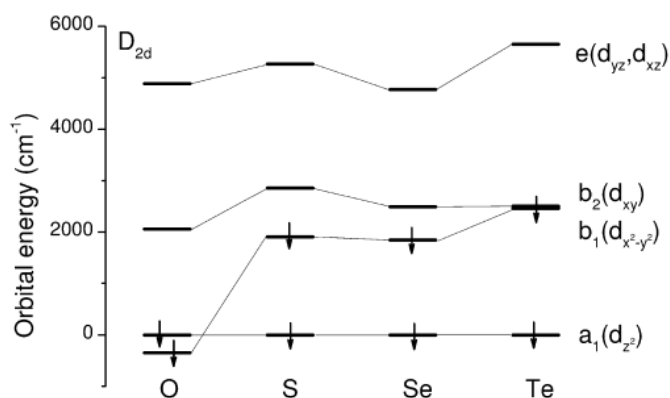


Figure 1.19 Energies of the d orbitals of the D_{2d} symmetrized $[\text{Co}(\text{XPh})_4]^{2-}$ ($\text{X} = \text{O}$ (**L7**); $\text{X} = \text{S}$ (**L8**); $\text{X} = \text{Se}$ (**L9**); $\text{X} = \text{Te}$) complexes computed by *ab initio* LFT.⁵⁵

Depending on the symmetry of the compound, the values of D can vary. For example, tetragonal elongations or compressions described by the angles between the donor atoms and the metal ion, θ , can be larger or smaller than the tetrahedral value $\theta_{T_d} = 109.47^\circ$, inducing a negative or positive D values, respectively.

Based on the above, soft donor atoms and elongated tetrahedral geometries are also responsible for generating large values of D in complex $[\text{Co}(\text{C}_3\text{S}_5)_2]^{2-}$ (**L13**) ($D = -161 \text{ cm}^{-1}$), in $[\text{CoL}_2]^{2-}$, where $\text{L} = o$ -carborane dithiolate ligand (**L14**) ($D = -71.6 \text{ cm}^{-1}$) and in $[\text{CoL}_4](\text{NO}_3)_2 \cdot \text{H}_2\text{O}$, where $\text{L} = \text{thiourea}$ (**L15**) ($D = -61.7 \text{ cm}^{-1}$), all of them with negligible rhombicity.⁵⁶⁻⁵⁸

It is not only the introduction of soft donor atoms that stabilizes the easy axis anisotropy, also other ligands such as halides can be useful in modulating the parameter D . Shanmugam and co-workers⁴⁷ synthesized a series of mononuclear distorted tetrahedral $\text{Co}(\text{II})$ complexes with a general molecular formula of $[\text{CoL}_2\text{X}_2]$ (where $\text{L} = \text{thiourea}$ and $\text{X} = \text{Cl}$ (**L16**), Br (**L17**) and I (**L18**)) (Figure 1.20).

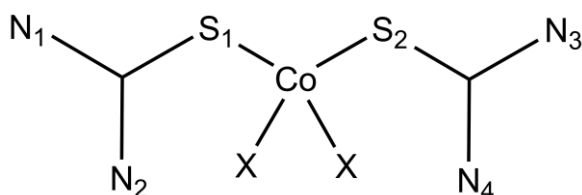


Figure 1.20 Molecular structure of compounds **L16** ($\text{X} = \text{Cl}$), **L17** ($\text{X} = \text{Br}$) and **L18** ($\text{X} = \text{I}$).⁴⁷

It revealed that the large spin-orbit coupling is associated with weak π -donation by heavier halides that reduces the energy gap between the ground and excited states. Therefore, the substitution of the chloride anion with bromide and iodide not only changed the sign of the parameter D but also its magnitude. The values of the zero-field splitting parameter D are +10.8, -18.7 and -19.3 cm^{-1} for compounds **L16**, **L17** and **L18**, respectively. The change in sign and magnitude of these values result from an elongated tetrahedral geometry in the case of complex **L18**.

Dunbar and Saber⁴⁶ also studied this effect when comparing compound $[\text{Co}(\text{PPh}_3)_2\text{I}_2]$ (**L11**) ($D = -36.9 \text{ cm}^{-1}$) with analogous $[\text{Co}(\text{PPh}_3)_2\text{Cl}_2]$ ⁵⁹ and $[\text{Co}(\text{PPh}_3)_2\text{Br}_2]$,⁶⁰ which displayed D values of -11.6 and -13 cm^{-1} , respectively.

Changing the anion or cation can also result in the increase of the magnetic anisotropy. By comparing complex $(\text{PPh}_4)_2[\text{Co}(\text{SPh})_4]$ ⁵² (**L1**) with $(\text{NEt}_4)_2[\text{Co}(\text{SPh})_4]$ ⁵⁵ (**L19**), it was revealed that despite similar Co-S bond lengths, the S-Co-S bond angles differ. While **L19** has a D_{2d} symmetry (elongated tetrahedron), possessing a very large easy axis anisotropy ($D = -62.0 \text{ cm}^{-1}$ and a relatively low rhombicity of $E/D < 0.09$), compound **L1** has a S_4 symmetry (compressed tetrahedron), possessing an anisotropy in the xy plane ($D = +11 \text{ cm}^{-1}$ and $E/D = 0.18$).

Despite all the strategies employed in order to increase the values of the magnetic anisotropy, the energy barriers in the majority of the compounds do not increase proportionally. Table 1.2 contains a comprehensive list of four-coordinate Co(II) complexes showing SIM behavior that have been reported in the last 12 years.

Noteworthy is the fact that only five complexes containing 4 coordinating nitrogen atoms can be found in the literature, which will be discussed in more detail in the next subsection.

Chapter 1

Table 1.2 A list of four-coordinate Co(II) complexes showing SIM behavior. Some of them are described in the text.

Donor set	Compound	H_{DC} (Oe)	D (cm ⁻¹)	U_{eff} (cm ⁻¹)	τ_0 (s)	Ref
P₂S₂	[Co(PNP)(SCN) ₂]	3000	-11.1	22.1	9.1×10 ⁻¹¹	61
	(PPh ₄) ₂ [Co(SPh) ₄]	0	-70	21	1.0×10 ⁻⁷	54
P₂O₂	(PPh ₄) ₂ [Co(OPh) ₄]	1400	-11.1	21	7.0×10 ⁻¹⁰	45
P₂Se₂	(PPh ₄) ₂ [Co(SePh) ₄]	0	-83	19	3.0×10 ⁻⁶	45
P₂X₂	[Co(PPh ₃) ₂ Cl ₂]	1000	-11.6	26	1.2×10 ⁻⁹	59
	[Co(DPEphos)Cl ₂]	1000	-14.4	24	2.1×10 ⁻¹⁰	59
	[Co(PPh ₃) ₂ Br ₂]	1000	-12.5	26	9.4×10 ⁻¹¹	60
	[Co(PPh ₃) ₂ I ₂]	1000	-36.9	21.3	4.7×10 ⁻¹⁰	46
	[Co(Xantphos)Cl ₂]	1000	-15.1	17.7	2.7×10 ⁻⁶	62
	[Co(Xantphos)Br ₂]	1000	-11.6	13	1.8×10 ⁻⁶	62
	[Co(Xantphos)I ₂]	1000	-7.3	6.4	1.2×10 ⁻⁶	62
	[Co(dppf)Cl ₂]	1000	-12.0	23.2	5.2×10 ⁻⁹	63
	[Co(dppf)Br ₂]	1000	-11.2	20.0	1.8×10 ⁻⁹	63
P₂N₂	[Co(Xantphos)(NCS ₂)]	1000	-16.2	20.92	6.2×10 ⁻⁶	62
As₂I₂	[Co(AsPh ₃) ₂ I ₂]	1000	-74.7	22.7	1.5×10 ⁻⁸	46
S₄	(PPh ₄) ₂ [Co(C ₃ S ₅) ₂]	0	-161	33.9	4.5×10 ⁻⁶	56
	[Co{iPr ₂ P(S)NP(S)iPr ₂ } ₂]	2000	-30.5	54.2	1.2×10 ⁻¹⁰	64
NOX₂	[Co(L ₁)(Cl) ₂ (MeCN)]	2500	+15.6	10.3	7.7×10 ⁻⁷	44
	[Co(L ₁)(Br) ₂ (MeCN)]	2500	+11.16	8.2	8.4×10 ⁻⁷	44
	[Co(L ₂)(Cl) ₂ (MeCN)]	2500	-11.30	20.2	1.5×10 ⁻⁹	44
	[Co(L ₂)(Br) ₂ (MeCN)]	2500	-10.32	13.8	8.1×10 ⁻⁸	44
N₂O₂	[Co(L ^{dppip}) ₂]	1000	-41	62	1.0×10 ⁻¹⁰	26
	[Co(L ^{dppip,6-OMe}) ₂]	1000	-35	44	2.6×10 ⁻⁹	26
	[Co(L ^{hpbdti}) ₂]	2000	-	39.4	1.3×10 ⁻⁸	65
	[Co(L ^{hpbdti}) ₂]	2000	-44	12.8	2.2×10 ⁻⁶	66
	[Co(L ^{hdeppdmti}) ₂]	400	-50	35	1.6×10 ⁻⁹	66
	[Co(L ^{Nph,4-Br}) ₂]	400	-36.7	36	5.6×10 ⁻¹⁰	67
	[Co(L ^{Nph,2-Ph}) ₂ ·CH ₂ Cl ₂]	400	-39.8	43	8.4×10 ⁻¹⁰	67
	[Co(L ^{Sal,2-Ph}) ₂]	10000	-23.1	49	2.9×10 ⁻¹¹	68
N₂X₂	[Co(dmph)Br ₂]	1000	+10.7	22.9	3.7×10 ⁻¹⁰	69
	[Co(biq)Cl ₂]	2000	+10.5	29.6	1.9×10 ⁻¹⁰	70
	[Co(biq)Br ₂]	2000	+12.5	27.5	1.2×10 ⁻¹⁰	70
	[Co(biq)I ₂]	2000	+10.3	39.6	3.2×10 ⁻¹³	70
	[Co(bzi) ₂ (NSC) ₂]	2000	-10.1	14.7	1.9×10 ⁻⁸	71
	[Co(CH ₃ -Im) ₂ Cl ₂]	2000	-14.5	23.3	2.1×10 ⁻⁹	72
N₃Cl	[(3G)CoCl](CF ₃ SO ₃)	1500	-12.7	24	1.9×10 ⁻¹⁰	73

1.1.4.1.2.1 Homoleptic tetra-coordinate Co(II)-based SIMs containing 4 coordinating nitrogen atoms

Since the discovery of the first SIM of the d-block, several four-coordinate Co(II) complexes showing SIM behavior have been reported. To the best of our knowledge, only five tetra-coordinate SIM-based Co(II) complexes containing four coordinating nitrogen atoms are found in the literature showing a strong magnetic anisotropy as a result of a strong axial distortion caused by the ligands, leading to small energy gaps between the ground and the first excited states (Figure 1.21). These are neutral, dianionic or dicationic distorted tetrahedral homoleptic complexes of Co(II) containing two symmetrical *N,N*-chelating ligands, which are, respectively, monoanionic triimidosulfonate (**L20**),⁷⁴ dianionic bisimido (**L21**, **L23** and **L24**)^{75,76} and neutral bipyridine (**L22**)⁷⁷ moieties.

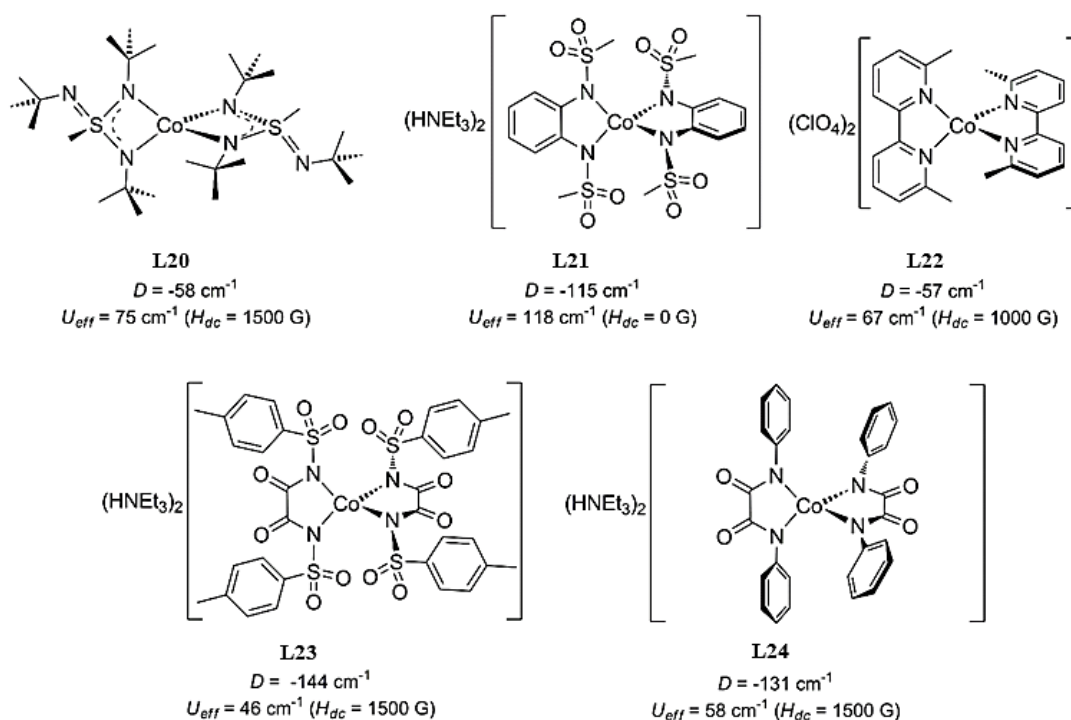


Figure 1.21 Tetrahedral N_4 -coordinated Co(II) complexes (**L20-L24**) displaying SIM behavior reported in the literature.

Although complexes **L21** and **L22-L24** display SIM behavior under zero external magnetic field, the frequency-dependent maximum in the out-of-phase component of the magnetic susceptibility (χ'') is not well defined indicating the presence of QTM process, which is then suppressed by applying a DC field. Despite all these five complexes

Chapter 1

showing high values of D , with the exception of complex **L21**, compounds **L20** and **L22-L24** display energy barriers lower than expected for a pure Orbach process, indicating the predominance of the Raman relaxation process in the studied range of temperatures.

1.1.5 Bis(2-iminopyrrolyl) metal complexes

The 2-iminopyrrolyl ligand precursors are monoanionic bidentate N,N' chelates, which consist of a pyrrolyl ring anion, prepared by deprotonation of the pyrrole group with a strong base, attached to a neutral $-C(H)=NR$ imine group in the ring position 2 (Figure 1.22a). The easy preparation of these compounds by condensation reaction of 2-formylpyrrole with a variety of aliphatic or aromatic amines allows them to be used intensively in the areas of organometallic and coordination chemistry. When coordinated to transition metals, they are mainly used as ligands in polymerization precatalysts (see below).

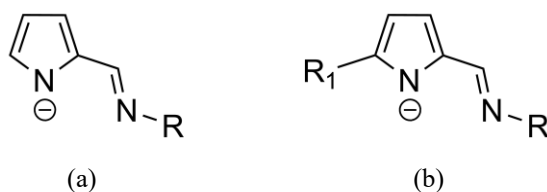


Figure 1.22 (a) 2-iminopyrrolyl and (b) 5-substituted-2-iminopyrrolyl ligands.

This chapter deals with the preparation of homoleptic Co(II) complexes bearing two 5-substituted-2-iminopyrrolyl ligands (Figure 1.22b). The corresponding 5-substituted pyrroles are synthesized by a cross coupling reaction of the pyrrolyl sodium salt with a bromide of the substituent group, which, upon formylation of the ring position 2 and subsequent condensation with a primary amine, yield the 5-substituted-2-iminopyrrole ligand precursors. The latter can be easily deprotonated with a strong base giving rise to the corresponding 5-substituted-2-iminopyrrolyl salts or complexes. The flexibility in introducing different steric and electronic groups into these ligand precursors improves certain properties (steric and electronic) and allows them to be used in different areas.

Various complexes containing 2-iminopyrrolyl in their framework have been reported in the literature, the great majority concerning ligands non-substituted at position 5 of the pyrrolyl ring. Despite many mono(2-iminopyrrolyl) compounds being reported, this subsection will only address bis(2-iminopyrrolyl) complexes.

Since the syntheses of the first bis(2-alkylimino)pyrrole-metal(II) compounds in 1966 by Holm *et al.*,⁷⁸ the number of iminopyrrolyl ligands coordinated to different metals with a variety of applications increased exponentially. The interest in this type of compounds escalated after the publication of new bis[(2-*N*-arylimino)pyrrolyl] metal complexes by Gibson *et al.*,⁷⁹ which used Cr(II) and Cr(III) as metal centers, Cr(II) presents a square planar geometry and Cr(III) a square pyramidal geometry (**L25-L27**). These compounds were prepared in high yields by reaction of the sodium and lithium iminopyrrolyl salts with [CrCl₂(THF)] and [CrCl₃(THF)], respectively, and behave as catalysts for ethylene polymerization in the presence of alkylaluminium activators (Figure 1.23).

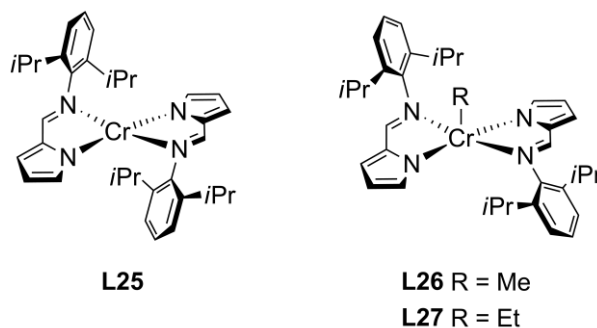


Figure 1.23 Bis(2-iminopyrrolyl) chromium complexes.

Since then, other research groups focused on the syntheses of several group 4 bis(iminopyrrolyl) metal complexes applied specially in the olefin polymerization. Bochmann *et al.*⁸⁰ and Mashima and co-workers⁸¹ reported a family of zirconium bis(chloride) (**L28-L32**) and bis(amido) (**L33-L36**) compounds that showed to be active precatalysts in ethylene polymerization (Figure 1.24). In Bochmann's work the compounds were obtained by reaction of the bis(imino)pyrrolyl lithium salt and bis(imino)pyrrole with ZrCl₄ and [Zr(NMe₂)₄] to give **L28** and **L33**, respectively, while in Mashima's work the bis(amido) compounds were obtained by reactions of [Zr(NEt₂)₄] with 2 equivalents (equiv.) of the corresponding neutral iminopyrrolyl ligand precursors, differing in electronic and stereochemical properties at the *N*-arylimino substituents (**L34-L36**, **L40** and **L41**). Ligands with bulkier *N*-arylimino substituents gave rise to complexes with trigonal bipyramidal geometries **L40** and **L41**, containing simultaneously a chelating and a mono-coordinated iminopyrrolyl ligand. The bis(chloride) **L29-L32** compounds were prepared through treatment of the previous complexes with Me₃SiCl in toluene.

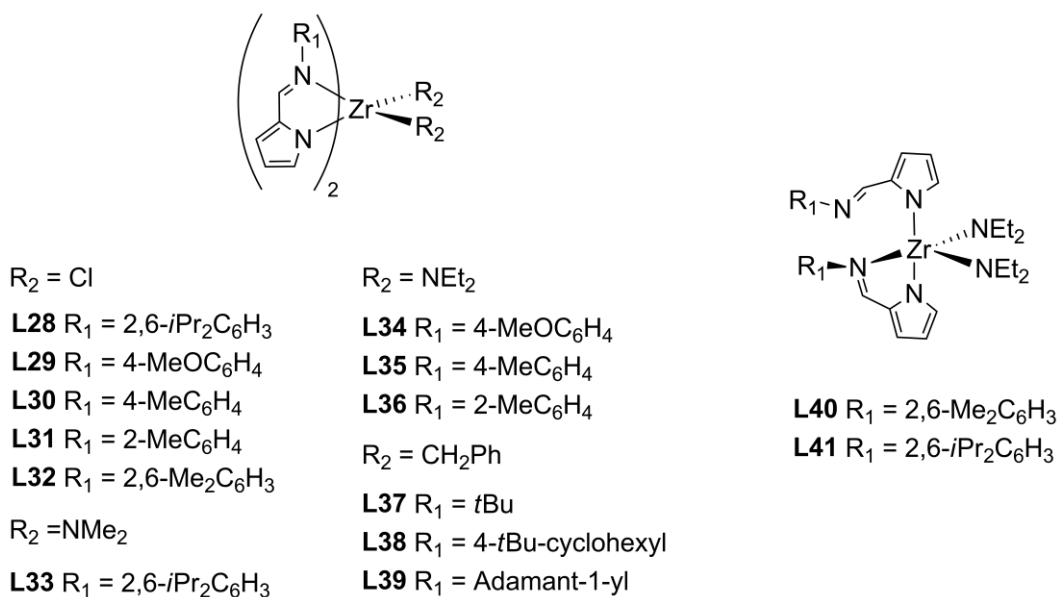


Figure 1.24 Bis(iminopyrrolyl) zirconium complexes.

Years later, Okuda *et al.*⁸² increased even more the zirconium family with the report of three dibenzyl-bis(iminopyrrolyl) complexes (**L37-L39**) prepared by reaction of $[\text{Zr}(\text{CH}_2\text{Ph})_4]$ with 2 equiv. of the corresponding 2-iminopyrrole ligand precursor. These compounds also showed high activity in ethylene polymerization when activated with methylaluminoxane (MAO).

Continuing through group 4 of the Periodic Table, we came across Fujita's work,⁸³ who in the early 2000s synthesized titanium bis(chloride) compounds containing iminopyrrolyl groups as ligands (**L42-L47**) (Figure 1.25). The compounds were prepared by metathetic reaction of TiCl_4 with 2 equiv. of the corresponding iminopyrrolyl lithium salts and demonstrated to be very active in ethylene polymerization when MAO is used.

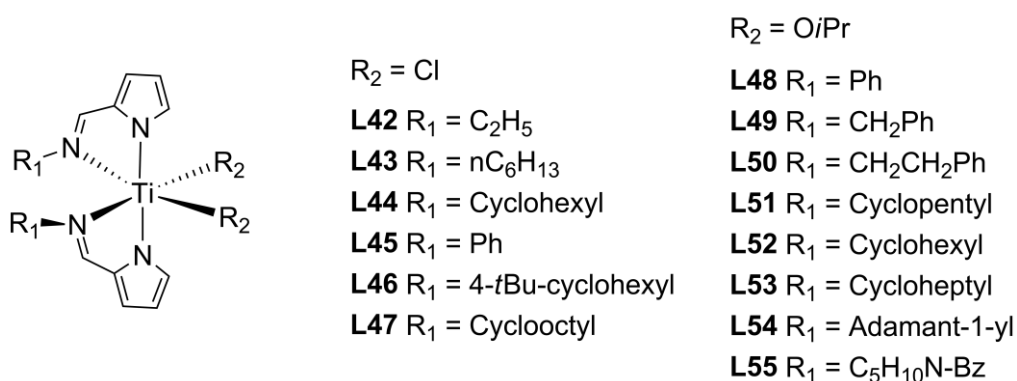
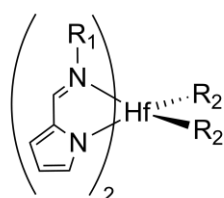


Figure 1.25 Bis(iminopyrrolyl) titanium complexes.

In 2014 and more recently in 2021, Liu *et al.*⁸⁴ and Hormnirun *et al.*⁸⁵ prepared the bis(isopropoxide) Ti complexes **L48-L50** and **L51-L55**, respectively, by reaction of $[\text{Ti}(\text{OiPr})_4]$ with 2 equiv. of the corresponding iminopyrrole. **L48-L50** displayed cytotoxic properties towards some tumorous cell lines, whereas **L51-L55** were active inhibitors for the ring-opening polymerization of cyclic esters.

Hafnium bis(iminopyrrolyl) complexes (**L51-L55**) were also prepared by Okuda *et al.*,⁸¹ who used the same procedure as for the syntheses of **L37-L39**, with $[\text{Hf}(\text{CH}_2\text{Ph})_4]$ as starting material (Figure 1.26). The selection of the substituents at the imine nitrogen proved to affect not only the activity in ethylene polymerization but also the stability of the compounds. Therefore, compounds **L51** and **L52** turn out to be unstable, and thus useless as catalysts, while complexes **L53-L55** were highly active towards ethylene polymerization when activated with $\text{B}(\text{C}_6\text{F}_5)_3$.



$\text{R}_2 = \text{CH}_2\text{Ph}$

L56 $\text{R}_1 = i\text{Pr}$

L57 $\text{R}_1 = 4\text{-}i\text{PrC}_6\text{H}_4$

L58 $\text{R}_1 = t\text{Bu}$

L59 $\text{R}_1 = 4\text{-}t\text{Bu-cyclohexyl}$

L60 $\text{R}_1 = \text{Adamant-1-yl}$

L61 $\text{R}_1 = 2,6\text{-}i\text{PrC}_6\text{H}_3$

$\text{R}_2 = \text{NMe}_2$

L62 $\text{R}_1 = 2,6\text{-Me}_2\text{C}_6\text{H}_3$

L63 $\text{R}_1 = 2,6\text{-}i\text{PrC}_6\text{H}_3$

L64 $\text{R}_1 = 4\text{-MeOC}_6\text{H}_4$

L65 $\text{R}_1 = 4\text{-MeC}_6\text{H}_4$

$\text{R}_2 = \text{Cl}$

L66 $\text{R}_1 = 2,6\text{-Me}_2\text{C}_6\text{H}_3$

L67 $\text{R}_1 = 2,6\text{-}i\text{PrC}_6\text{H}_3$

L68 $\text{R}_1 = 4\text{-MeOC}_6\text{H}_4$

L69 $\text{R}_1 = 4\text{-MeC}_6\text{H}_4$

Figure 1.26 Hafnium bis(iminopyrrolyl) complexes.

The family of bis(iminopyrrolyl) hafnium complexes increased when, in 2006, Mashima *et al.*⁸⁶ prepared the dibenzyl (**L56-L61**), diamido (**L62-L165**) and dichloro (**L66-L69**) derivatives with different bulky 2-(*N*-arylimino)pyrrolyl ligands, using the same procedure as for the syntheses of the zirconium compounds described above. The diamido and dichloro hafnium complexes, when combined with modified methylaluminoxane (MMAO), become active catalysts for ethylene polymerization, but their catalytic activities are lower when compared with the benzyl complexes **L56-L60**.

Vanadium, molybdenum and tungsten compounds (from groups 5 and 6) bearing

Chapter 1

iminopyrrolyl ligand precursors (Figure 1.27) were also reported by Li *et al.*,⁸⁷ Heinze *et al.*⁸⁸ and Mayr *et al.*⁸⁹

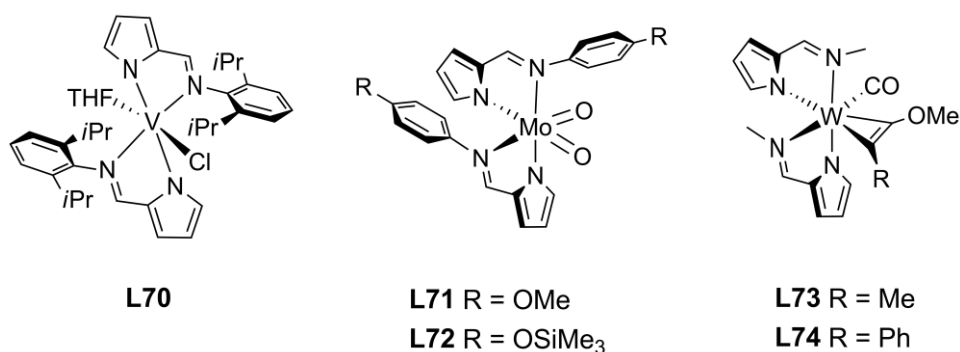


Figure 1.27 Group 5 and 6 metal complexes with 2-iminopyrrolyl ligands.

The bis(2-iminopyrrolyl) vanadium complex **L70** was synthesized by reaction of $[\text{VCl}_3(\text{THF})_3]$ with 2 equiv. of the sodium salt of the ligand and proved to be active in ethylene polymerization and ethylene/1-hexene copolymerization, requiring activation with diethylaluminium chloride. Compounds **L71** and **L72** were obtained by reaction of 2 equiv. of the corresponding ligand with $[\text{MoCl}_2\text{O}_2(\text{dme})]$ in the presence of triethylamine and the objective was to understand the mechanism of oxygen atom transfer (OAT) in metalloenzymes. As for η^2 -acetylene tungsten complexes **L73** and **L74**, Mayr *et al.* reported their syntheses and characterization.

Compounds with late transition metals bearing 2-iminopyrrolyl ligands are the most common, especially in our research group, with different applications. Homoleptic Co(II), Ni(II) and Fe(II) were studied for the first time in polymerization by Bochmann *et al.*⁸⁰ (**L75-L77**) (Figure 1.28). The compounds **L75** and **L77** were prepared from the reaction of 2 equiv. of the corresponding lithium salts with CoCl_2 and $[\text{NiBr}_2(\text{DME})]$, respectively, while **L76** was obtained from the reaction of 2,5-bis[N-(2,6-diisopropylphenyl)formimino]pyrrolyl lithium salt with FeCl_2 . They showed no activity when tested as catalysts for the oligo-polymerization of ethylene in the presence of MAO. Years later Cui *et al.*⁹⁰ reacted the lithium salt of a bulkier unsymmetrical iminopyrrolyl ligand with *trans*- $[\text{Ni}(\text{Ph})(\text{PPh}_3)_2\text{Cl}]$ to afford the complex **L78**, which revealed to be highly active catalyst for the polymerization of MMA in the presence of a small amount of MAO.

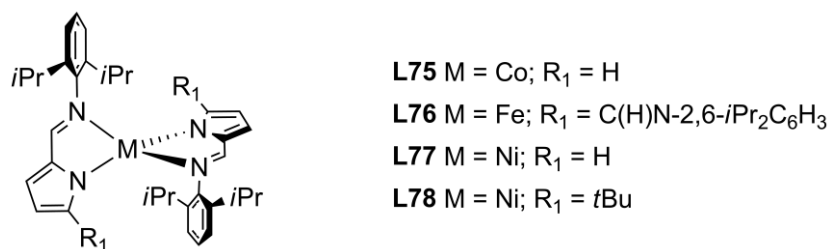


Figure 1.28 Homoleptic bis[2-(N-arylimino)pyrrolyl] metal complexes.

Concerning homoleptic Co(II) complexes, our research group prepared and characterized a series of compounds of the type [M(2-iminopyrrolyl)₂]^{91–93} and [M(5-substituted-2-iminopyrrolyl)₂] (M = Co and Fe) (**L83–L85**) (Figure 1.29).⁹⁴

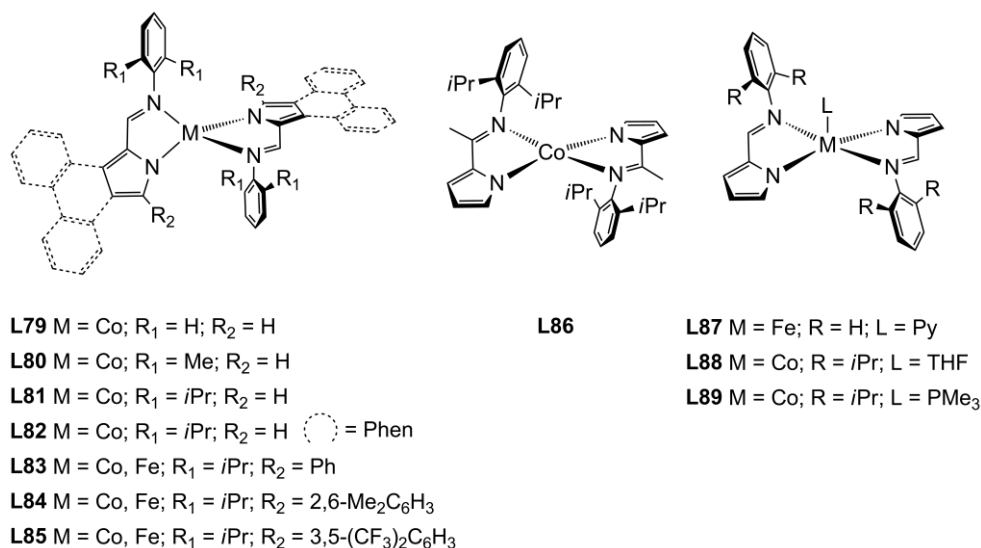


Figure 1.29 Iron and cobalt complexes bearing 2-iminopyrrolyl ligands reported by our research group.

The use of different ligands encompassing different degrees of bulkiness allowed the geometry of the Co(II) center to change from tetrahedral (**L79–L82**) to square planar (**L86**).⁹¹ Pentacoordinate complexes of Fe(II) (**L87**)⁹² and Co(II) (**L88**, **L89**)⁹³ containing the bis(2-iminopyrrolyl) framework were also reported by our group, which were stabilized with pyridine in the case of Fe(II) and trimethylphosphine and tetrahydrofuran in the case of Co(II) (Figure 1.29).^{92,93}

Similar homoleptic compounds of Ni(II) (**L90–L95**),⁹⁵ Cu(II) (**L96–L104**)⁹⁶ and Zn(II) (**L105–L108**)⁹⁷ were also synthesized and characterized, some of them by our research group^{92,98} (Figure 1.30). The homoleptic Zn(II) complexes, all prepared by our group, exhibited fluorescence properties. The modifications on the iminopyrrolyl core,

Chapter 1

by introducing steric and electronic modifications, including a phenanthro[9,10-*c*]pyrrolyl moiety fused onto the pyrrolyl C3-C4 bond, allowed to enhance this behavior in this type of compounds due to the extension of π -conjugation.

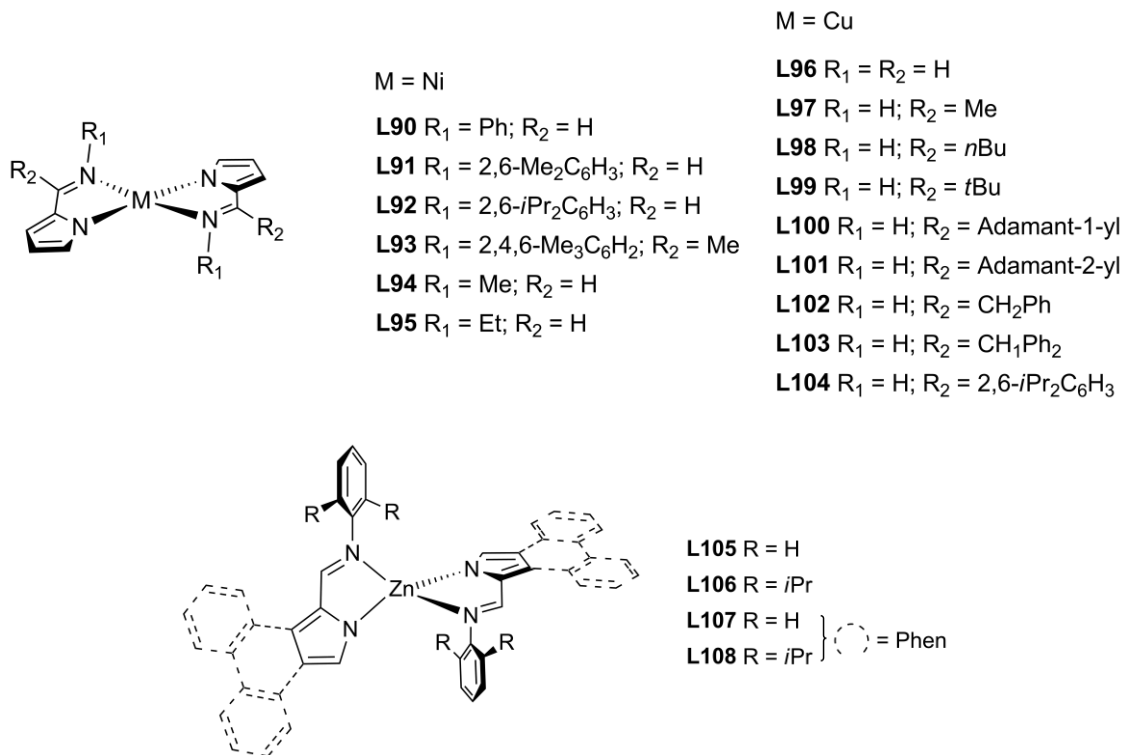


Figure 1.30 Homoleptic nickel(II), copper(II) and zinc(II) compounds bearing 2-iminopyrrolyl ligands.

Mashima and co-workers⁹⁹ and *Panda et al.*¹⁰⁰ used alkaline earth metals to synthesize a series of bis(2-iminopyrrolyl) complexes **L110-L113** and **L109, L114-L116**, respectively (Figure 1.31).

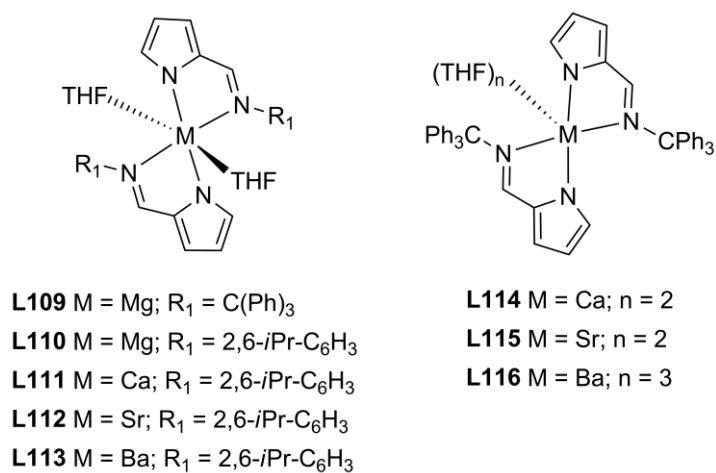


Figure 1.31 Alkaline-earth metal complexes with 2-iminopyrrolyl ligands.

All the complexes were prepared by reaction of 2 equiv. of the respective ligand precursor with $[\text{Mg}(\text{CH}_2\text{Ph})_2]$ and $[\text{M}(\text{N}(\text{SiMe}_3)_2)(\text{THF})_n]$ ($\text{M} = \text{Ca}, \text{Sr}$ and Ba).

Concerning rare-earth metal complexes with 2-iminopyrrolyl ligands, Arnold *et al.*¹⁰¹ (**L117-L120**) and Cui *et al.*¹⁰² (**L121-L122**) were the pioneers synthesizing yttrium, samarium, lutetium, and scandium complexes (Figure 1.32). Compound **L117** was obtained by reaction of 2 equiv. of the ligand precursor potassium salt with $[\text{YCl}_3(\text{THF})_{3.5}]$ and then adding $\text{LiCH}_2\text{SiMe}_3$. **L118** was synthesized using a similar procedure with SmCl_3 as starting material, and **L119** and **L120** were obtained from the reaction of **L118** with the appropriate alkyl lithium. The introduction of a *t*Bu group at the position 5 of the pyrrole ring led exclusively to the formation of the bis(2-iminopyrrolyl) complexes. Catalytic tests were performed, revealing that complex **L120** is a highly active catalyst for the polymerization of methyl methacrylate (MMA). On the other hand, compounds **L121** and **L122**, which were obtained by reaction of $[\text{Ln}(\text{CH}_2\text{SiMe}_3)_3(\text{THF})_2]$ ($\text{Ln} = \text{Lu}, \text{Sc}$) with 2 equiv. of the ligand precursor, showed no catalytic activity in isoprene polymerization. Years later, Anwander *et al.*¹⁰³ also reported the pentamethylcyclopentadienyl (Cp^* , C_5Me_5) yttrium compounds with two 2-iminopyrrolyl ligands **L123**, which were obtained through the reaction of 2 equiv. of the ligand precursor with $[\text{Y}(\text{C}_5\text{Me}_5)\text{Me}_2]_3$.

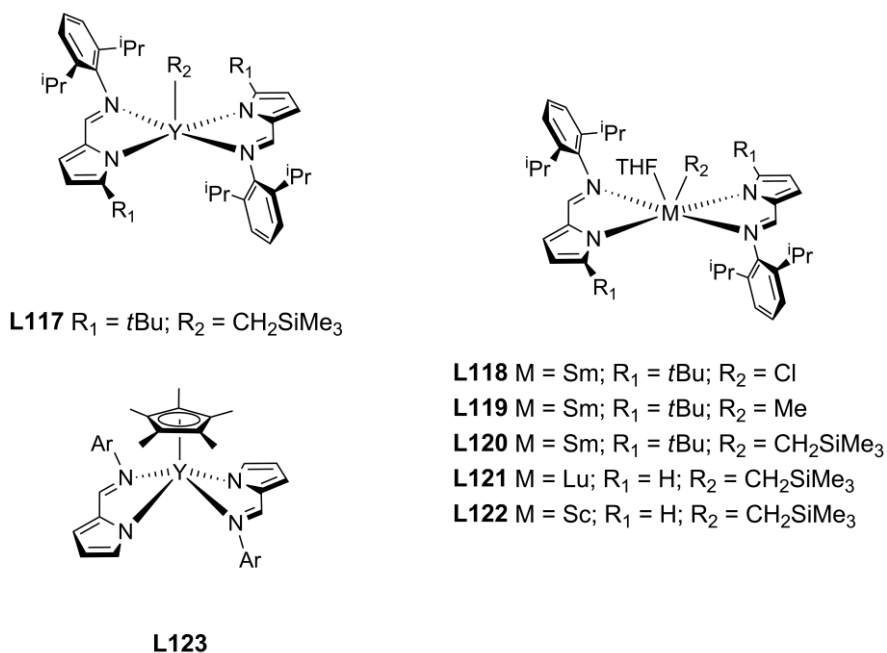


Figure 1.32 Rare-earth metal complexes bearing iminopyrrolyl ligands.

1.1.6 Objectives of the present work

Nowadays, one of the main goals in the field of information technology is the search for more efficient ways to store and process digital information, preferably on a small scale. Therefore, the pursuit for materials with unique magnetic properties has increased over the years, leading to the investigation of new materials as candidates to be developed as nanoswitch or nanomemory devices based on Spin Crossovers (SCO), Single-Molecule Magnets and Single-Chain Magnets (SCM).¹⁰⁴ Among them, SMMs are widely considered to be the class of molecular compounds that shows the most promising features to be employed in numerous applications, and thus becoming an important topic of research. As mentioned before, below a certain temperature, these molecules show slow relaxation of the magnetization, which arises from the behavior of individual isolated molecules, functioning as molecular nanomagnets.

Unlike lanthanide ions, which since the early 2000s have been the subject of intensive study in this field, the quest for SIM behavior in 3*d* metal-based compounds only gained interest after 2010. Since then, many complexes have been reported, in particular cobalt-based compounds, but only a few stood out. Therefore, driven by this fascinating field and the constant need to overcome in terms of magnetic properties the compounds already reported in the literature, one of the objectives of this PhD work was to explore new distorted tetrahedral homoleptic Co(II) complexes bearing monoanionic *N,N'*-bidentate 2-iminopyrrolyl ligands as Single-Ion Magnets. The main goal is to understand how the ligand field and geometry of these compounds affect this behavior by introducing different ligands with different steric and electronic features.

Therefore, this Chapter intends to describe:

- the syntheses and characterization by ¹H and ¹³C NMR spectroscopies and elemental analysis of new 5-substituted-2-iminopyrrole ligand precursors;
- the syntheses of a series of new homoleptic [Co(5-substituted-2-iminopyrrolyl)₂] complexes bearing ligands of varying steric bulkiness and different electronic substituents;

- the characterization of the isolated compounds by ^1H NMR spectroscopy, FT-IR, magnetic susceptibility measurements in solution and in solid state, and by single-crystal X-ray diffraction;
- the static (direct-current DC) magnetization measurements performed using a SQUID magnetometer in order to detect SIM behavior in these complexes;
- the dynamic (alternating-current AC) measurements in order to evaluate their SIM behavior, namely through the calculation of the energy barriers and relaxation times;
- the high field EPR measurements (performed at the Institut für Physikalische Chemie, University of Stuttgart, Germany) showing the transition between the M_s states in order to quantify the axial and rhombic ZFS parameters (D and E);
- the theoretical calculations (performed at the Faculty of Sciences, University of Lisbon– BioISI research center) as a way to support the experimental values and to understand the origin of the magnetic anisotropy in this system.

1.2 RESULTS AND DISCUSSION

1.2.1 The 5-substituted-2-iminopyrrolyl ligand precursors

1.2.1.1 Synthesis and characterization

Iminopyrrole ligand precursors have been widely used in our research group. This work uses 5-substituted-2-iminopyrrolyl ligands to support Co(II) paramagnetic complexes. The synthesis of the corresponding 5-substituted-2-iminopyrrole ligand precursors was carried out through a sequence of three reaction steps (Figure 1.33).

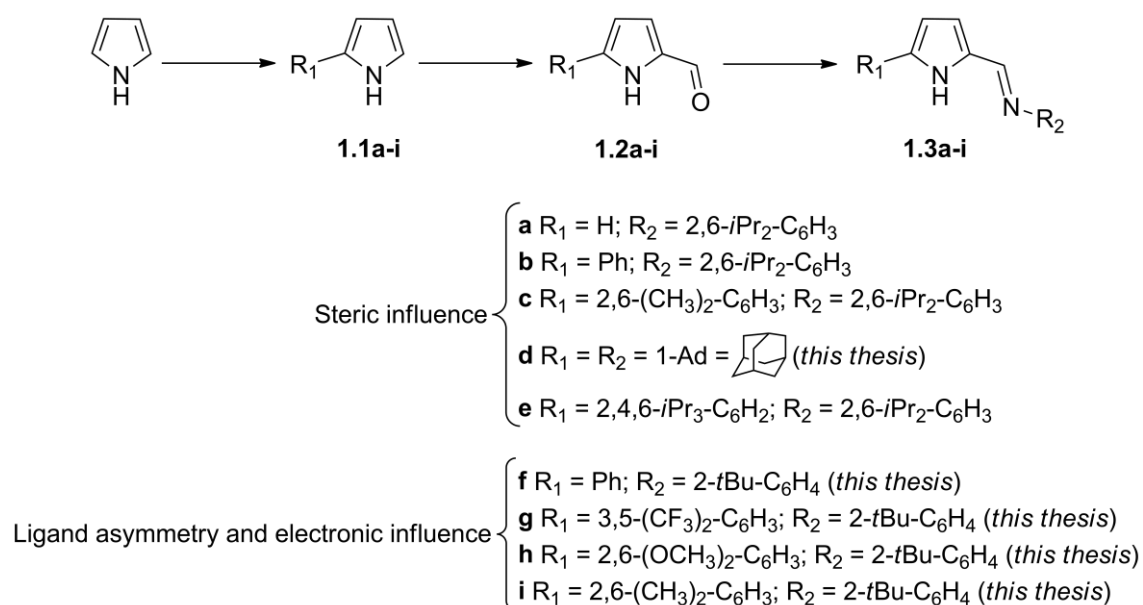


Figure 1.33 Synthetic route used to prepare the 5-substituted-2-iminopyrrolyl ligand precursors **1.3a-i**.

The three sequential steps are:

i) the cross-coupling reaction of pyrrolylzinc chloride, which is prepared *in situ* by reaction of the pyrrolyl sodium salt with anhydrous ZnCl₂ in THF, with the corresponding aryl bromide catalyzed by palladium complexes (Pd(OAc)₂ and Pd₂dba₃) and a sterically demanding phosphine (Figure 1.34, route i). This method was reported by Sadighi *et al.*,¹⁰⁵ giving rise to the 2-substituted pyrroles in moderated yields. The only exception was **1.1d**, which was prepared through a completely different multistep synthetic route.¹⁰⁶

In the latter route, 2-pyrrolyl trichloromethyl ketone is obtained by reaction of distilled pyrrole with trichloroacetyl chloride, followed by ethanolysis to afford ethyl pyrrole-2-carboxylate; Friedel-Crafts alkylation of the pyrrole ring followed by saponification and decarboxylation of the resulting ethyl ester affords the intended product in good yield (86 %) (Figure 1.34, route ii).

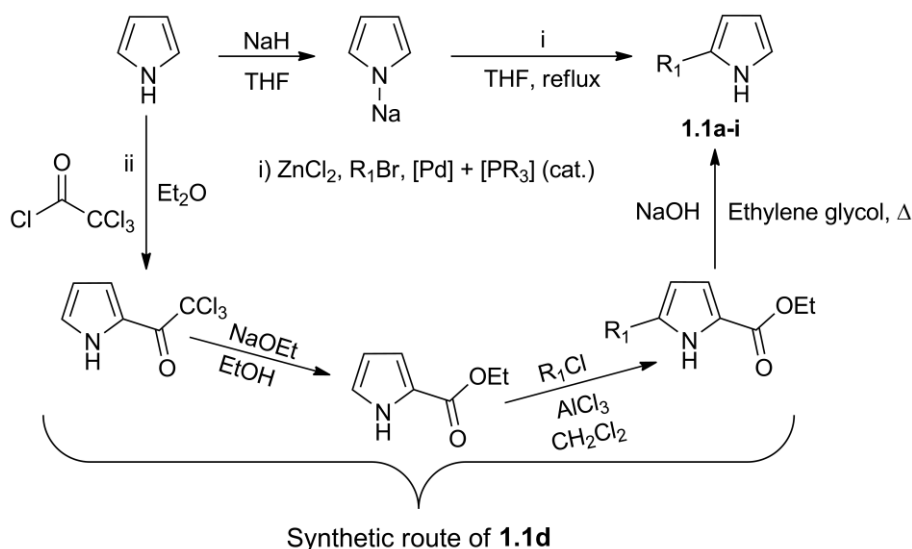


Figure 1.34 Synthetic routes used to prepare the 2-substituted pyrroles **1.1a-i**.

ii) the Vilsmeier-Haak formylation, which consists in the use of *N,N'*-dimethylformamide (DMF) and phosphorus oxychloride for the *in situ* generation of the Vilsmeier reagent, which will then react with the 2-substituted pyrroles via an electrophilic aromatic substitution reaction. The iminium salt formed is then hydrolyzed to afford the corresponding 5-aryl-2-formylpyrroles **1.2a-i** in good yields (Figure 1.35). This reaction follows a procedure described in the literature.¹⁰⁷

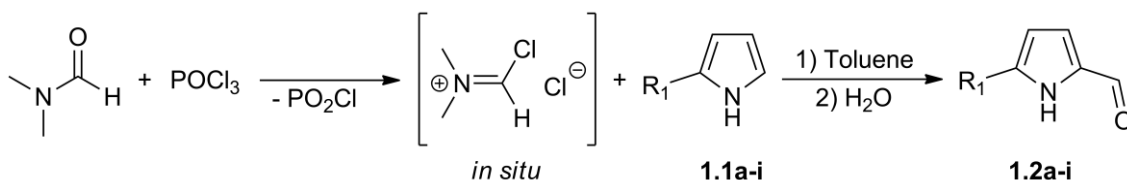


Figure 1.35 Synthesis of 5-substituted-2-formylpyrroles **1.2a-i**.

iii) the condensation reaction that consists in the reaction of the 5-substituted-2-formylpyrroles with 2,6-bis(isopropyl)aniline or 2-*t*-(butyl)aniline in refluxing toluene or

Chapter 1

ethanol to give the 5-substituted-2-iminopyrrole ligand precursors **1.3a-i** in moderate yields (58-70 %) (Figure 1.36). The reaction procedure was adapted from the one used previously in the preparation of 2-(*N*-arylimino)pyrroles reported by our group.¹⁰⁸ A Soxhlet extractor with pre-activated molecular sieves 4 Å was used to remove water formed, allowing the reaction to proceed preferentially towards the formation of the imine product.

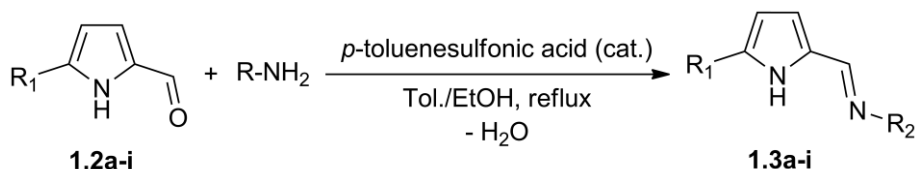


Figure 1.36 Synthesis of 5-substituted-2-iminopyrrolyl ligand precursors **1.3a-i**.

Compounds **1.3d** and **1.3f-i** were characterized by 1H and ^{13}C NMR spectroscopies and elemental analysis. The 1H and ^{13}C NMR spectra of compounds **1.3d** and **1.3f-i** showed the expected resonances characteristic of an iminopyrrolyl moiety with the *NH* proton appearing as a broad signal around 10 ppm, an iminic $C(H)=N$ proton resonance appearing as a singlet around 8.10 ppm and the pyrrolyl protons at positions 3 and 4 appearing as doublets around 6.5 ppm. For **1.3f-i** besides these resonances, it was also possible to observe a singlet around 1.5 ppm integrating 9 protons corresponding to the *t*-butyl group, and for **1.3h** and **1.3i** an additional singlet resonance appears in the 1H NMR spectra integrating 6 protons corresponding to the methoxy and methyl groups at 3.99 and 2.32 ppm, respectively.

1.2.2 Homoleptic bis(5-substituted-2-iminopyrrolyl) Co(II) complexes

1.2.2.1 Synthesis and characterization

The 5-substituted-2-iminopyrrole derivatives **1.3d-i** were used as ligand precursors for the synthesis of the cobalt(II) complexes. The Co(II) complexes **1.4a-c** had been reported previously by our research group, and were synthesized accordingly (Figure 1.37).^{91,94} The remaining homoleptic Co(II) compounds **1.4d-i** were obtained by reaction of the sodium salt of the respective ligand precursors, which were prepared *in situ* by

reaction of ligand precursors **1.3d-i** with NaH in THF, with CoCl₂ also in THF, using a molar ratio of 2:1. The workup of the reaction mixtures consisted in the complete evaporation of the solvent followed by the multiple extraction of the solid residues with the appropriate solvent until colorless extracts were obtained. The crystallization at -20 °C afforded red (**1.4d-e** and **1.4h**), dichroic red/green (**1.4f-g**) and purple (**1.4i**) crystals that confirmed to be the intended complexes [Co{κ²N,N'-5-(1-Ad)-NC₄H₂-2-C(H)=N(1-Ad)}₂] (Ad = Adamantyl) (**1.4d**), [Co{κ²N,N'-5-(2,4,6-*i*Pr₃-C₆H₂)-NC₄H₂-2-C(H)=N(2,6-*i*Pr₂-C₆H₃)}₂] (**1.4e**), [Co{κ²N,N'-5-(C₆H₅)-NC₄H₂-2-C(H)=N(2-*t*Bu-C₆H₄)}₂] (**1.4f**), [Co{κ²N,N'-5-(3,5-(CF₃)₂C₆H₃)-NC₄H₂-2-C(H)=N(2-*t*Bu-C₆H₄)}₂] (**1.4g**), [Co{κ²N,N'-5-(2,6-(OCH₃)₂C₆H₃)-NC₄H₂-2-C(H)=N(2-*t*Bu-C₆H₄)}₂] (**1.4h**) and [Co{κ²N,N'-5-(2,6-(CH₃)₂C₆H₃)-NC₄H₂-2-C(H)=N(2-*t*Bu-C₆H₄)}₂] (**1.4i**), which were obtained in moderate yields (62-75 %) (Figure 1.37).

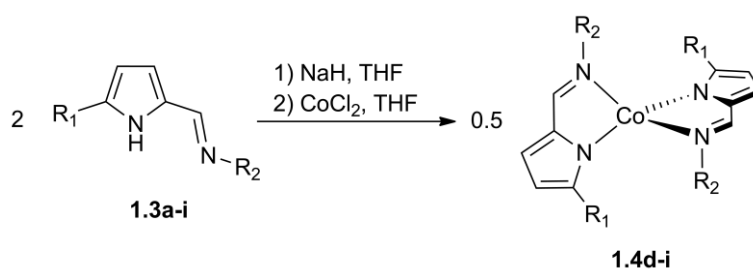


Figure 1.37 Synthesis of homoleptic Co(II) complexes **1.4d-i**.

All new compounds, which are stable in air when in a crystalline state, were characterized by single crystal X-ray diffraction, elemental analysis, FTIR and solution ¹H NMR spectroscopies, and magnetic susceptibility measurements in solution and in solid state. The FTIR spectra of **1.4d-i** show a strong band around 1560 cm⁻¹, being in the range of the characteristic values of the C=N bond stretching vibration. Due to the paramagnetic nature of these complexes, their ¹H NMR spectra lie in the range δ 118 to -125 ppm. The effective magnetic moment, μ_{eff}, was measured in toluene-*d*₈ solution by the Evans method,¹⁰⁹ and in solid state by means of SQUID magnetometry, both at room temperature (Table 1.3).

The experimental values of μ_{eff} lie within the range of known tetrahedral Co(II) complexes with *S* = 3/2,¹¹⁰ being similar to other 5-substituted-2-iminopyrrolyl compounds reported by our research group (4.79-5 μ_B).⁹⁴ These values are higher than the expected spin-only value of 3.88 μ_B, which suggests a significant contribution of

Chapter 1

angular momentum to the magnetic moments of the complexes, due to spin-orbit coupling effects.

Table 1.3 Effective magnetic moments μ_{eff} (μ_B) measured in toluene- d_8 solution (Evans method) and in solid state (SQUID method), at r.t. for complexes **1.4d-i**.

Complex	μ_{eff} (μ_B)	
	solution	solid state
1.4d	4.7	5.1
1.4e	5.2	4.7
1.4f	4.9	4.5
1.4g	4.8	5.1
1.4h	5.0	5.0
1.4i	5.3	4.7

1.2.2.2 X-ray diffraction studies

Crystals suitable for X-ray diffraction were grown from concentrated *n*-hexane (**1.4d-e**, **1.4g** and **1.4i**), diethyl ether (**1.4f**) and toluene (**1.4h**) solutions, cooled to -20 °C. Complex **1.4f** crystallized in the triclinic system, in the *P*-1, space group, while the remaining compounds in the monoclinic crystal system in the *P*2₁/*c* (for **1.4g-h** and **1.4d**) and *P*2₁/*n* (**1.4i** and **1.4e**) space groups. These Co(II) complexes are tetracoordinated where two 5-substituted-2-iminopyrrolyl ligands are bound to the metal center in a bidentate mode through the iminic (N2 and N4) and pyrrolyl (N1 and N3) nitrogen atoms. The molecular structures of all complexes are shown in Figure 1.38 while the selected bond distances, angles and τ_4 parameters are listed in Table 1.4. Complex **1.4g** has two independent molecules in the asymmetric unit, labelled as molecules 1 and 2.

The intrinsic geometrical nature of the *N,N'*-2-iminopyrrolyl five-membered chelating ligand inflicts relatively small values in the N-Co-N chelating bite angles θ (Table 1.4). For complexes **1.4d-f**, the θ angles are deviated from the ideal angle of a perfect tetrahedron (109.47°), showing distorted tetrahedral geometries. This is reflected in the calculated values of their τ_4 parameter,¹¹¹ which quantifies the geometry of four-coordinate species, 0 for pure square planar and 1 for pure tetrahedral geometries ($\tau_4 = 360^\circ - (\alpha + \beta) / 141^\circ$, where α and β are the two largest θ angles) (Table 1.4).

Results and Discussion

Table 1.4 Selected bond distances (Å), bond angles (°) and parameters τ_4 for complexes **1.4d-i**.

Complexes	1.4d	1.4e	1.4f	1.4g		1.4h	1.4i
				mol. #1	mol. #2		
<i>Distances (Å)</i>							
Co-N1	1.979(2)	1.999(3)	1.982(2)	1.969(3)	1.994(3)	2.003(4)	1.975(1)
Co-N2	2.036(2)	2.034(4)	2.069(2)	2.037(3)	2.050(3)	2.104(5)	2.028(1)
Co-N3	1.979(2)	2.004(4)	1.9969(18)	1.980(3)	1.979(3)	1.997(4)	1.977(1)
Co-N4	2.038(2)	2.036(4)	2.033(2)	2.049(3)	2.049(3)	2.088(4)	2.037(1)
N1-C5	1.349(3)	1.368(5)	1.361(3)	1.367(5)	1.354(5)	1.367(6)	1.352(2)
N1-C2	1.382(3)	1.387(6)	1.385(3)	1.371(4)	1.377(5)	1.367(6)	1.388(2)
N2-C6	1.290(3)	1.304(5)	1.305(3)	1.307(5)	1.299(5)	1.299(6)	1.300(2)
N2-Cx ^a	1.480(3)	1.432(5)	1.440(3)	1.437(5)	1.442(5)	1.438(7)	1.433(2)
C1-C5	1.505(4)	1.490(6)	1.466(3)	1.459(5)	1.467(6)	1.456(7)	1.492(2)
C2-C3	1.386(4)	1.393(5)	1.394(3)	1.388(5)	1.392(5)	1.390(7)	1.389(2)
C2-C6	1.419(4)	1.412(5)	1.410(4)	1.419(5)	1.412(5)	1.436(7)	1.416(2)
C3-C4	1.389(5)	1.380(7)	1.375(4)	1.388(6)	1.377(6)	1.374(7)	1.393(2)
C4-C5	1.397(4)	1.397(6)	1.408(3)	1.408(3)	1.410(5)	1.391(7)	1.395(2)
<i>Angles (°)</i>							
N1-Co-N3	116.67(9)	118.72(14)	123.88(8)	111.32(13)	111.3(1)	147.52(17)	112.59(5)
N2-Co-N4	124.51(9)	124.82(15)	111.75(8)	106.37(13)	106.4(1)	124.10(17)	136.82(4)
N1-Co-N4	124.85(10)	122.35(15)	128.86(8)	139.61(13)	139.6(1)	110.39(17)	120.73(4)
N3-Co-N2	126.18(10)	126.98(15)	128.51(8)	143.23(13)	143.3(1)	116.60(17)	123.36(4)
N1-Co-N2 (θ_1) ^a	84.63(10)	84.43(15)	85.03(8)	83.78(13)	83.8(1)	81.51(18)	82.89(4)
N3-Co-N4 (θ_2) ^a	84.8(1)	84.38(15)	83.80(8)	84.03(13)	84.0(1)	82.63(17)	83.03(4)
C6-N2-C ^b	121.0(2)	118.0(4)	117.0(2)	118.3(3)	118.3(3)	116.1(5)	121.6(1)
N2-C6-C2	119.4(3)	119.5(4)	121.0(2)	119.0(4)	119.0(3)	118.1(5)	118.9(1)
C5-N1-C2	107.0(2)	106.4(3)	106.1(2)	106.1(3)	106.1(3)	106.8(4)	107.1(1)
N1-C2-C3	109.7(2)	110.0(4)	110.2(2)	110.5(4)	110.5(3)	110.3(5)	109.3(1)
N1-C2-C6	118.0(2)	117.6(4)	118.0(2)	116.7(3)	116.7(3)	117.6(5)	115.7(1)
N1-C5-C4	109.6(2)	109.2(4)	109.6(2)	110.0(4)	110.0(3)	108.6(5)	109.7(1)
N1-C5-C1	121.8(2)	123.2(4)	123.4(2)	120.9(4)	120.9(3)	122.7(5)	119.7(1)
C3-C2-C6	132.3(3)	131.4(4)	131.8(2)	132.8(4)	132.8(4)	132.1(5)	135.0(1)
C2-C3-C4	106.4(3)	106.3(4)	106.5(2)	106.4(4)	106.3(4)	105.8(5)	106.7(1)
C3-C4-C5	107.3(3)	108.1(4)	107.5(2)	107.1(4)	107.1(4)	108.5(5)	107.2(1)
C4-C5-C1	128.6(3)	126.5(4)	126.9(2)	129.1(4)	129.0(4)	128.7(5)	130.2(1)
<i>Parameter τ_4^c</i>	0.77	0.77	0.73	0.55		0.63	0.71

^a θ = N-Co-N chelating ligands bite angles, ^b Cx corresponds to the iminic carbon, ^c Ref. 111

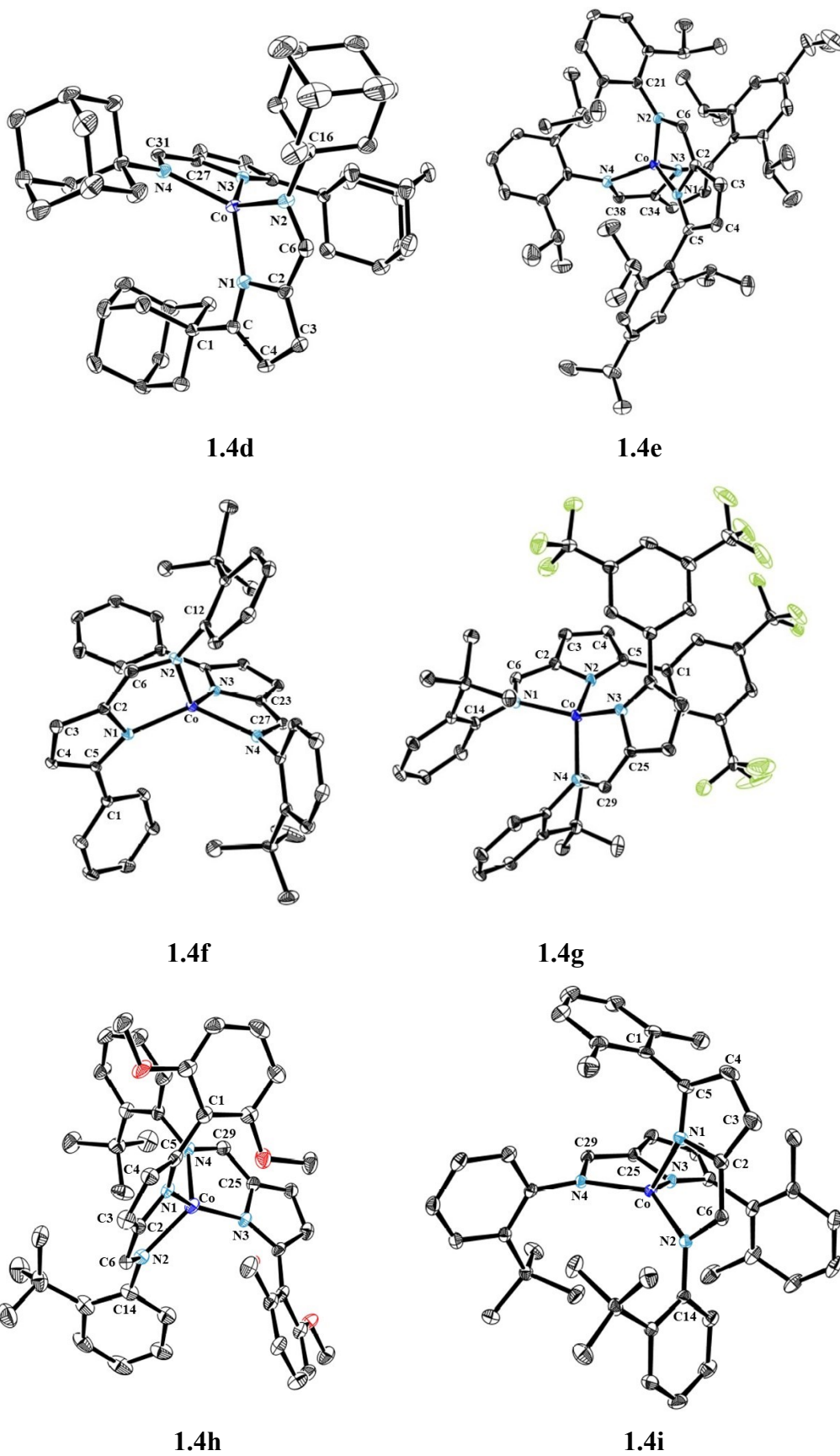


Figure 1.38 ORTEP-3 diagrams with ellipsoids drawn at 30% probability level. All hydrogen atoms were omitted for clarity.

However, throughout the second series of compounds **1.4f-i**, bearing the bulky and unsymmetrical *N*-2-(*t*-butyl)phenyl group, the conformation acquired is such that, depending on the type and position of the substituents in the 5-phenyl group, the geometry shifts away from the tetrahedron. Surprisingly, for complexes **1.4g-h** this shift is very noticeable in their strong deviations from tetrahedral geometries, observed in angles N1-Co-N4 and N3-Co-N2 for **1.4g** and N1-Co-N3 angle for **1.4h**, and also reflected in the values of the τ_4 parameters (which are considerably lower than 1). Compound **1.4g** shows a geometry between a tetrahedral and a square planar and **1.4h** shows a seesaw-like geometry, in which the N1-Co-N3 bond angle ($147.52(17)^\circ$) tends to linearity, forming the plank in the axial position, and the N2-Co-N4 bond angle ($124.10(17)^\circ$) forming the pivot in the equatorial position. These changes also result from interactions existing between the neighboring molecules and solvent, which will be discussed below in the following pages. As for complex **1.4i**, when compared to the tetrahedral **1.4c**, which bears a *N*-2,6-bis(isopropyl)phenyl substituent and was already reported by our research group,⁹⁴ it shows a significant distortion toward a trigonal pyramidal geometry (Figure 1.39), in which N2, N3 and N4 may be envisaged as forming the trigonal plane and the N1 appears positioned in the apical position. This is due to steric congestion and asymmetry caused by the bulky *N*-2-(*t*-butyl)phenyl group. In Figure 1.39 it is also possible to observe the distortions caused by the increase in the ligand volume of the pyrrolyl 5-substituents.

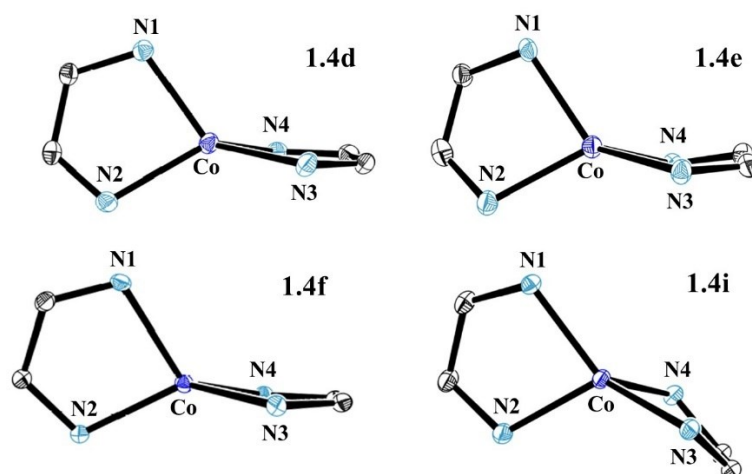


Figure 1.39 ORTEP-3 diagrams with ellipsoids drawn at 30% probability level, showing the geometry of the five-membered coordinating chelates in compounds **1.4d-e**, **1.4f** and **1.4i**. The hydrogen atoms and the remaining ligand carbon atoms were omitted for clarity.

Chapter 1

The torsion angles of the *N*-aryl ring and the 5-aryl ring in relation to the 2-iminopyrrolyl moieties of complexes **1.4d-i** are listed in Table 1.5. For compounds **1.4e** and **1.4i** the two planes are close to perpendicularity due to the steric hindrance imparted by the bulky 2,6-dimethyl-phenyl and 2,4,6-triisopropyl-phenyl substituents. Also, the five-membered chelates (defined by the atoms Co1-N1-C2-C6-N2 and Co1-N3-C_x-C_y-N4, x and y being the labels of the corresponding atoms of the second chelate) are deviated from planarity 17.9(3)–21.9(3)° for **1.4e** and 17.72(9)–23.5(8)° for **1.4i**, as opposed to the near planar chelates observed in the remaining compounds (1.4(2)–9.6(2)° for **1.4f**, 2.3(2)–3.8(2)° for **1.4f**, 9.8(3)–13.5(3)° for **1.4h** and 8.2(2)–10.9(2)° for **1.4d**).

Table 1.5 Dihedral angles of *N*-aryl ring and 5-aryl ring relative to the 2-iminopyrrolyl moiety of complexes **1.4e-i**

Complex	Dihedral angle <i>N</i> -Ar and iminopyrrolyl planes (°)	Dihedral angle 5-Ar and iminopyrrolyl planes (°)
1.4e	72.79(17) and 85.38(18)	74.88(15) and 76.50(16)
1.4f	68.39(10) and 84.73(8)	21.72(7) and 18.7(1)
1.4g	mol. 1 75.58(16) and 76.51(15)	29.84(13) and 34.64(13)
	mol. 2 69.53(1) and 73.8(15)	25.37(12) and 34.24(12)
1.4h	57.85(18) and 85.3(2)	36.30(18) and 46.57(15)
1.4i	82.65(5) and 87.59(5)	83.96(5) and 87.96(5)

The analysis of the crystalline supramolecular arrangements revealed that complex **1.4g** exhibits non-classical hydrogen-bonds. In this case, the asymmetric unit is composed of two independent molecules (labelled as 1 and 2), where each molecule 1 interacts with two neighboring molecules 2 via two non-classical C–H···F hydrogen bonds, in a donor-acceptor relationship. Two other C–H···F interactions are also observed with the corresponding counterpart of a neighboring molecule (Table 1.6). Also, the crystal packing view of compound **1.4g** shows a parallel displaced π - π stacking between the two *N*-2-(*t*-butyl)phenyl rings by a distance of 3.466 Å (Figure 1.40).¹¹²

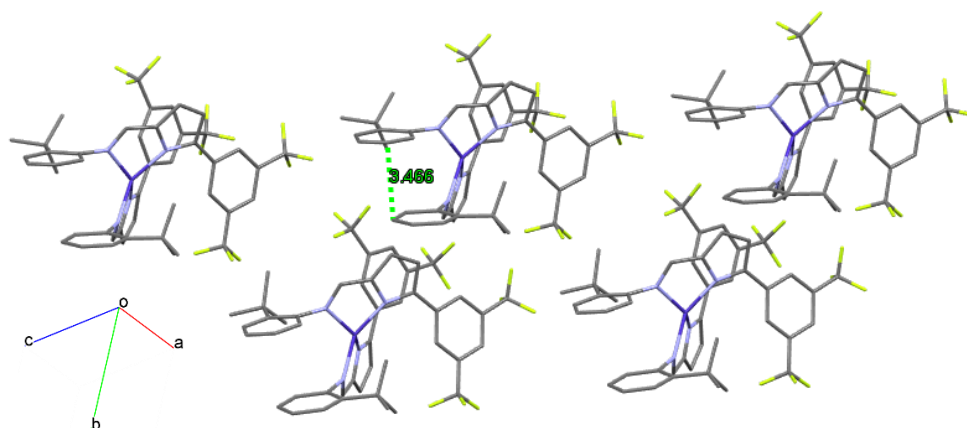


Figure 1.40 Crystal packing of complex **1.4g**, when viewed along *b*. The interactions mentioned in the text are not shown for clarity.

Complex **1.4h** also exhibits non-classical hydrogen bonds in this case involving the methoxy groups and solvate molecules. Its crystal structure revealed that it co-exists with a diethyl ether solvate in a ratio of 1:3 (complex:Et₂O) (Figure 1.41). From the six interactions with a neighboring complex and three solvate molecules, two of them are C–H··· π C interactions, as donor-acceptor, two non-classical hydrogen-bonds C–H···O between the complex and the oxygen of the solvate and the last two C–H··· π C interactions between the complex and the solvate.

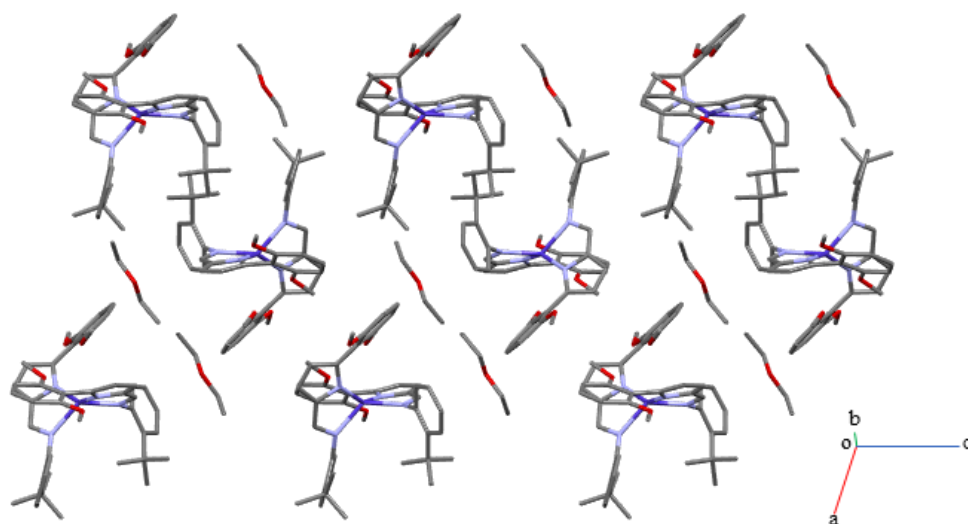


Figure 1.41 Crystal packing of complex **1.4h**, when viewed along *b*. The interactions mentioned in the text are not shown for clarity.

Table 1.6 List of intermolecular interactions for complexes 1.4g–h.

Complex	D–H···A	d(H···A) (Å)	d(D···A) (Å)	(DĤA) (°)
1.4g	C ₄₅ /mol. 1–H _{45E} ···F ₅ /mol. 2	2.623	4.009	117.33
	C ₃₄ /mol. 2–H ₃₄ ···F ₁₁ /mol. 1	2.521	3.403	158.45
	C ₁₇ /mol. 1–H ₁₇ /mol. 1···F ₂ /mol. 1	2.633	3.275	126.73
1.4h	C ₃₅ –H _{35C} ···πC ₁	2.791	3.635	147.06
	C ₈ –H ₈ ···O ₅	2.518	3.362	150.95
	C ₂₉ –H ₂₉ ···O ₅	2.655	3.560	164.34
	C ₄₄ –H _{50C} ···πC ₅₀	2.900	3.619	132.60
	C ₁₇ –H ₁₇ ···πC ₄₉	2.864	3.617	139.04

1.2.2.3 Complexes 1.4a-e: influence of sterically bulky ligands and geometrically congested iminopyrrolyl Co(II) complexes on the SIM behavior

Single-Ion systems containing cheap and abundant first-row *d*-block metal centers started to be the subject of intensive study in 2010.⁴⁹ Since then, several tetracoordinate Co(II) complexes displaying SIM behavior have been reported, but only a few showed slow relaxation of magnetization in the absence of an external magnetic field. Therefore, the search for better SIMs is the main objective of this work, as well as the in-depth study of the origin of the magnetic anisotropy of this family of compounds and how the ligand field and geometry, namely the geometric distortion caused by the ligands, affect this behavior.

Our research group previously reported three highly electronically unsaturated homoleptic Co(II) complexes encompassing 2-formiminopyrrolyl *N,N'*-chelating ligands **1.4a-c**,^{91,94} which showed large magnetic anisotropy through static (DC) magnetic measurements. Motivated by these results, five of such homoleptic Co(II) compounds **1.4a-e** of increasing steric bulk (Figure 1.42) were fully magnetically characterized, being **1.4d-e** newly synthesized complexes.

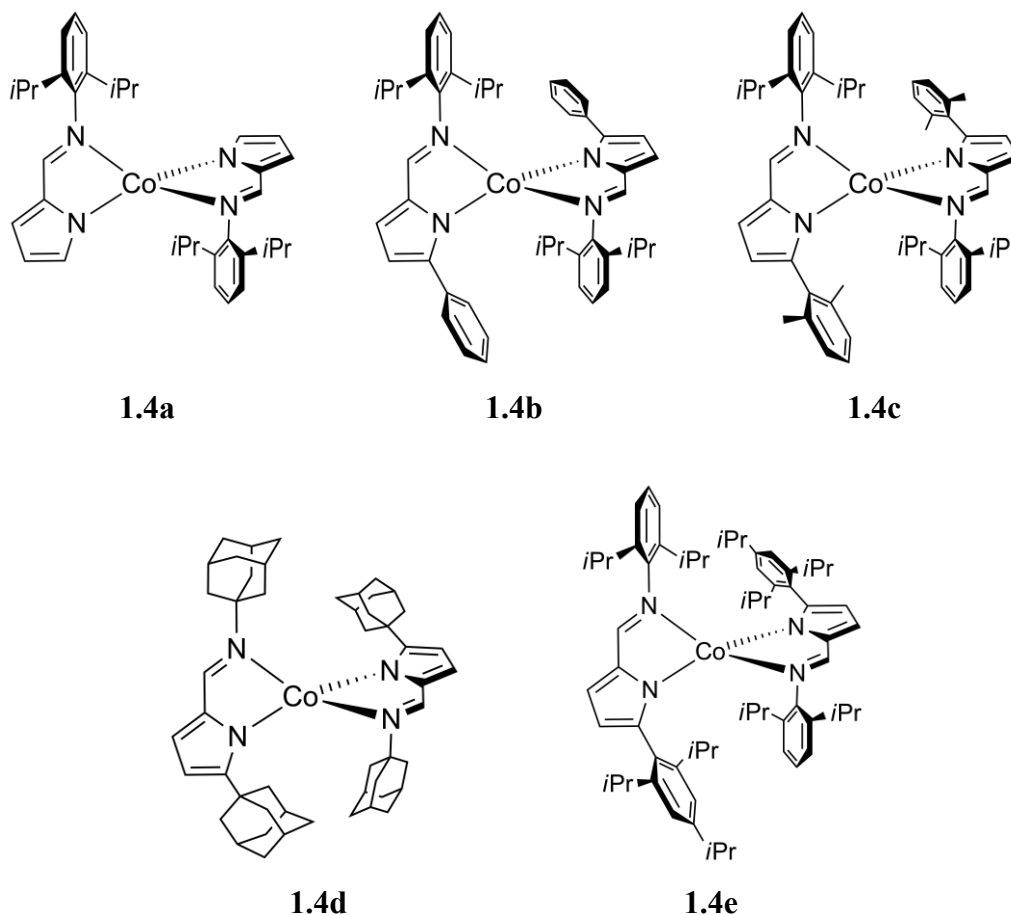


Figure 1.42 Complexes **1.4a-e** studied in this work.

The AC and DC measurements, HFEPR and theoretical studies will be presented in the next pages for this family of distorted tetrahedral Co(II) complexes, in an attempt to rationalize the SIM behavior exhibited by all the five compounds.

1.2.2.3.1 Static (DC) magnetic measurements of complexes **1.4a-e**

The static magnetic susceptibility measurements were performed for complexes **1.4a-e** at the Solid-State Group laboratory of C²TN-IST. The $\chi_M T$ vs. T plots measured at 500 Oe in the range of 1.8-300 K are shown in Figure 1.43. The curves show a similar trend for all compounds except for **1.4e**. At room temperature, the χ_M values are of 3.03 for **1.4a**, 2.86 for **1.4b**, 2.67 for **1.4c**, 3.28 for **1.4d** and 2.81 cm³.K.mol⁻¹ for **1.4e**, corresponding to the expected value for a high spin Co(II) ion, but much higher than the

Chapter 1

calculated spin-only value for a high spin Co(II), $1.875 \text{ cm}^3\cdot\text{K}\cdot\text{mol}^{-1}$ ($S = 3/2$ and $g = 2.00$), indicating a substantial contribution of orbital angular momentum.^{45,54,56,75,76,110}

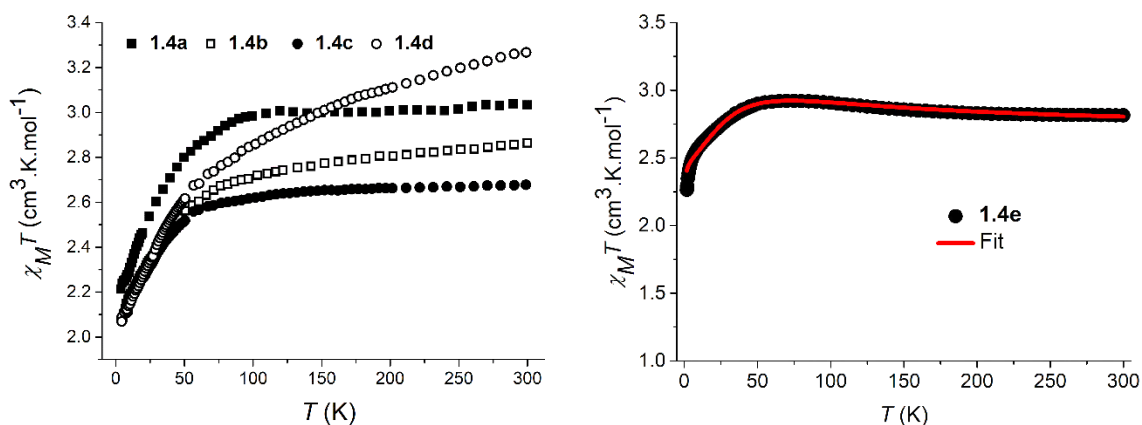


Figure 1.43 $\chi_M T$ vs. T plot measured at 500 Oe for complexes **1.4a-d** (left) and $\chi_M T$ vs. T plot measured at 500 Oe for complex **1.4e**. The red line represents the simulation on the basis of the spin Hamiltonian parameters (right).

Upon decreasing the temperature, the $\chi_M T$ values remain almost constant down to *ca.* 100 K for **1.4a** and **1.4c**, while **1.4b** and **1.4d** decrease more rapidly. Below 100 K a continuous decrease is observed for all the compounds reaching 2.24 for **1.4a**, 2.09 for **1.4b**, 2.06 for **1.4c** and $2.32 \text{ cm}^3\cdot\text{K}\cdot\text{mol}^{-1}$ for **1.4d** at 5 K (Figure 1.43, left). This sudden decrease appears to be due to the presence of a strong axial magnetic anisotropy rather than to intermolecular antiferromagnetic interactions between Co atoms of adjacent molecules in the crystal structure, since their minimum distance is larger than 9 Å. As for **1.4e**, the $\chi_M T$ values rise slightly with decreasing temperature down to 60 K and drop from there on, reaching $2.26 \text{ cm}^3\cdot\text{K}\cdot\text{mol}^{-1}$ at 1.8 K (Figure 1.43, right). For this complex the experimental data was fitted to the spin Hamiltonian (Equation 1.22, next subsection), where the ZFS parameters D and E were obtained (see Table 1.10, p. 78).

The field-dependence of the magnetization, measured at different fixed temperatures showed the absence of hysteresis for all the five complexes **1.4a-e**. This can be attributed to QTM or due to the slow magnetic sweeping rate of the used SQUID magnetometer, which only runs in persistent mode with sweeping rates up to $20 \text{ Oe}\cdot\text{s}^{-1}$ during measurements (Figure 1.44).

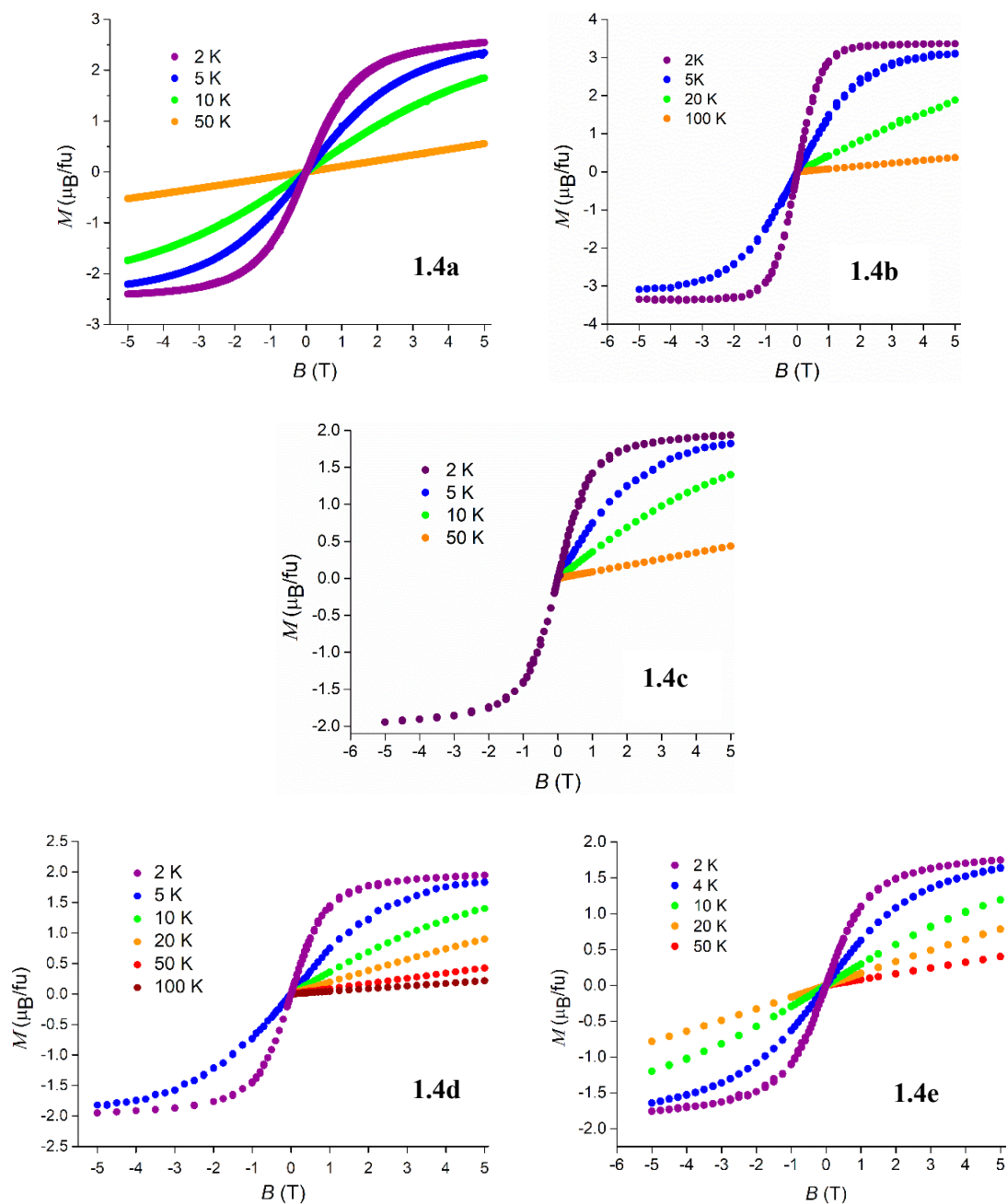


Figure 1.44 M vs. B plot measured from 0 to 5 T at different fixed temperatures for complexes 1.4a-e.

1.2.2.3.2 The calculation of ZFS parameters D and E

There are three routes to quantify the axial and rhombic ZFS parameters D and E in a sample:

Chapter 1

- by fitting the experimental $\chi_M T$ vs. T and M vs. B plots to the spin Hamiltonian, Equation 1.22:

$$H = \mu_B g \cdot \widehat{S} + D\widehat{S}_z^2 + E(\widehat{S}_x^2 - \widehat{S}_y^2) \quad (1.22)$$

where μ_B is the Bohr magneton and g the Landé g -factor. For complex **1.4e** (and further below for complex **1.4i**) it was possible to fit the $\chi_M T$ vs. T plots, obtaining the values of these two parameters;

- by HFEPR experiments, where the frequency-dependent signals in a EPR spectrum is based on transitions between the M_s levels, where the selection rule in EPR is $\Delta M_s = 1$. These data are then fitted to the spin Hamiltonian (Equation 1.22), from which the D , E and g values are obtained. In this work, all of these experiments were carried out at the University of Stuttgart, using different frequencies and temperatures and by sweeping the magnetic field from 0 to 15 T;

- by using theoretical calculations according to the *ab initio* Ligand-Field Theory (AILFT), based on the crystallographic X-ray structures, to obtain the same parameters. In this work, all these calculations were carried out at Faculty of Sciences, University of Lisbon.

The first complexes to be studied were **1.4a-d** in order to understand the influence of the ligand volume on their magnetic properties. As the results became more and more promising, the idea of preparing a chelating ligand of this family bulkier than that of compound **1.4d** and evaluate its impact in the SIM behavior emerged. Therefore, inspired by the excellent results, complex **1.4e** was synthesized.

In the next subsections, the characterization of compounds **1.4a-d** as candidates to Single-Ion Magnets will be presented as well as the clarification of this behavior in order for the reader to understand the results obtained and consequently what led us to prepare **1.4e**.

1.2.2.3.2.1 HFEPR spectroscopy of complexes 1.4a-d

All the HFEPR measurements presented in this thesis were performed and interpreted at the University of Stuttgart, Germany, by Doctor Joris van Slageren and his PhD students David Hunger and Alexander Allgaier, in a collaborative work.

To investigate the zero-field splitting and hence to assess the viability of compounds **1.4a-d** as SMMs, the HFEPR measurements were carried out on all complexes at different frequencies and temperatures. The spectra of complex **1.4a** at 5 K display one strong, frequency-dependent resonance line in the $g = 2$ region (Figure 1.45, left).

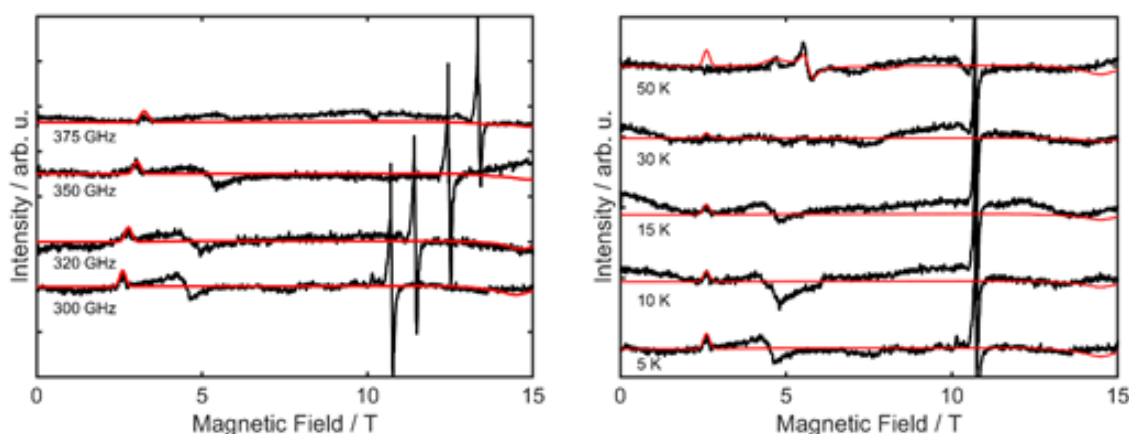


Figure 1.45. HFEPR spectra of a pressed powder pellet of complex **1.4a** at $T = 5$ K and different frequencies (left) and HFEPR spectra of a pressed powder pellet of complex **1.4a** at $\nu = 300$ GHz and different temperatures (right). The black lines represent the measurement, red lines the simulation on the basis of the spin Hamiltonian parameters. The strong resonance line at fields higher than 10 T is due to an instrumental artefact.

Empty sample-holder measurements revealed this resonance line to be an instrumental artefact that was traced to the gold mirror employed. In addition, these spectra show a weak, frequency-dependent upward-pointing resonance line around 3 T for frequencies between 300-375 GHz. This resonance line is attributed to the intra-doublet transition within the ground Kramers doublet (KD). Its weak intensity, as well as the absence of further resonance lines suggest that axial ZFS parameter D is large and negative. A further broad feature at around 5 T could not be assigned. Upon increasing the temperature, the intensity of the 3 T resonance line decreases in line with its attribution to a ground state transition (Figure 1.45, right). At 50 K, further resonance

Chapter 1

lines become visible in the 5 T region, which are attributed to transitions within the excited KD. A fit of the spectra to the spin Hamiltonian (Equation 1.22), yielded a slightly rhombic g -tensor (Table 1.7, next subsection). The D -value was found to be large and negative ($D = -69(5) \text{ cm}^{-1}$), which is beneficial for SMM behavior, and the rhombic ZFS parameter E (transverse anisotropy) is less than 10 % of the D -value ($E/D = 0.094$) making the ZFS of this system rather axial.

HFEPR spectra recorded on a sample of **1.4b** at 5 K display three very weak resonance lines (Figure 1.46).

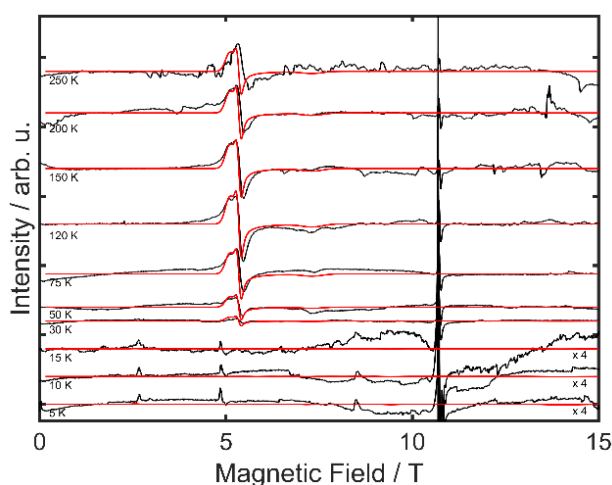
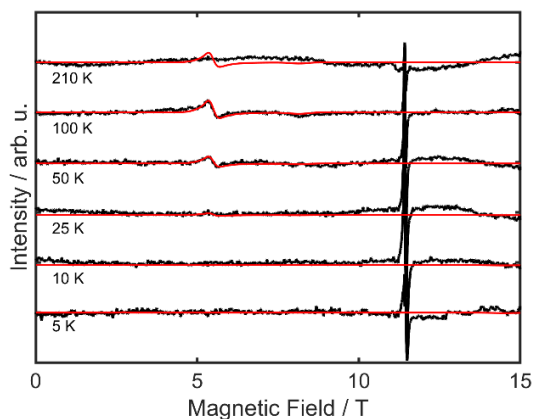


Figure 1.46 HFEPR spectra of a pressed powder pellet of complex **1.4b** at $\nu = 300$ GHz and different temperatures. Black lines represent the measurement, red lines the simulation on the basis of the spin Hamiltonian parameters. The strong resonance line at fields higher than 10 T is due to an instrumental artefact.

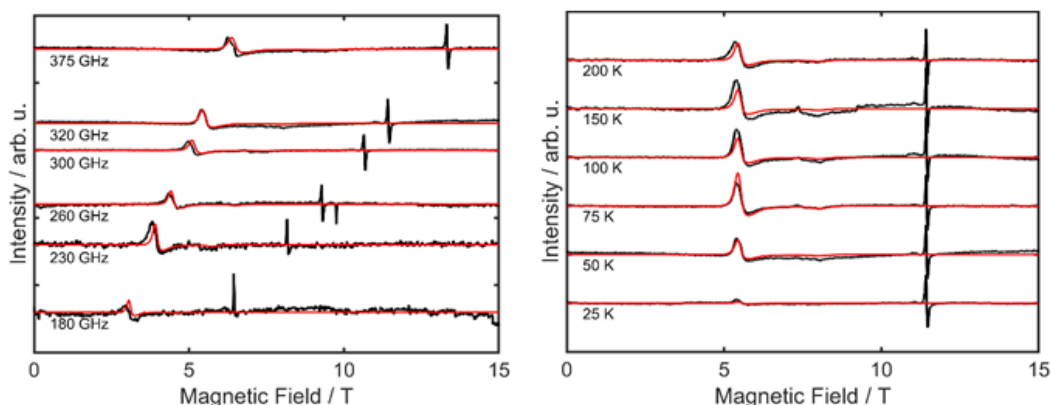
The lowest-field resonance line is again attributed to the intra-ground-KD transition, and the other two to a minimum amount of solid oxygen trapped in the sample holder.¹¹³ At higher temperatures, the resonance line due to the excited KD is clearly observed just above 5 T ($\nu = 300$ GHz, Figure 1.46).

Simulations revealed that the g - and D -tensors are even more axial than for **1.4a** (Table 1.7).

Low-temperature HFEPR spectra recorded on samples of **1.4c** and **1.4d** did not show any signal, and at higher temperatures spectra again displayed resonance lines assigned to the excited KD (Figure 1.47). The extracted spin Hamiltonian parameters are very similar to those for the other complexes (Table 1.7, see below).



(a)



(b)

Figure 1.47 HFEPR spectra of a pressed powder pellet of complexes (a) **1.4c** at $\nu = 320$ GHz and different temperatures and (b) **1.4d** at $T = 50$ K and different frequencies (left) and at $\nu = 320$ GHz and different temperatures (right). Black lines represent the measurement, red lines the simulation on the basis of the spin Hamiltonian parameters. The strong resonance line at fields higher than 10 T is due to an instrumental artefact.

HFEPR spectroscopy revealed the studied compounds to possess highly axial magnetic anisotropies, with rhombicity in the case of **1.4a**.

1.2.2.3.2 Theoretical studies of complexes 1.4a-d

All the theoretical calculations presented in this thesis were performed and interpreted by Doctor Nuno Bandeira, at the Biosystems & Integrative Sciences Institute, Center of Chemistry and Biochemistry, Faculty of Sciences, University of Lisbon.

Chapter 1

In order to understand the electronic processes at play in these complexes, a multi-reference wavefunction analysis was undertaken employing the Quasi-Degenerate N-Electron Valence Perturbational Theory (QD-NEVPT2) method to reproduce their zero-field splitting and determine the source of their magnetic anisotropy.

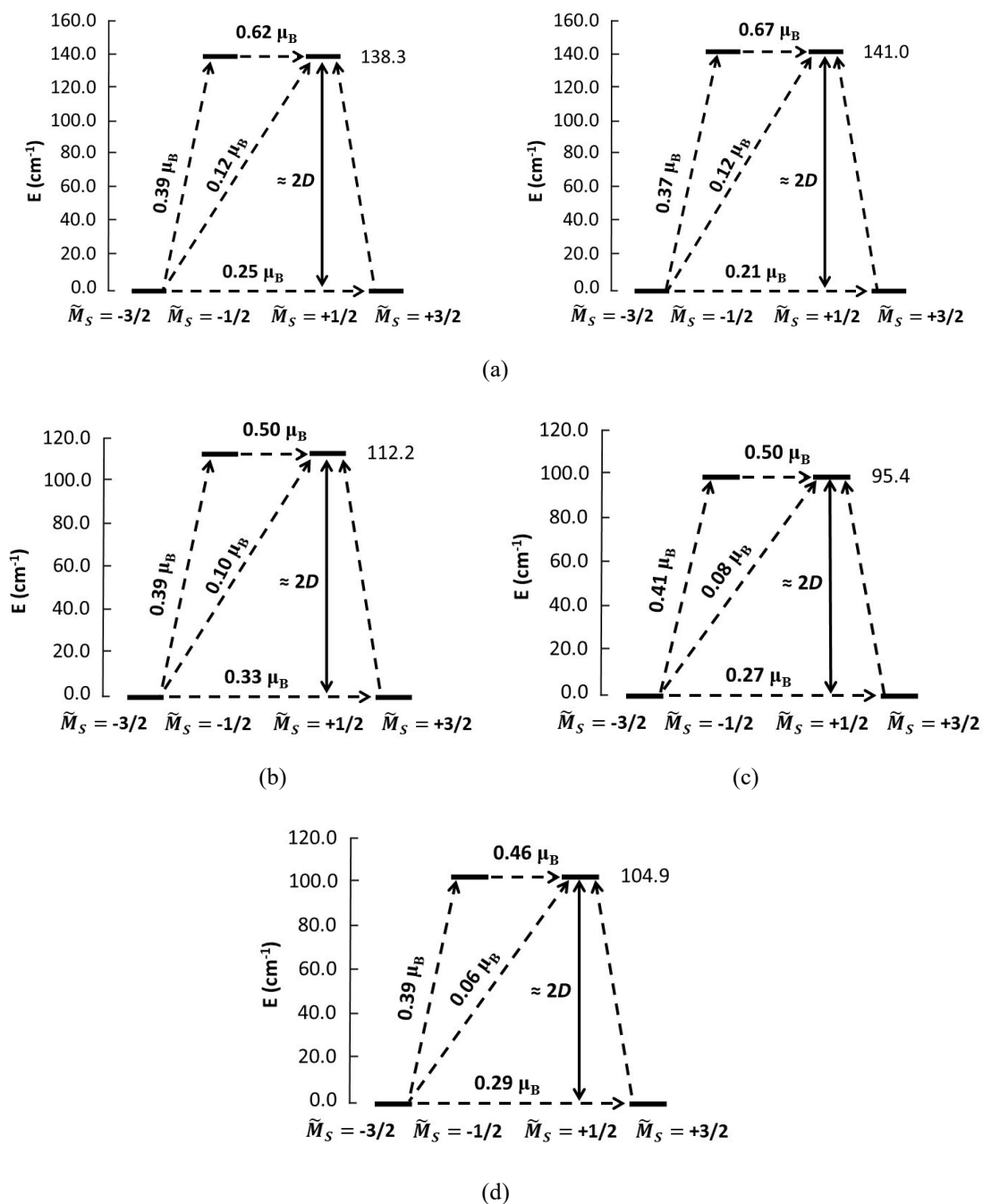


Figure 1.48 Calculated zero-field splitting plots with transition moments between each spin-orbit state. The two crystallographic units of complex **1.4a** are shown in plot (a), **1.4b** in (b), **1.4c** in (c) and **1.4d** in (d).

The calculations were performed on the experimentally determined crystal structures, and the corresponding energetics of the KDs and respective transition moments are displayed in Figure 1.48. Since complex **1.4a** has two crystallographically distinct units⁹¹ both were treated separately in the calculations.

It may be seen that all complexes display some measure of QTM with a sizable transition moment between the $\pm 3/2$ components. They are however generally inferior to those with $\Delta\tilde{M}_S \pm 1$. If one defines the best SMM (or SIM) character as the molecule with the largest negative D value this may be observed in complex **1.4a**, where the easy axis generally bisects the nitrogen base chelate in this family of complexes (Figure 1.49).

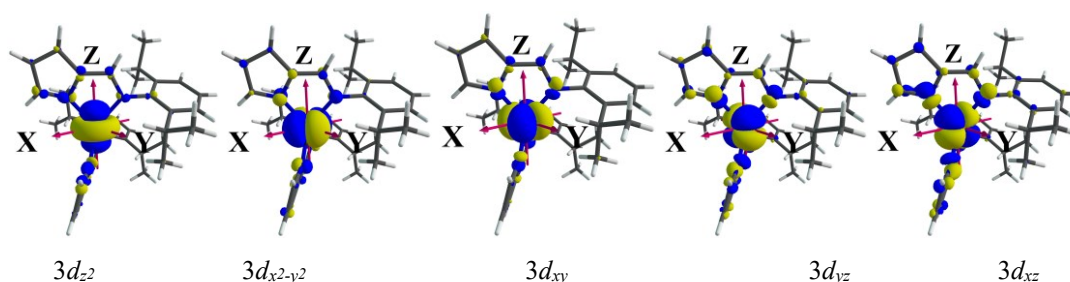


Figure 1.49 Active space orbitals of complex **1.4a** shown in their magnetic axis frame.

The *ab initio* LFT analysis was performed and allowed to map the 3d orbitals of all the complexes studied (Figure 1.50).

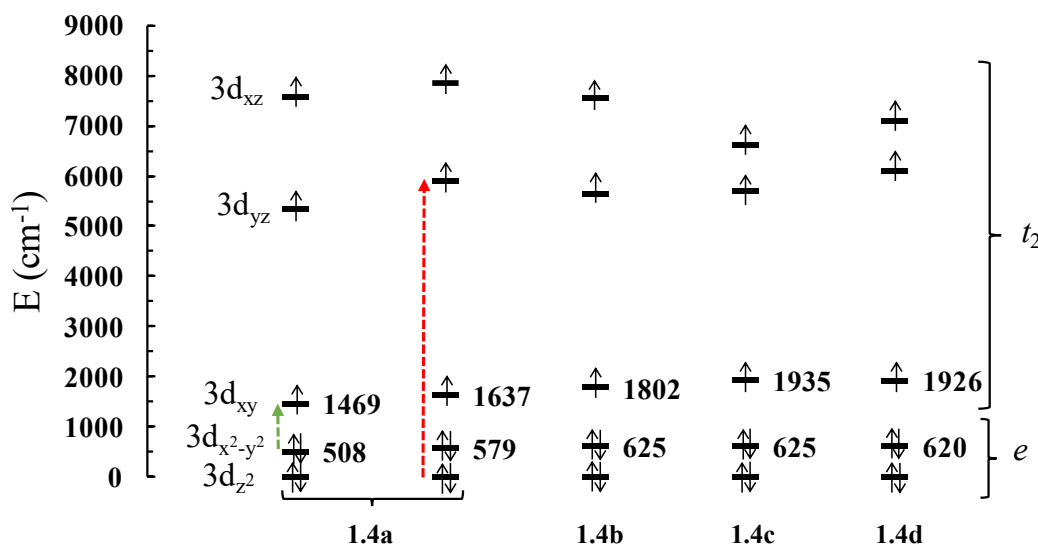


Figure 1.50 AILFT-NEVPT2 3d orbital splitting of metal complexes **1.4a-d**. The green and red arrows correspond to the energy gap between the $3d_{x^2-y^2} \rightarrow 3d_{xy}$ and $3d_{z^2} \rightarrow 3d_{yz}$ orbitals, respectively.

Chapter 1

The origin of the high ZFS parameter D is predominantly due to the first excited state of quartet multiplicity, corresponding to the transition from the $3d_{x^2-y^2} \rightarrow 3d_{xy}$ orbitals, where the magnitude of D is inversely proportional to the energy gap between those $3d$ orbitals. On the other hand, the largest contributor to E is the second excited state quartet, corresponding to the transition from the $3d_{z^2} \rightarrow 3d_{yz}$ orbitals, where E is also inversely proportional to the energy gap between those $3d$ orbitals. The calculated values of D , E and g are represented in Table 1.7 and correspond remarkably well to those found in the HFEP R measurements.

Table 1.7 Calculated and experimental (HFEP R) D , E and g values for complexes **1.4a-d**.

Complex	D (cm ⁻¹)		E (cm ⁻¹)		g -tensor	
	Calc.	Exp.	Calc.	Exp.	Calc.	Exp.
1.4a	-69.8	-69(5)	1.7	6.5(5)	2.068, 2.120, 2.906 ^a	2.05(5), 2.22(2), 2.77(5)
					2.061, 2.107, 2.908 ^b	
1.4b	-56.6	-53(4)	1.5	0.85(5)	2.088, 2.133, 2.778	2.05(5), 2.05(5), 2.91(2)
1.4c	-47.7	-48(3)	0.9	1.0(2)	2.117, 2.143, 2.702	2.10(3), 2.17(3), 2.80(5)
1.4d	-52.4	-52(4)	0.8	1.0(2)	2.102, 2.126, 2.739	2.00(5), 2.15(5), 2.85(5)

^a Molecule #1 of the unit cell of **1.4a**; ^b Molecule #2 of the unit cell of **1.4a**.

As the structural distortion of the tetracoordinate metal site holds the key to optimize the SMM performance of the complexes, it was decided to perform a magnetostructural analysis of a model complex. A Co(II) square planar compound investigated by Carabineiro *et al.*⁹¹ serves as a simple example in this family of homoleptic Co(II) complexes, although employing a (*E*)-2-[*N*-(2,6-bis(isopropyl)phenyl)acetimidino]pyrrolyl ligand, which contains a methyl group substituent of the iminic carbon instead the H atom of complexes **1.4a-d**. For this analysis, the ligand was simplified by removing the two isopropyl groups from the phenyl ring and replacing them with hydrogens at a standard bond length.

Two types of distortions were examined with this model: (1) planarization and (2) pyramidalization of the tetrahedron.

In the first instance, it is evident that the switch from tetrahedral to square planar geometry leads to a drop in the D value (Figure 1.51). Eventually upon reaching a square planar geometry (interplanar dihedral angle between the two ligands $\phi < 15^\circ$), the ligand

field is high enough for the ground state configuration to change to a doublet, in which case there is no ZFS.

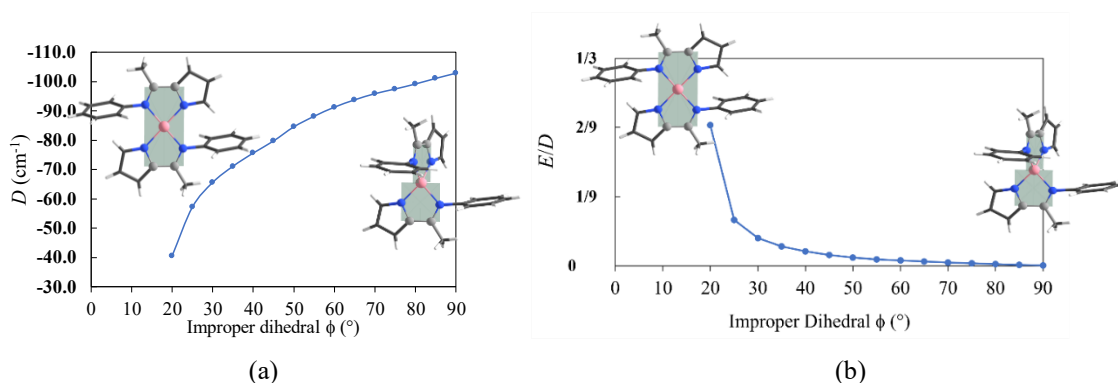


Figure 1.51 Magnetostructural analysis of the D parameter (a) and E/D (b) as a function of planarization (improper dihedral angle ϕ) of a tetrahedral bis(2-iminopyrrolyl) Co(II) model complex.

Complexes **1.4a-d** show experimental dihedral angles ϕ in the range of 81.03(3)-85.2(1) (Table 1.8) by which, from the Figure 1.51a, this range lies in the most negatively valued region of the model, meaning that the axial anisotropy cannot be much more improved in this way. These results are also typical of other Co(II) tetrahedral complexes as reported by Rajaraman and co-workers.¹¹⁴ Conversely, the E parameter value is very low in the above-mentioned range of experimental dihedral angles (Figure 1.51b).

In the second case, the model calculations consisted of monitoring the D value upon sweeping the interligand angle ω , formed between the dummy bonds defined by the Co atom and each of the centroids of the chelating five-membered rings C-C bonds, while keeping the position of the chelating ligands orthogonal to each other (Figure 1.52). This type of distortion goes from a symmetrical tetrahedral environment ($\omega = 180^\circ$, represented at the center of Figure 1.52a) to a trigonal based pyramid (represented at left and right in Figure 1.52a).

The changes in D are significant with regards to the ones at the tetrahedral baseline ($\omega = 180^\circ$). D becomes more negative by more than 50 % (Figure 1.52a), thus indicating that an induced distortion by a sterically constrained ligand presents an optimum value for a Co(II) tetrahedral site, which is the case in this family of compounds that present experimental values of angles ω in the range 162.42(5) to 177.12(12) $^\circ$ (Table 1.8). This can be explained by a decrease in the $3d_{x^2-y^2} \rightarrow 3d_{xy}$ energy gap from 842 to 540 cm^{-1} in AILFT (Figure 1.52c). On the other hand, the E parameter value is in general very low,

Chapter 1

especially displaying the lowest values in the range of the experimental values of angles ω (Figure 1.52b).

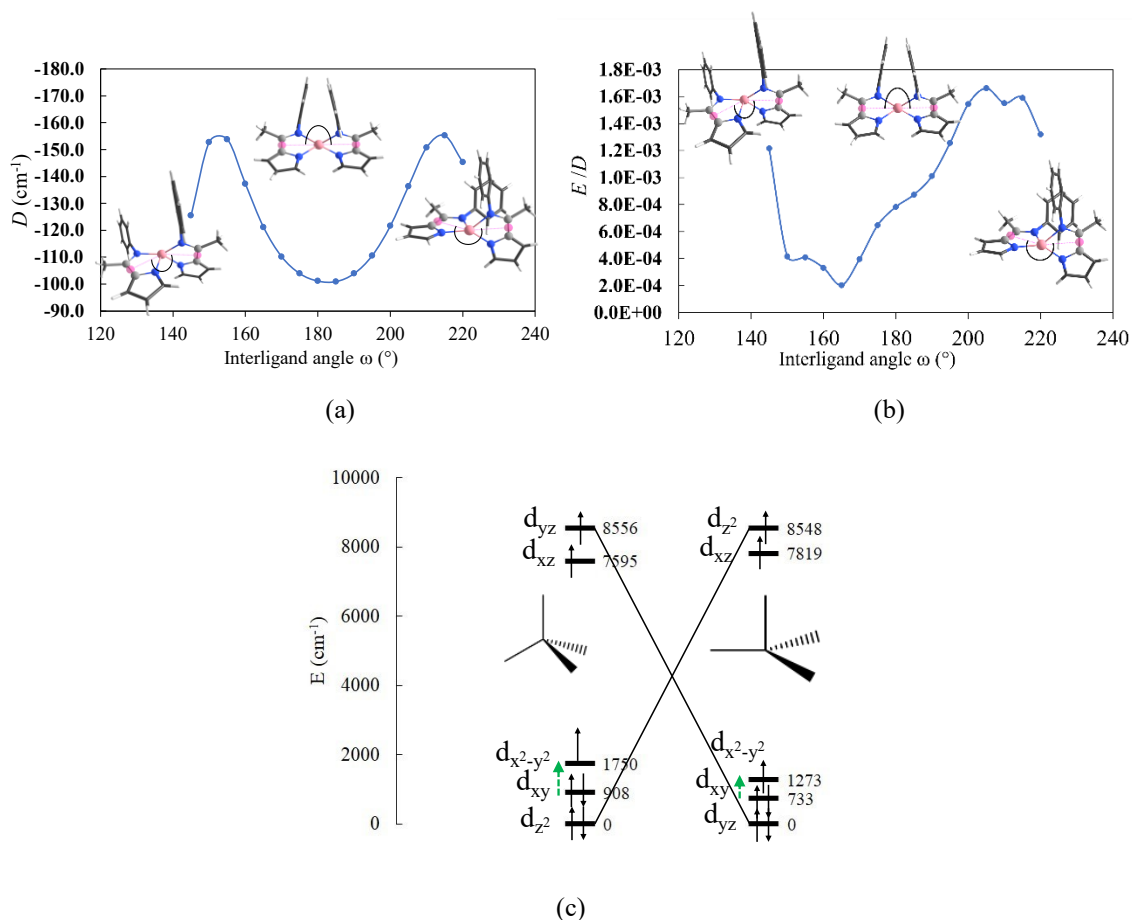


Figure 1.52 Magnetostructural analysis of the D parameter (a), E/D (b) and ligand field (c) as a function of angle ω , representing the pyramidalization of a tetrahedral bis(2-iminopyrrolyl) Co(II) model complex (at the center of the left plot). In left, the dummy atoms used as a reference for the angle value are shown in pink.

Table 1.8 Bite angles θ , dihedral angles ϕ and interligand angles ω for complexes **1.4a-d**.

Complexes	1.4a		1.4b	1.4c	1.4d
	Mol. #1	Mol. #2			
N1-Co-N2 (θ_1) ^a	82.5(3)	83.0(3)	83.8(1)	84.15(7)	84.63(10)
N3-Co-N4 (θ_2) ^a	82.8(3)	83.4(3)	83.91(14)	85.11(7)	84.8(1)
Dihedral ϕ ^b	81.03(3)	82.00(4)	82.20(17)	84.68(8)	85.2(1)
Angle ω ^c	173.5(2)	174.7(2)	177.12(12)	162.42(5)	170.61(6)

^a θ = N-Co-N chelating ligands bite angles; ^b ϕ = dihedral angle formed between planes defined by atoms (Co, N1, N2) and (Co, N3, N4); ^c ω = interligand angle formed between dummy bonds Co-(C2-C6)_{centroid} and Co-(Cx-Cy)_{centroid}.

Another parameter that can be explored is the ligand bite angle, also known as the polar angle θ .¹¹⁵ As these 2-iminopyrrolyl derivatives have two carbon atoms between the coordinating nitrogen atoms, a simple model such as *cis*-[Co(NH₂)₂(NH₃)₂] can be used to account for the changes in D with angular changes. The chemical nature of the ligands is entirely different, but the complex is still isoelectronic with the ones reported in this work. This allows for a qualitative understanding of the result of the structural changes (Figure 1.53).

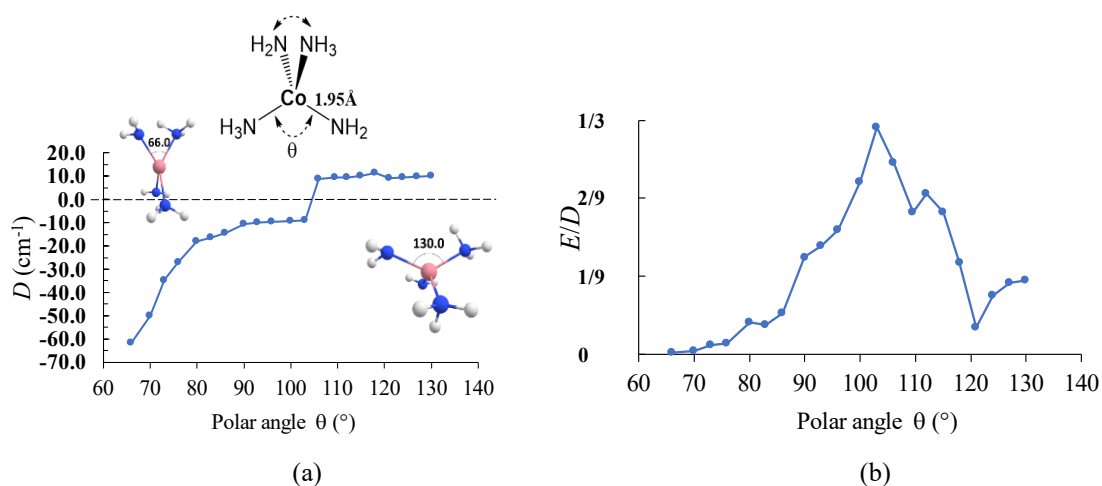


Figure 1.53 Variation of D (a) and E/D (b) with the ligand bite angle θ .

It may be seen that tetrahedral flattening towards a square planar geometry (symmetrical increase of both θ angles) causes considerable rhombic anisotropy, so much so that the sign of D loses any meaning (Figure 1.53a). Upon approaching T_d type symmetry ($\theta = 109.47^\circ$) the sign of D is small and positive, but as this angle decreases it tends towards zero. At about 85° the system gains axial anisotropy that increases consistently as the bite angle becomes tighter, moreover the rhombic anisotropy parameter E also tends towards zero (Figure 1.53b). Because complex **1.4a** displays a more elongated tetrahedral geometry (see experimental values of ligand bite angles θ in Table 1.8), the values of D are more negative than those calculated for the remaining compounds **1.4b-d**.

Owing to their intrinsic structural rigidity, the bite angle variation in the 2-iminopyrrolyl chelates is limited to a few degrees, as it can be observed in Table 1.8 for complexes **1.4a-d** ($82.5(3)$ to $85.11(7)^\circ$), essentially depending on the steric constraints of the coordination sphere. Nevertheless, the bite angles θ in all the studied

Chapter 1

compounds are already in the favorable range of axial anisotropy and cannot be much improved.

1.2.2.3.3 Dynamic (AC) magnetic measurements for complexes **1.4a-d**

The dynamic magnetic measurements were performed for complexes **1.4a-d** at the Solid-State Group laboratory of C²TN-IST.

To investigate the magnetic relaxation dynamics, frequency- and temperature-dependent AC susceptibility measurements were performed on all compounds. The temperature-dependent measurements, at AC magnetic field frequencies from 95 Hz to 9995 Hz, showed that, apart from complex **1.4a**, all the other compounds exhibit frequency-dependent maxima in the out-of-phase component of the magnetic susceptibility (χ'') in the absence of a DC field (Figure 1.54).

The lack of signal in complex **1.4a** is probably caused not only by the occurrence of the QTM process, usually observed in most of Co(II)-based SIMs,^{46,59,61,62,69} but mainly due to the presence of a transverse magnetic anisotropy (E). This result is also in good agreement with the high experimental value of E obtained for **1.4a**, in comparison with those of the remaining compounds (see above in Table 1.7).

For compounds **1.4b-d**, although a blocking of the magnetization is observed, the maxima in the χ'' plots are not well defined, probably due to the presence of fast QTM between the M_s levels, corroborating the results obtained by the theoretical studies (see diagrams presented in Figure 1.48), which is then suppressed by applying a static field.

Nevertheless, for complexes **1.4c** and **1.4d** it was still possible to perform the frequency-dependent measurements at different temperatures in the absence of a DC field. The magnetization relaxation rate for **1.4c** and **1.4d** was determined by measuring the dependence of both χ' , and χ'' with the frequency, ν , in the range of 10-10000 Hz, at fixed temperatures (Figures 1.55 and 1.56, respectively).

From these χ (AC) data, the Argand diagrams (or Cole-Cole plots) were obtained and fitted using a generalized Debye model (see above Equations 1.10 to 1.12) (Figures 1.57, left for **1.4c** and 1.58, left for **1.4d**).

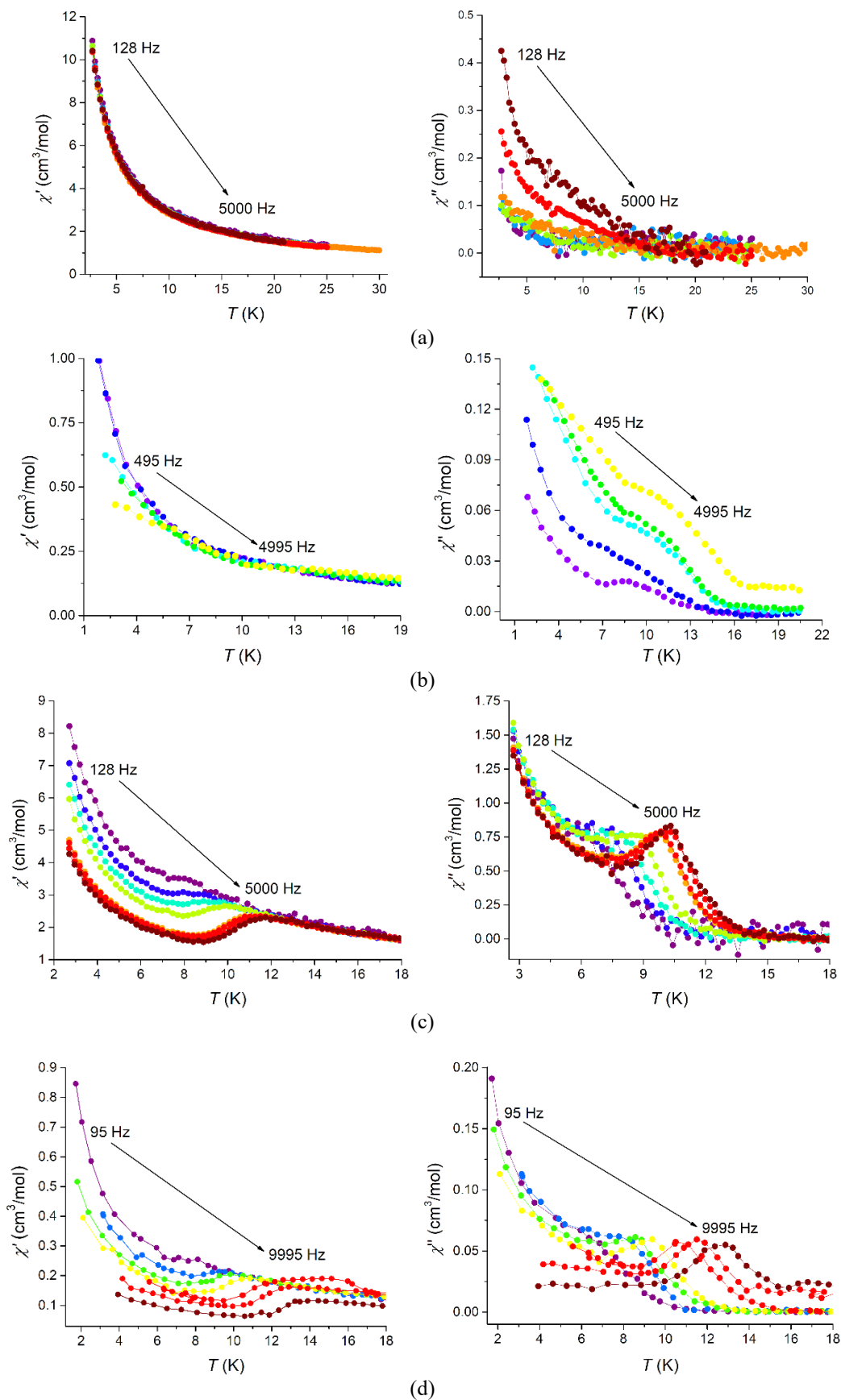


Figure 1.54 Temperature dependence of the in-phase χ' (left) and out-of-phase χ'' (right) magnetic susceptibilities in the absence of an external magnetic field at different frequencies for complexes (a) **1.4a**, (b) **1.4b**, (c) **1.4c** and (d) **1.4d**.

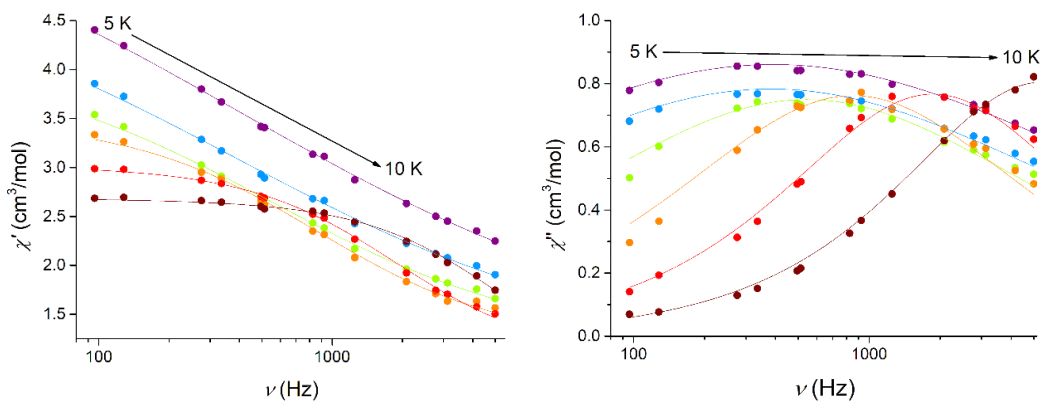


Figure 1.55 Frequency dependence of the in-phase χ' (left) and out-of-phase χ'' (right) magnetic susceptibilities at different temperatures for complex **1.4c** under zero DC field. The solid lines are for guidance.

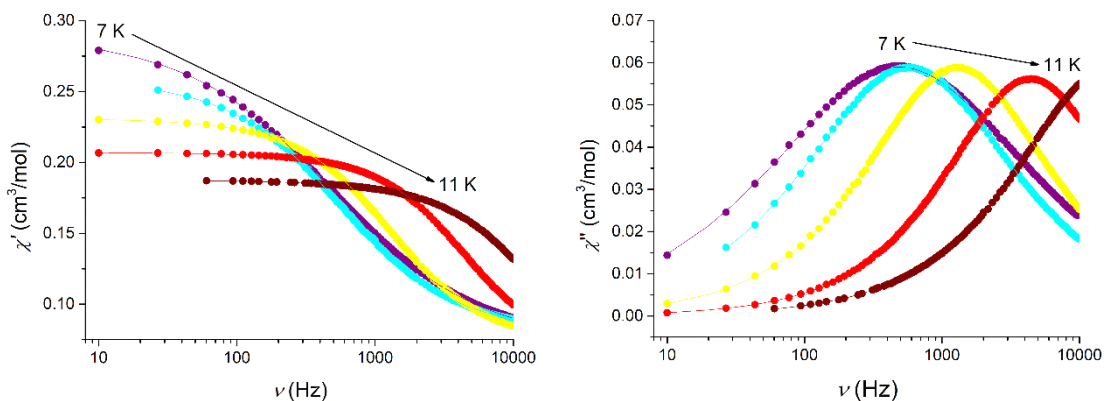


Figure 1.56 Frequency dependence of the in-phase χ' (left) and out-of-phase χ'' (right) magnetic susceptibilities at different temperatures for complex **1.4d** under zero DC field. The solid lines are for guidance.

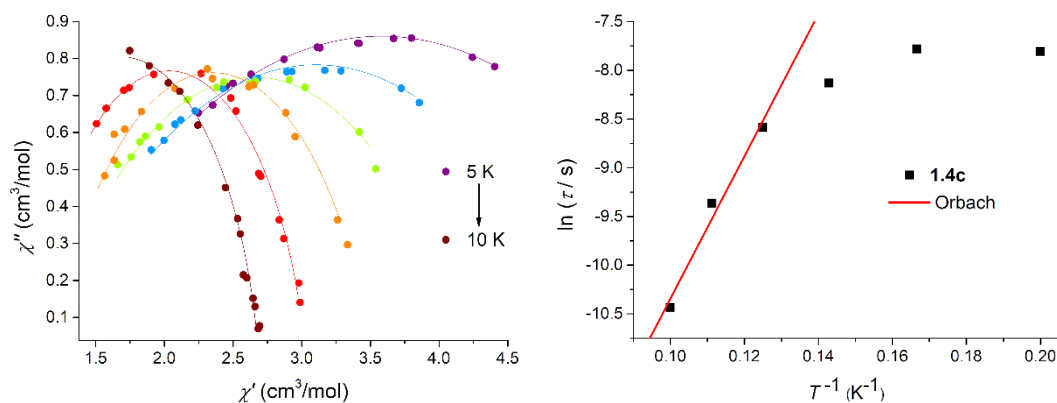


Figure 1.57 Cole-Cole plot for complex **1.4c** in the absence of an external magnetic field. The solid lines represent the best fits to the experimental data using the generalized Debye model (left) and $\ln(\tau)$ vs. T^{-1} plot for **1.4c** in the absence of an external magnetic field; the red line is the fit for the Orbach process using the Arrhenius law (right).

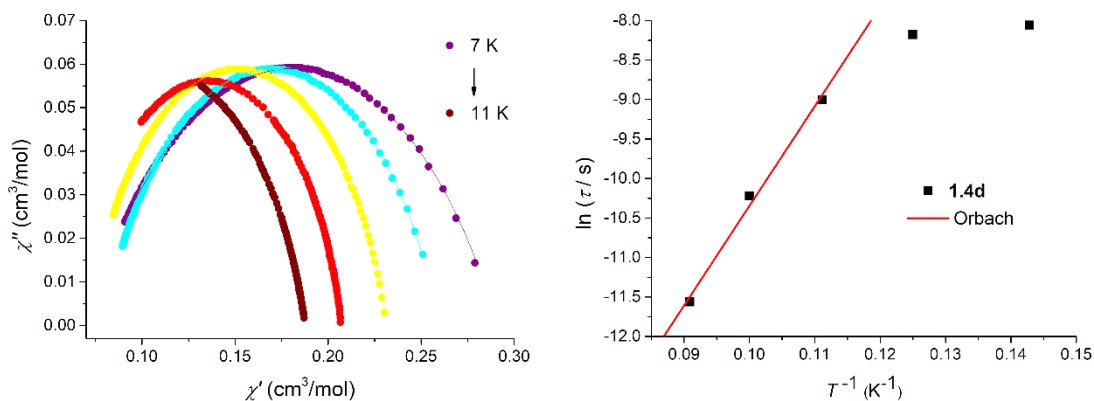


Figure 1.58 Cole-Cole plot for complex **1.4d** in the absence of an external magnetic field. The solid lines represent the best fits to the experimental data using the generalized Debye model (left) and $\ln(\tau)$ vs. T^{-1} plot for **1.4d** in the absence of an external magnetic field; the red line is the fit for the Orbach process using the Arrhenius law (right).

From both compounds **1.4c-d** these diagrams exhibit semi-circular shapes, indicating that a single relaxation process is involved. By fitting the data several parameters were obtained such as the relaxation time (τ) and α . The latter is related to the distribution of the relaxation times ($0 \leq \alpha \leq 1$), α being near 0 if only a single relaxation process is present (see Appendix III, Tables III.3 and III.5).^{15,25} Therefore, in order to determine the different spin relaxation processes involved and calculate the energy barrier, U_{eff} , the $\ln(\tau)$ vs. T^{-1} plot was achieved using the parameters obtained from the Debye fits (Figures 1.57, right for **1.4c** and 1.58, right for **1.4d**). As mentioned in the introduction (see subsection 1.1.2.1.2), for an ideal SMM, the spin relaxation should occur only through a thermally activated or pure Orbach process, where the energy barrier is determined by a linear fit, using the Arrhenius law (see Equation 1.17). Therefore, by fitting the data with this equation the effective relaxation barrier and the pre-exponential factor were obtained: $U_{\text{eff}} = 51(11) \text{ cm}^{-1}$ with $\tau_0 = 2.2(1) \times 10^{-8} \text{ s}$ for **1.4c**, and $U_{\text{eff}} = 88(11) \text{ cm}^{-1}$ with $\tau_0 = 1.1(1) \times 10^{-10} \text{ s}$ for complex **1.4d** under zero DC field. However, deviations from linearity means that other relaxation processes may be involved. In fact, the temperature-independent behavior at lower temperatures indicates that the QTM process is present, thus requiring the application of an external magnetic field to overcome this unwanted process. Consequently, the study of the field-dependence of the AC susceptibility performed at 9 K indicates that the longest relaxation time occurs approximately at 3000 Oe for **1.4a**, 1000 Oe for **1.4b** and 800 Oe both for **1.4c** and **1.4d**. As shown in Figure 1.59, the application of such fields significantly enhance the frequency and temperature dependence of the AC susceptibility maxima.

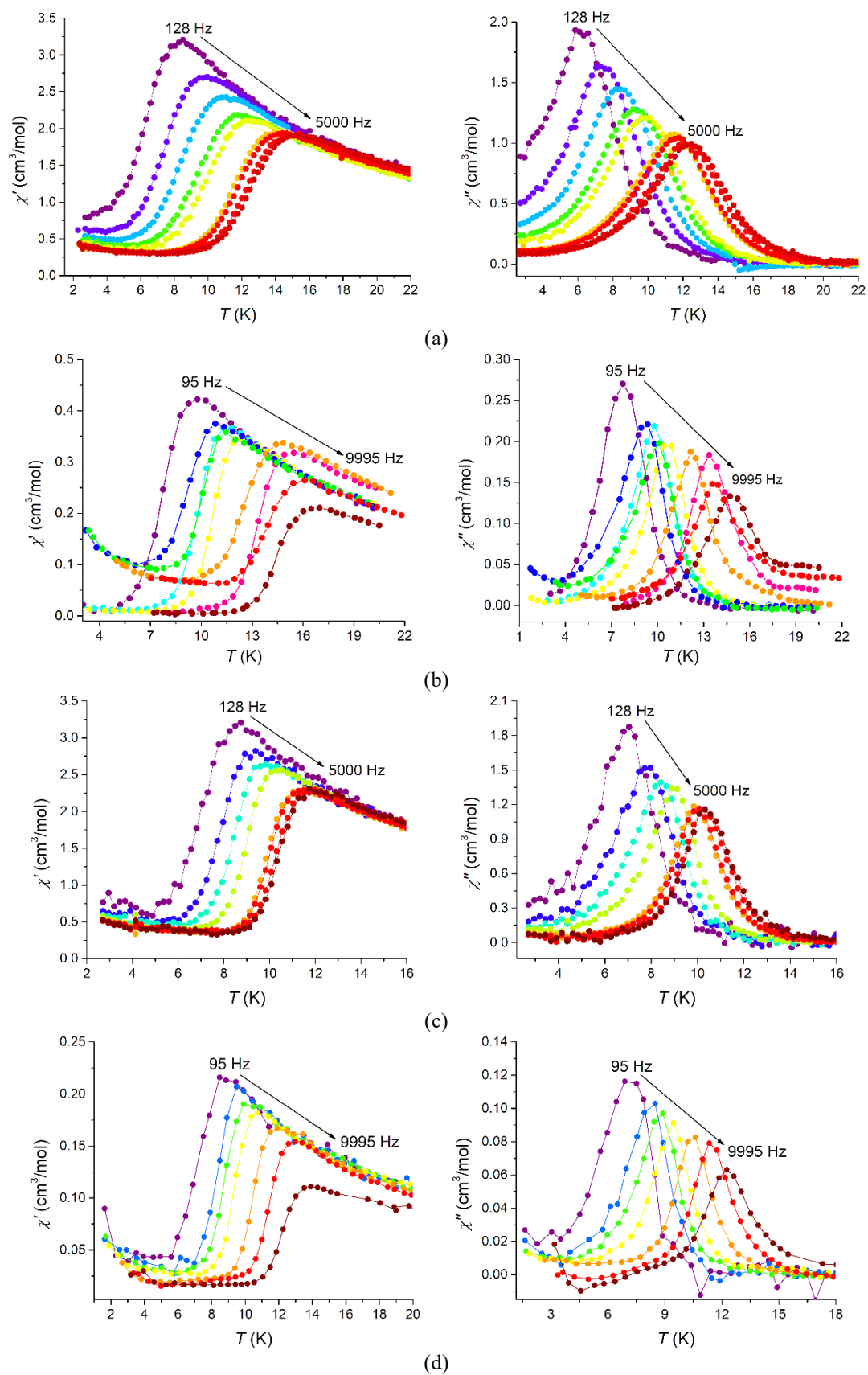


Figure 1.59 Temperature dependence of the in-phase χ' (left) and out-of-phase χ'' (right) magnetic susceptibilities at different frequencies for complexes (a) **1.4a** under 3000 Oe, (b) **1.4b** under 1000 Oe, (c) **1.4c** under 800 Oe and (d) **1.4d** under 800 Oe.

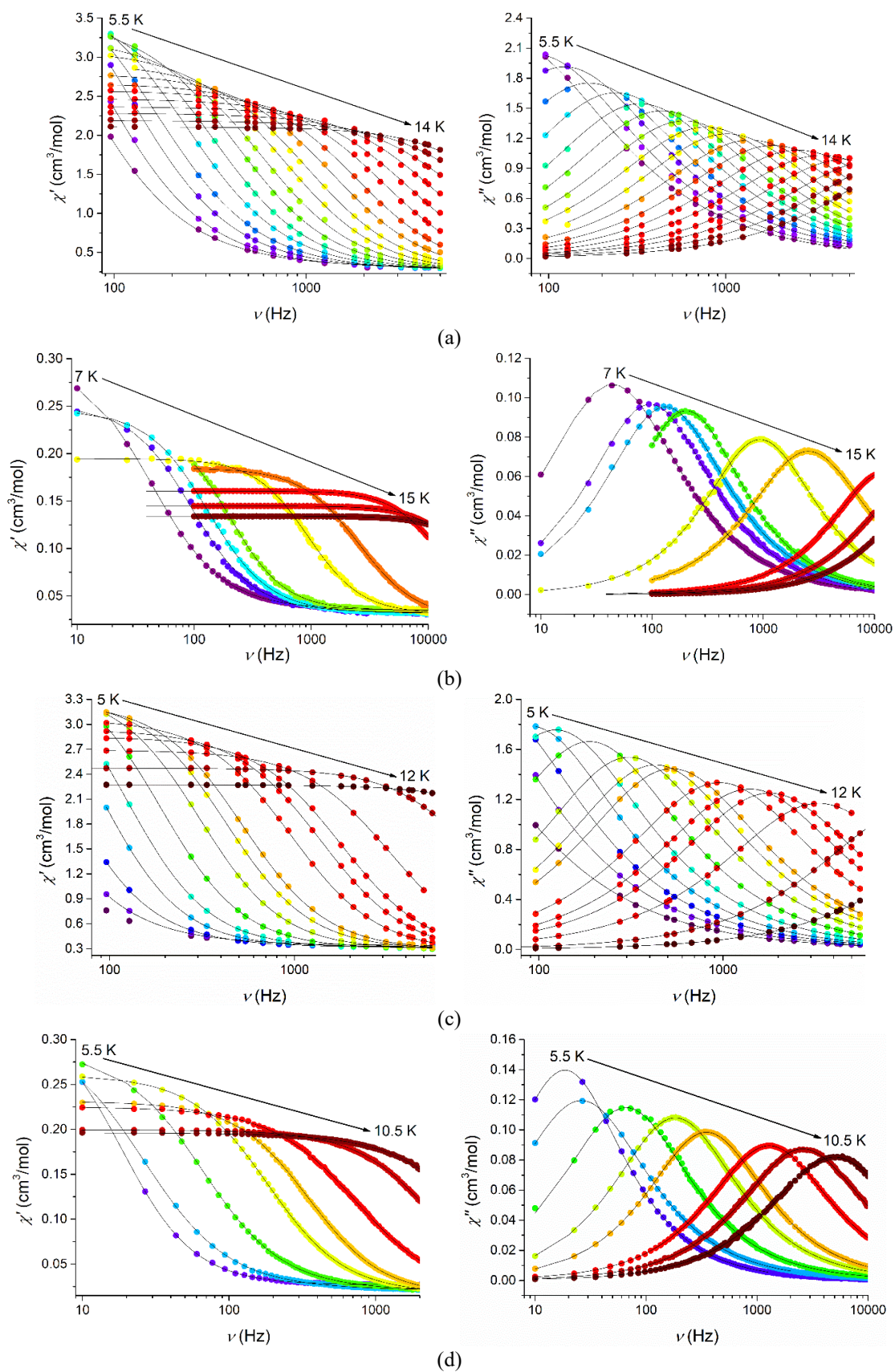


Figure 1.60 Frequency dependence of the in-phase χ' (left) and out-of-phase χ'' (right) magnetic susceptibilities at different temperatures for complexes (a) **1.4a** at 3000 Oe, (b) **1.4b** at 1000 Oe, (c) **1.4c** at 800 Oe and (d) **1.4d** at 800 Oe. The solid lines are for guidance.

Chapter 1

Once the optimum field for the slowest relaxation of magnetization was established, the frequency dependence measurements at different temperatures were carried out (Figure 1.60).

The small α values obtained from the fits of the Cole-Cole plots also revealed, along with almost perfect semicircle shapes, the existence of a single relaxation process (Figure 1.61 and Appendix III, Tables III.1, 2, 4 and 6).

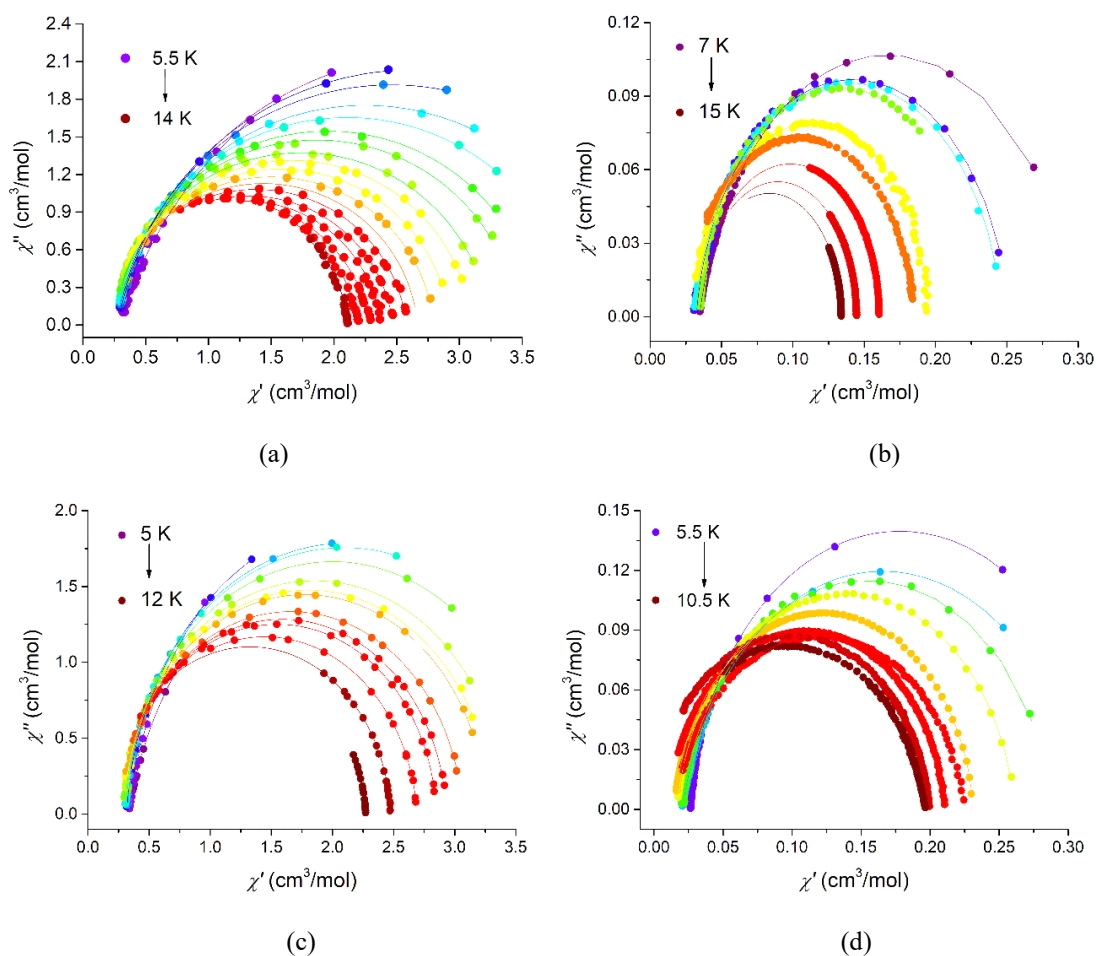


Figure 1.61 Cole-Cole plots for complexes (a) **1.4a** under a DC field of 3000 Oe, (b) **1.4b** under a DC field of 1000 Oe, (c) **1.4c** under a DC field of 800 Oe and (d) **1.4d** under a DC field of 800 Oe. The solid lines represent the best fits to the experimental data using the generalized Debye model.

The $\ln(\tau)$ vs. T^{-1} plot is represented for all the four compounds (**1.4a-d**) in Figure 1.62. At higher temperatures these results show an activated temperature dependency based on the Arrhenius law (Equation 1.17), with the following parameters: $U_{\text{eff}} = 76(4) \text{ cm}^{-1}$ and $\tau_0 = 5.1(3) \times 10^{-9} \text{ s}$ for **1.4a**, $U_{\text{eff}} = 90.6(5) \text{ cm}^{-1}$ with $\tau_0 = 6.0(4) \times 10^{-10} \text{ s}$ for **1.4b**, $U_{\text{eff}} = 88(3) \text{ cm}^{-1}$ with $\tau_0 = 1.5(3) \times 10^{-10} \text{ s}$ for **1.4c** and $U_{\text{eff}} = 85(4) \text{ cm}^{-1}$ with $\tau_0 = 5.1(4) \times 10^{-10} \text{ s}$ for **1.4d**

(Figure 1.62, blue dashed lines). However, these values of the energy barrier are smaller than expected from the energy gap between $M_s = \pm 3/2$ and $M_s = \pm 1/2$, *i.e.* $2|D|$ (138 cm^{-1} for **1.4a**, 106 cm^{-1} for **1.4b**, 96 cm^{-1} for **1.4c** and 104 cm^{-1} for complex **1.4d**), which is also observed for other Co(II) complexes with a similar behavior. In addition, for all the complexes there is a clear curvature in the $\ln(\tau)$ vs. T^{-1} plot at lower temperatures, indicating that other relaxation mechanisms, such as Raman or Direct, may be involved.

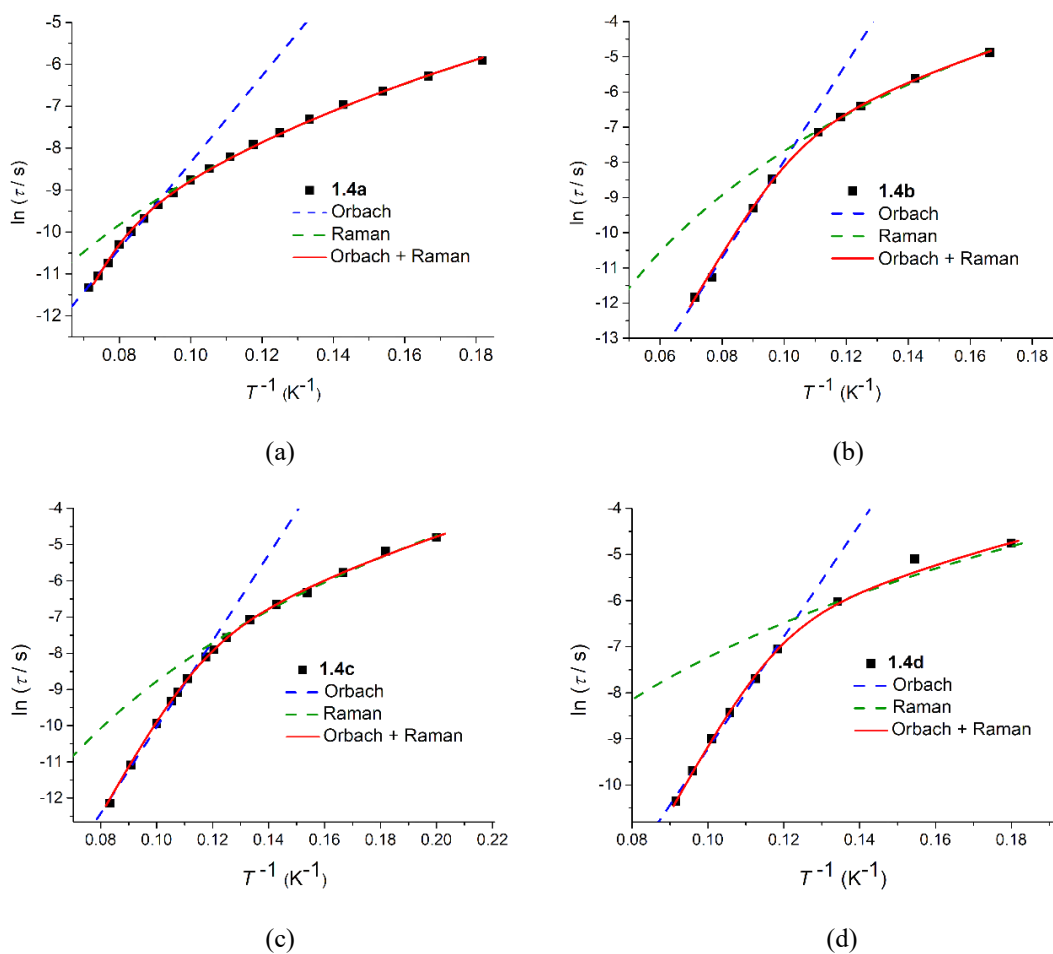


Figure 1.62 $\ln(\tau)$ vs. T^{-1} plots, the red lines are the best fits to the sum of Raman and Orbach processes (a) for **1.4a** under 3000 Oe, (b) for **1.4b** under 1000 Oe, (c) **1.4c** under 800 Oe and (d) **1.4d** under 800 Oe.

Considering this, several attempts were done in order to find the relaxation mechanisms present for each compound. Thus, the best description of the results was obtained by the sum (Figure 1.62, red lines) of the Orbach (Figure 1.62, blue dashed lines) and Raman (Figure 1.62, green dashed lines) processes, given by Equation 1.23:¹¹⁶

$$\tau^{-1} = CT^n + \tau_0^{-1} \exp(-U_{\text{eff}}/k_B T) \quad (1.23)$$

where the first and second terms refer to the Raman and Orbach paths, respectively, C being the Raman coefficient and n the Raman exponent. The calculated parameters obtained from these magnetic relaxation processes fittings are listed in Table 1.9.

From Equation 1.23, and keeping the energy barrier parameter fixed in the experimentally obtained $2|D|$ values, these results suggest that this system of tetracoordinate Co(II) complexes shows different magnetic behaviors depending on the temperature range, with a clear dominance of the Orbach process at higher temperatures. However, as temperature decreases, the Raman mechanism becomes dominant.

Table 1.9 Orbach and Raman relaxation parameters for complexes **1.4a-d**

Parameters	1.4a	1.4b	1.4c	1.4d
H_{DC} (Oe)	3000	1000	800	800
C ($\text{K}^{-n} \text{s}^{-1}$)	0.086(9)	0.02(3)	0.021(4)	0.11(3)
n	4.86(5)	4.9(7)	5.4(1)	4.1(2)
U_{eff} (cm^{-1})	138	106	96	104
τ_0 (s)	$1.14(6) \times 10^{-11}$	$1.3(2) \times 10^{-10}$	$6.8(2) \times 10^{-11}$	$3.8(1) \times 10^{-11}$

All the complexes **1.4a-d** present high easy axis magnetic anisotropy as a result of tetrahedral elongations imposed by the chelating geometry of the 2-iminopyrrolyl ligands. The more elongated structure (smaller values of the bite angle θ) and the slight decreasing covalency in the metal-ligand bond for complex **1.4a** (calculated for all the complexes) are the main factors for the increase of magnetic anisotropy when compared to the remaining compounds **1.4b-d**, leading to a smaller gap between the filled $3d_{x^2-y^2}$ orbital and the singly occupied $3d_{xy}$ orbital. For complex **1.4a**, the calculated parameters g and E , by HFEPFR and *ab initio* calculations, showed a pronounced transverse magnetic anisotropy, which led to differences in the magnetic properties of this compound. The E values in this system are controlled by the ligands' interplanar dihedral angle ϕ , which is lower for complex **1.4a**, leading to changes in the $3d$ orbital mapping, namely the stabilization of the $3d_{xz}$ and destabilization of the orbital $3d_{x^2-y^2}$, thus reducing the energy gap between these two states.

The substitutions in the second coordination sphere (in the position 5 of the pyrrolyl ring) with bulky groups in complexes **1.4b-d** revealed to be beneficial, despite the lower

values of D obtained. The dynamic AC magnetic measurements revealed that these 3 compounds exhibit SIM behavior in the absence of an external magnetic field, whereas this important feature is not observed for complex **1.4a**. This is assigned to the higher values of E in complex **1.4a**, which triggers the QTM process rather than the thermally assisted Orbach relaxation mechanism. In addition to the lack of signal under zero static magnetic field, a much higher field is required to overcome the QTM process in complex **1.4a**. The energy barriers are considerably high for all the compounds studied, higher than the majority of tetracoordinated Co(II)-based SIMs found in the literature, because of the occurrence of two relaxation processes: Raman mechanism, at low temperatures, and Orbach mechanism, at higher temperatures.

1.2.2.3.4 Magnetic studies on complex 1.4e

In the light of the previous results, the [Co(2-iminopyrrolyl)₂] framework could be considered as a very promising system, since all the complexes **1.4a-d** presented high and negative values of D , indicating a magnetic anisotropy of the easy axis type. Their X-ray molecular structures indicated that an increase of the ligand bulkiness leads to a geometry closer to tetrahedral (confirmed by the corresponding τ_4^{111} parameter and the ϕ angles), resulting in the appearance of frequency-dependent maxima in χ' and χ'' vs. T plots, without the application of a DC field for complexes **1.4c-d**.

Up to now, there have been few tetrahedral Co(II) complexes displaying SIM behavior in the absence of an external magnetic field.^{45,54,56,74,75,76,77} Among these complexes, various examples containing four coordinating nitrogen atoms were reported (see subsection 1.1.4.1.2.1 of the introduction), although most of them exhibited QTM, which is later suppressed by the application of a DC field. Driven by these evidences, the preparation and magnetic characterization of the extremely bulky complex **1.4e** (Figure 1.42) was performed in the hope of achieving reasonably high values of D and U_{eff} under zero external magnetic field. Before it was achieved, the synthesis of **1.4e** was considered as challenging because it was not known whether it would be synthetically possible to employ a N,N' -2-formiminoiminopyrrolyl chelating ligand bulkier than that of the highly hindered and previously synthesized adamant-1-yl derivative **1.4d**, while still holding a stable 1:2 Co:ligand stoichiometry ratio (i.e. [Co(2-iminopyrrolyl)₂]). However, its

preparation under conditions similar to those of its analogous **1.4a-d**, by reaction of the *in situ* prepared sodium salt of the ligand precursor with CoCl_2 in THF, revealed to be quite feasible in yields similar to the previous analogous. The pure product is stable in air when crystalline, and was structurally characterized by elemental analysis, FTIR and solution ^1H NMR spectroscopies, and by single crystal X-ray diffraction.

1.2.2.3.4.1 HF-EPR measurements for complex **1.4e**

The electronic structure of complex **1.4e** was investigated by means of HF-EPR at 320 GHz (Figure 1.63). Below 50 K no signal was observed, suggesting that the EPR lines are due to transitions within the excited Kramers doublet. This immediately points towards a large negative D and small E for this complex, which make the EPR-transition within the ground doublet highly forbidden and thus unobservable by EPR. The fits represent the measurement data well at all temperatures and confirm the ZFS parameters obtained by the simulations performed on $\chi_M T$ vs. T plot (see Figure 1.43, right). The extracted spin Hamiltonian parameters are presented in Table 1.10.

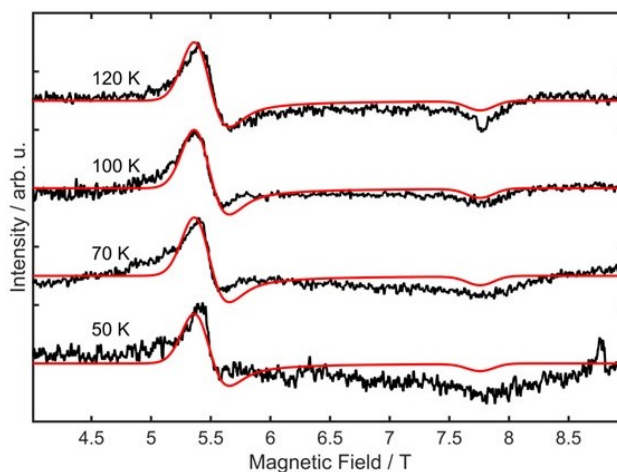


Figure 1.63 HF-EPR spectra of a pressed powder pellet of complex **1.4e** at $\nu = 320$ GHz and different temperatures, in the range of 4-9 T. Black lines represent the measurement and red lines the simulation on the basis of the spin Hamiltonian parameters.

1.2.2.3.4.2 Theoretical calculations for complex 1.4e

The D and E parameters were calculated by the QD-NEVPT2 approach, being very close to the experimental values obtained by HFEPR (Table 1.10). The splitting of the Kramers doublets of the spin-orbit coupled states is represented in Figure 1.64, showing a weak QTM process governed by a small transition moment ($0.049 \mu_B$) between the $\pm 3/2$ states, whereas the Orbach route has a transition moment of $0.203 \mu_B$. These results are in line with experiment (see below).

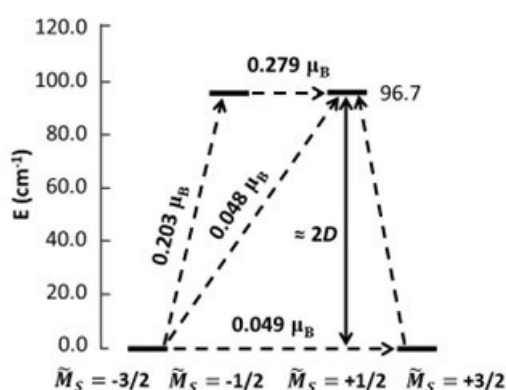


Figure 1.64 Kramers doublets and zero-field splitting of complex **1.4e** with associated transition magnetic moments between each state.

Table 1.10 Calculated and experimental D , E and g values for complex **1.4e**.

Complex	D (cm^{-1})		E (cm^{-1})		g -tensor	
	Calc.	Exp.	Calc.	Exp.	Calc.	Exp.
1.4e	-48.4	-42.6(4)	0.4	0.4(2)	2.125, 2.136, 2.688	2.08(3), 2.12(3), 2.93(3)

1.2.2.3.4.3 Dynamic (AC) magnetic measurements of complex 1.4e

The dynamic magnetic measurements of complex **1.4e** was performed using a PPMS magnetometer (Quantum Design) from the Physics Department, University of Coimbra.

Temperature and frequency dependence of the AC susceptibility components χ' and χ'' were performed with an AC field of 10 Oe. Figure 1.65 shows the temperature dependence at different AC frequencies under zero external magnetic field.

Chapter 1

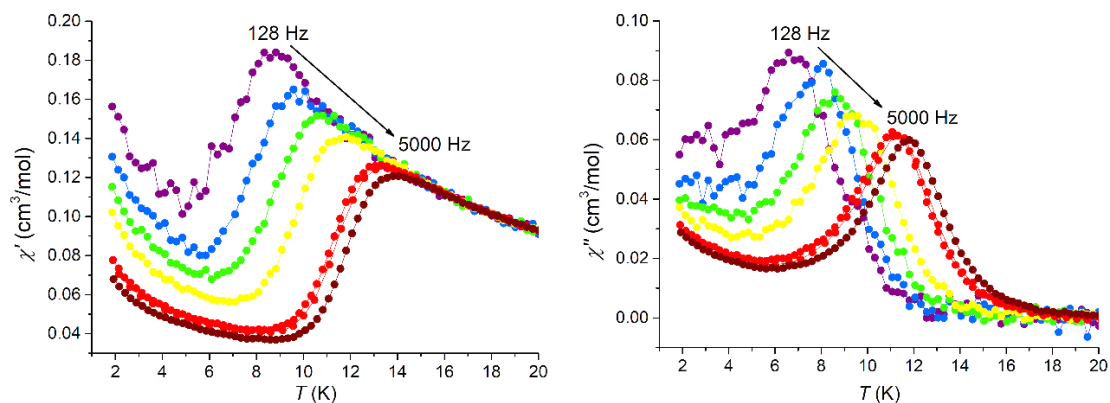


Figure 1.65 Temperature dependence of the in-phase χ' (left) and out-of-phase χ'' (right) magnetic susceptibilities for complex **1.4e** in the absence of a DC field, at different frequencies.

From these plots there is a clear frequency dependence of both χ' and χ'' components that shifts to higher temperatures as the frequency increases. This indicates slow relaxation of the magnetization.

The frequency dependence of the measurements at different temperatures between 6 and 13.5 K were also carried out (Figure 1.66).

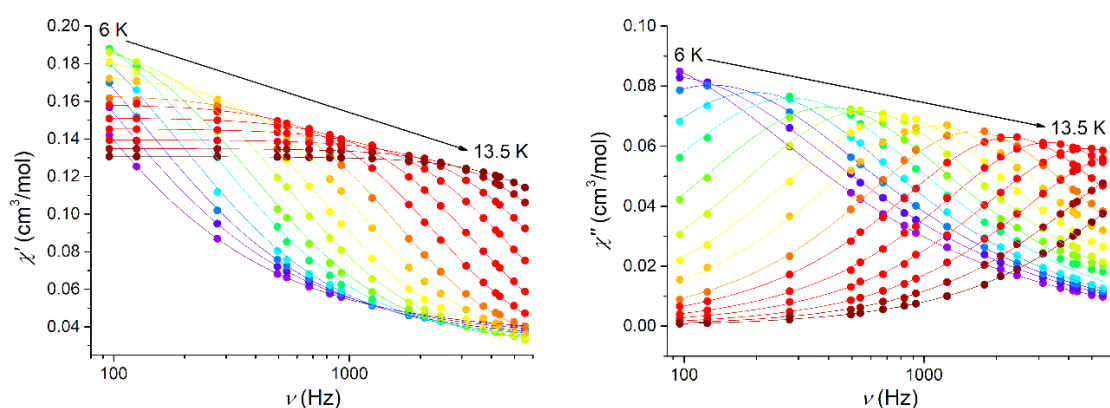


Figure 1.66 Frequency dependence of the in-phase χ' (left) and out-of-phase χ'' (right) magnetic susceptibilities at different temperatures for complex **1.4e** in the absence of a DC field. The solid lines are for guidance.

The corresponding Cole-Cole plots are shown in Figure 1.67, left. The resulting data were fitted using a Debye model (Equations 1.10 to 1.12), where the parameters τ and α were determined. The nearly semi-circular and symmetrical shape of the Argand diagrams along with small values of α in the range 0.01-0.30 (see Appendix III, Table III.7) support the existence of a single relaxation process.

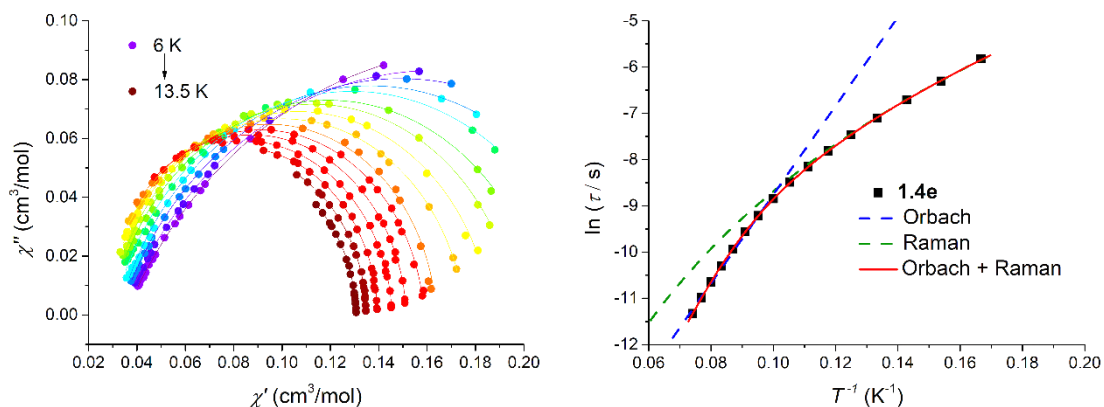


Figure 1.67 Cole-Cole plot for **1.4e** in the absence of an external magnetic field. The solid lines represent the best fits to the experimental data using the generalized Debye model (left) and $\ln(\tau)$ vs. T^{-1} plot for **1.4e** in the absence of an external magnetic field, the red lines are the best fits to the sum of Raman (green line) and Orbach (blue line) processes (right).

In order to probe the value of the energy barrier for the magnetization reversal, the natural logarithm of these single relaxation times, τ , were plotted with the correspondent inverse of temperature (Figure 1.67, right). The same considerations used in the above studied complexes **1.4a-d**, were also used in this case in order to fit τ using an Arrhenius law (Equation 1.17), giving the parameters $U_{\text{eff}} = 96(3) \text{ cm}^{-1}$ and $\tau_0 = 1.1(3) \times 10^{-8} \text{ s}$. However, below 9.5 K, the fit deviates from linearity, indicating that a Raman process is also involved. Therefore, the best fit for the data was the combination of both mechanisms as in the previous cases: Orbach (at higher temperatures) and Raman (at lower temperatures) (Equation 1.23). By keeping the energy barrier fixed at 85 cm^{-1} (the value of the U_{eff} expected from the energy gap between the $M_s = \pm 3/2$ and $M_s = \pm 1/2$, obtained by HFEP R measurements), the remaining parameters were calculated as $C = 0.040(9) \text{ K}^{-n} \text{ s}^{-1}$, $n = 5.1(1)$ and $\tau_0 = 2.1(1) \times 10^{-9} \text{ s}$, where n is found to be within the values calculated for other Co(II) complexes reported in the literature. The energy barrier of 85 cm^{-1} is calculated from $U_{\text{eff}} = (S^2 - 1/4)|D| = 2|D|$, for $S = 3/2$ using the experimental value of $D = 42.6(4) \text{ cm}^{-1}$ and, to the best of our knowledge, could be considered, at this point of the work, as the second largest value for the spin-reversal energy barrier so far reported for a four-coordinate Co(II)-N₄ complex in the absence of an external field.

Up to a field H_{DC} of 1200 Oe no changes in the magnetic relaxation parameters were observed since, by overlaying the $\ln(\tau)$ vs. T^{-1} plots, both curves remain almost superimposable (Figure 1.68). This result suggest that the same magnetic relaxation

Chapter 1

processes are involved in complex **1.4e** with or without an applied external magnetic field as predicted by the theoretical calculations.

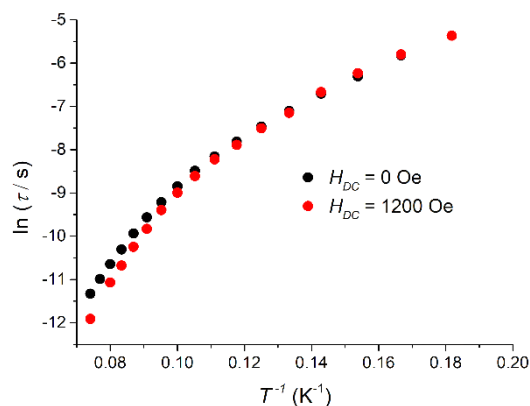


Figure 1.68 Superposition of both $\ln(\tau)$ vs. T^{-1} plots under $H_{DC} = 0 \text{ Oe}$ (black) and $H_{DC} = 1200 \text{ Oe}$ (red) for complex **1.4e**.

In conclusion, the preparation of this complex **1.4e** with the objective of enhancing the SIM behavior was a success. As can be observed in Table 1.11, the elongated tetrahedral geometry (ligand bite angles θ of 84.38(15) and 84.43(15) $^\circ$), the large value of the angle ϕ and the relatively low value of angle ω contribute all together to the observed negative value of D ($-42.6(4) \text{ cm}^{-1}$), which lies around the values obtained for its analogous bis(2-iminopyrrolyl) Co(II) complexes **1.4a-d**, in agreement with the magnetostructural analysis previously carried out (see above in subsection 1.2.2.3.2.2).

Additionally, the QTM process at zero field exhibits a residual value in complex **1.4e**, as confirmed by the similar behavior observed with and without an applied magnetic field, and in agreement with the theoretical calculations. This is attributed to a lower value of the zero-field splitting parameter E ($0.4(2) \text{ cm}^{-1}$), and is also in agreement with the magnetostructural analysis presented above (subsection 1.2.2.3.2.2), where the E/D vs. ϕ plot shows that for $\phi = 90^\circ$ the value of E tends to zero (Figure 1.51b). These results suggest that E is controlled by the chelating ligands interplanar angle ϕ and consequently explain the lower values of E when increasing the steric volume of the ligand in this molecular system.

Table 1.11 Bite angles θ , dihedral angle ϕ and interligand angle ω for complex **1.4e**.

Angles ($^{\circ}$)	1.4e
N1-Co-N2 (θ_1) ^a	84.43(15)
N3-Co-N4 (θ_2) ^a	84.38(15)
Dihedral ϕ ^b	87.32(15)
Angle ω ^c	163.69(9)

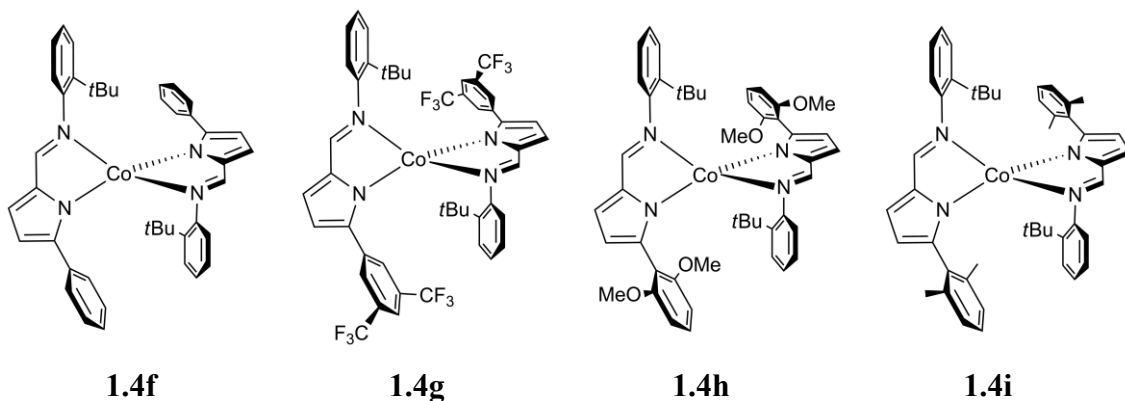
^a θ = N-Co-N chelating ligands bite angles;

^b ϕ = dihedral angle formed between planes defined by atoms (Co, N1, N2) and (Co, N3, N4);

^c ω = interligand angle formed between dummy bonds Co-(C2-C6)_{centroid} and Co-(C34-C38)_{centroid}.

1.2.2.4 Complexes **1.4f-i**: influence of the ligand asymmetry and electron-donor ability on the SIM behavior

The next step of our investigation was the study of the influence of using more unsymmetrical chelating ligands, also with different electron donating or withdrawing abilities. Therefore, a new family of homoleptic Co(II) complexes were magnetically characterized (Figure 1.69). Compared to the first series of compounds these complexes have an unsymmetrically substituted *N*-aryl ring, 2-*N*-(*t*-butyl)phenyl group, instead of 2-*N*-2,6-bis(isopropyl)phenyl and 2-*N*-adamant-1-yl groups, which would enable different types of geometric distortions about the Co(II) center. Additionally, 5-phenyl rings substituents in the *ortho* and *meta* positions with different electron-donor or electron-withdrawing features would provide an insight into the electronic effect.

**Figure 1.69** Complexes studied in this work **1.4f-i**.

1.2.2.4.1 Static (DC) magnetic studies

The static magnetic susceptibility measurements were performed on complexes **1.4f-i** at the Solid-State Group laboratory of C²TN-IST.

Figure 1.70 shows the $\chi_M T$ vs. T plots measured at 500 Oe in the range of 1.8-300 K for compounds **1.4f-i**. The curves show a similar trend for all compounds except for **1.4i**.

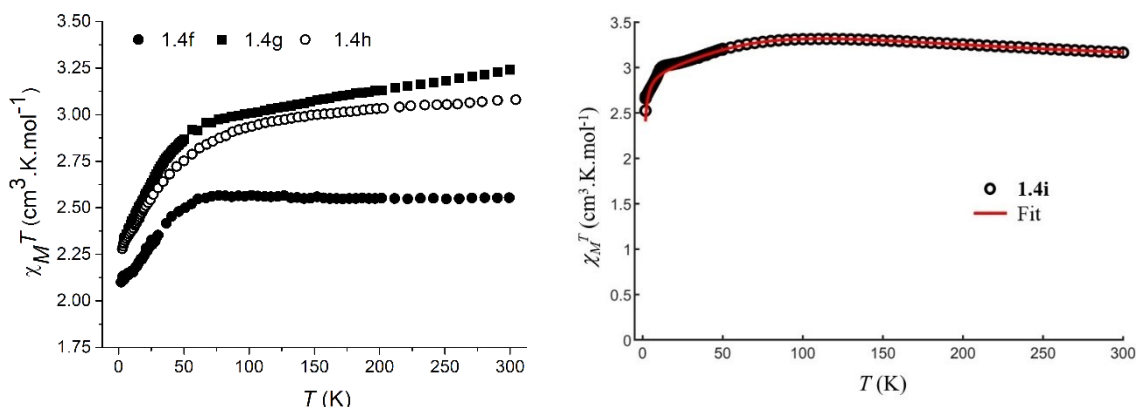


Figure 1.70 $\chi_M T$ vs. T plot measured at 500 Oe for complexes **1.4f-h** (left) and $\chi_M T$ vs. T plot measured at 500 Oe for complex **1.4i**. The red line represents the simulation on the basis of the spin Hamiltonian parameters (right).

The magnetic susceptibilities at room temperature are of 2.55 for **1.4f**, 3.22 for **1.4g**, 3.08 for **1.4h** and 3.19 cm³·K·mol⁻¹ for **1.4i**, in good agreement with the expected value for a high spin ($S = 3/2$) Co(II). Because these values are much higher than the calculated spin-only value, the angular momentum contribution cannot be neglected. The decrease of the $\chi_M T$ values upon cooling, reaching 2.12 for **1.4f**, 2.34 for **1.4g** and 2.32 for **1.4h** at 5 K, can be explained by the depopulation of the M_s levels, which were split by the ligand field, suggesting a significant magnetic anisotropy (Figure 1.70, left). As for **1.4i**, the $\chi_M T$ values increase slightly with decreasing temperature down to 50 K and drop from there until 1.8 K, reaching 2.61 cm³·K·mol⁻¹ (Figure 1.70, right). At around 15 K, a shoulder is present that cannot be clearly assigned. It might be due to a paramagnetic impurity (which is unlikely since the complex was in its crystalline form and pure by elemental analysis) or due to interactions between the cobalt atoms. The shape is typical of a strong negative zero-field splitting. The experimental data was then fitted with Equation 1.22, in order to obtain the ZFS parameters D and E (see Table 1.12).

Figure 1.71 exhibits the field-dependence of the magnetization, measured at different fixed temperatures up to 5 T, with a sweeping rate of the DC field of $20 \text{ Oe}\cdot\text{s}^{-1}$ for complexes **1.4f-i**. As in the previous complexes, no hysteresis was observed due to the presence of a QTM process or due to the magnetic sweeping rate, which seem to be inadequate to reveal the magnetic relaxation of these complexes. The low saturation value at 5 T and 2 K, far lower than the theoretical saturation value of $3 \mu_B$ for an isolated Co(II) ion ($g = 2, S = 3/2$), is also an evidence for the existence of magnetic anisotropy in these complexes.

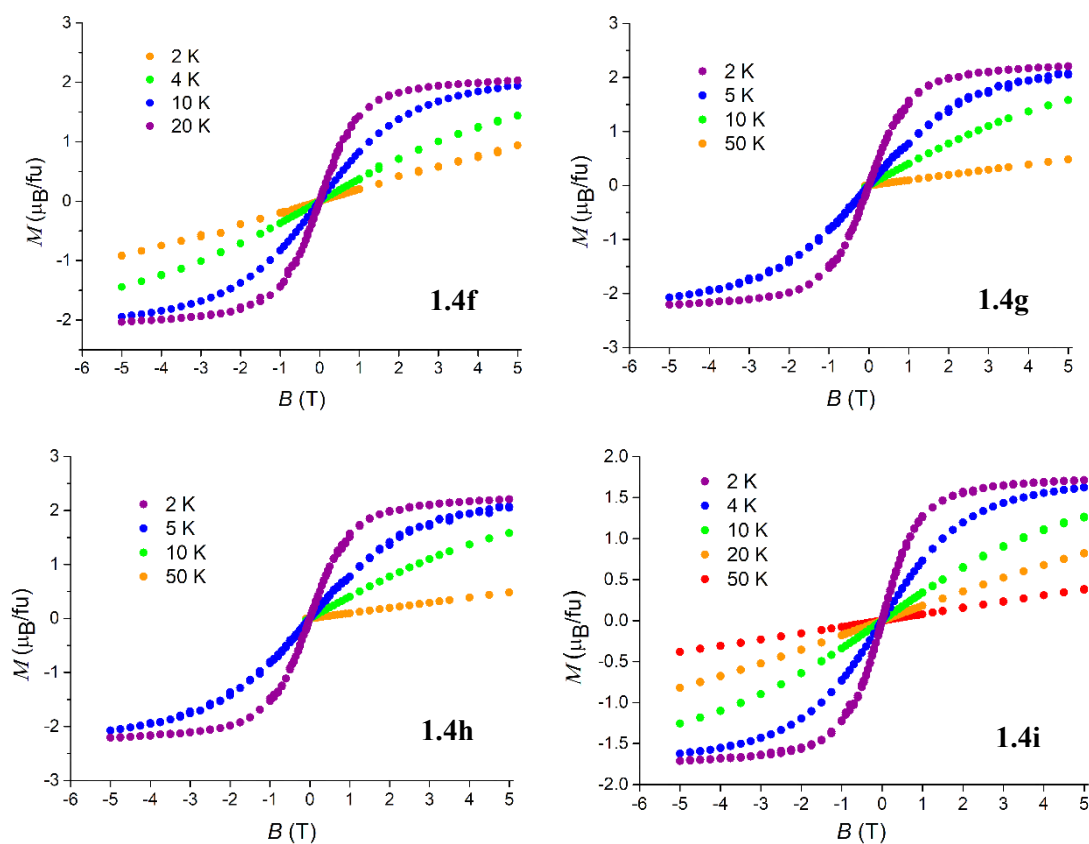


Figure 1.71 M vs. B plot measured from 0 to 5 T at different fixed temperatures for complexes **1.4f-i**.

1.2.2.4.2 HFEPR measurements

The HFEPR measurements were carried out in order to study the zero-field splitting in this series of complexes **1.4f-i**. However, for compound **1.4h** the results were not conclusive probably due to a sample degradation during the measurements. For the remaining complexes the HFEPR spectra are shown in Figure 1.72.

Chapter 1

Below 50 K no signal was detected for complexes **1.4f** and **1.4i**. In compound **1.4g**, due to high rhombicity (see Table 1.12), it allowed the visualization of the forbidden transition from the $M_s = -3/2$ to $M_s = +3/2$ at low temperatures, which starts to decrease with increasing temperature (*ca.* 4 T, Figure 1.72b). The spectra at 10 K also displays one strong frequency-dependent resonance line in the $g = 2$ region, corresponding to an instrumental artefact that was traced to the gold mirror employed (Figure 1.72b).

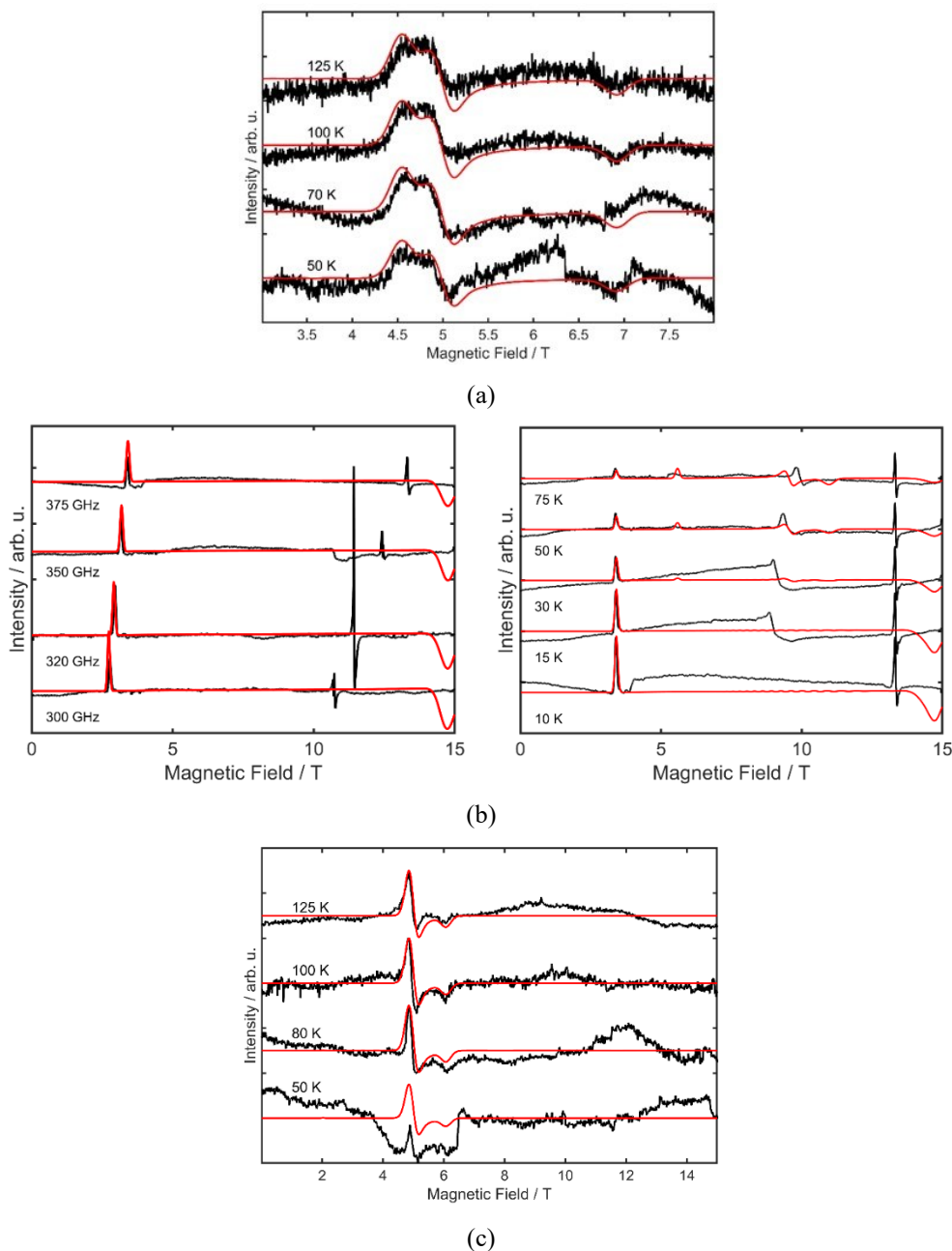


Figure 1.72 HFEPR spectra of a pressed powder pellet (a) of complex **1.4f** at $\nu = 275$ GHz at different temperatures, (b) of complex **1.4g** at $T = 10$ K at different frequencies (left) and at $\nu = 375$ GHz at different temperatures (right) and (c) of complex **1.4i** at $\nu = 275$ GHz at different temperatures. Black lines represent the measurement, red lines the simulation on the basis of the spin Hamiltonian parameters.

The remaining resonances in all the spectra correspond to the transition of the excited Kramers doublet, which become sharper with increasing temperature (Figure 1.72). The fit of the spectra to the spin Hamiltonian, Equation 1.22, yielded the values of D , E and g (Table 1.12), which confirm the ZFS parameters obtained by the simulations performed on $\chi_M T$ vs. T plot (see Figure 1.70, right).

1.2.2.4.3 Theoretical calculations

For this family of complexes **1.4f-i**, the D and E parameters were calculated by the QD-NEVPT2 approach. Except for compound **1.4i**, all the remaining complexes present a good agreement of parameters D , E and g with those obtained experimentally (Table 1.12).

Table 1.12 Calculated and experimental D , E and g values for complexes **1.4f-i**.

Complex	D (cm ⁻¹)		E (cm ⁻¹)		g -tensor	
	Calc.	Exp.	Calc.	Exp.	Calc.	Exp.
1.4f	-54.5	-52(3)	1.9	2.1(1)	2.090, 2.149, 2.772	2.0(5), 2.1(1), 2.8(5)
1.4g	-47.5	-45(2)	7.1	8(1)	2.052, 2.259, 2.755 ^a 2.049, 2.260, 2.746 ^b	1.9(5), 1.9(5), 2.7(3)
1.4h	-66.6	–	5.4	–	2.043, 2.214, 2.899	–
1.4i	-73.3	-91(3)	0.7	0.7(3)	2.074, 2.096, 2.939	2.0(1), 2.0(2), 3.2(4)

^a Molecule #1 of the unit cell of **1.4g**; ^b Molecule #2 of the unit cell of **1.4g**.

From the diagrams presented in Figure 1.73, complexes **1.4g** and **1.4i** display a strong QTM processes between the $M_S = \pm 3/2$ states with a transition moment of 1.163 (average value for the two molecules in the asymmetric unit) and 0.723 μ_B at zero DC field, respectively, much higher than those obtained for the Orbach mechanism (0.452 and 0.190 μ_B , respectively).

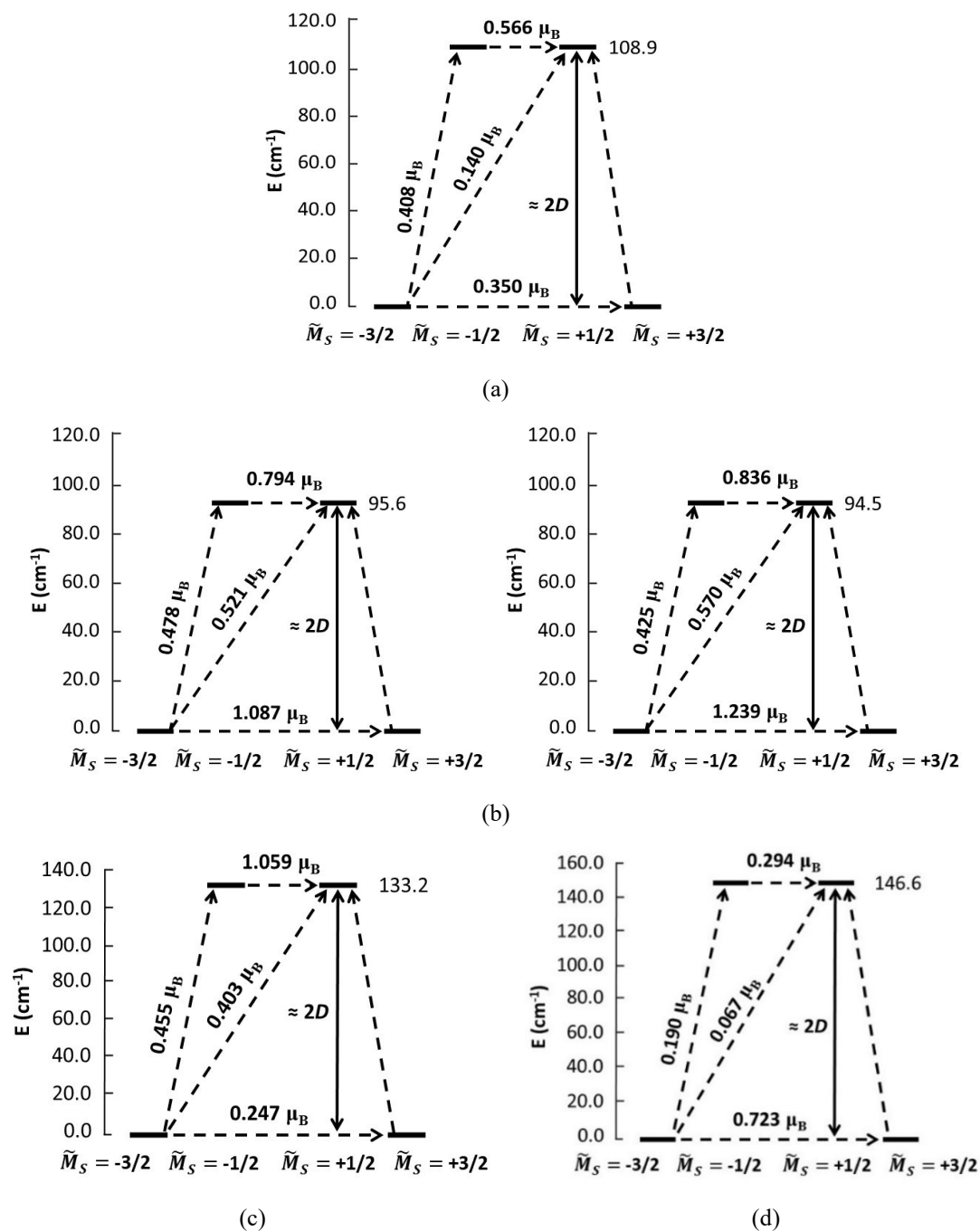


Figure 1.73 Calculated zero-field splitting plots with transition moments between each spin-orbit state for (a) complex **1.4f**, (b) the two crystallographic units of **1.4g**, (c) for **1.4h** and (d) for **1.4i**.

1.2.2.4.4 Dynamic (AC) magnetic studies

The dynamic magnetic measurements were performed for complexes **1.4f-h** at the Solid-State Group laboratory of C²TN-IST and for complex **1.4i** at the Physics Department, University of Coimbra.

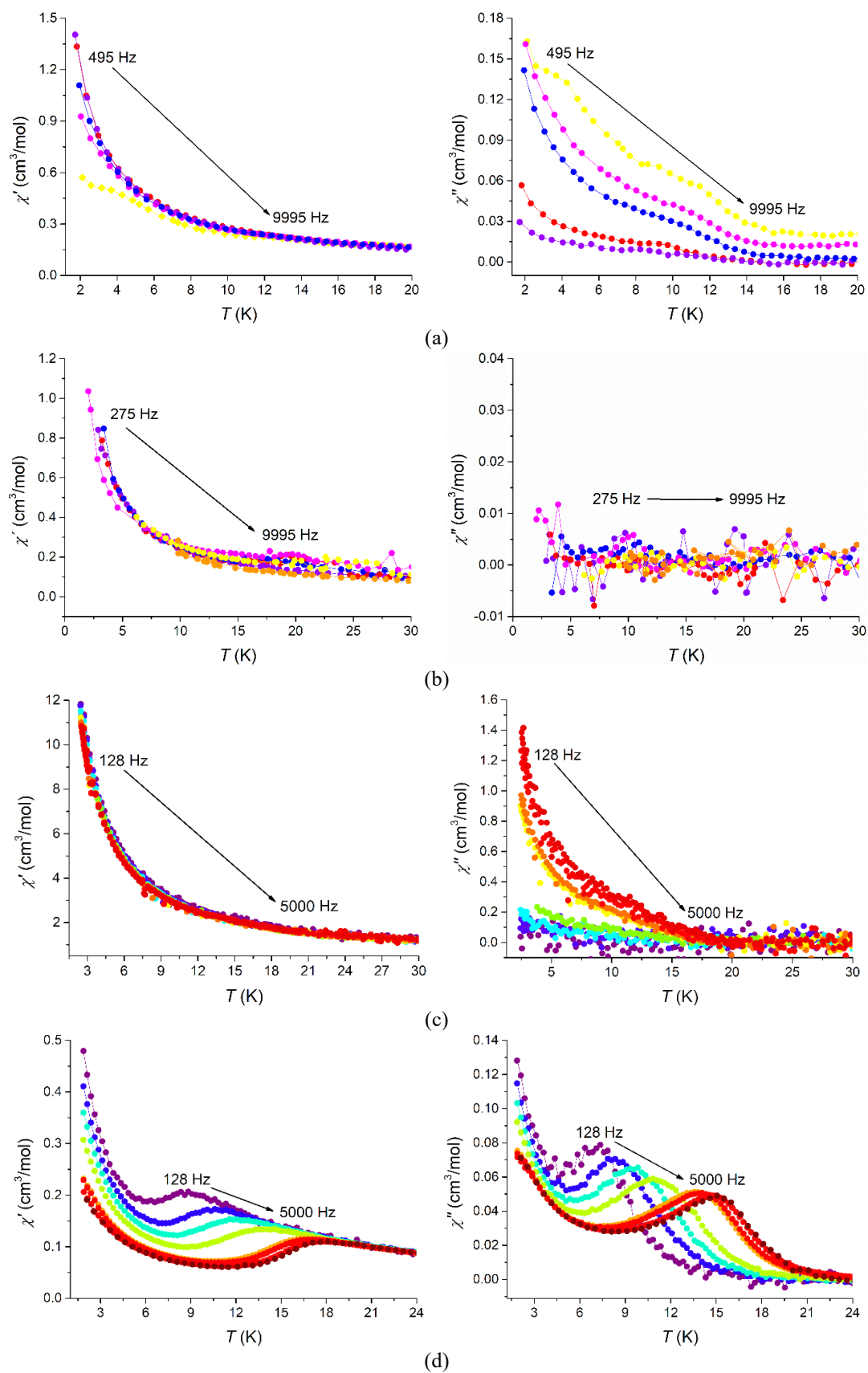


Figure 1.74 Temperature dependence of the in-phase χ' (left) and out-of-phase χ'' (right) magnetic susceptibilities in the absence of an external magnetic field at different frequencies for complexes (a) **1.4f**, (b) **1.4g**, (c) **1.4h** and (d) **1.4i**.

Chapter 1

The magnetization dynamics at low temperatures of these compounds were investigated by AC susceptibility measurements as a function of temperature and frequency, in zero and under an applied DC field. Except for compound **1.4i**, in the absence of a static magnetic field, no maxima in the $\chi''(T)$ plots are observed, although **1.4f** already display some enhancement as the frequency increases (Figure 1.74).

The absence of signal in complexes **1.4g** and **1.4h**, just like in compound **1.4f**, is attributed to the presence of a transverse magnetic anisotropy (very large values of E), as confirmed by HFEPR measurements and theoretical calculations (Table 1.12), which can be resolved by the application of a DC field.

Complex **1.4i** was another good surprise, showing an exceptional SIM behavior at zero DC field. Figure 1.74d shows the temperature-dependent AC susceptibility measurements at frequencies from 128 Hz to 5000 Hz, where strong frequency dependence is visible in both components, below 18 K. Furthermore, at all frequencies these maxima show an upturn at low temperature, which could be due to the impact of QTM on the relaxation process, confirmed by the theoretical studies (Figure 1.73).

The frequency-dependent measurements were also performed for **1.4i** in the absence of an external magnetic field (Figure 1.75)

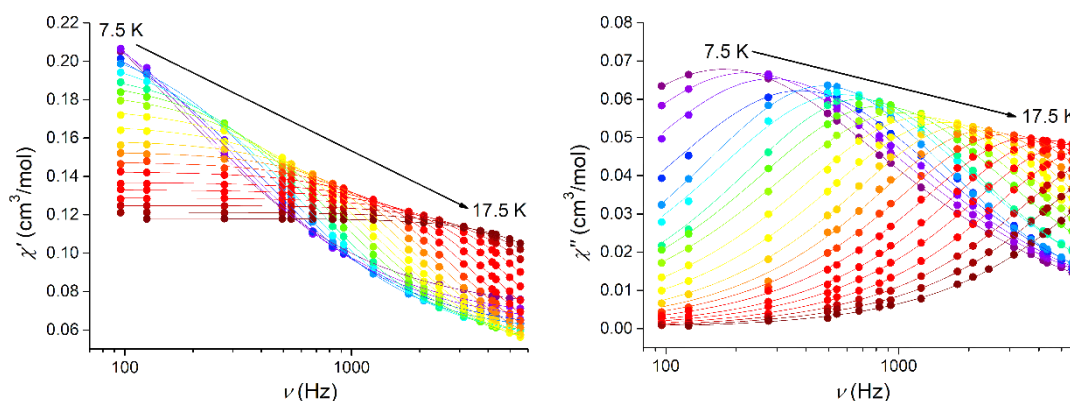


Figure 1.75 Frequency dependence of the in-phase χ' (left) and out-of-phase χ'' (right) magnetic susceptibilities at different temperatures for complex **1.4i** in the absence of a DC field. The solid lines are for guidance.

The Argand representation is shown in Figure 1.76, left, in which the semicircles obtained, characteristic of a single relaxation process (see α values in Appendix III, Table III.12), were fitted to the generalized Debye model (Equations 1.10 to 1.12). The magnetization relaxation times (τ) obtained from these fits were plotted as $\ln(\tau)$ vs. T^{-1}

(Figure 1.76, right). Similarly to the previous studied compounds these data were first fitted to an Arrhenius law (Equation 1.17), giving an energy barrier of $109(3) \text{ cm}^{-1}$ and a pre-exponential factor of $2.5(2) \times 10^{-8} \text{ s}$. However, a clear curvature in the plot, indicate the presence of other relaxation processes. In agreement with the results obtained for the previous compounds, the best fit was obtained by a sum (red line) of the Orbach (blue dashed line) and Raman (green dashed line) mechanisms through Equation 1.23, giving $U_{\text{eff}} = 135(8) \text{ cm}^{-1}$, $C = 0.23(3) \text{ K}^{-n} \text{ s}^{-1}$, $n = 4.19(6)$ and $\tau_0 = 3.0(2) \times 10^{-10} \text{ s}$. The experimentally obtained value of U_{eff} is in moderate agreement with the value obtained by the theoretical studies at zero DC field, $U_{\text{cal.}} = 146.6 \text{ cm}^{-1}$.

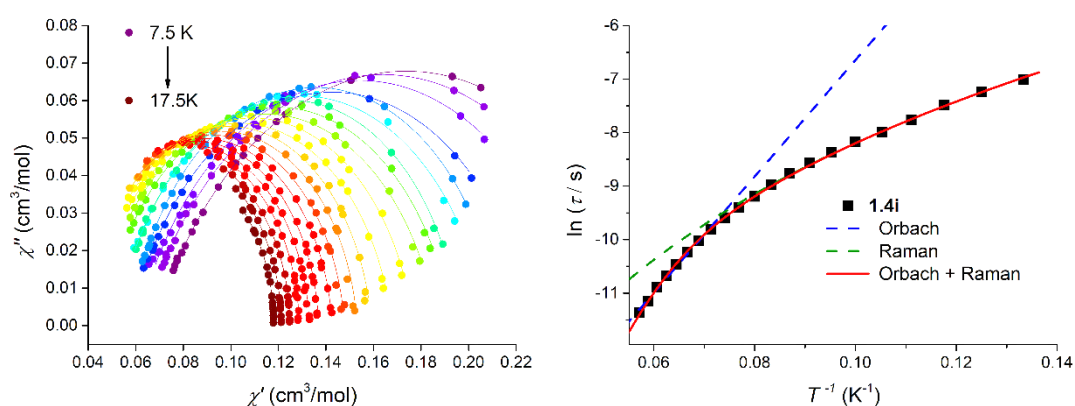


Figure 1.76 Cole-Cole plot for complex **1.4i** in the absence of an external magnetic field. The solid lines represent the best fits to the experimental data using the generalized Debye model (left) and $\ln(\tau)$ vs. T^{-1} plot for **1.4i** in the absence of an external magnetic field, the red line is the best fit to the sum of Raman and Orbach processes (right).

The application of a static field was expected to reduce the QTM and, in fact, is visible the strong frequency dependence of the signals at 2000 Oe for **1.4f**, 1000 Oe for **1.4g** and 1500 Oe for **1.4h**, which confirms the presence of slow relaxation of the magnetization. As for complex **1.4i**, the upturn at low temperature disappeared, indicating that the QTM has been successfully suppressed (Figure 1.77).

Once the optimum field was established, the frequency-dependent measurements at different temperatures were also carried out (Figure 1.78).

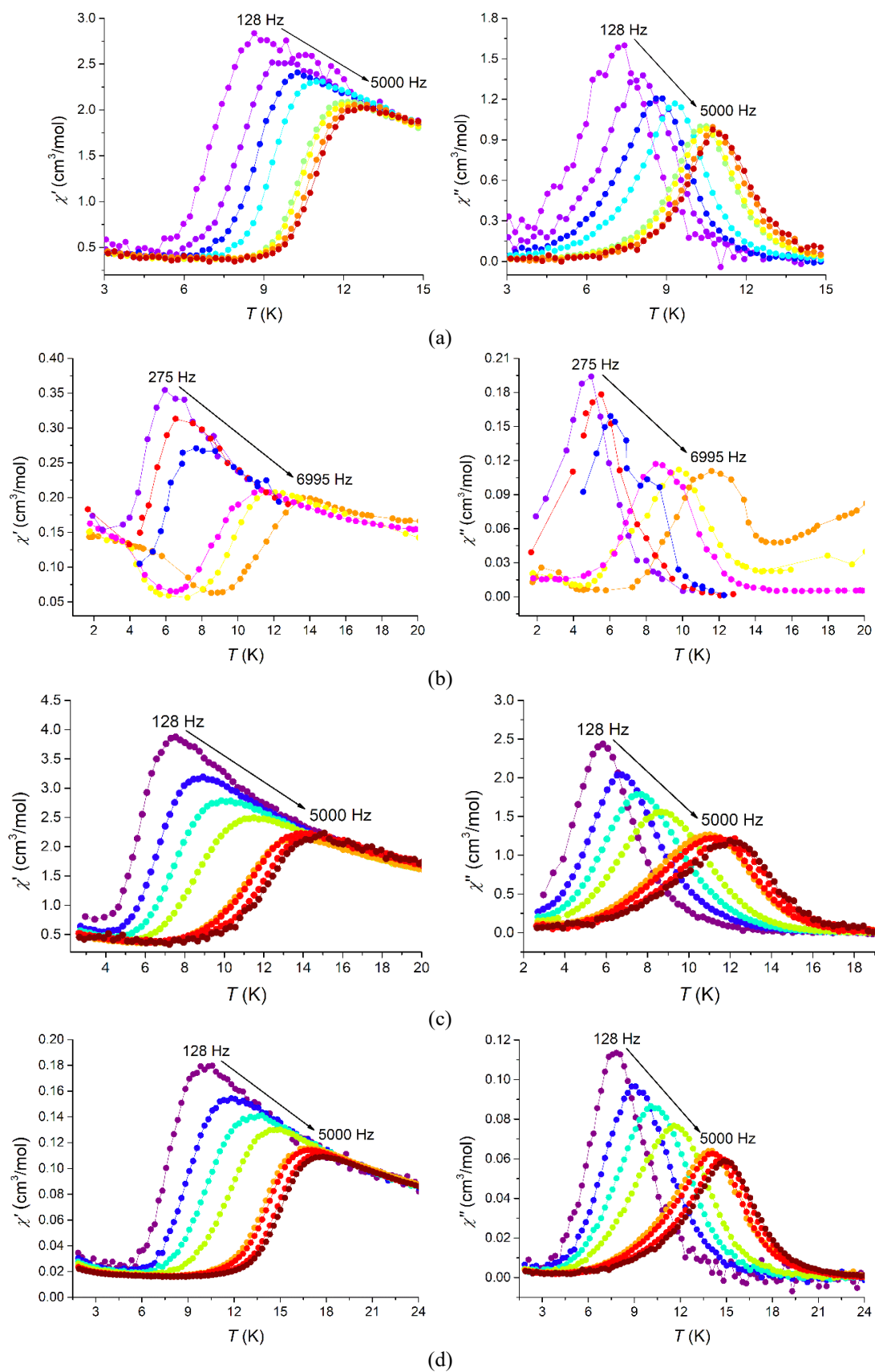


Figure 1.77 Temperature dependence of the in-phase, χ' (left) and out-of-phase, χ'' (right) magnetic susceptibilities at different frequencies for complexes (a) **1.4f** under 2000 Oe, (b) **1.4g** under 1000 Oe, (c) **1.4h** under 1500 Oe and (d) **1.4i** under 1200 Oe.

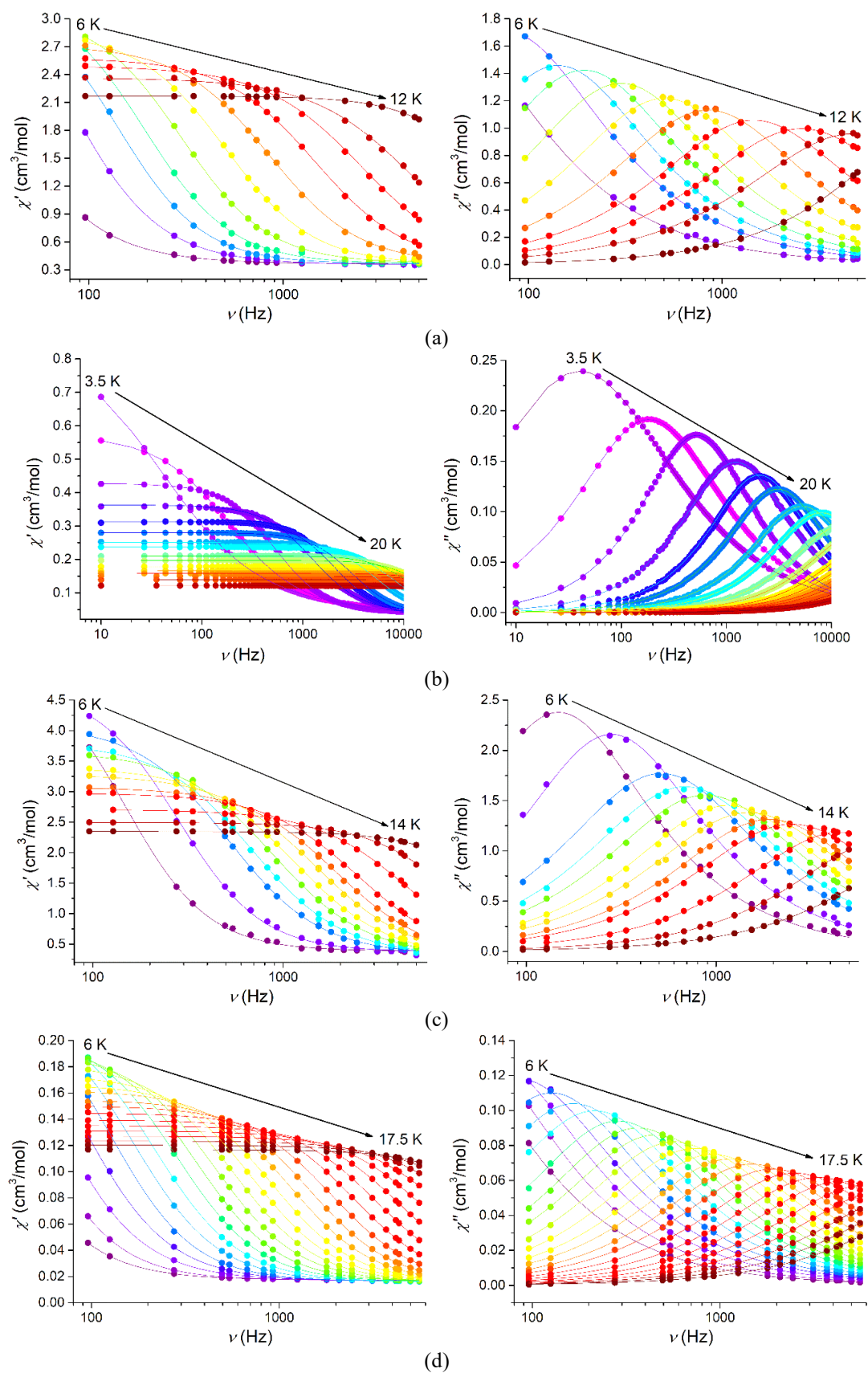


Figure 1.78 Frequency dependence of the in-phase χ' (left) and out-of-phase χ'' (right) magnetic susceptibilities at different temperatures for complexes (a) **1.4f** at 2000 Oe, (b) **1.4g** at 1000 Oe, (c) **1.4h** at 1500 Oe and (d) **1.4i** at 1200 Oe. The solid lines are for guidance.

Chapter 1

The Argand diagrams in the temperature range 3.5-20 K were fitted using the generalized Debye model (Equations 1.10 to 1.12) (Figure 1.79).

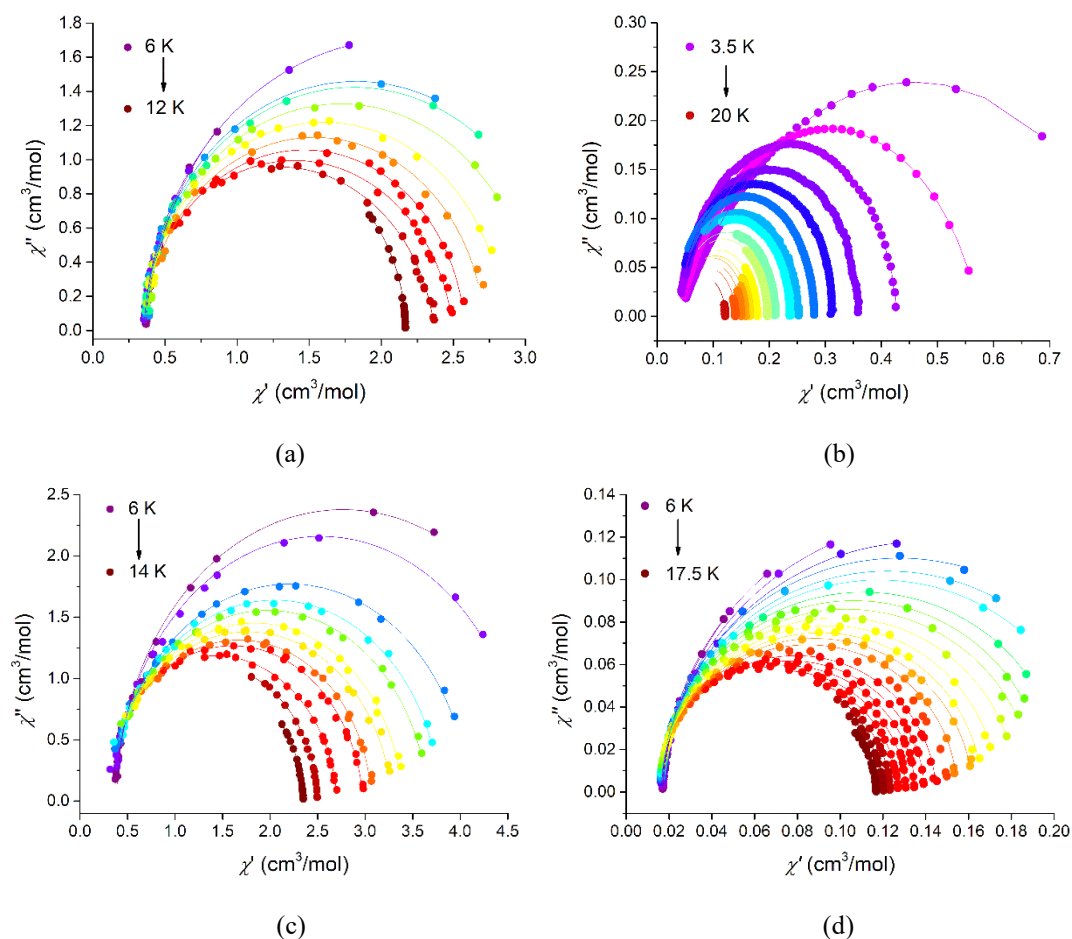


Figure 1.79 Cole-Cole plots for complexes (a) **1.4f** under a DC field of 2000 Oe, (b) **1.4g** under a DC field of 1000 Oe, (c) **1.4h** under a DC field of 1500 Oe and (d) **1.4i** under a DC field of 1200 Oe. The solid lines represent the best fits to the experimental data using the generalized Debye model.

The parameters obtained from the Debye fits to the Argand diagrams (see Appendix III, Tables III.9-11 and III.13) show that α supports the existence of a single relaxation process. By plotting $\ln(\tau)$ vs. T^{-1} (Figure 1.80) for each complex and fitting considering only the presence of the Orbach process (Equation 1.17) yields the following parameters: $U_{\text{eff}} = 128(5) \text{ cm}^{-1}$ and $\tau_0 = 2.7(5) \times 10^{-10} \text{ s}$ for **1.4f**, $U_{\text{eff}} = 46.5(4) \text{ cm}^{-1}$ and $\tau_0 = 2.22(3) \times 10^{-7} \text{ s}$ for **1.4g**, $U_{\text{eff}} = 106(13) \text{ cm}^{-1}$ and $\tau_0 = 5(1) \times 10^{-9} \text{ s}$ for **1.4h** and $U_{\text{eff}} = 126.7(4) \text{ cm}^{-1}$ and $\tau_0 = 7.1(3) \times 10^{-9} \text{ s}$ for **1.4i**. However, the linearity of the Arrhenius plots are lost at lower temperatures with $\ln(\tau)$ increasing at a slower rate with decreasing T , meaning that once again more than one relaxation process is operating in different ranges of temperatures.

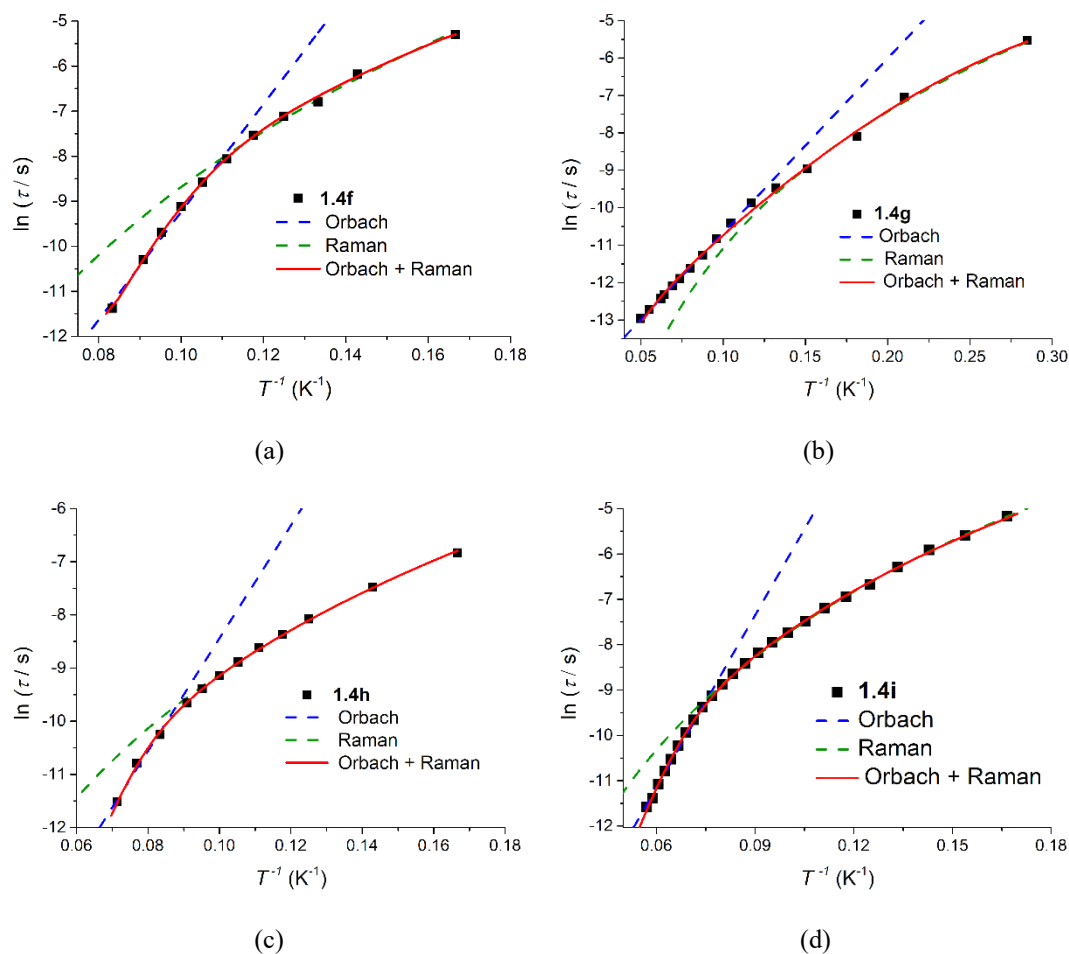


Figure 1.80 $\ln(\tau)$ vs. T^{-1} plots, the red lines are the best fits to the sum of Raman and Orbach processes (a) for **1.4f** under 2000 Oe, (b) for **1.4g** under 1000 Oe, (c) **1.4h** under 1500 Oe and (d) **1.4i** under 1200 Oe.

The best description of the results is obtained by a sum (red lines) of the Orbach (blue dashed lines) and Raman (green dashed lines) processes, given by Equation 1.23, fixing the U_{eff} values ($U_{\text{eff}} = 2|D|$) for complexes **1.4f** and **1.4i**. Table 1.13 shows the calculated parameters obtained from these fits.

Table 1.13. Orbach and Raman relaxation parameters for complexes **1.4f-i**.

Parameters	1.4f	1.4g	1.4h	1.4i
H_{DC} (Oe)	2000	1000	1500	1200
C ($K^{-n} s^{-1}$)	0.008(2)	1(1)	0.28(9)	0.018(2)
n	5.7(2)	4.1(7)	4.5(2)	5.11(4)
U_{eff} (cm^{-1})	104	38(8)	127.3(6)	182
τ_0 (s)	$5.1(2) \times 10^{-11}$	$8(9) \times 10^{-7}$	$3.6(5) \times 10^{-11}$	$3.7(2) \times 10^{-12}$

Chapter 1

In the case of compound **1.4h** the value of U_{eff} calculated from the AC experiments is very close to the value obtained from the theoretical calculations, $U_{\text{calc.}} = 133.2 \text{ cm}^{-1}$. Therefore, we can assume that the D values are very close to the experimental ones. In fact, the reproduction of the computed susceptibility and magnetization curves display a good agreement with the experimental ones (Figure 1.81).

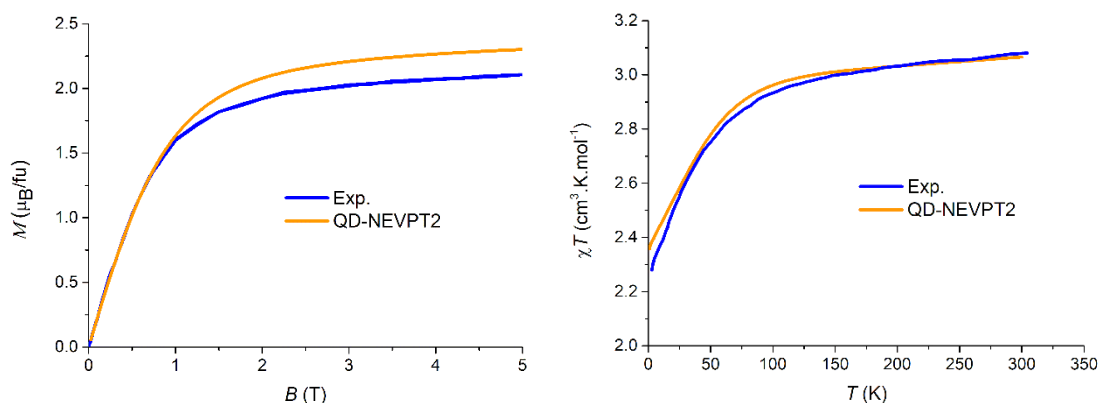


Figure 1.81 Experimental and calculated χT vs T curves ($H = 500 \text{ Oe}$) (left) and magnetization curves ($T = 2 \text{ K}$) (right) of the **1.4h** complex.

In this series of complexes **1.4f-i**, we intended to study the effect of the ligand asymmetry and donor strength on the magnetic anisotropy and slow relaxation of magnetization. Similarly to what was found in the first studied series (**1.4a-e**), in this case, the high and negative values of D are due to the bite angles θ , for which below 85° the system gains axial anisotropy, and also the E values are controlled by the chelating ligands interplanar angle ϕ . In the latter case, the variations are more pronounced since the ϕ values varies from 59.5 to 89.95° and the E values from 8 to 0.7 cm^{-1} , respectively (Tables 1.12 and 1.14).

The E/D vs. ϕ plot (Figure 1.51b, in subsection 1.2.2.3.2.2) shows that E is inversely proportional to ϕ and thus for $\phi = 90^\circ$ the value of E is closer to zero. Therefore, as the interplanar angle decreases the geometry of the complexes changes gradually from tetrahedral to square planar, also leading to less negative values of D , likewise seems to happen in compound **1.4g**. The high values of the transverse anisotropy in complexes **1.4g-h** are the reason for the presence of QTM processes, which are responsible for the lack or low frequency-dependent behavior of the χ'' vs. T plots.

Table 1.14. Bite angles θ , dihedral angles ϕ and interligand angles ω for complexes **1.4f-i**.

Complexes	1.4f	1.4g		1.4h	1.4i
		mol. #1	mol. #2		
Angles ($^{\circ}$)					
N1-Co-N2 (θ_1) ^a	85.03(8)	83.78(13)	83.8(1)	81.51(18)	82.89(4)
N3-Co-N4 (θ_2) ^a	83.80(8)	84.03(13)	84.0(1)	82.63(17)	83.03(4)
Dihedral ϕ ^b	79.38(9)	59.09(13)	59.60(13)	70.08(17)	89.95(5)
Angle ω ^c	168.31(6)	174.99(8)	172.25(9)	173.01(11)	152.82(3)

^a θ = N-Co-N chelating ligands bite angles; ^b ϕ = dihedral angle formed between planes defined by atoms (Co, N1, N2) and (Co, N3, N4); ^c ω = interligand angle formed between dummy bonds

Co-(C2-C6)_{centroid} and Co-(Cx-Cy)_{centroid}.

Complex **1.4i** behaves as a SIM at zero field, displaying very high values of U_{eff} . The observation of the D vs. ω plot (Figure 1.52a, in subsection 1.2.2.3.2.2) indicates that a shift from tetrahedral to trigonal pyramidal geometry greatly increases the magnetic anisotropy. In fact, compound **1.4i** presents $\omega = 152.82^{\circ}$, which corresponds to the region of more negative values of D (close to the maximum of the D vs. ω plot), indicating a geometry that tend to trigonal pyramidal, also confirmed by the X-ray structure (see subsection 1.2.2.2). This feature, combined with the low values of E , since the ϕ is almost 90° , demonstrates that this structure has almost a perfect uniaxial symmetry, overcoming the value obtained for complex **1.4e**, now displaying (to the best of our knowledge) the second largest value for the spin-reversal energy barrier ($U_{\text{eff}} = 135(8)$ cm^{-1}) so far reported for tetracoordinate Co(II)-N₄ complex in the absence of an external field. The geometrical distortion from tetrahedral toward trigonal pyramidal is very likely possible owing to the asymmetry of the *N*-2-*t*Bu-C₆H₄ ring. This asymmetrically substituted ring certainly presents more degrees of freedom for distortion due to the non-substitution of the position 6 of the *N*-phenyl ring, although still keeping a very bulky *t*-butyl group in position 2.

Long and co-workers,⁴⁸ have been studied the influence of the ligand field in relation to the static and dynamic magnetic behavior in a family of trigonal pyramidal Fe(II) complexes supported by tris(pyrrolyl- α -methyl)amine ligands. From those works, they concluded that the increase in the basicity of the *N*-ligands is one of the main parameters required to enhance the magnetic anisotropy. This type of effect also seems to be verified in the present study, since the least basic ligand (containing CF₃ substituents in the 5-phenyl ring) in compound **1.4g** presents worst results. As for the energy barrier, the lower values obtained $U_{\text{eff}} = 38(8)$ cm^{-1} , much lower than expected ($U_{\text{eff}} = 90$ cm^{-1}

Chapter 1

obtained from $U_{\text{eff}} = (S^2 - 1/4)|D| = 2|D|$ with $D = -45(2) \text{ cm}^{-1}$, can be likely explained by the fact that the Raman process in this compound seems to be the dominant mechanism in the studied temperature range. Alternatively, the strong intermolecular interactions observed in the crystalline structure may also contribute to this partial quenching phenomenon.

1.2.3 Conclusion

The work developed throughout this chapter allowed to draw some conclusions:

- New 5-substituted-2-iminopyrrole ligand precursors were synthesized in moderate yields (58-70 %), via a synthetic route encompassing three reaction steps, and characterized by NMR spectroscopy and elemental analysis;
- New homoleptic bis(5-aryl-2-iminopyrrolyl) Co(II) complexes **1.4d-i** were synthesized in moderate yields (62-75 %) by reaction of the *in situ* prepared sodium salt of the ligand precursors with CoCl_2 , in THF;
- All the Co(II) compounds were characterized by elemental analysis, FTIR and solution ^1H NMR spectroscopies and single crystal X-ray diffraction. Crystals suitable for X-ray diffraction exhibited two chelating ligands coordinated to the metal center in a essentially tetrahedral geometry that can be distorted toward either square planar or trigonal pyramidal;
- Magnetic susceptibility measurements were also performed for all the complexes in solution (by the Evans method) and in solid state (by SQUID magnetometry) presenting values within the known tetrahedral high spin Co(II) compounds, with $S = 3/2$;

- DC magnetic measurements, HF-EPR spectroscopy and theoretical calculation showed that all the complexes display strongly negative values of magnetic anisotropy (D varying from $-42.6(4)$ to $-91(3)$ cm^{-1}), because the values of the bite angles θ , dihedral angles ϕ and interligand angles ω lie in the range of the most negatively valued regions of the magnetostructural model presented in the theoretical calculations subsection 1.2.2.3.2.2;
- Despite displaying SIM behavior at zero DC field, the maxima of the χ'' vs. T plots for complexes **1.4b-d** and **1.4f** were not well resolved due to QTM processes; the QTM is successfully suppressed when an external magnetic field is applied, enhancing significantly the frequency and temperature dependence of the ac susceptibility peaks. For the remaining compounds **1.4a** and **1.4g-h** the lack of maxima in χ'' vs. T plots is caused mainly by the presence of a transverse anisotropy, in good agreement with the high experimental and calculated values of E .
- For complexes **1.4e** and **1.4i** it was possible to highly enhance the SIM behavior by controlling their molecular structure and thus reducing E values in order to gain axiality. Therefore, these compounds presented high values of U_{eff} (84 and $135(8)$ cm^{-1} , respectively), being to the best of our knowledge, respectively, the third and second largest values for the spin-reversal energy barrier so far reported for a tetrahedral Co(II)-N₄ complex in the absence of an external magnetic field;
- In this molecular system, the tuning of the geometry seems to be the key parameter for the enhancement of the SIM behavior: compound **1.4g**, characterized by a geometry between square planar and tetrahedral, displays the lowest SIM behavior with the worst anisotropy results (high values of E and low values of U_{eff}), whereas **1.4i**, exhibits a distorted trigonal pyramidal geometry, displaying the highest SIM behavior with the best results (high values of D and U_{eff} at zero DC field and lower values of E).

1.3 EXPERIMENTAL SECTION

1.3.1 General considerations

All operations dealing with air- and/or moisture-sensitive materials were carried out under inert atmosphere using a dual vacuum/nitrogen line, glovebox and standard Schlenk techniques. All solvents used were pre-dried with 4 Å molecular sieves and purified by refluxing over a suitable drying agent (sodium/benzophenone for diethyl ether and THF; CaH₂ for *n*-hexane) followed by distillation under nitrogen and stored in glass ampoules. Solvents and solutions were transferred using a positive pressure of nitrogen through stainless steel cannulas and mixtures were filtered in a similar way using modified cannulas that could be fitted with glass fiber filter disks. Pyrrole, *N,N*-dimethylformamide, POCl₃, and 2-*tert*-butylaniline were dried over CaH₂, distilled under reduced pressure and stored under dinitrogen. Anhydrous CoCl₂ was prepared by heating CoCl₂·6H₂O at 100 °C under dynamic vacuum until constant weight. The 2-substituted pyrroles **1.1b-c** and **1.1e**,¹⁰⁵ the 5-substituted-2-formylpyrroles **1.2a-c** and **1.2e**,^{91,117} the 5-substituted-2-iminopyrrole ligand precursors **1.3a-c**^{91,94} and **1.3e**¹¹⁸ and the homoleptic Co(II) complexes **1.4a-c**^{91,94} were prepared by the reported methods. 2-(1-Adamantyl)-1*H*-pyrrole was prepared as described in the literature.¹⁰⁶ The remaining reagents were used as received from commercial sources, namely 1-adamantyl chloride (Alfa Aesar), 1-adamantylamine (Alfa Aesar) and 2-*tert*-butylaniline (Aldrich).

1.3.2 Characterization techniques and methodologies

1.3.2.1 Nuclear Magnetic Resonance (NMR)

NMR spectra were recorded on a Bruker AVANCE III 300 MHz spectrometer at 299.995 MHz (¹H), 75.4296 MHz (¹³C) and 282.404 MHz (¹⁹F). The spectra were referenced internally using the residual protio-resonances (¹H) and the solvent carbon (¹³C) resonances of the corresponding solvents to tetramethylsilane ($\delta = 0$). The samples of air- and/or moisture-stable organic compounds were prepared in common NMR tubes using CDCl₃ as solvent. For air- and/or moisture-sensitive compounds, samples were

dissolved in degassed and dried toluene-*d*₈ or C₆D₆ prepared inside a glovebox, and the corresponding solutions transferred to J. Young NMR tubes. The deuterated solvents were dried over activated 4 Å molecular sieves and degassed by the freeze-pump-thaw technique. The magnetic susceptibility measurements in solution were carried out by the Evans method,¹¹⁹ using a 3% solution of hexamethyldisiloxane in C₆D₆ as reference. All resonances were characterized by their chemical shifts (δ), quoted in ppm, and coupling constants (*J*), given in Hz. Multiplicities were abbreviated as follows: broad (br), singlet (s), doublet (d), triplet (t) and multiplet (m). In order to perform nuclei resonance assignments, the one-dimensional ¹H and ¹³C NMR experiments referred above were complemented with twodimensional NMR techniques: homonuclear ¹H-¹H COSY (*CORrelated SpectroscopY*) and/or ¹H-¹H NOESY (*Nuclear Overhauser Enhancement SpectroscopY*), for the ¹H spectra, and heteronuclear ¹H-¹³C HSQC (*Heteronuclear Single Quantum Coherence*) and/or ¹H-¹³C HMBC (*Heteronuclear Multiple Bond Correlation*) for the ¹³C spectra.

1.3.2.2 Single crystal X-ray diffraction

Crystals suitable for X-ray diffraction were selected under an inert atmosphere, covered with covered with polyfluoroether oil, and mounted on a nylon loop. The crystallographic data were collected using graphite monochromated Mo-K α radiation ($\lambda = 0.71073$ Å) on a Bruker AXS-KAPPA APEX II diffractometer equipped with an Oxford Cryosystem open-flow nitrogen cryostat, at 150 K. Cell parameters were retrieved using Bruker SMART software and refined using Bruker SAINT¹²⁰ on all observed reflections. Absorption corrections were applied using SADABS.¹²¹ Structure solution and refinement were performed using direct methods with the programs SIR2014¹²² and SHELXL¹²³ included in the package of programs WINGX-Version 2014.1.¹²⁴ All non-hydrogen atoms were refined anisotropically and the hydrogen atoms were inserted in idealized positions and refined as riding on the parent carbon atom. All the structures refined to a perfect convergence. The graphic presentations were generated using ORTEP-3,¹²⁵ where ellipsoids were drawn with a 30% probability, and the hydrogen atoms were omitted for clarity. The most relevant crystallographic data for each compound is presented along the thesis text while the experimental details are presented in Appendix II.

Chapter 1

1.3.2.3 Elemental analysis

The elemental analyses were performed in a Fisons Instrument Mod EA-108, at *Laboratório de Análises of Instituto Superior Técnico (IST)*. All samples were prepared in sealed glass ampoules, under inert atmosphere and quickly weighed and mounted in air prior to combustion. Two independent determinations for each compound were executed.

1.3.2.4 HFEPR spectroscopy

The spectra were recorded between 300 and 375 GHz, 0–15 T and 5–210 K on a home-built spectrometer consisting of a VDI signal generator, VDI broadband frequency multipliers, a Thomas Keating Ltd. quasioptical bridge and probe, and a QMC Instruments InSb bolometer detector.¹²⁶ The samples were mounted in a 15 T Oxford Instruments helium bath magnetocryostat. The external field is modulated at kHz frequencies to allow for lock-in detection.

1.3.2.5 Computational studies

The ORCA program¹²⁷ package version 4.2.1 was used for all the property calculations using the structures derived from single-crystal X-ray diffraction as input. The N-Electron Valence perturbational method^{128,129} to second order was employed with the Resolution of Identity¹³⁰ (RI-NEVPT2) approximation. The Complete Active Space Self-Consistent Field (CASSCF)¹³¹ wavefunction was determined in the full configuration interaction (CI) space as the state-average of 10 quartets and 40 doublets (seven electrons in five 3*d* orbitals). The single state perturbed NEVPT2 wavefunctions underwent a multi-state extension to quasi-degenerate NEVPT2 (QD-NEVPT2)¹³² in the Nakano¹³³ formulation.

The exchange integrals were calculated through the RIJCOSX^{134,135} density fitting technique with 5 accuracy points (GridX5).

The Douglas-Kroll-Hess^{136–138} scalar relativistic Hamiltonian truncated to second order (DKH2) was applied with the correspondingly contracted triple zeta polarized basis sets (DKH-TZVP) for all the elements except hydrogen, the latter having been assigned a split-valence basis set (DKH-SVP). The density fitting auxiliary basis sets were chosen to be the generic Karlsruhe¹³⁹ def2-TZVP/C specific basis set for the treatment of the perturbative RI section in addition to the segmented relativistically contracted (SARC/J) set¹⁴⁰ for the non-perturbative Coulomb integrals.

The anisotropy (D , E) parameters and g values were calculated in the framework of QD-NEVPT2 via the spin-orbit mean field^{141,142} formalism using an effective Hamiltonian¹⁴³ by projection of the CI matrix onto the model states. The spin orbit states were projected onto the giant spin Hamiltonian:

$$\hat{H} = \hat{S}\mathbf{D}\hat{S} \quad (1.24)$$

where \mathbf{D} is the zero-field splitting tensor possessing the following scalar parameters in the magnetic axis frame: $D = 3/2D_{zz}$ and $E = (D_{xx} - D_{yy})/2$. By convention $D_{xx} \geq D_{yy}$ so that E is always positive. If $D < 0$ there may be a barrier for magnetization reversal ($-M_s \rightarrow +M_s$), whereas for $D > 0$ there can be no magnetization reversal and the spin aligns itself in the xy plane.

1.3.2.6 Magnetic measurements

Polycrystalline samples of the compounds (10–20 mg) used in the magnetic measurements were transferred to the sample holder in a glovebox, due to their air sensitivity.

The static (DC) magnetic measurements were performed using a 6.5 T S700X SQUID (Cryogenic Ltd.) magnetometer. The magnetic susceptibility was measured as a function of temperature under a static magnetic field of 500 G in the temperature range of 5–300 K. The magnetization curves were also obtained from 0 to 5 T at different temperatures (2, 4, 5, 10, 20, 50 and 100 K). The diamagnetism correction for the experimental data was estimated using the Pascal approach.³⁴

Chapter 1

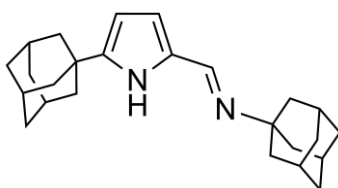
The dynamic (AC) magnetic measurements were performed using a MagLab 2000 (Oxford Instruments), a Vibrating Sample Magnetometer, VSM (Cryogenic Ltd.) and a PPMS magnetometer (Quantum Design), depending on the samples, with an AC field of 10 Oe. The temperature dependence of the in-phase and out-of-phase susceptibility components were studied at different frequencies, from 95 up to 9995 Hz, under zero and a pre-selected applied DC field (3000 Oe for **1.4a**, 1000 Oe for **1.4b** and **1.4g**, 800 Oe for **1.4c-d**, 0 Oe and 1200 Oe for **1.4e** and **1.4i**, 2000 Oe for **1.4f** and 1500 Oe for **1.4h**). The frequency dependence of the AC susceptibility was performed at different temperatures from 3.5 K to 20 K under zero DC field and applied external magnetic fields.

1.3.3 Synthetic procedures

1.3.3.1 General procedure for the synthesis of 5-substituted-2-(*N*-formimino)-1*H*-pyrroles (**1.3d** and **1.3f-i**)

In a round-bottom flask, the 5-substituted-2-formyl-1*H*-pyrrole, the corresponding amine and a catalytic amount of *p*-toluenesulfonic acid were dissolved in toluene or ethanol. A Soxhlet extractor, containing pre-dried molecular sieves 4 Å (to remove the water from the reaction mixture), a condenser and a CaCl₂ guard tube were fitted to the flask. The mixture was refluxed for the appropriate time required to achieve the maximum of conversion, as indicated by ¹H NMR spectroscopy. After cooling down to room temperature, the solvent was removed under reduced pressure and the pure products were achieved by recrystallization with an appropriate solvent at -20 °C or by column chromatography.

1.3.3.1.1 Synthesis of 5-(adamant-1-yl)-2-[*N*-(adamant-1-yl)formimino] pyrrole (**1.3d**)



The preparation of this compound followed the general procedure described above, using formylpyrrole **1.2d** (2.53 g, 11.0 mmol) and 1-adamantylamine (1.66 g; 11.0 mmol) in toluene, followed by recrystallization from a diethyl ether solution at -20 °C to yield a light brown powder.

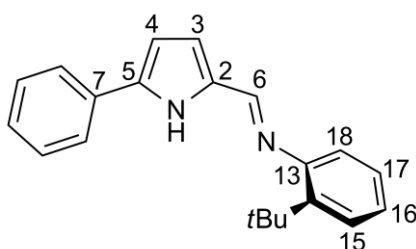
Yield: 2.14 g (60 %).

Anal. Calc. for C₂₅H₃₄N₂ 0.9C₄H₁₀O, obtained (calculated): C 79.89 (80.01), H 9.85 (10.10), N 6.45 (6.53).

¹H NMR (300 MHz, CDCl₃): δ 7.96 (s, 1H, N=CH), 6.37 (br, 1H, H3 *pyrr*), 5.95 (br, 1H, H4 *pyrr*), 5.79 (br, 1H, NH), 2.21-1.66 (m, 30H, 5-(1-Ad) + N-(1-Ad)).

¹³C{¹H} NMR (75 MHz, CDCl₃): δ 146.0 (N=CH), 122.0 (C5 *pyrr*), 114.5 (C2 *pyrr*), 106.5 (C3 *pyrr*), 103.9 (C4 *pyrr*), 43.3 (1-Ad CH₂), 42.6 (1-Ad CH₂), 36.7 (1-Ad CH₂), 36.6 (1-Ad CH₂), 29.7 (1-Ad CH), 28.5 (1-Ad CH).

1.3.3.1.2 Synthesis of 5-phenyl-2-[N-(2-*t*-butylphenyl)formimino]pyrrole (1.3f)



The preparation of this compound followed the general procedure described above, using formylpyrrole **1.2f** (0.88 g, 5.15 mmol) and 2-*t*-butylaniline (0.8 mL, 5 mmol) in ethanol, followed by purification by column chromatography using a 1:5 mixture of ethyl acetate and *n*-hexane as eluent to yield a yellow powder.

Yield: 1.1 g (70 %).

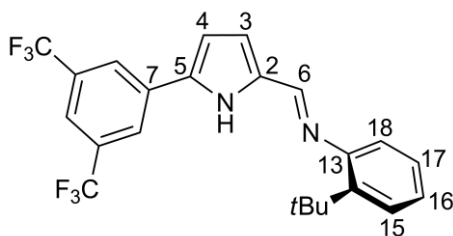
Chapter 1

Anal. Calc. for C₂₁H₂₂N₂, obtained (calculated): C 83.55 (83.40), H 7.05 (7.33), N 9.01 (9.26).

¹H NMR (300 MHz, CDCl₃): δ 9.5 (br, 1H, NH) 8.13 (s, 1H, N=CH), 7.88 (d, ³J_{HH} = 7.6 Hz, 2H, 5-Ph-H_{ortho}) 7.42 (d, ³J_{HH} = 7.3 Hz, 1H, H18), 7.31 (t, ³J_{HH} = 7.20 Hz, 2H, 5-Ph-H_{meta}), 7.23 (t, ³J_{HH} = 7.11 Hz, 1H, 5-Ph-H_{para}) 7.08 (d, ³J_{HH} = 6.96 Hz, 2H, H16, H17), 6.81 (d, ³J_{HH} = 6.71 Hz, 1H, H15), 6.73 (d, ³J_{HH} = 3.5 Hz, 1H, H3), 6.68 (d, ³J_{HH} = 3.4 Hz, 1H, H4), 1.48 (s, 9H, C(CH₃)₃).

¹³C{¹H} NMR (75 MHz, CDCl₃): δ 150.48 (C13), 148.22 (N=CH), 142.39 (CC(CH₃)₃), 137.77 (C7), 134.05 (C5), 128.41 (5-Ph-C_{meta}), 127.30 (5-Ph-C_{para}), 126.29 (C18), 125.24 (5-Ph-C_{ortho}), 124.43 (C15), 124.29 (C2), 124.01 (C16, C17), 123.40 (C3), 108.75 (C4), 36.19 (C(CH₃)₃), 31.31 (C(CH₃)₃).

1.3.3.1.3 Synthesis of 5-(3,5-trifluoromethyl)-2-[N-(2-*t*-butylphenyl)]formimino]pyrrole (1.3g)



The preparation of this compound followed the general procedure described above, using formylpyrrole **1.2g** (1.29 g, 4.12 mmol) and 2-*t*-butylaniline (0.6 mL, 3.95 mmol) in ethanol, followed by purification by column chromatography using a 1:5 mixture of ethyl acetate and *n*-hexane as eluent to yield a yellow powder.

Yield: 1.0 g (58%)

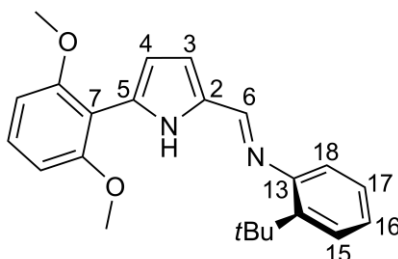
Anal. Calc. for C₂₃H₂₀N₂F₆, obtained (calculated): C 62.75 (63.01), H 4.82 (4.60), N 6.12 (6.39).

$^1\text{H NMR}$ (300 MHz, CDCl_3): δ 9.5 (br, 1H, *NH*), 8.13 (s, 1H, *N=CH*), 7.96 (s, 2H, 5-Ph-*H_{ortho}*), 7.77 (s, 1H, 5-Ph-*H_{para}*), 7.40 (d, $^3J_{\text{HH}} = 7.4$ Hz 1H, H15), 7.20 (m, 2H, H16, H17), 6.82 (d, $^3J_{\text{HH}} = 6.82$ Hz, 1H, H18), 6.76 (m, 2H, H3, H4), 1.48 (s, 9H, $\text{C}(\text{CH}_3)_3$).

$^{13}\text{C}\{^1\text{H}\}$ NMR (75 MHz, CD_3CN): δ 147.41 (*N=CH*), 145.31 (C13), 143.73 ($\text{CC}(\text{CH}_3)_3$), 135.18(C7), 132.68 (C5), 131.95 (C2), 131.48 (CCF3), 130.62 (5-Ph-*C_{meta}*), 127.91 (C17), 127.02 (C18), 126.71 (C16), 124.72 (C15), 124.40 (CF3) 124.19 (5-Ph-*C_{para}*), 123.28 (C3), 110.31 (C4), 35.71 ($\text{C}(\text{CH}_3)_3$), 30.19 ($\text{C}(\text{CH}_3)_3$)

$^{19}\text{F}\{^1\text{H}\}$ NMR (282 MHz, CDCl_3): δ -63.06 (CF₃).

1.3.3.1.4 Synthesis of 5-(2,6-dimethoxyphenyl)-2-[*N*-(2-*t*-butylphenyl)formimino]pyrrole (1.3h)



The preparation of this compound followed the general procedure described above, using formylpyrrole **1.2h** (0.96 g, 4.15 mmol) and 2-*t*-butylaniline (0.64 mL, 4 mmol) in ethanol, followed by purification by a column chromatography using a 1:5 mixture of ethyl acetate and *n*-hexane as eluent to yield a yellow powder.

Yield: 0.99 g (68 %).

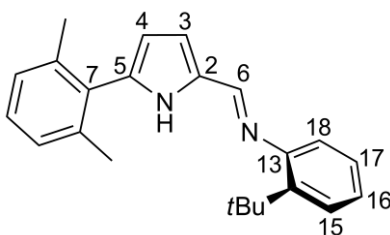
Anal. Calc. for $\text{C}_{23}\text{H}_{26}\text{N}_2\text{O}_2$ obtained (calculated): C 75.98 (76.21) H 7.29 (7.23) N 7.85 (7.73).

$^1\text{H NMR}$ (300 MHz, CDCl_3): δ 10.90 (br, 1H, *NH*), 8.16 (s, 1H, *N=CH*), 7.40 (d, $^3J_{\text{HH}} = 7.8$ Hz, 1H, H18), 7.25 (m, 2H, 5-Ph-*H_{meta}*), 7.15 (m, 2H, H16, H17), 6.92 (d, $^3J_{\text{HH}} = 7.5$ Hz, 1H, H15), 6.74 (s, 2H, H3,H4), 6.71 (s, 1H, 5-Ph-*H_{para}*), 3.99 (s, 6H, OCH_3), 1.54 (s, 9H, $\text{C}(\text{CH}_3)_3$).

Chapter 1

$^{13}\text{C}\{^1\text{H}\}$ NMR (75 MHz, CDCl_3): δ 157.45 (COCH_3), 151.71 (C13), 147.15 ($\text{N}=\text{CH}$), 142.91 ($\text{CC}(\text{CH}_3)_3$), 130.12 (C2), 127.77 (5-Ph- C_{meta}), 127.10 (C17), 125.98 (C18), 124.81 (C16), 119.31 (C15), 115.26 (C3, C4), 113.73 (C5), 109.47 (5-Ph- C_{para}), 104.74 (C7), 55.92 (OCH_3), 35.73 ($\text{C}(\text{CH}_3)_3$), 30.58 ($\text{C}(\text{CH}_3)_3$).

1.3.3.1.5 Synthesis of 5-(2,6-dimethylphenyl)-2-[N-(2-*t*-butylphenyl)]formimino]pyrrole (1.3i)



The preparation of this compound followed the general procedure described above, using formylpyrrole **1.2i** (1.095 g, 5.5 mmol) and 2-*t*-butylaniline (0.82 g, 5.5 mmol) in ethanol, followed by recrystallization from *n*-hexane solution at $-20\text{ }^\circ\text{C}$ to yield orange crystals.

Yield: 1.33 g (72 %).

Anal. Calc. for $\text{C}_{23}\text{H}_{26}\text{N}_2$ obtained (calculated): C 83.28 (83.10) H 8.05 (7.93) N 8.15 (8.42).

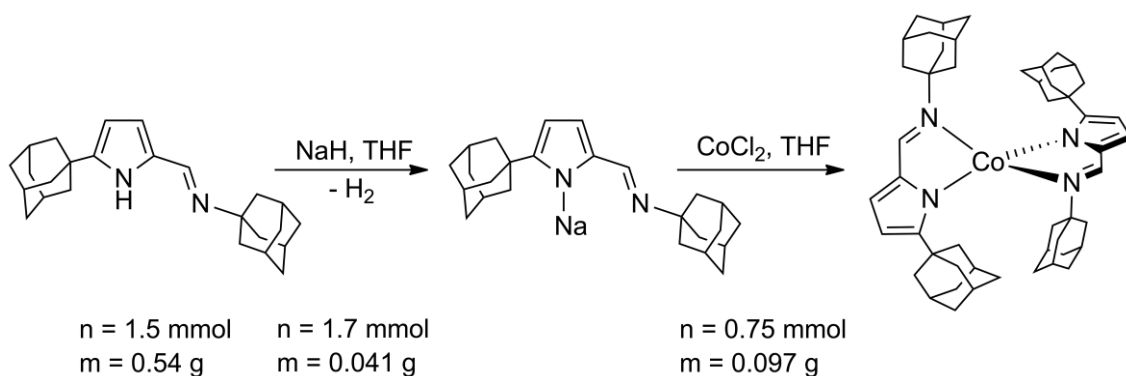
^1H NMR (300 MHz, CDCl_3): δ 9.04 (br, 1H, NH), 8.18 (s, 1H, $\text{N}=\text{CH}$), 7.43 (d, $^3J_{\text{HH}} = 7.5$ Hz, 1H, H18), 7.29 (m, 2H, H17, 5-Ph- H_{para}), 7.20 (m, 3H, H16 5-Ph- H_{meta}), 6.93 (d, $^3J_{\text{HH}} = 7.2$ Hz, 1H, H15), 6.81 (d, $^3J_{\text{HH}} = 3.3$ Hz, 1H, H3), 6.28 (d, $^3J_{\text{HH}} = 3.3$ Hz, 1H, H4), 2.32 (s, 6H, CH_3), 1.50 (s, 9H, $\text{C}(\text{CH}_3)_3$).

$^{13}\text{C}\{^1\text{H}\}$ NMR (75 MHz, CDCl_3): δ 151.78 (C13), 147.77 ($\text{N}=\text{CH}$), 143.01 ($\text{CC}(\text{CH}_3)_3$), 138.50 (C7), 134.69 (C5), 132.67 (CCH_3), 131.32 (C2), 128.62 (5-Ph- C_{para}), 127.76 (5-Ph- C_{meta}), 127.27 (C17), 126.18 (C18), 125.17 (C16), 119.71 (C15), 116.07 (C3), 111.08 (C4), 35.70 ($\text{C}(\text{CH}_3)_3$), 30.72 ($\text{C}(\text{CH}_3)_3$), 20.87 (CH_3).

1.3.3.2 General procedure for the syntheses of homoleptic bis(5-substituted-2-iminopyrrolyl) Co(II) complexes (1.4d-i)

The first step of the preparation of the Co(II) complexes is the *in situ* synthesis of the ligand precursor's sodium salt. Therefore, a little excess of NaH was suspended in THF in a Schlenk tube and a THF solution of the corresponding ligand precursor was added dropwise. The mixture was allowed to stir for 2 hours, at 90 °C, under nitrogen. After cooling to room temperature, the solution was filtered and added dropwise to a suspension of anhydrous CoCl₂ in THF, which was cooled to -80 °C. The mixture was allowed to warm up to room temperature while stirring overnight. All volatiles were evaporated under reduced pressure, the residue being extracted with the appropriate solvent until extracts were colorless.

1.3.3.2.1 Synthesis of [Co{κ²N,N'-5-(adamant-1-yl)-NC₄H₂-2- C(H)=N (adamant-1-yl)}] (1.4d)



The general procedure described above was applied. All volatiles were evaporated under reduced pressure, and the red residue was extracted with *n*-hexane until extracts were colorless. The solution was concentrated under vacuum and stored at -20 °C, from which red crystals of **1.4d** suitable for X-ray diffraction were obtained.

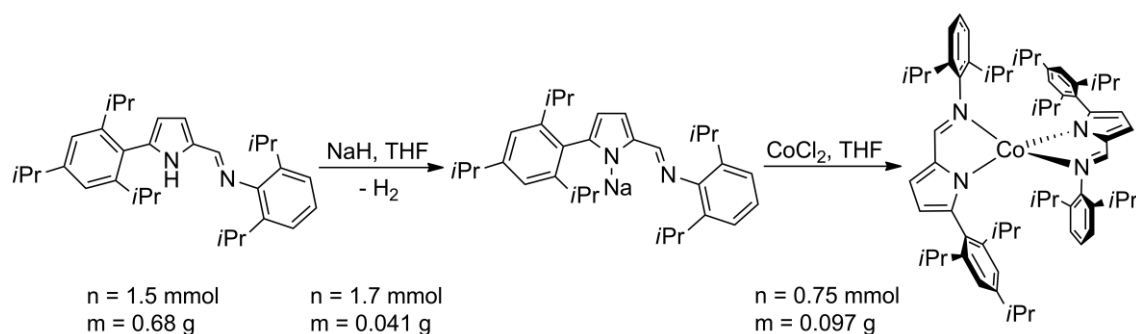
Yield: 0.41 g (69%).

Anal. Calc. for C₅₀H₆₆CoN₄, obtained (calculated): C 76.56 (76.79), H 8.55 (8.51), N 6.87 (7.16).

Chapter 1

$^1\text{H NMR}$ (300 MHz, C_6D_6): δ 116.36 (br), 30.43 (br), 0.07 (br), -6.50, -7.07, -7.81 (br), -10.35 (br), -14.23, -16.18 (br), -47.45, -55.95 (br). μ_{eff} (toluene- d_8) = 4.7 μ_{B} . FTIR (ATR, cm^{-1}): 1566 (s, C=N).

1.3.3.2.2 Synthesis of $[\text{Co}\{\kappa^2\text{N},\text{N}^{\prime}\text{-5-(2,4,6-}i\text{Pr}_3\text{-C}_6\text{H}_2)\text{-NC}_4\text{H}_2\text{-2-C(H)=N(2,6-}i\text{Pr}_2\text{-C}_6\text{H}_3)\}_2]$ (**1.4e**)



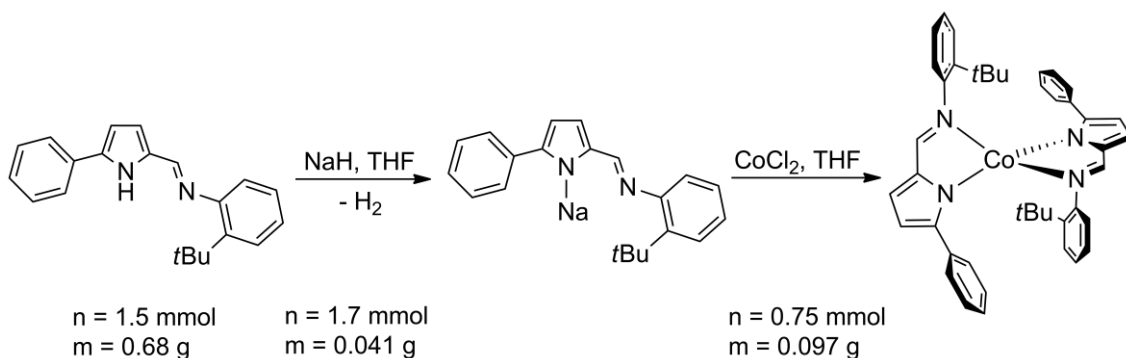
The general procedure described above was applied. All volatiles were evaporated under reduced pressure, and the red residue was extracted with *n*-hexane until extracts were colorless. The solution was concentrated and stored at -20 °C, from which red crystals of **1.4e** suitable for X-ray diffraction were obtained.

Yield: 0.42 g (62%).

Anal. Calc. for $\text{C}_{64}\text{H}_{86}\text{CoN}_4$, obtained (calculated): C 79.10 (79.22), H 9.37 (8.93), N 5.80 (5.77).

$^1\text{H NMR}$ (300 MHz, C_6D_6): δ 113.64 (br), 44.29 (br), 32.76 (br), 9.47 (br), 4.27 (br), 0.67 (br), -2.05 (br), -4.41 (br), -5.77 (br), -6.14 (br), -6.31 (br), -7.75 (br), -12.85 (br), -17.21 (br), -20.59 (br), -22.85 (br). μ_{eff} (toluene- d_8) = 5.2 μ_{B} . FTIR (ATR, cm^{-1}): 1569 (s, C=N).

1.3.3.2.3 Synthesis of $[\text{Co}\{\kappa^2\text{N},\text{N}'\text{-5-(C}_6\text{H}_5\text{)-NC}_4\text{H}_2\text{-2-C(H)=N(tBu-C}_6\text{H}_4\text{)}\}_2]$ (1.4f)



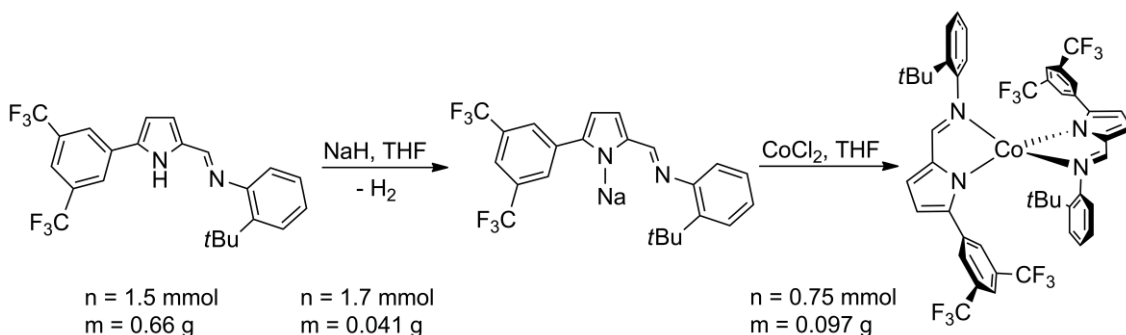
The general procedure described above was applied. All volatiles were evaporated under reduced pressure, and the green residue was extracted with diethyl ether until extracts were colorless. The solution was concentrated and stored at $-20 \text{ }^\circ\text{C}$, from which dichroic green/red crystals of **1.4f** suitable for X-ray diffraction were obtained.

Yield: 0.68 g (67%).

Anal. Calc. for $\text{C}_{42}\text{H}_{42}\text{CoN}_4$, obtained (calculated): C 75.93 (76.23), H 6.18 (6.40), N 8.46 (8.47).

$^1\text{H NMR}$ (300 MHz, C_6D_6): δ 118.28 (br), 42.65 (br), 9.24 (br), 6.54 (br), 5.14 (br), 1.52 (br), 0.06 (br), -3.46 (br), -15.74 (br), -25.88 (br), -44.51 (br), -84.49 (br). $\mu_{\text{eff}}(\text{toluene-}d_8) = 4.9 \mu_{\text{B}}$. FTIR (ATR, cm^{-1}): 1553 (s, C=N).

1.3.3.2.4 Synthesis of $[\text{Co}\{\kappa^2\text{N},\text{N}'\text{-5-(3,5-(CF}_3\text{)}_2\text{-C}_6\text{H}_3\text{)-NC}_4\text{H}_2\text{-2-C(H)=N(tBu-C}_6\text{H}_4\text{)}\}_2]$ (1.4g)



Chapter 1

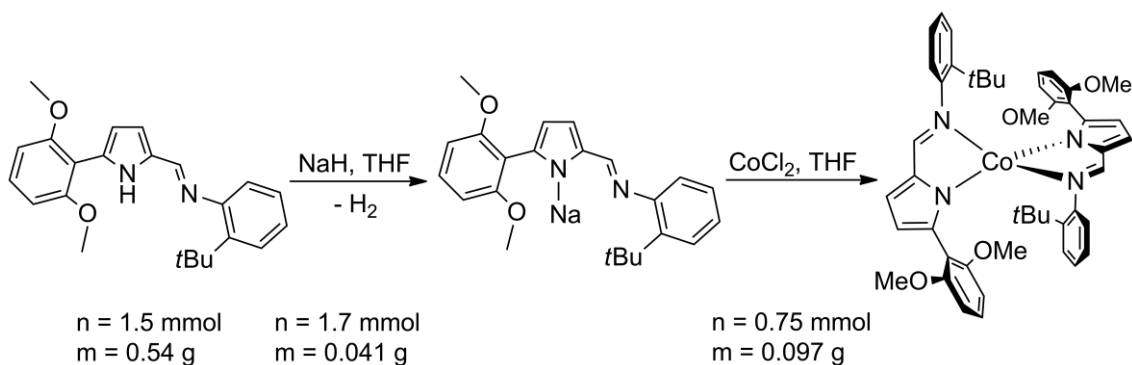
The general procedure described above was applied. All volatiles were evaporated under reduced pressure, and the green residue was extracted with *n*-hexane until extracts were colorless. The solution was concentrated and stored at -20 °C, from which dichroic green/red crystals of **1.4g** suitable for X-ray diffraction were obtained.

Yield: 0.91 g (65%).

Anal. Calc. for C₄₆H₃₈CoF₁₂N₄, obtained (calculated): C 59.45 (59.17), H 4.24 (4.10), N 5.92 (6.00).

¹H NMR (300 MHz, C₆D₆): δ 113.76 (br), 43.55 (br), 8.49 (br), 1.49 (br), 0.21 (br), -1.21 (br), -4.53 (br), -12.56 (br), -23.96 (br), -50.96 (br), -83.68 (br). $\mu_{eff}(\text{toluene-}d_8) = 4.8 \mu_B$.
FTIR (ATR, cm⁻¹): 1549 (s, C=N).

1.3.3.2.5 Synthesis of [Co{ $\kappa^2 N, N'$ -5-(2,6-(OCH₃)₂-C₆H₃)-NC₄H₂-2-C(H)=N(*t*Bu-C₆H₄))₂] (**1.4h**)



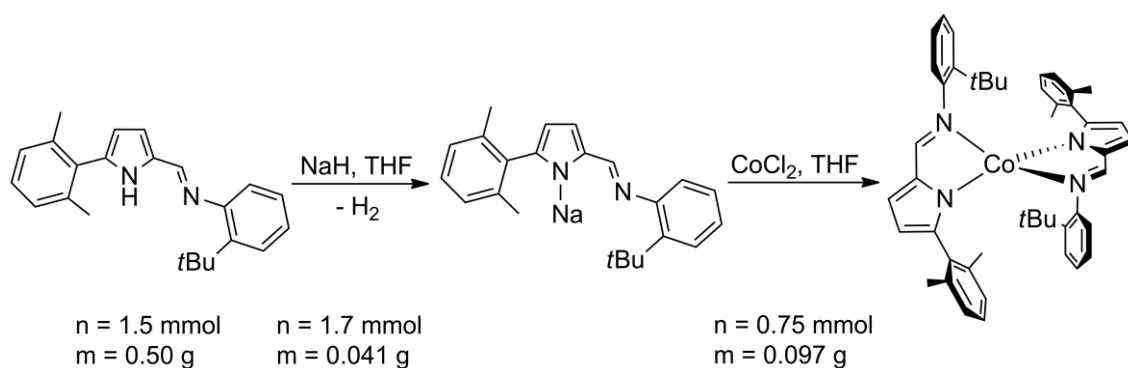
The general procedure described above was applied. All volatiles were evaporated under reduced pressure, and the brown/deep red residue was extracted with *n*-hexane until extracts were colorless. The solution was concentrated and stored at -20 °C, from which red crystals of **1.4h** suitable for X-ray diffraction were obtained.

Yield: 0.84 g (72%).

Anal. Calc. for C₄₆H₅₀CoO₄N₄, obtained (calculated): C 70.8 (70.67) H 6.44 (6.45), N 7.12 (7.17).

^1H NMR (300 MHz, C_6D_6): δ 117.80 (br), 62.05 (br), 3.36 (br), 2.09(br) 1.58 (br), -0.75 (br), -1.45 (br), -8.04 (br), -13.00 (br), -17.66 (br), -30.56 (br). $\mu_{\text{eff}}(\text{toluene-}d_8) = 5.0 \mu_{\text{B}}$. FTIR (ATR, cm^{-1}): 1560 (s, C=N).

1.3.3.2.6 Synthesis of $[\text{Co}\{\kappa^2\text{N}_2\text{N}'\text{-5-(2,6-(CH}_3)_2\text{-C}_6\text{H}_3)\text{-NC}_4\text{H}_2\text{-2-C(H)=N(tBu-C}_6\text{H}_4)\}_2]$ (**1.4i**)



The general procedure described above was applied. All volatiles were evaporated under reduced pressure, and the red residue was extracted with *n*-hexane until extracts were colorless. The solution was concentrated and stored at $-20 \text{ }^\circ\text{C}$, from which purple crystals of **1.4i** suitable for X-ray diffraction were obtained.

Yield: 0.81 g (75%).

Anal. Calc. for $\text{C}_{46}\text{H}_{50}\text{CoN}_4$, obtained (calculated): C 77.21 (76.96) H 7.43 (7.02), N 7.87 (7.80).

^1H NMR (300 MHz, C_6D_6): δ 118.58 (br), 43.57 (br), 3.37 (br), 2.08 (br), 1.49 (br), 0.01 (br), -0.89 (br), -8.22 (br), -9.78 (br), -10.97 (br), -35.28 (br), -75.32 (br). $\mu_{\text{eff}}(\text{toluene-}d_8) = 5.3 \mu_{\text{B}}$. FTIR (ATR, cm^{-1}): 1553 (s, C=N).

1.4 REFERENCES

- 1 Fondo, M.; Escuer, A.; Herrera, J. M. *Front. Chem.* **2019**, *7*, 229.
- 2 Aubin, S. M. J.; Wemple, M. W.; Adams, D. M.; Tsai, H.; Christou, G.; Hendrickson, D. N. *J. Am. Chem. Soc.* **1996**, *118*, 7746.
- 3 Gatteschi, D.; Sessoli, R.; Villain, J. *Molecular Nanomagnets*, Oxford University Press, **2006**.
- 4 Ghimire, N. *Introduction to Single Molecular Magnet*, Solid State Physics II, Department of Physics and Astronomy, University of Tennessee at Knoxville, Spring **2010**.
http://sces.phys.utk.edu/~dagotto/condensed/HW1_2010/NirmalGhimire_SingleMolecularMagnet.pdf (last accessed in 04/07/2022).
- 5 Christou, G.; Hendrickson, D. N. *Inorg. Chem.* **2001**, *40*, 2127.
- 6 Neese, F.; Pantazis, D. A. *Faraday Discuss.* **2011**, *148*, 229.
- 7 Craig, G. A.; Murrie, M. *Chem. Soc. Rev.* **2015**, *44*, 2135.
- 8 Feltham, H. L. C.; Brooker, S. *Coord. Chem. Rev.* **2014**, *276*, 1.
- 9 Christou, G.; Gatteschi, D.; Hendrickson, D.; Sessoli, R. *MRS Bull.*, **2000**, *25*, 66.
- 10 Frost, J. M.; Harriman, K. L. M.; Murugesu, M. *Chem. Sci.* **2016**, 2470.
- 11 Harris, I. R.; Williams, A. J. *Magnetic Materials*. In: Rawlings, R.D. (Ed.), *Material Science and Engineering*, Vol. II, EOLSS, Oxford, UK, **2000**; p. 49.
- 12 Pascal, P. *Ann. Chim. Phys.* **1913**, *28*, 218.
- 13 Bain, G. A.; Berry, J. F. *J. Chem. Educ.* **2008**, *85*, 532.
- 14 Landee, C. P.; Turnbull, M. M. *J. Coord. Chem.* **2014**, *67*, 375.
- 15 Benelli, C.; Gatteschi, D. *Introduction to Molecular Magnetism: from transition metals to lanthanides*, Wiley - VCH, Weinheim, **2015**.
- 16 MagLab 2000 Manual, Oxford Instruments Ltd, Oxford, UK, **1997**.
- 17 S700X SQUID Magnetometer Manual, Cryogenic Limited.
- 18 Martien, D., *Introduction to AC Susceptibility*, Quantum Design, **2010**.
http://www.lao.cz/data/ke-stazeni/AC_Susceptibility_eu_1_.pdf (last accessed in 04/07/2022).
- 19 Gatteschi, D.; Sessoli, R.; Cornia, A. *Chem. Commun.* **2000**, 725.
- 20 Layfield, R. A. *Organometallics*, **2014**, *33*, 1084.
- 21 Woodruff, D. N.; Winpenny, R. E. P.; Layfield, R. A. *Chem. Rev.* **2013**, *113*, 5110.
- 22 Youssif, M. I.; Baghta, A. A.; Ali, I. A. *Egypt. J. Sol* **2000**, *23*, 231.

- 23 Balanda, M. *Acta Phys. Pol. A*, **2013**, *124*, 964.
- 24 Brechin, E. K.; Soler, M.; Davidson, J.; Hendrickson, D. N.; Parsons, S.; Christou, G. *Chem. Commun.*, **2002**, 2252.
- 25 Boskovic, C.; Brechin, E. K.; Streib, W. E.; Folting, K.; Bollinger, J. C.; Hendrickson, D. N.; Christou, G. *J. Am. Chem. Soc.* **2002**, *124*, 3725.
- 26 Buchholz, A.; Eseola, A. O.; Plass, W. *C. R. Chim.* **2012**, *15*, 929.
- 27 Ho, L. T. A.; Chibotaru, L. F. *Phys. Rev. B* **2016**, *94*, 104422.
- 28 Domingo, N.; Luis, F.; Nakano, M.; Muntó, M.; Gómez, J.; Chaboy, J.; Ventosa, N.; Campo, J.; Veciana, J.; Ruiz-Molina, D. *Phys. Rev. B* **2009**, *79*, 214404.
- 29 Guo, Y.-N.; Xu, G.-F.; Gamez, P.; Zhao, L.; Lin, S.-Y.; Deng, R.; Tang, J.; Zhang, H.-J. *J. Am. Chem. Soc.* **2010**, *132*, 8538.
- 30 Tang, J.; Zhang, P. *Lanthanide Single Molecule Magnets*, Springer, Berlin, **2015**.
- 31 Spree, L.; Popov, A. A. *Dalton Trans.* **2019**, *48*, 2861.
- 32 Liddle, S. T.; van Slageren, J. *Chem. Soc. Rev.* **2015**, *44*, 6655.
- 33 McAdams, S. G.; Ariciu, A.; Kostopoulos, A. K.; Walsh, J. P. S.; Tuna, F. *Coord. Chem. Rev.* **2017**, *346*, 216.
- 34 Carlin, R. L. *Magnetochemistry*, Springer, Berlin, **1986**.
- 35 Hübner, W.; Bennemann, K. H. *Phys. Rev.* **1996**, *53*, 3422.
- 36 Wang, L.; Qiu, J.; Chen, Y.; Liu, J.; Li, Q.; Jia, J.; Tong, M. *Inorg. Chem. Front.* **2017**, *4*, 1311.
- 37 (a) Lis, T. *Acta Cryst. B* **1980**, *36*, 2042; (b) Caneschi, A.; Gatteschi, D.; Sessoli, R. *J. Am. Chem. Soc.* **1991**, *113*, 5873; (c) Sessoli, R.; Gatteschi, D.; Caneschi, A.; Novak, M. A. *Nature*, **1993**, *365*, 141; (d) Thomas, L.; Lioni, F.; Ballou, R.; Gatteschi, D.; Sessoli, R.; Barbara, B. *Nature*, **1996**, *383*, 145; (e) Rinehart, J. D. *Magnetic Exchange Coupling and Single-Molecule Magnetism in Uranium Complexes*, Berkeley: University of California, PhD Thesis, **2010**; (f) Milios, C. J.; Winpenny, R. E. P. *Cluster-Based Single-Molecule Magnets*, Springer, Berlin, **2014**. (g) Barra, A. L.; Gatteschi, D.; Sessoli, R. *Phys. Rev.* **1997**, *56*, 8192. (h) Ako, A. M.; Hewitt, I. J.; Mereacre, V.; Clérac, R.; Wernsdorfer, W.; Anson, C. E.; Powell, A. K. *Angew. Chem. Int. Ed.* **2006**, *45*, 4926.
- 38 Bagai, R.; Christou, G. *Chem. Soc. Rev.* **2009**, *38*, 1011.
- 39 Sessoli, R.; Tsai, H. L.; Schake, A. R.; Wang, S.; Vincent, J. B.; Folting, K.; Gatteschi, D.; Christou, G.; Hendrickson, D. N. *J. Am. Chem. Soc.* **1993**, *115*, 1804.

Chapter 1

- 40 Inglis, R.; Milios, C. J.; Jones, L. F.; Piligkos, S.; Brechin, E. K. *Chem. Comm.* **2011**, 47, 181.
- 41 (a) Wieghardt, K.; Pohl, K.; Jibril, I.; Huttner, G. *Angew. Chem. Int. Ed. Engl.* **1984**, 23, 77; (b) Barra, A. L.; Debrunner, P.; Gatteschi, D.; Schulz, C. E.; Sessoli, R. *Europhys. Lett.* **1996**, 35, 133; (c) Vincent, B.; Christmas, C.; Chang, H.-R.; Li, Q.; Boyd, P. D. W. J.; Huffman, C.; Hendrickson, D. N.; Christou, G. *J. Am. Chem. Soc.* **1989**, 111, 2086; (d) Delfs, D.; Gatteschi, L.; Pardi, R.; Sessoli, K.; Wieghardt, D. *Inorg. Chem.* **1993**, 32, 3099; (e) Gatteschi, D.; Sessoli, R.; Cornia, A. *Chem. Commun.* **2000**, 725; (f) Barra, A. L.; Gatteschi, D.; Sessoli, R. *Chem. Eur. J.* **2000**, 6, 1608; (g) Gatteschi, D.; Sessoli, R. *Angew. Chem. Int. Ed.* **2003**, 42, 268.
- 42 Ako, A. M.; Hewitt, I. J.; Mereacre, V.; Clerac, R.; Wernsdorfer, W.; Anson, C. E.; Powell, A. K. *Angew. Chem., Int. Ed.* **2006**, 45, 4926.
- 43 Milios, C. J.; Vinslava, A.; Wernsdorfer, W.; Moggach, S.; Parsons, S.; Perlepes, S. P.; Christou, G.; Brechin, E. K. *J. Am. Chem. Soc.* **2007**, 129, 2754.
- 44 Vaidya, S.; Upadhyay, A.; Singh, S. K.; Gupta, T.; Tewary, S.; Langley, S.K.; Walsh, J.P.S.; Murray, K.S.; Rajaraman, G.; Shanmugam, M. *Chem Commun.* **2015**, 51, 3739.
- 45 Zadrozny J. M.; Telser, J.; Long, J. R. *Polyhedron*, **2013**, 64, 209.
- 46 Saber, M. R.; Dunbar, K. R. *Chem Commun.* **2014**, 50, 12266.
- 47 Vaidya, S.; Singh, S. K.; Shukla, P.; Ansari, K.; Rajaraman, G.; Shanmugam, M. *Chem Eur J.* **2017**, 23, 9546.
- 48 Harman, W. H.; Harris, T. D.; Freedman, D. E.; Fong, H.; Chang, A.; Rinehart, J. D.; Ozarowski, A.; Sougrati, M. T.; Grandjean, F.; Long, G. J.; Long, J. R.; Chang, C. J. *J. Am. Chem. Soc.* **2010**, 132, 18115.
- 49 Freedman, D. E.; Harman, W. H.; Harris, D.; Long, G. J.; Chang, C. J.; Long, J. R. *J. Am. Chem. Soc.* **2010**, 132, 1224.
- 50 Chandrasekhar, V.; Pointillart, F. (Eds.) *Organometallic Magnets*, Springer, Berlin, **2019**.
- 51 Cremades, E.; Ruiz, E. *Inorg. Chem.* **2011**, 50, 4016.
- 52 Holah, D. G.; Coucouvanis, D. *J. Am. Chem. Soc.* **1975**, 97, 6917.
- 53 Fukui, K.; Kojima, N.; Ohya-Nishiguchi, H.; Hirota, N. *Inorg. Chem.* **1992**, 31, 1338.
- 54 Zadrozny, J. M.; Long, J. R. *J. Am. Chem. Soc.* **2011**, 133, 20732.

- 55 Suturina, E. A.; Maganas, D.; Bill, E.; Atanasov, M.; Neese, F. *Inorg. Chem.* **2015**, *54*, 9948.
- 56 Fataftah, M. S.; Zadrozny, J. M.; Rogers, D. M.; Freedman, D. E. *Inorg. Chem.* **2014**, *53*, 10716.
- 57 Vaidya, S.; Tewary, S.; Singh, S. K.; Langley, S. K.; Murray, K. S.; Lan, Y.; Wernsdorfer, W.; Rajaraman, G.; Shanmugam, M. *Inorg. Chem.* **2016**, *55*, 9564.
- 58 Tu, D.; Shao, D.; Yan, H.; Lu, C. *Chem. Commun.* **2016**, *52*, 14326.
- 59 Yang, F.; Zhou, Q.; Zhang, Y.; Zeng, G.; Li, G.; Shi, Z.; Wang, B.; Feng, S. *Chem. Commun.* **2013**, *49*, 5289.
- 60 Boča, R.; Miklovič, J.; Titiš, J. *Inorg. Chem.* **2014**, *53*, 2367.
- 61 Zhai, Y.; Deng, Y.; Zheng, Y. *Dalton Trans.* **2018**, *47*, 8874.
- 62 Mondal, A. K.; Sundararajan, M.; Konar, S. *Dalton Trans.* **2018**, *47*, 3745.
- 63 Hrubý, J.; Dvořák, D.; Squillantini, L.; Mannini, M.; van Slageren, J.; Herchel, R.; Nemeč, I.; Neugebauer, P. *Dalton Trans.* **2020**, *49*, 11697.
- 64 Sottini, S.; Poneti, G.; Ciattini, S.; Levesanos, N.; Ferentinos, E.; Krzystek, J.; Sorace, L.; Kyritsis, P. *Inorg. Chem.* **2016**, *55*, 9537.
- 65 Cao, D.; Feng, J.; Ren, M.; Gu, Y.; Song, Y.; Ward, M. D. *Chem. Commun.* **2013**, *49*, 8863.
- 66 Cao, D.; Wei, R.; Li, X.; Gu, Y. *Dalton Trans.* **2015**, *44*, 5755.
- 67 Ziegenbalg, S.; Hornig, D.; Görls, H.; Plass, W. *Inorg. Chem.* **2016**, *55*, 4047.
- 68 Böhme, M.; Ziegenbalg, S.; Aliabadi, A.; Schnegg, A.; Görls, H.; Plass, W. *Dalton Trans.* **2018**, *47*, 10861.
- 69 Huang, W.; Liu, T.; Wu, D.; Cheng, J.; Ouyang, Z. W.; Duan, C. *Dalton Trans.* **2013**, *42*, 15326.
- 70 Smolko, L.; Černák, J.; Dušek, M.; Miklovič, J.; Titiš, J.; Boča, R. *Dalton Trans.* **2015**, *44*, 17565.
- 71 Nemeč, I.; Herchel, R.; Trávníček, Z. *Scientific Reports*, **2015**, *5*, 10761.
- 72 Nemeč, I.; Herchel, R.; Kern, M.; Neugebauer, P.; van Slageren, J.; Trávníček, Z. *Materials*, **2017**, *10*, 249.
- 73 Zadrozny, J. M.; Liu, J.; Piro, N. A.; Chang, C. J.; Hill, S.; Long, J. R. *Chem. Commun.* **2012**, *48*, 3927.
- 74 Carl, E.; Demeshko, S.; Meyer, F.; Stalke, D. *Chem. Eur. J.* **2015**, *21*, 10109.
- 75 Rechkemmer, Y.; Breitgoff, F. D.; van der Meer, M.; Atanasov, M.; Hakl, M.; Orlita, M.; Neugebauer, P.; Neese, F.; Sarkar, B.; van Slageren, J. *Nat. Commun.*

Chapter 1

- 2016, 7, 10467.
- 76 Cui, H.; Lu, F.; Chen, X.; Zhang, Y.; Tong, W.; Xue, Z. *Inorg. Chem.* **2019**, 58, 12555.
- 77 Vallejo, J.; Pardo, E.; Viciano-Chumillas, M.; Castro, I.; Amorós, P.; Déniz, M.; Ruiz-Pérez, C.; Yuste-Vivas, C.; Krzystek, J.; Julve, M.; Lloret, F.; Cano, J. *Chem. Sci.* **2017**, 8, 3694.
- 78 Holm, R. H.; Chakravorty, A.; Theriot, L. J. *Inorg. Chem.* **1966**, 5, 625.
- 79 (a) Gibson, V. C.; Maddox, P. J.; Newton, C.; Redshaw, C.; Solan, G. A.; White, A. J. P.; Williams, D. J. *Chem. Commun.* **1998**, 1651; (b) Gibson, V. C.; Newton, C.; Redshaw, C.; Solan, G. A.; White, A. J. P.; Williams, D. J. *J. Chem. Soc. Dalton Trans.* **2002**, 4017.
- 80 Dawson, D. M.; Walker, D. A.; Thornton-Pett, M.; Bochman, M. *Dalton Trans.* **2000**, 459.
- 81 Matsuo, Y.; Mashima, K.; Tani, K. *Chem. Lett.* **2000**, 29, 1114.
- 82 Matsui, S.; Yoshida, Y.; Takagi, Y.; Spaniol, T. P.; Okuda, J. *J. Organomet. Chem.* **2004**, 689, 1155.
- 83 (a) Yoshida, Y.; Matsui, S.; Takagi, Y.; Mitani, M.; Nitabaru, M.; Nakano, T.; Tanaka, H.; Fujita, T. *Chem. Lett.* **2000**, 29, 1270; (b) Yoshida, Y.; Matsui, S.; Takagi, Y.; Mitani, M.; Nakano, T.; Tanaka, H.; Kashiwa, N.; Fujita, T., *Organometallics*, **2001**, 20, 4793.
- 84 Lin, M.; Cao, Y.; Pei, H.; Chen, Y.; Wu, J.; Li, W.; Liu, W. *RSC Adv.* **2014**, 4, 9255.
- 85 Upitak, K.; Wattanathana, W.; Nanok, T.; Chuawong, P.; Hormnirun, P. *Dalton Trans.* **2021**, 50, 10964.
- 86 Tsurugi, H.; Matsuo, Y.; Mashima, K. *J. Mol. Cat. A: Chem.* **2006**, 254, 131.
- 87 Mu, J.-S.; Wang, Y.-X.; Li, B.-X.; Li, Y.-S. *Dalton Trans.* **2011**, 40, 3490.
- 88 (a) Heinze, K.; Marano, G.; Fischer, A. *J. Inorg. Biochem.* **2008**, 102, 1199; (b) Hüttinger, K.; Förster, C.; Bund, T.; Hinderberger, D.; Heinze, K. *Inorg. Chem.* **2012**, 51, 4180.
- 89 Mayr, A.; McDermott, G. A.; Dorries, A. M.; Van Engen, D. *Organometallics*. **1987**, 6, 1503.
- 90 Li, J.; Song, H.; Cui, C. *Appl. Organometal. Chem.* **2010**, 24, 82.
- 91 Carabineiro, S. A.; Silva, L. C.; Gomes, P. T.; Pereira, L. C. J.; Veiros, L. F.; Pasco, S. I.; Duarte, M. T.; Namorado, S.; Henriques, R. T. *Inorg. Chem.* **2007**, 46, 6880.

- 92 Gomes, C. S. B.; Duarte, M. T.; Gomes, P. T. *J. Organomet. Chem.*, **2014**, *767*, 167.
- 93 Carabineiro, S. A.; Bellabarba, R. M.; Gomes, P. T.; Pascu, S. I.; Veiros, L. F.; Freire, C.; Pereira, L. C. J.; Henriques, R. T.; Oliveira, M. C.; Warren, J. E. *Inorg. Chem.* **2008**, *47*, 8896.
- 94 Cruz, T. F. C.; Figueira, C. A.; Waerenborgh, J. C.; Pereira, L. C. J.; Li, Y.; Lescouëzec, R.; Gomes, P. T. *Polyhedron*, **2018**, *143*, 179.
- 95 Pérez-Puente, P.; de Jesús, E.; Flores, J. C.; Gómez-Sal, P. *J. Organomet. Chem.* **2008**, *693*, 3902.
- 96 (a) Wansapura, C. M.; Juyoung, C.; Simpson, J. L.; Szymanski, D.; Eaton, G. R.; Eaton, S. S.; Fox, S. *J. Coord. Chem.* **2003**, *56*, 975; (b) Grushin, V. V.; Marshall, W. *J. Adv. Synth. Catal.* **2004**, *346*, 1457; (c) Castro, J. A.; Romero, J.; Garcia-Vazquez, J. A.; Castiñeiras, A.; Duran, M. L.; Sousa, A. *Z. Anorg. Allg. Chem.* **1992**, *618*, 155.
- 97 Gomes, C. S. B.; Gomes, P. T.; Duarte, M. T.; Di Paolo, R. E.; Maçanita, A. L.; Calhorda, M. *J. Inorg. Chem.* **2009**, *48*, 11176.
- 98 Gomes, C. S. B.; Carabineiro, S. A.; Gomes, P. T.; Duarte, M. T.; Lemos, M. A. N. D. A. *Inorg. Chim. Acta*, **2011**, *369*, 151.
- 99 Panda, T. K.; Yamamoto, K.; Yamamoto, K.; Kaneko, H.; Yang, Y.; Tsurugi, H.; Mashima, K. *Organometallics*, **2012**, *31*, 2268.
- 100 Kottalanka, R. K.; Harinath, A.; Reja, S.; Panda, T. K. *Dalton Trans.* **2015**, *44*, 19865.
- 101 Cui, C.; Shafir, A.; Reeder, C. L.; Arnold, J. *Organometallics*, **2003**, *22*, 3357.
- 102 Yang, Y.; Liu, B.; Lv, K.; Gao, W.; Cui, D.; Chen, X.; Jing, X. *Organometallics*, **2007**, *26*, 4575.
- 103 Kaneko, H.; Dietrich, H. M.; Schädle, C.; Maichle-Mössmer, C.; Tsurugi, H.; Törnroos, K. W.; Mashima, K.; Anwender, R. *Organometallics*, **2013**, *32*, 1199.
- 104 Brooker, S.; Kitchen, J. A. *Dalton Trans.* **2009**, 7331.
- 105 Rieth, R. D.; Mankad, N. P.; Calimano, E.; Sadighi, J. P. *Org. Lett.* **2004**, *6*, 3981.
- 106 (a) Bailey, D. M.; Johnson, R. E.; Albertson, N. F. *Org. Synth.* **1971**, *51*, 100; (b) Harman, W. H.; Harris, T. D.; Freedman, D. E.; Fong, H.; Chang, A.; Rinehart, J. D.; Ozarowski, A.; Sougrati, M. T.; Grandjean, F.; Long, G. J.; Long, J. R.; Chang, C. J. *J. Am. Chem. Soc.* **2010**, *132*, 18115; (c) King, E. R.; Hennessy, E. T.; Betley, T. A. *J. Am. Chem. Soc.* **2011**, *133*, 4917.

Chapter 1

- 107 Garrido, D. O.; Buldain, G.; Frydman, B. *J. Org. Chem.* **1984**, *49*, 2619.
- 108 a) Bellabarba, R. M.; Gomes, P. T.; Pascu, S. I. *Dalton Trans.* **2003**, 4431; b) Gomes, C. S. B.; Suresh, D.; Gomes, P. T.; Veiros, L. F.; Duarte, M. T.; Nunes, T. G.; Oliveira, M. C. *Dalton Trans.* **2010**, *39*, 736; c) Suresh, D.; Gomes, C. S. B.; Gomes, P. T.; Di Paolo, R. E.; Maçanita, A. L.; Calhorda, M. J.; Charas, A.; Morgado, J.; Duarte, M. T. *Dalton Trans.* **2012**, *41*, 8502; d) Calhorda, M. J.; Suresh, D.; Gomes, P. T.; Di Paolo, R. E.; Maçanita, A. L. *Dalton Trans.* **2012**, *41*, 13210; e) Suresh, D.; Lopes, P. S.; Ferreira, B.; Figueira, C. A.; Gomes, C. S. B.; Gomes, P. T.; Di Paolo, R. E.; Maçanita, A. L.; Duarte, M. T.; Charas, A.; Morgado, J.; Calhorda, M. J. *Chem. Eur. J.* **2014**, *20*, 1; f) Gomes, C. S. B.; Duarte, M. T.; Gomes, P. T. *J. Organomet. Chem.* **2014**, *760*, 167; g) Suresh, D.; Gomes, C. S. B.; Lopes, P. S.; Figueira, C. A.; Ferreira, B.; Gomes, P. T.; Di Paolo, R. E.; Maçanita, A. L.; Duarte, M. T.; Charas, A.; Morgado, J.; Vila-Viçosa, D.; Calhorda, M. J. *Chem. Eur. J.* **2015**, *21*, 1.
- 109 a) Evans, D. F. *J. Chem. Soc.* **1959**, 2003; b) Kur, S. K. *J. Magn. Reson.* **1989**, *82*, 169.
- 110 a) Cotton, F. A.; Wilkinson, G.; Murillo, C. A.; Bochmann, M. *Advanced Inorganic Chemistry*; 6th ed., Wiley, 1999, p. 821; b) Greenwood, N.; Earnshaw, N. A. *Chemistry of the Elements*, 2nd ed., Elsevier Butterworth-Heinemann, 1997, p. 1132.
- 111 Yang, L.; Powell, D. R.; Houser, R. P. *Dalton Trans.* **2007**, 955.
- 112 Janiak, C. *Dalton Trans.* **2000**, 3885.
- 113 Pardi, L.; Krzystek, J.; Telsler, J.; Brunel, L. *J. Magnetic Resonance*, **2000**, *146*, 375.
- 114 Sarkar, A.; Dey, S.; Rajaraman, G. *Chem. Eur. J.* **2020**, *26*, 14036.
- 115 Sarkar, A.; Tewary, S.; Sinkar, S.; Rajaraman, G. *Chem. Asian J.*, **2019**, *14*, 4696.
- 116 Abragam, A.; Bleaney, B. *Electron Paramagnetic Resonance of Transition Ions*, Dover Publications, **1986**.
- 117 Figueira, C. A.; Lopes, P. S.; Gomes, C. S. B.; Veiros, L. F.; Gomes, P. T. *CrystEngComm.* **2015**, *17*, 6406.
- 118 Cruz, T. F. C.; Lopes, P. S.; Pereira, L. C. J.; Veiros, L. F.; Gomes, P. T. *Inorg. Chem.* **2018**, *57*, 8146.
- 119 (a) Evans, D. F. *J. Chem. Soc.* **1959**, 2003; (b) Kur, S. K. *J. Magn. Reson.* **1989**, *82*, 169.

- 120 *SAINTE Software for the CCD Detector System*, Version 7.03, Bruker AXS Inc., Madison, WI, USA, **2004**.
- 121 Sheldrick, G. M. *SADABS, Program for Empirical Absorption Correction*, Univ. of Göttingen, German, **1996**.
- 122 Burla, M. C.; Caliandro, R.; Carrozzini, B.; Cascarano, G. L.; Cuocci, C.; Giacovazzo, C.; Mallamo, M.; Mazzone, A.; Polidori, G. *J. Appl. Cryst.* **2015**, *48*, 306.
- 123 (a) Sheldrick, G. M. *Acta Crystallogr.* **2015**, *71*, 3; (b) Hübschle, C. B.; Sheldrick, G. M.; Dittrich, B. *J. Appl. Crystallogr.* **2011**, *44*, 1281.
- 124 (a) Farrugia, L. J. *J. Appl. Crystallogr.* **1999**, *32*, 837; (b) Farrugia, L. J. *J. Appl. Crystallogr.* **2012**, *45*, 849.
- 125 (a) Burnett, M. N.; Johnson, C. K. *ORTEP-III: Oak Ridge Thermal Ellipsoid Plot Program for Crystal Structure Illustration*, Oak Ridge National Laboratory, **1996**, 6895; (b) Farrugia, L. J. *J. Appl. Crystallogr.* **1997**, *30*, 565.
- 126 Neugebauer, P.; Bloos, P.; Marx, R.; Lutz, P.; Kern, M.; Aguilà, D.; Vaverka, J.; Laguta, O.; Dietrich, C.; Clérac, R.; van Slageren, J. *Phys. Chem. Chem. Phys.* **2018**, *20*, 15528.
- 127 Neese, F. *Comput. Mol. Sci.* **2017**, *8*, e1327.
- 128 Angeli, C.; Cimiraglia, R.; Evangelisti, S.; Leininger, T.; Malrieu, J.-P. *J. Chem. Phys.* **2001**, *114*, 10252.
- 129 Angeli, C.; Cimiraglia, R.; Malrieu, J.-P. *Chem. Phys. Lett.* **2001**, *350*, 297.
- 130 Vahtras, O.; Almlöf, J.; Feyereisen, M. W. *Chem. Phys. Lett.* **1993**, *213*, 514.
- 131 Roos, B. O. *The Complete Active Space Self-Consistent Field Method and its Applications in Electronic Structure Calculations*. In: K. P. Lawley (Ed.), *Advances in Chemical Physics*, John Wiley & Sons, Inc., **1987**, pp. 399–445.
- 132 Angeli, C.; Borini, S.; Cestari, M.; Cimiraglia, R. *J. Chem. Phys.* **2004**, *121*, 4043.
- 133 Nakano, H. *J. Chem. Phys.* **1993**, *99*, 7983.
- 134 Kossmann, S.; Neese, F. *Chem. Phys. Lett.* **2009**, *481*, 240.
- 135 Neese, F.; Wennmohs, F.; Hansen, A.; Becker, U. *Chem. Phys.* **2009**, *356*, 98.
- 136 Hess, B. A. *Phys. Rev. A* **1986**, *33*, 3742.
- 137 Jansen, G.; Hess, B. A.; *Phys. Rev. A* **1989**, *39*, 6016.
- 138 Douglas, N.; Kroll, N. M. *Ann. Phys.* **1974**, *82*, 89.
- 139 Hellweg, A.; Hättig, C.; Höfener, S.; Klopper, W. *Theor. Chem. Acc.* **2007**, *117*, 587.

Chapter 1

- 140 Weigend, F. *Phys. Chem. Chem. Phys.* **2006**, *8*, 1057.
- 141 Heß, B. A.; Marian, C. M.; Wahlgren, U.; Gropen, O. *Chem. Phys. Lett.* **1996**, *251*, 365.
- 142 Neese, F. *J. Chem. Phys.* **2005**, *122*, 034107.
- 143 Vallet, V.; Maron, L.; Teichteil, C.; Flament, J. P. *J. Chem. Phys.* **2000**, *113*, 1391.

CHAPTER 2

Pentamethylcyclopentadienyl nickel(II) complexes stabilized by
N-heterocyclic carbenes (NHCs) as spin equilibrium molecules

The following work resulted from this chapter: Ferreira, P. S.; Cruz, T. F. C.; Almeida, M.; Pereira, L. C. J.; Gomes, P. T. **2022**, manuscript in preparation.

2.1 INTRODUCTION

2.1.1 Cyclopentadienyl ligand

Cyclopentadiene (Figure 2.1a) is an organic molecule with the formula C_5H_6 , which can be readily deprotonated by strong bases such as alkali metal hydrides or amides to produce the cyclopentadienyl anion ($C_5H_5^-$), abbreviated as Cp (Figure 2.1b).

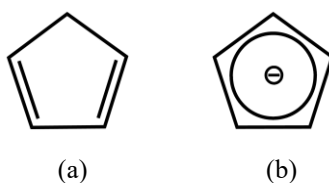


Figure 2.1 (a) Cyclopentadiene and (b) cyclopentadienyl anion.

The Cp anion has been one of the most versatile and widely used ligands in organometallic chemistry. Due to its aromaticity and high stability, it plays an active role in stabilizing organometallic complexes. In 1951, Kealy and Pauson¹ successfully synthesized and isolated the compound dicyclopentadienyl iron or, as it is commonly known, ferrocene. This was a huge breakthrough in the field of organometallic chemistry, since all previous and numerous works done regarding the reaction of Grignard reagents with anhydrous ferric chloride to form any organo-iron compounds had been unsuccessful. Since then numerous complexes have been synthesized, including Ni-Cp compounds stabilized by ligands of different nature, which is the subject of this chapter. These compounds have attracted attention of spectroscopists and theoreticians owing to their practical applications as synthetic and catalytic precursors.

2.1.1.1 Coordination to metals

Cp are monoanionic ligands that can have different forms of coordination to metals (Figure 2.2).²

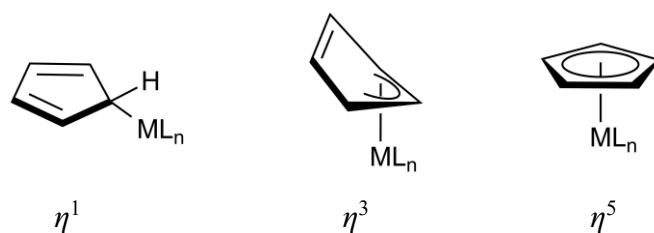


Figure 2.2 Different Cp binding modes to metals.

These ligands almost invariably bind to metals as a pentahapto (η^5), in which the interaction between the metal and the cyclopentadienyl is typically drawn as a single line from the metal center to the center of the Cp ring. In this case the M–Cp bonding arises from the overlap of the five π molecular orbitals of the Cp ligand with the s , p , and d orbitals on the metal, being referred to as π -complexes. In rare cases, Cp can bind to metals via only one carbon center (*i.e.* monohapto, η^1) and via three carbons (*i.e.* trihapto, η^3). These three cases are the ones with the greatest interest because they all are involved in ring slippage processes.²

Thus, depending on the needs of the resulting complexes, this ligand can change the number of electrons donated through a haptotropic modification since in η^5 , η^1 and η^3 bonds the Cp ligand donates 5, 1 and 3 electrons, respectively. This process is called ring slippage and in some of the cases it is promoted by the addition of donor ligands, in order to accommodate them in the coordination sphere of the metal (Figure 2.3). Perutz and co-workers³ reported the monohapto nature of $[(\eta^5\text{-Cp})(\eta^1\text{-Cp})\text{Re}(\text{CO})_2\text{H}]$ obtained from a ring slippage reaction in which the η^5 coordination mode is transformed into a η^3 and then η^1 ligand coordinated to ruthenium. Therefore, in this case, the hapticity of the Cp ligand in the ruthenium complex changes, allowing the coordination of one or two CO molecules, but maintaining an electron-count of 18 valence electrons. When the Cp coordinates in the trihapto form, the carbon atoms of the C=C double bond move away from the metal, causing the ring to bend. Generally, this is not a favorable process for Cp and, in most cases, it requires photoinduction.²⁻⁴

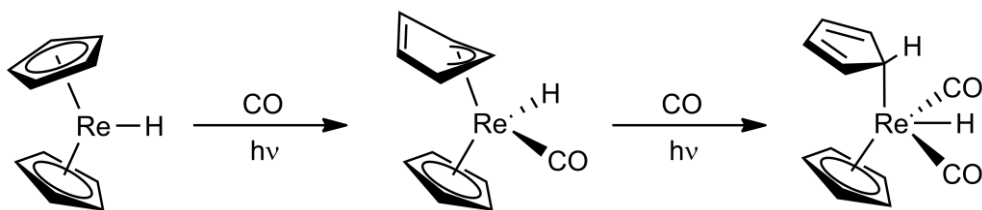


Figure 2.3 Cp slippage promoted by the addition of CO by photoinduction.³

Regarding nickel, a number of $\text{Ni}(\eta^5\text{-Cp})$ compounds were reported over the years, being the nickelocene $[\text{NiCp}_2]$ the first cyclopentadienyl nickel complex synthesized, in 1953, by two independent research groups.⁵ This 20 valence electrons metallocene readily reacts with numerous compounds to form 18 valence electrons species, either by the Cp displacement or by a 1,2-addition. As for $\text{Ni}(\eta^3\text{-Cp})$, there are no examples of this type of bonding. However, some complexes of the type $\text{Ni}(\eta^1\text{-Cp})$ can be found in the literature. A rare example of a reaction of nickelocene where one of the Cp ligands switches coordination mode from η^5 to η^1 is $[\text{Ni}(\eta^5\text{-C}_5\text{H}_5)(\eta^1\text{-C}_5\text{H}_5)(\text{R}_2\text{Im})]$, $\text{R}_2\text{Im} = 1,3\text{-bis}(2,6\text{-dimethyl-4-bromophenyl})\text{imidazol-2-ylidene}$ **L1**, reported by Abernethy *et al.* in 1999.⁶ More than a decade after this discovery, this method has been extended to the 1,3-bis(2,6-diisopropylphenyl) analogue **L2** (Figure 2.4).⁷

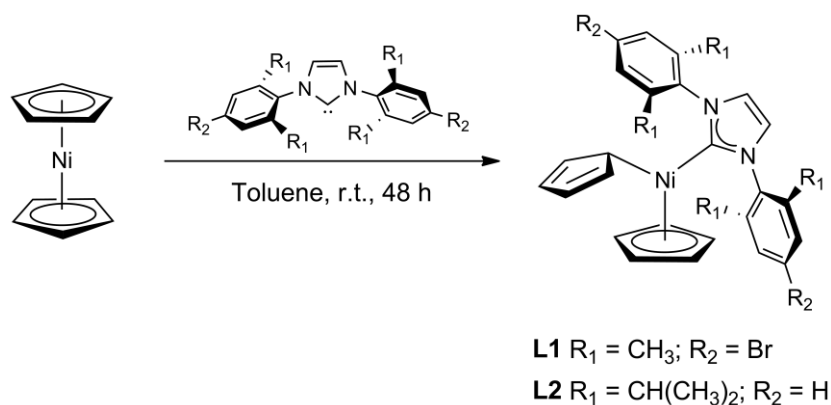


Figure 2.4 Synthesis of $[\text{Ni}(\eta^5\text{-C}_5\text{H}_5)(\eta^1\text{-C}_5\text{H}_5)(\text{R}_2\text{Im})]$ compounds **L1** and **L2**.

The linear combination of five p orbitals of the Cp (one at each carbon atom) gives rise to five molecular orbitals ($\Psi_1\text{--}\Psi_5$) (three bonding and two anti-bonding) residing in three different energy levels, as shown in Figure 2.5. The lowest energy orbital Ψ_1 is represented by an a_2 state, which does not contain any node, followed by a doubly degenerate e_1 state that comprise the Ψ_2 and Ψ_3 orbitals having a nodal plane, and another doubly degenerate e_2 state consisting of Ψ_4 and Ψ_5 orbitals having two nodal planes. The energy of the states increases as the number of nodes increases from 0 to 2. The a_2 and e_1 orbitals are both fully occupied, whereas the e_2 orbitals are unfilled.

The interactions between the Cp and the metal are essentially settled between the a_2 orbital and the metallic s , p_z and d_{z^2} orbitals (interactions with σ symmetry) and also between the two e_1 orbitals and the metallic p_x , p_y , d_{xz} and d_{yz} orbitals (σ interactions).

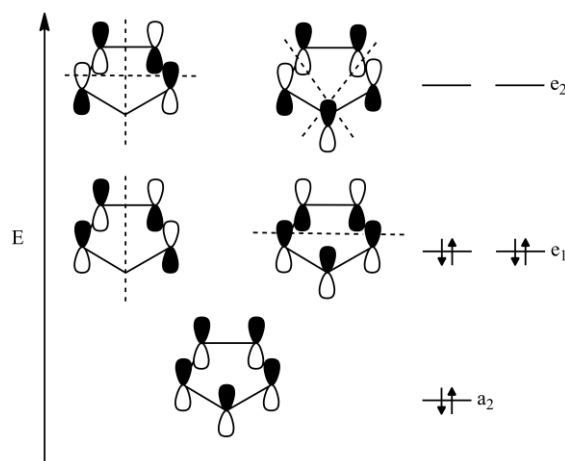


Figure 2.5 Molecular orbital diagram of cyclopentadienyl ligand.

The empty e_2 orbitals interact only slightly with the metallic d_{xy} and $d_{x^2-y^2}$ (π interactions). As this interaction is weak, Cp does not behave as an excellent π -acceptor, encouraging metal backdonation to the remaining ligands. For this reason, the Cp ligand can stabilize metals with high oxidation states and reduced π -backdonation capacity.^{4,8,9}

For a long time, it was considered that the five carbon atoms of the η^5 -Cp ligand interacted uniformly with the metal. However, in the 1960s, some authors began to give greater importance to the asymmetries of the $M-(\eta^5\text{-Cp})$ and also to the internal asymmetries of the ligand. In fact, a rigorous analysis of the X-ray structures of various compounds show that there are no pure η^5 -Cp ligands with five equivalent $M-C$ bonds.¹⁰

Andersen *et al.*¹¹ systematized the distortions of cyclopentadienyl rings observed in Ni(II) pentamethylcyclopentadienyl (Cp*) complexes of the type $[\text{NiCp}^*(\text{PET}_3)\text{X}]$, X = Br, O(*p*-C₆H₄Me), NH(*p*-C₆H₄Me), S(*p*-C₆H₄Me), OMe, Me, CH₂Ph, H, and PET₃ (for the latter there is a CF₃SO₃⁻ triflate counter-anion). These distortions were classified into three categories (Figure 2.6):

- ene-allyl: in this type of distortion two adjacent C-C bonds are short, and the C-C bond opposite these two bonds is even shorter, near the length expected for a double bond. Furthermore, the two carbon atoms closest to the metal plane with the remaining ligands (L-Ni-X) are equidistant from the plane.

- diene: two nonadjacent C-C bonds are shorter than the others and one carbon atom is on the L-Ni-X plane.

- intermediate: between the previous two distortions. The bonds farthest from the L-Ni-X plane are shortest and those that intersect it are the longest.

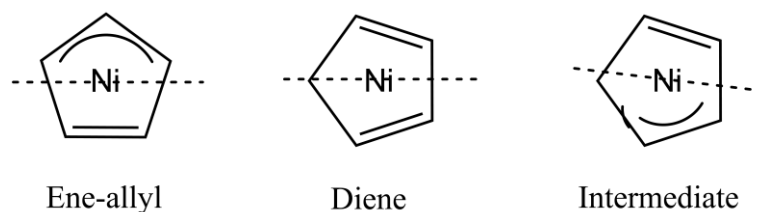


Figure 2.6 Ene-allyl, diene and intermediate distortions of the η^5 -Cp ligand. In each case, the L-Ni-X plane is indicated by a dashed line.

Unfortunately, these studies did not allow to establish a relationship between the type of distortion of the Cp and the electronic nature of the ligands. According to the authors, distortions result from low-energy random effects, such as packing in the crystalline structure, even allowing a compound to present molecules with different distortions in the same batch.¹¹

2.1.1.2 Types of metal-cyclopentadienyl complexes

The cyclopentadienyl ligands are known to form a wide array of organometallic compounds showing diverse properties depending upon the structural integrity. Some of the general types of metal complexes containing Cp ligands are shown in the Figure 2.7,¹² being the metallocenes among the most recognized compounds:

- half sandwich or “piano stool” complexes which consist in cyclic polyhapto ligand attached to a ML_n center, with the general formula $(\eta^x-Cp)ML_n$, in which the number (n) of the ligands may vary from 1 to 4 and the hapticity (x) may be 5 or 3. In these compounds the Cp group is regarded as the “seat” while the remaining ligands are referred to as the “legs” of the piano stool.

- metallocenes or “sandwich” complexes, with the general formula Cp_2M , consist in two Cp anions being parallel to each other with the metal atom in between. The first sandwich structure was the ferrocene complex synthesized in 1951.

Chapter 2

- bent metallocene complexes, with the general formula Cp_2ML_n . In these compounds the Cp groups coordinated to the metal are not parallel, but are tilted at an angle that depends on the electron count of the complex and on the substituents of the cyclopentadienyl ring, which avoid steric interference between the groups.

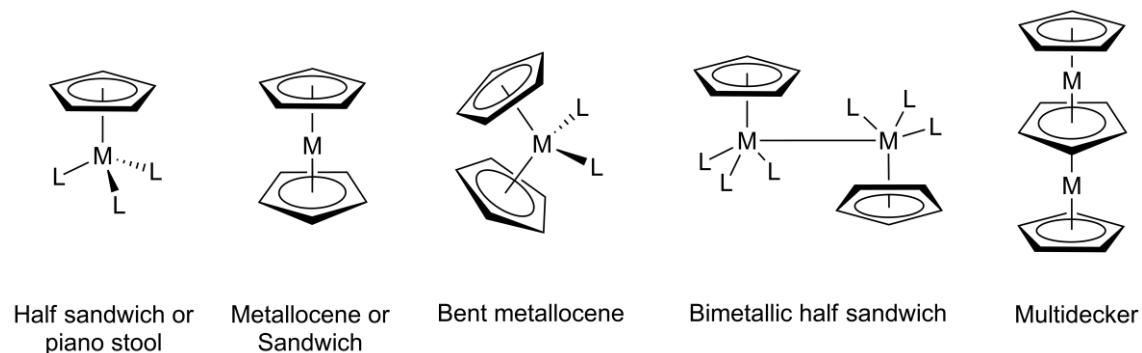


Figure 2.7 Structural varieties of Cp based-metal complexes.

- bimetallic or multimetallic half sandwich compounds, with the general formula $Cp_mM_yL_n$, consists in having more than one metal-Cp fragment bound together by one or more metal–metal bonds. The metals present can be the same or different.

- multi-decker compounds, which are relatively less known than other metal Cp complexes. It consists of two or more metals stacked through three or more Cp rings in multi-decker sandwich compounds (Cp_mM_y). The metals can be the same or different. In these complexes, the Cp rings can be parallel to each other or tilted, the $[Ni_2Cp_3](BF_4)_2$ being the first triple-decker sandwich having 34 valence electrons, which was discovered by Werner and Salzer, in 1972.¹³

2.1.1.3 Spin equilibrium

While studying the forms of coordination of Cp ligands and their distortions in nickel complexes, Andersen *et al.*¹⁴ discovered a strange behavior of the compound $[Ni(\eta^5-C_5(CH_3)_5)(acac)]$ in solution (Figure 2.8). This complex, prepared by the reaction of anhydrous $[Ni(acac)_2]$ with $LiCp^*$, in THF,¹⁵ is often used as starting material for the synthesis of $NiCp^*$ compounds.

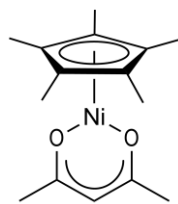


Figure 2.8 Chemical structure of $[\text{Ni}(\eta^5\text{-C}_5(\text{CH}_3)_5)(\text{acac})]$.

They observed that, at low temperatures, the ^1H NMR resonances of the two ligands ($\text{C}_5(\text{CH}_3)_5^- = \text{Cp}^*$ and acac) are in the range of the expected values for a diamagnetic compound. However, as the temperature increases, the signals undergo a pronounced paramagnetic shift, followed by loss of resolution. Therefore, by varying the temperature between -80 and $+100$ $^\circ\text{C}$, the methyl ^1H NMR resonance of the $\text{C}_5(\text{CH}_3)_5^-$ ligand shifts downfield by about 80 ppm. The non-linear variation of δ with the inverse of temperature means that the compound does not obey the Curie's Law. This phenomenon was attributed to the existence of a spin equilibrium between a singlet ground state $S = 0$ (diamagnetic), favored by low temperatures, and a triplet excited state $S = 1$ (paramagnetic), favored by high temperatures. Considering a Boltzmann distribution between the two states, the ΔG_{298} value calculated from the spin transition process was $0.5 \text{ kcal.mol}^{-1}$.¹⁴

The spin equilibrium is only possible because there is a small energetic gap between the HOMO and LUMO orbitals, of the order of kT , which allows one of the electron pairs of the HOMO orbital to occupy the empty LUMO orbital (Figure 2.9).

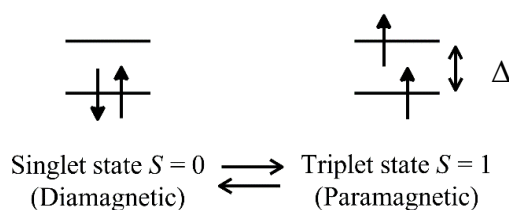


Figure 2.9 Schematic representation of singlet ($S = 0$) and triplet ($S = 1$) states.

The HOMO-LUMO energy difference (Δ) depends on the electronic properties of the ligands, *e.g.* π -donor ligands such as halides, which decrease the value of Δ and, in principle, facilitate the spin transition, while π -acceptor ligands have the opposite effect.¹⁴

Therefore, according to the ligand field theory (LFT):

– when the crystal field splitting energy (Δ) $<$ spin pairing energy, the complex will be high spin and the triplet state is the ground state.

Chapter 2

– when the crystal field splitting energy (Δ) > spin pairing energy, the complex will be low spin and the singlet state is the ground state.

The spin transition can be promoted through external stimulus such as temperature, pressure or irradiation.¹⁶ This effect was detected for the first time in metallic complexes by Cambi and collaborators, in 1931.¹⁷ Since then, it has been identified in numerous complexes both in solid state and in solution.¹⁸ Concerning nickel compounds,¹⁹ the spin equilibrium is less common, the vast majority of studies referring to inorganic compounds usually containing nitrogen chelating ligands.²⁰ In these cases, the spin transition from $S = 0$ to $S = 1$ is associated with a clear isomerization of the complex from a square planar geometry (diamagnetic) to a tetrahedral geometry (paramagnetic).²¹

2.1.1.4 Dynamic processes

The existence of fluxional processes or dynamic behavior in molecules attracted much interest since the early 1960s,²²⁻²⁴ when Cotton *et al.*²⁵ proposed the term “stereochemically nonrigid” molecules. The development of variable-temperature (VT) NMR spectroscopy transformed fluxionality in molecules into a familiar phenomenon, but by no means diminished its interest. Cyclopentadienyl complexes are often fluxional and of special interest are mixed-hapticity species with one η^1 - and one η^5 -Cp. In some of the cases, intramolecular haptotropic rearrangements leading to the interchange of the two Cp ligands may occur, as well documented for a number of molecules.²⁶

The ^1H NMR spectrum of the compound $[\text{Ni}(\eta^5\text{-C}_5\text{H}_5)(\eta^1\text{-C}_5\text{H}_5)(\text{R}_2\text{Im})]$ **L1** revealed two resonances one broad and another sharp corresponding to the five protons of the η^1 - and η^5 -Cp ligands, respectively. These results are due to the existence of two different fluxional processes (Figure 2.10):

- the “ring whizzing” of the η^1 -Cp ligand in which the metal hops between two adjacent carbons, in a 1,2-shift with simultaneous breaking of one M-C bond and formation of the other.^{2,4,27,28}

- the rotation of the η^5 -Cp ligand around the metal coordination axis. The energy barrier associated with this process is usually quite low (between 1 and 2 kcal.mol⁻¹), being practically impossible to stop the rotation of the ligand in solution.^{4,29}

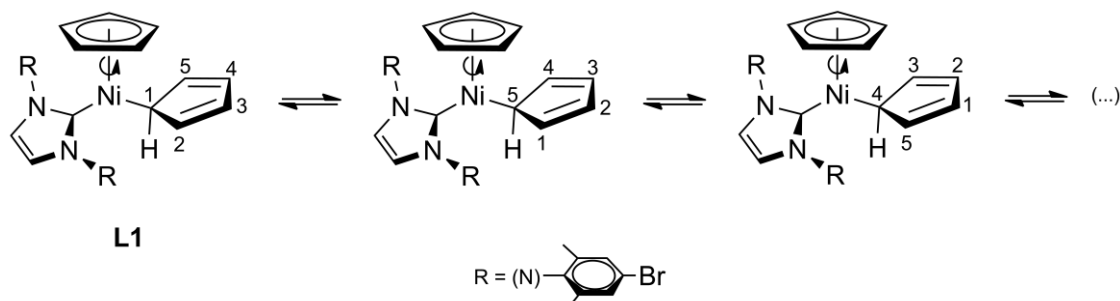


Figure 2.10 Fluxional processes of Cp ligands in the **L1** complex: ring whizzing of η^1 -Cp and rotation of η^5 -Cp around the metal coordination axis.

At room temperature, the **L1** complex shows no evidence of interconversion between the two Cp rings of different hapticity.

However, the presence of bulky substituent groups in the Cp ligand, as well as the stereochemical constraints imposed by other ligands, can increase considerably the energy of the process. This is the case of the compound [Ni{1,2,3-(SiMe₃)₃-C₅H₂}(PPh₃)Cl], synthesized by Okuda *et al.* which, at -80 °C, shows a static Cp. The enthalpy of activation corresponding to its η^5 -Cp rotation was calculated to be 10.5 kcal.mol⁻¹.³⁰

2.1.1.5 Reactivity

Cp has a dual role in the stability of complexes: it electronically stabilizes the metallic center through the donation of five electrons and also stereochemically protects the metal from outside attacks by blocking several coordination positions. For these reasons, Cp often behaves as a spectator ligand (*i.e.* it does not take part in the reaction and it is unchanged at the end). This can be considered an advantage in complexes such as [M(η^5 -Cp)L_n] or [M(η^5 -Cp)₂L_n], where M is an early transition metal, if one wants the reaction chemistry to occur specifically at the ML_n fragment.^{4,8} However, when the metal is electronically richer, as in the case of a late transition metal, the Cp ligand can become reactive. For example, nickelocene in the presence of certain organic species and inorganic

Chapter 2

substances can easily eliminate one or both Cp ligands, in order to reduce the electron count. Since $[\text{NiCp}_2]$ is a rare case of a 20 valence electrons organometallic complex, with two unpaired electrons in antibonding orbitals, this behavior is understandable. Some examples:

- $[\text{NiCp}_2]$ reacts with trityl chloride, $(\text{C}_6\text{H}_5)_3\text{CCl}$, forming a mixture of substituted cyclopentadiene isomers **L4** and **L5** (Figure 2.11). Possibly, this reaction occurs through the formation of a 18 electrons cationic intermediate, **L3**.³¹

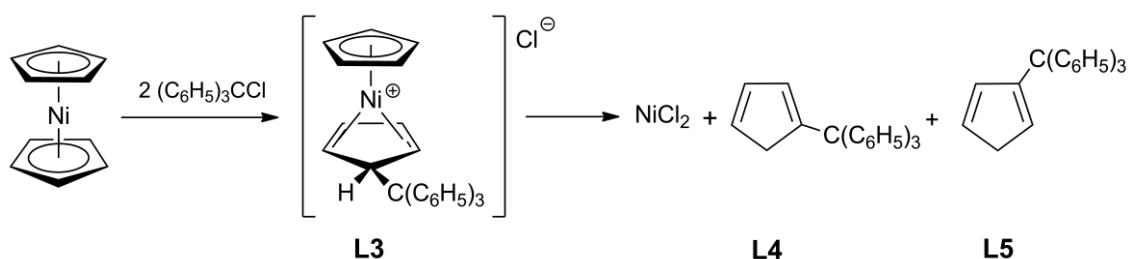


Figure 2.11 Synthesis of compounds **L4** and **L5**.

- nickelocene can also react with organolithium or organomagnesium compounds with substitution of a Cp ligand by a R= alkyl, vinyl or acetylenic group. The species formed $\{\text{Ni}(\eta^5\text{-Cp})\text{R}\}$ are quite unstable due to its coordinative and electronic unsaturation and evolves into new species through several processes.³²

- protonation of the Cp group with Brønsted acids, such as HBF_4 , with formation of the highly reactive cationic intermediate $[\text{Ni}(\eta^5\text{-Cp})(\eta^4\text{-C}_5\text{H}_6)]\text{BF}_4$ (**L6**). This cation is a good starting reagent for the synthesis of complexes of the type $[\text{Ni}(\eta^5\text{-Cp})\text{L}_2]^+$ (**L7**) and $[\text{Ni}(\eta^5\text{-Cp})\text{LX}]$ (**L8**) (Figure 2.12).³³

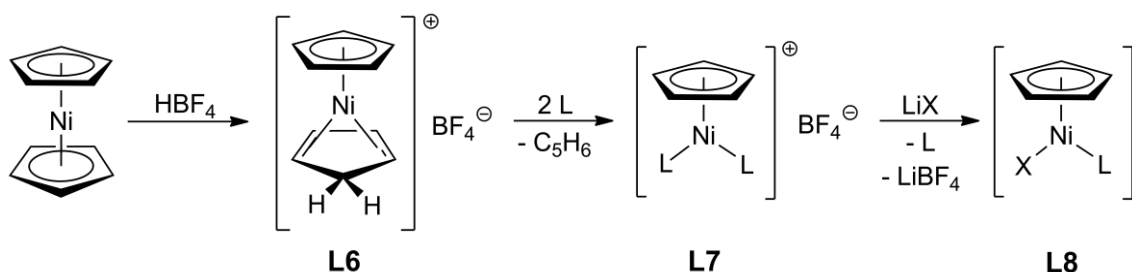


Figure 2.12 Synthesis of compounds **L7** and **L8**.

- $[\text{NiCp}_2]$ can also react with phosphonium salts to form neutral complexes of general formula $[\text{Ni}(\eta^5\text{-Cp})(\text{PR}_3)\text{X}]$ (**L9**) in a one-pot reaction (Figure 2.13).³⁴

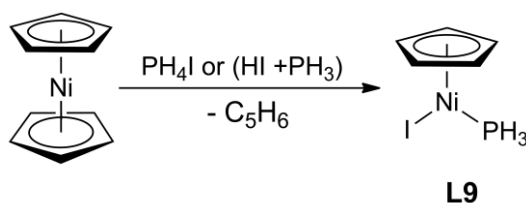


Figure 2.13 Synthesis of compound **L9**.

2.1.2 Pentamethylcyclopentadienyl ligand

The 1,2,3,4,5-pentamethylcyclopentadiene ligand precursor, with general formula $(\text{C}_5(\text{CH}_3)_5\text{H})$, is a cyclic diolefin in which the hydrogen atoms of the Cp are replaced with methyl groups. It is the precursor to the pentamethylcyclopentadienyl ligand $(\text{C}_5(\text{CH}_3)_5^-)$, which is often denoted as Cp^* (to signify the five methyl groups radiating from the periphery of this ligand as in a five-pointed star) (Figure 2.14). In contrast to less substituted cyclopentadiene derivatives, Cp^*H is not prone to dimerization.

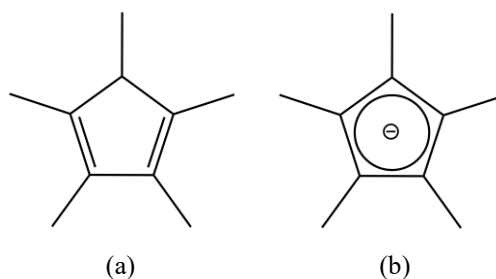


Figure 2.14 (a) Pentamethylcyclopentadiene and (b) pentamethylcyclopentadienyl anion.

Relative to the more common Cp ligand, the introduction of electron donating methyl groups offers certain features that are often advantageous:³⁵

- the Cp^* is electron-richer, being a better nucleophile than the Cp ligand.
- the thermal stability of the Cp^* derivatives increase, making possible detailed investigations concerning the fluxional behavior, even at higher temperatures.
- its steric bulk allows stabilization of unusual bonding situations and attenuates intermolecular interactions, decreasing the tendency to form polymeric structures.

Chapter 2

- its complexes tend to be highly soluble in non-polar solvents.

2.1.3 Carbenes

Carbenes are neutral compounds featuring a divalent carbon atom containing two nonbonding electrons. The existence of these electrons allows carbenes to be very reactive, and stabilize the coordination of the carbene to metal through a strong bond with little dissociative tendency.^{36,37} The carbene carbon can assume two different geometries depending on the hybridization: the linear geometry, which implies an sp -hybridized carbene center with two nonbonding degenerate orbitals (p_x and p_y), and the bent geometry, in which the carbon atom adopts a sp^2 -type hybridization. The bent geometry is the most common one, where the p_y orbital remains almost unchanged (usually called p_π), while the orbital that starts as pure p_x is stabilized and, since it acquires some s character, it is called σ (Figure 2.15).³⁸

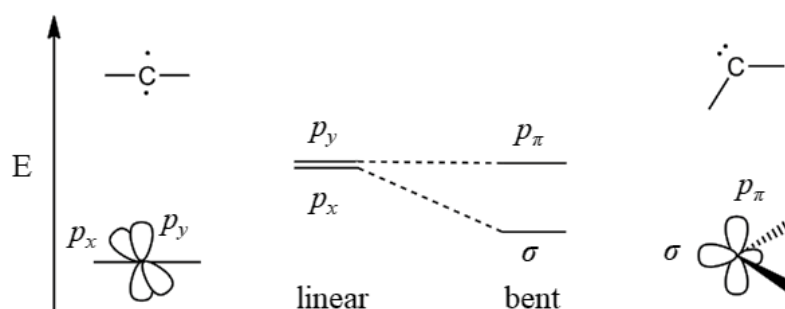


Figure 2.15 Relationship between the carbene bond angle and the nature of the frontier orbitals.

2.1.3.1 Electronic structure and stabilization

The two nonbonding electrons can be paired in the same orbital (singlet state) or unpaired in two different orbitals with parallel spins (triplet state), depending on the energy of the two orbitals (p_x and p_y) (Figure 2.16). When there is a large energy separation between p_x and p_y orbitals, the singlet state is favored.³⁷

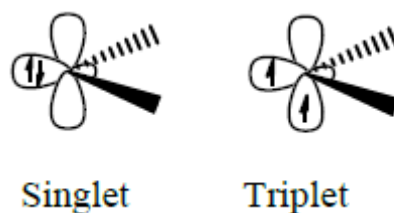


Figure 2.16 Representation of the singlet and triplet states of the carbene.³⁸

The multiplicity of the ground state spin is important in determining the reactivity/stability of the carbene, which consequently is influenced by the substituents on the carbene. This influence is similar to the crystal-field theory (strong-field low spin and weak field high spin configurations) and can be analyzed in terms of electronic and steric effects.³⁷

There are two electronic effects involved in the reactivity/stabilization of the carbenes:

- the inductive effect, where the use of substituents that are σ -electron-withdrawing favor the singlet versus the triplet state, due to inductive stabilization of σ non-bonding orbitals, by increasing its s character and leaving the p_{π} orbital unchanged. Whilst the use of σ -electron-donating substituents induce a small σ - p_{π} gap that favors the triplet state.^{37,39}
- the mesomeric effect, where the use of substituents that are π -electron-donating favor the singlet state. In this case the energy of the p_{π} orbital is increased by interaction with the substituent lone pairs while the σ orbital remains almost unchanged, resulting in a high σ - p_{π} gap.

Although the inductive effects may play an important role in the ground state multiplicity, the mesomeric effects play an even bigger role. If both electronic effects are negligible, the steric effects may also dictate the ground state spin multiplicity. As mentioned before, a linear geometry will favor the triplet state (Figure 2.15) in the same way the use of steric bulky substituents broadens the carbene bond angle, stabilizing the triplet state carbenes.^{37,40}

2.1.3.2 Classification of carbenes

Carbenes have played an important role in organometallic chemistry as they allow the formation of new carbon–carbon bonds. Fischer, Schrock and N-heterocyclic carbenes (NHCs) have been used for this purpose, each of them presenting different electronic properties of the metal-carbene carbon ($M-C_{\text{carbene}}$) bond:

The Fischer type carbenes, named after Ernst Otto Fischer, who with Maasböl in 1964 synthesized the first transition metal complex with a $M-C_{\text{carbene}}$ bond (Figure 2.17a).⁴¹ It consists in σ -electron-donation from the filled lone pair orbital of the carbene atom to an empty metal d -orbital, and π -electron-backdonation from a filled metal d -orbital to the empty p -orbital on carbon. Since the $\sigma R_2C: \rightarrow M$ interaction is predominant, the carbene carbon behaves as an electrophile.^{8,37,42}

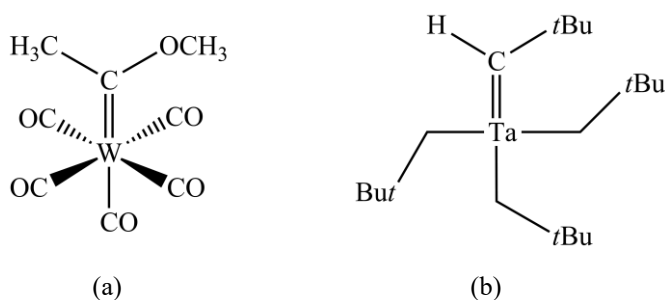


Figure 2.17 (a) Fisher type carbene and (b) Schrock type carbene.

The Schrock type carbenes, named after Richard R. Schrock, who in the 1970's isolated a tantalum complex (Figure 2.17b),⁴³ consists in interactions of the triplet state of the carbene with the triplet state of the metal center. The bonding to the metal occurs through two symmetry interactions σ and π , where in each one the metal and the ligand contribute with one electron each. Therefore, the carbene forms two covalent bonds with the metal ($M=CR_2$). Because Schrock's carbenes have a negative charge localized on the carbene carbon, they are nucleophiles and increase the oxidation state of the metal by +2.^{37,41,42}

While Fischer carbenes interact with low-valent metals with substituents that possess π -donation ability, the Schrock carbenes interact with high oxidation state metals, and the substituents are usually alkyl substituted. The difference in bonding between the two carbenes is illustrated in Figure 2.18.

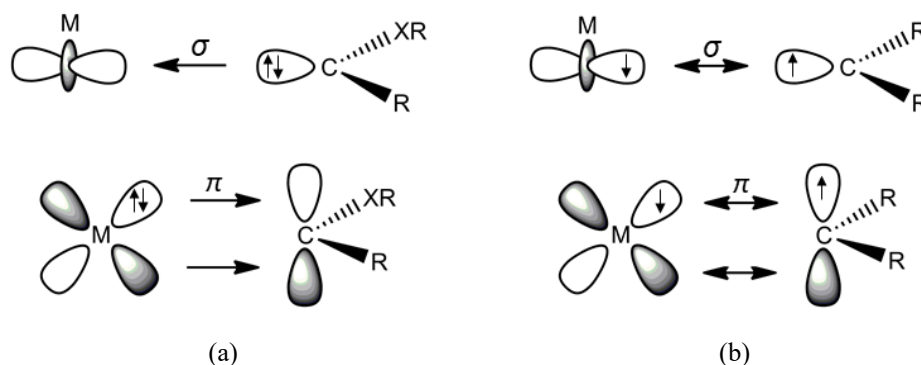


Figure 2.18 Illustration of the difference in bonding between (a) Fischer carbenes showing donor-acceptor bonding, and (b) Schrock carbenes showing covalent bonding.

2.1.3.2.1 N-Heterocyclic carbene ligands

N-Heterocyclic carbene (NHC) ligands, the most common class of carbenes, are defined as heterocyclic species containing a carbene carbon and at least one nitrogen atom within the ring structure. Although NHCs were first reported by Wanzlick⁴⁴ and Öfele⁴⁵ in the 1960's, who almost simultaneously synthesized Hg and Cr complexes bearing NHC ligands, it was only 20 years later, with the isolation of a stable free carbene for the first time, that NHCs became established as widespread ligands in organometallic chemistry. NHCs are electron rich nucleophilic species in which the σ -electron-withdrawing and π -electron-donating character of the nitrogen atoms stabilize the carbene center, both inductively and mesomerically. Their ability to act as σ -electron-donors results in strong bonds to most transition metals, making them excellent ligands in coordination chemistry.⁴⁶

2.1.3.2.1.1 Historical overview

As previously mentioned, the pioneers in the synthesis of the first transition metal complex bearing NHCs ligands were Wanzlick and Öfele, with two separate works published in the same year.^{44,45} Both attempts to isolate the free carbene failed, thus the complexes were obtained by *in situ* deprotonation of imidazolium salts using mercury acetate or dimethylimidazolium hydridopentacarbonylchromate, followed by coordination of the carbene to the metal center (Figure 2.19).

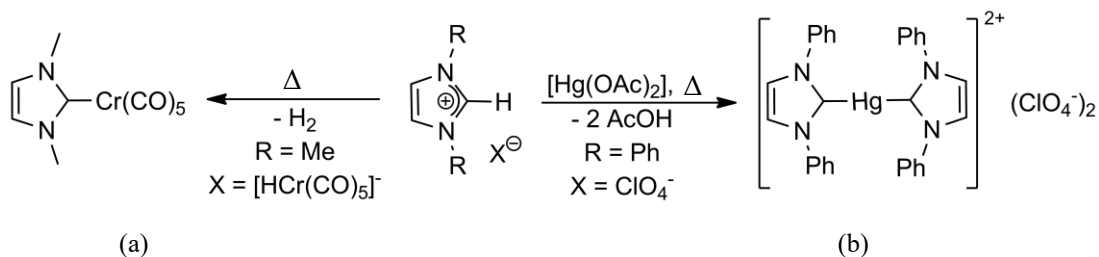


Figure 2.19 Synthesis of complexes with imidazol-2-ylidene: (a) by Öfele and (b) by Wanzlick.

Two years after, in 1970, Wanzlick and co-workers⁴⁷ demonstrated that imidazolium salts could be deprotonated by potassium *tert*-butoxide to afford the corresponding imidazol-2-ylidenes **L10** and **L11**, the compounds being synthesized but, once again, not isolated. They were trapped with phenyl isothiocyanate ($\text{S}=\text{C}=\text{NPh}$), which simultaneously coordinated and stabilized the carbene (Figure 2.20).

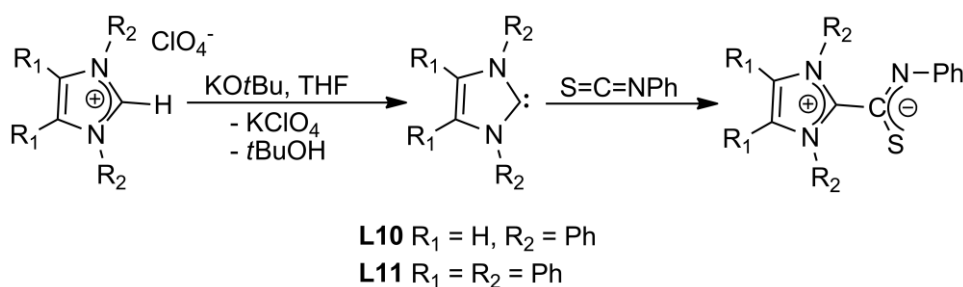


Figure 2.20 NHCs trapped but not isolated by Wanzlick.

It was only in 1991 that Arduengo *et al.*⁴⁸ succeeded in the preparation and isolation of 1,3-bis(1-adamantyl)imidazol-2-ylidene, the first stable nucleophilic N-heterocyclic carbene, using a deprotonation method similar to that already reported by Wanzlick (Figure 2.21).

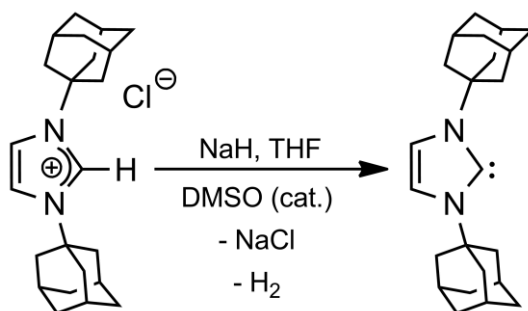


Figure 2.21 First isolated stable imidazol-2-ylidene.

In this case, the imidazolium salt reacted with NaH in THF, in the presence of a catalytic amount of KO^tBu or DMSO, under anhydrous conditions. The stable isolated carbene was obtained in crystalline form, leading to the preparation of metal-NHC complexes by direct reaction with the metal precursor.

Initially, the stabilization of this carbene was thought to be a combination of electronic effects on the part of the nitrogen donor atoms and steric hindrance caused by the adamantly substituents. Then, it was concluded that the π -electron-donating and σ -electron-withdrawing properties of the nitrogen atoms in donating electron density into the empty p -orbitals (the mesomeric effect) and receiving electron density (the inductive effect) to and from the carbene carbon, respectively, are the main reasons for the stabilization of the carbene (Figure 2.22).

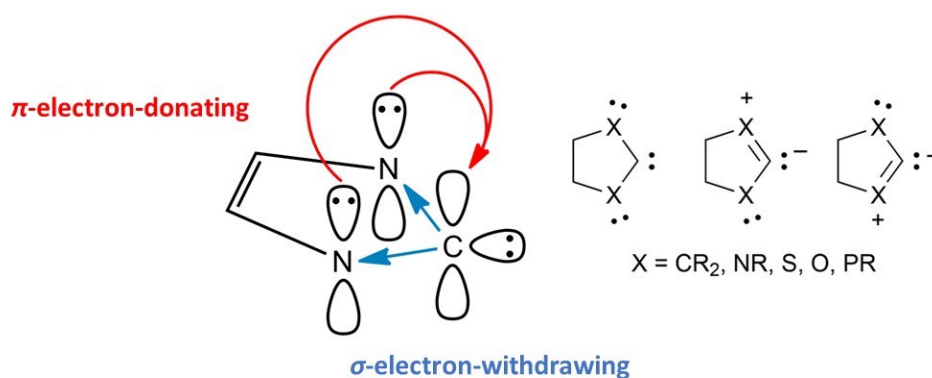


Figure 2.22 Ground state electronic configuration showing the π -electron-donating and σ -electron-withdrawing effects of the nitrogen atoms in the stabilization of the singlet carbene structure (adapted from Ref. 46) and resonance structures of an NHC ligand.⁴⁹

Since Arduengo's initial work, many research groups focused their investigation on the preparation and isolation of free carbenes and metal complexes stabilized by them. Figure 2.23 shows the most important classes of isolated NHCs varying the substituent, size of the ring, and the heteroatoms.^{39,50}

Whenever the term NHC is used during this work, from now on it will refer specifically to derivatives **(a)** and **(b)** as they are, among the examples presented, the most widely used.³⁷

NHCs may be considered as Fischer carbenes due to their π -donating nitrogen substituents that stabilize the singlet state. However, unlike classical Fischer carbenes, these ligands behave as nucleophiles and present M–C_{carbene} bond lengths of a typical single

Chapter 2

bond, which is generally attributed to the absence of π -backdonation $M \rightarrow \text{NHC}$.^{46,51} This single bond is also confirmed by the free rotation of the NHC ligand around the metal bond, depending on the stereochemical constraints imposed by the N-substituent groups.

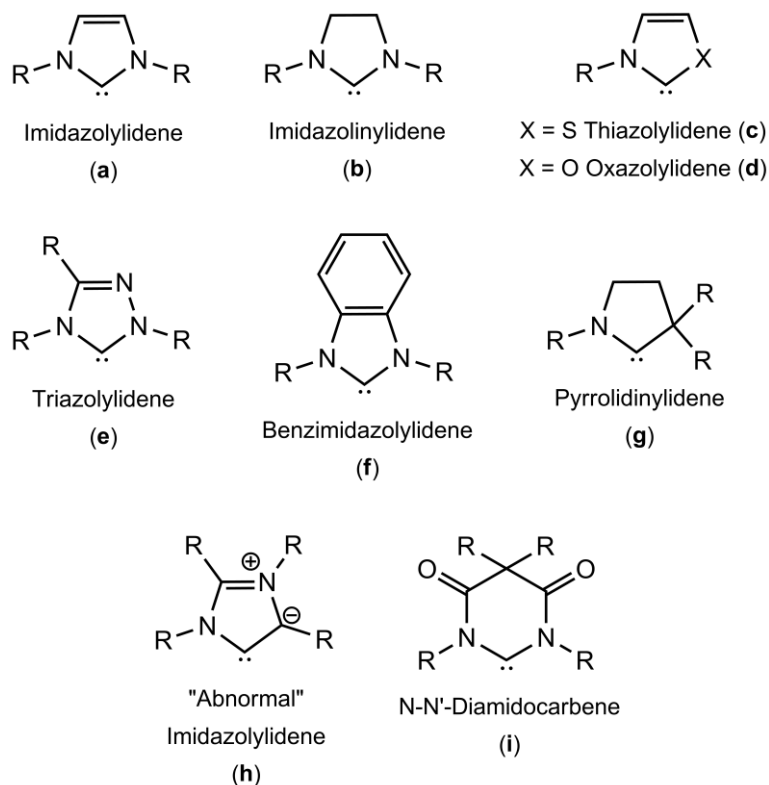


Figure 2.23 Structures of some of the most important classes of NHCs.

2.1.3.2.1.2 Coordination of NHCs to metals

The σ -donation is the most important feature regarding NHCs due to their ability to donate the lone pair into a σ -accepting orbital of the metal. Despite some of the researchers describe these ligands as pure σ -donors, the contribution of the π -donation and -acceptance cannot be neglected. In 1994, through NMR studies, Arduengo suggested the existence of some degree of π -backdonation in homoleptic compounds of Pt and Ni of the type $[\text{M}(\text{Mes}_2\text{Im})_2]$.⁵² Years later, Frenking and co-workers⁵³ confirmed that this contribution accounts for about 20 % of the overall bond energy in group-11 metal-imidazol-2-ylidene and imidazolin-2-ylidene complexes. Investigations, both at the theoretical and experimental level, showed that NHC ligands can also behave as reasonable π -acceptors, depending on the substituent groups, co-ligands and the nature of

the metal, although they lag behind the classical carbenes or tertiary phosphines.^{36,41,51,54} However, as mentioned above, the single bond metal–NHC with π -contributions restricted to delocalization within the NHC ring, and the free rotation of the carbene around the metal bond emphasize the idea that these ligands are strong σ -donors and comparatively weak π -acceptors. This explains the stabilization of main-group metal complexes (Mg, Be, Al, Tl),^{36,55} or of transition metals not possessing d electrons for π -backdonation, such as the case of the Ti(IV) complex $[\text{Ti}(\text{R}_2\text{Im})\text{Cl}_4]$,^{37,41} by these ligands. In addition, photoelectron spectroscopy (PES) studies demonstrated that even in electronically rich group 10 metals, the coordination of the NHC ligand occurs predominantly through σ -donation.⁵⁶

These properties show some similarities to the coordination characteristics of phosphines with the difference that NHCs are in general more electron-donating, leading to thermodynamically stronger metal–ligand bonds, which is reflected in the typically greater bond dissociation energies and shorter metal–ligand bond lengths. Therefore, the number of compounds stabilized by NHCs increased over the years, being Herrmann and Köcher^{37,57} the pioneers in its use in homogeneous catalysis, where tertiary phosphines used to play a prominent role. The success of these ligands in this area results largely from the possibility of controlling its electronic properties and stereochemistry through changes in the substituent groups, which has consequences on the activity, selectivity and stability of the catalysts.

2.1.3.2.1.3 Electronic influence on the M–NHC bond

The electronic properties of NHCs are most commonly described using the Tolman electronic parameter (TEP).⁵⁸ Originally developed for phosphines, the TEP specifically evaluates the electron-donating ability of a ligand (L) by measuring the frequency of the C–O vibrational mode ($\bar{\nu}(\text{CO})$) of a (pseudo)- C_{3v} symmetric complex, $[\text{LNi}(\text{CO})_3]$ by infrared spectroscopy, where L is the ligand of interest. Upon coordination of CO to a metal, $\bar{\nu}(\text{CO})$ typically decreases in relation to 2143 cm^{-1} of free CO. Basically, the metal forms a π bond with the carbonyl ligand by donating electrons through its d orbitals into the empty π^* anti-bonding orbitals of CO. This interaction strengthens the metal-carbon

Chapter 2

bond but also weakens the carbon-oxygen bond, resulting in a lower vibrational frequency (or wavenumber). Thus, if L competes with CO for π -backbonding, $\bar{\nu}(\text{CO})$ increases, and if not, the C-O bond is weakened and $\bar{\nu}(\text{CO})$ decreases (Figure 2.24).

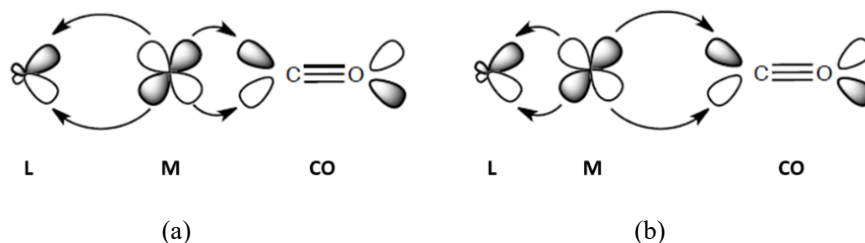


Figure 2.24 π -Backdonation in metallic carbonyls containing the ligand L: (a) a good π -acceptor disfavors M \rightarrow CO backdonation, increasing the frequency of stretching of the C-O bond and (b) a bad π -acceptor favors M \rightarrow CO backdonation, decreasing the frequency of bond stretching C-O.

Although $[\text{LNi}(\text{CO})_3]$ complexes were initially the model species for TEP calculation, the less toxic *cis*- $[\text{LIrCl}(\text{CO})_2]^{59,60}$ and *cis*- $[\text{LRhCl}(\text{CO})_2]^{61}$ complexes are nowadays more prevalent. Therefore, the TEP allows to rank and consequently compare NHCs and PR_3 ligands in order of increasing donor power. Therefore:^{37,51,59,62–66}

- even the most basic tertiary phosphines such as PCy_3 and $\text{P}t\text{Bu}_3$,⁶⁷ are overtaken by NHC ligands in σ -donor character.

- despite the donor character of NHC ligands not being very sensitive to the nature of the N-substituents, the alkyl substituent groups make the ligands slightly more basic than aryl groups. In the case of tertiary phosphines, the basicity is much more dependent on the nature of the substituents.

- the donor character of NHC ligands depends both on the N–C–N angle and the existence of acceptor or donor substituent groups in the posterior part of the skeleton of these ligands.

The previous conclusions have been confirmed by thermochemical studies^{63,68,69} and theoretical calculations.^{37,70,71} The latter, in particular, made it possible to establish an order of basicity for the NHC ligands from theoretical pK_a values (Figure 2.25).

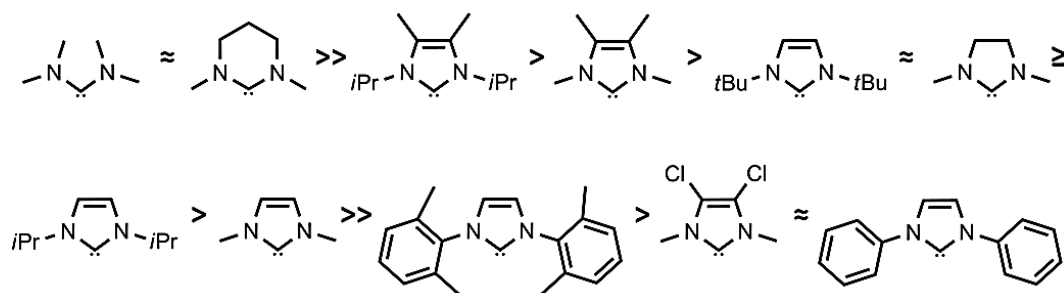


Figure 2.25 Classification of carbenes in descending order of basicity.

2.1.3.2.1.4 Stereochemical influence on the M–NHC bond

In general, dissociation energies of the metal–ligand bond are higher for NHC ligands than for tertiary phosphines, which is in agreement with the greater donor character of carbenes.⁷² However, NHC with very bulky N-substituents, such as adamantyl or *tert*-butyl, have low dissociation energies due to less interaction between metal and ligand orbitals, by stereochemical imposition.³⁷ For example, in $[\text{Ni}(\text{R}_2\text{Im})(\text{CO})_2]$, $\text{R} = t\text{Bu}$ and adamantyl complexes, carbenes are easily replaced by a molecule of CO, while $[\text{Ni}(\text{R}_2\text{Im})(\text{CO})_3]$ complexes with less bulky carbenes are stable in a pressurized CO atmosphere.⁶³

The steric properties of NHCs can be conveniently quantified using the “buried volume” parameter ($\%V_{\text{bur}}$) developed by Nolan, Cavallo and co-workers.⁷³ As shown in Figure 2.26, the $\%V_{\text{bur}}$ value of an NHC refers to the percentage of a sphere occupied by the ligand upon coordination to a metal at the center of the sphere. Fixed parameters of 2 Å for the metal–carbene bond distance, d , and 3 Å or 3.5 Å for the sphere radius, r , are typically used with a larger $\%V_{\text{bur}}$, corresponding to a greater steric influence of the ligand on the metal center.

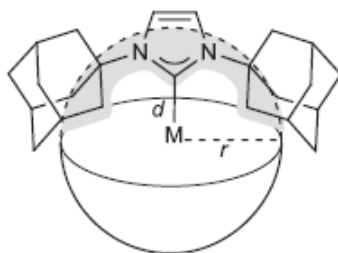


Figure 2.26 Representation of the dimensions of the sphere for determination of the $\%V_{\text{bur}}$ parameter in NHC ligands.

Chapter 2

The volume can be determined from crystallographic data or theoretical calculations and conclude that:^{37,63,68,69,72,73}

- NHC ligands are able to be larger than the bulkier tertiary phosphines ($\%V_{\text{bur}}(\text{PtBu}_3) = 30\%$; $\%V_{\text{bur}}(\text{tBu}_2\text{Im}) = 37\%$).

- the higher the $\%V_{\text{bur}}$ of the NHC ligand, the lower the dissociation energy of the metal binding. A comparison of relative bond dissociation energy values for a range of imidazol-2-ylidene–Ru(II) and imidazolin-2-ylidene–Ru(II) complexes $[\text{Cp}^*\text{Ru}(\text{NHC})\text{Cl}]$ plotted against $\%V_{\text{bur}}$ shows a linear decrease in NHC-Ru bond strength of about 12 kcal mol⁻¹ with increasingly bulky NHCs ($\%V_{\text{bur}}$ from 23 to 37 %).

Thus, the M–NHC interaction essentially depends on the volume of the carbene substituent groups and not so much on its donor character.

2.1.3.2.1.5 Applications of organometallic complexes stabilized by NHC ligands

Once established the characteristics of N-heterocyclic carbenes, it is concluded that these ligands have several advantages over tertiary phosphines, in particular they:^{51,73,74}

- are more basic and, consequently, they coordinate more strongly to metals.
- can be bigger, creating greater protection to the metallic center.
- form more thermally stable and oxidation resistant complexes.
- have reduced toxicity.
- can be synthesized using a variety of methods.

Due to their unique characteristics, NHC ligands find applications in several areas. However, it is in metal catalysis that have been more widely used, where the two most extensively studied classes of catalytic reactions are cross-coupling (catalyzed by palladium or other metals) and ruthenium-catalyzed olefin metathesis. Much of the success of these ligands in this field can be attributed to the increased catalyst stability, and consequent lower rates of catalyst decomposition, resulting from strong metal–ligand

binding. The distinct steric and electronic influence of the NHC on the metal center may also lead to improved catalytic activity.

2.1.4 Pentamethylcyclopentadienyl Nickel complexes stabilized by NHC ligands

Several cyclopentadienyl nickel complexes stabilized by NHC ligands have been reported over the years.⁷⁵ On the contrary, nickel compounds bearing Cp* and NHC ligands, which are the focus of this research work, are less common,⁷⁵ and will be discussed in more detail in the following pages.

In the year 2000 Abernethy *et al.*⁷⁶ reported the synthesis of $[\text{NiCp}(\text{R}_2\text{Im})(\text{Cl})]$, where $\text{R}_2\text{Im} = 1,3\text{-bis(mesityl)imidazol-2-ylidene}$ (**L12**), obtained from the reaction of nickelocene with an imidazolium chloride as a carbene source (Figure 2.27).

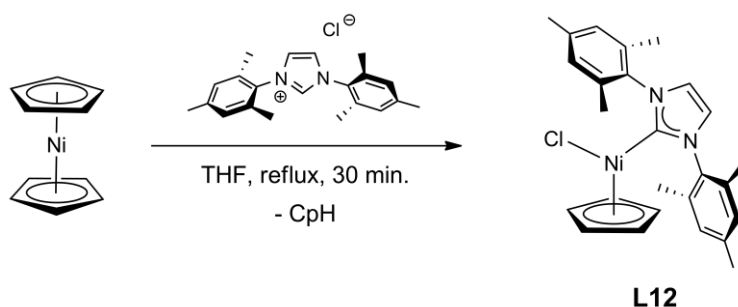
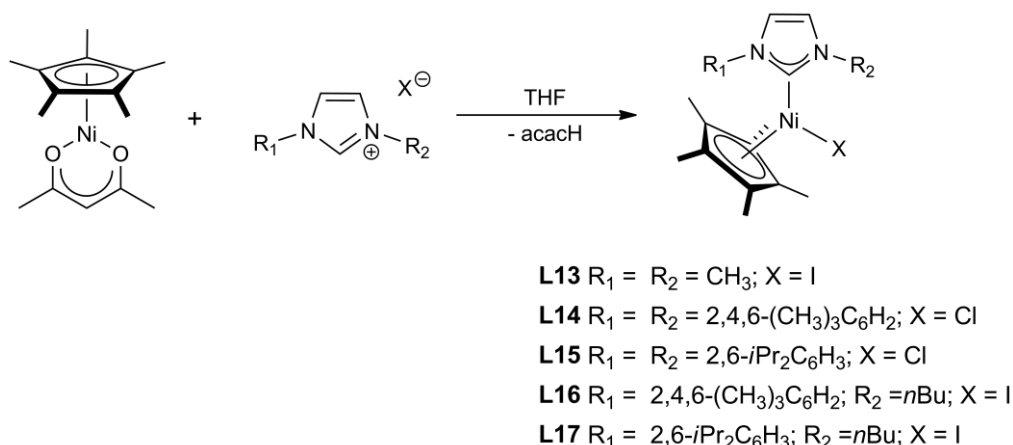


Figure 2.27 Synthesis of compound **L12** by Abernethy.

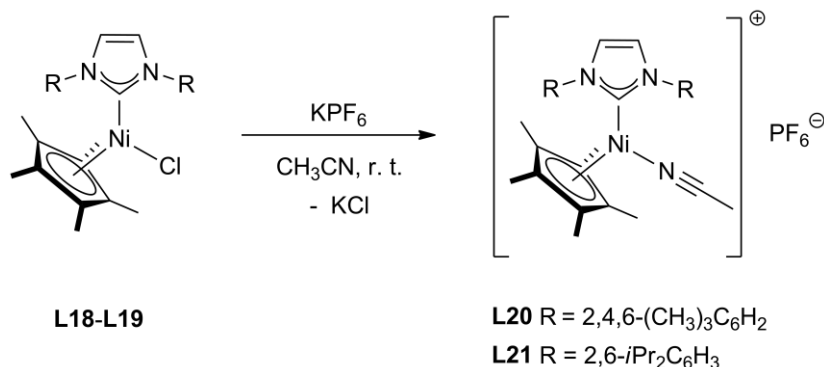
Although this method is the most used in the synthesis of complexes of the type $[\text{NiCp}(\text{NHC})\text{X}]$, $\text{X} = \text{Cl}, \text{Br}$ and I , it had little impact at the time it was synthesized. It was only in 2005 with the work of Kelly *et al.*,⁷⁷ who tested these reaction conditions with some bis(aryl)-NHC chlorides (both saturated and unsaturated) to obtain the expected nickel complexes, that this approach became very popular and used in numerous reactions.

Due to the success of this procedure, its use for the synthesis of $[\text{Ni}(\text{Cp}^*)(\text{NHC})(\text{X})]$ from decamethylnickelocene and ionic NHC precursors was attempted, though with unfruitful results. Therefore, other synthetic methods have been developed, namely that by Chetcuti and co-workers, whereby the reaction of *in situ* prepared complex $[\text{NiCp}^*(\text{acac})]$ with imidazolium salts gave complexes **L13-L17**, as red to violet solids, in reasonable yields (Figure 2.28).^{78,79}

Figure 2.28 Synthesis of compounds **L13-L17**.

The molecular structures of **L13-L17** are similar to each other and comparable to those reported for the related Cp analogous, with pseudo-trigonal planar geometries. The ^1H NMR spectra indicated restricted rotation at the Ni-C_{carbene} bonds in complexes **L14-L17** and oscillations around N-C_{carbene} axes. Full rotation of the N-aryl groups is not possible owing to the strong steric interactions between the N-substituents and the Cp* group, the larger the groups the more pronounced are the steric effects. The VT- ^1H NMR spectra of **L14** and **L15** in toluene- d_8 allowed to determine the free activation energies of Ni-C_{carbene} bond rotation (ΔG^\ddagger) of 67 ± 2 kJ/mol and 65 ± 2 kJ/mol, respectively.

In another work by the same author, cationic half-sandwich nickel complexes were prepared in high yields from the reaction of their neutral homologues **L18** and **L19** with 1 equiv. of KPF_6 in acetonitrile at room temperature (Figure 2.29).⁸⁰

Figure 2.29 Synthesis of compounds **L20** and **L21**.

Despite having no substantial structural differences, **L20** and **L21** show no significant rotational barriers about the Ni-C_{carbene} bonds at room temperature in solution,

indicating free rotation, in contrast to their neutral analogous **L18** and **L19**. Both neutral and cationic complexes catalyzed the cross-coupling of phenylboronic acid with aryl halides in the absence of co-catalysts or reducing agents, with no significant differences on the reaction yields and rates between them. However, complexes bearing the bulky electron-rich Cp* ligand were much more active than those bearing the Cp, allowing 92-95 % conversion, in only 10 to 15 min., for the coupling of 4'-bromoacetophenone with phenylboronic acid in the presence of 3 mol% precatalyst and of K₃PO₄ as the sole additive, giving TOFs of up to 190 h⁻¹.

Also using the same approach for related picolyimidazolide chelating ligands, three new Cp* complexes **L22-L24** were obtained in high yields (70-80 %) as green solids. The nickel atom lies in the center of a pseudo-trigonal plane formed by the η⁵-C₅Me₅ ring centroid, the nitrogen of the pyridine moiety and the NHC ligand (Figure 2.30).⁸¹

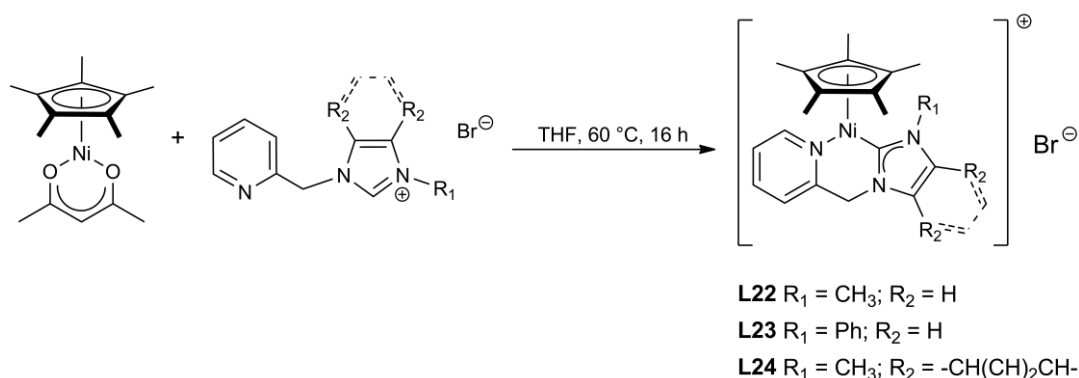


Figure 2.30 Synthesis of cationic Cp* compounds **L22-L24**.

Complexes **L22** and **L23** demonstrated great efficiency and versatility towards Suzuki-Miyaura coupling reactions, hydroaminations of activated olefins and C-S cross-coupling reactions of aryl halides and thiols, under mild conditions.

While investigating the reactivity of a bis-NHC square planar Ni(II) complex, Fischer *et al.*⁸² discovered another approach to the half-sandwich complexes with Cp* ligand. The reaction of [Ni(NHC)₂Br₂] (**L25**) with LiCp* in toluene, at 80 °C, causes the loss of one NHC ligand and affords [Ni(η⁵-C₅Me₅)(NHC)Br] (**L26**) (Figure 2.31).

Generally, the ¹³C NMR spectra of NiCp* complexes show a shift to higher fields of the carbene carbon resonances when compared to their NiCp analogous. This is due to the electron-richer nickel atom of NiCp*.

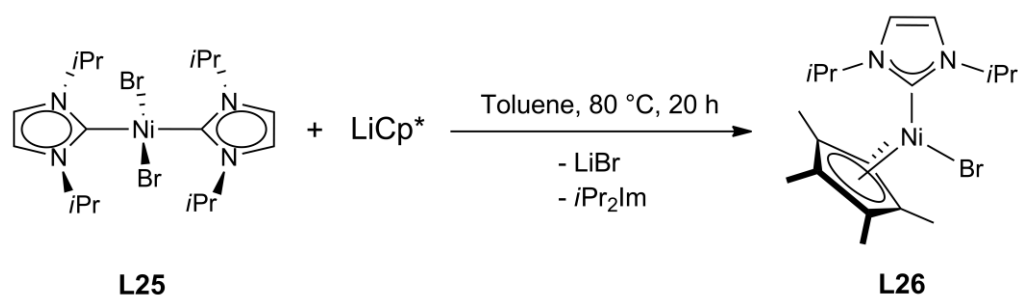


Figure 2.31 Synthesis of compounds **L26** from **L25** and LiCp^* .

Another example of Cp^* complexes stabilized by NHC ligands are the *ansa*- Cp^* -NHC compounds of the type $[\text{Ni}(\text{Cp}^*\text{-NHC})\text{X}]$ (**L28-L32**), with NHCs linked to the tetramethylcyclopentadienyl moiety, which was obtained by the double deprotonation procedure reported by Sun *et al.*⁸³ (Figure 2.32).

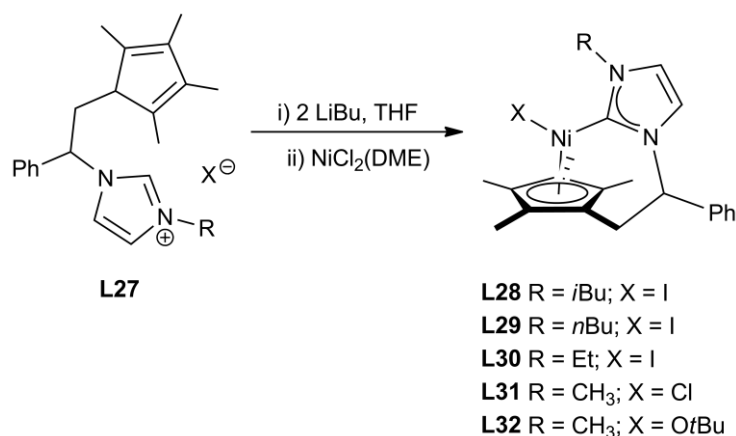


Figure 2.32 Synthesis of compounds **L28-L32** with chelating Cp -NHC ligands.

With the exception of complex **L32** all the other compounds were obtained by reaction of **L27** with two equiv. of LiBu in THF, generating *in situ* the corresponding lithium salts $\text{Li}(\text{Cp}^*\text{-NHC})$, which subsequently were reacted with $[\text{NiCl}_2(\text{DME})]$ to afford the complexes $[\text{Ni}(\text{Cp}^*\text{-NHC})\text{X}]$ (**L28-L31**), in good yields. As for complex **L32**, it was prepared by reaction of complex **L31** with 1 equiv. of $\text{KO}t\text{Bu}$, in THF, at room temperature.

The use of different N-substituents in the carbene changed the catalytic efficiency of these compounds. Therefore, complexes **L28-L30** selectively catalyzed the coupling of aromatic thiols with triethylsilane (Et_3SiH) to give the corresponding silylthioethers (Et_3SiSR), with **L31** showing the worst results. As for complex **L32**, it displayed high

catalytic activity in the reduction of aldehydes, affording quantitative conversions to the corresponding alcohols in 5 min at 25 °C (TOF up to 2304 h⁻¹).^{84,85}

Previously, our research group synthesized and fully characterized three nickel complexes of the type [Ni(η^5 -C₅H₅)(*t*Bu₂Im)X], X = Cl (**L33**), Br (**L34**) and I (**L35**) (Figure 2.33), among others.⁸⁶ The synthesis of the chlorinated derivative **L33** was carried out by substitution reaction of PPh₃ by the *t*Bu₂Im carbene in [Ni(η^5 -C₅H₅)(PPh₃)Cl], whereas the synthesis of the Br (**L34**) and I (**L35**) derivatives were obtained by metathetic exchange of the Cl atom of **L33** with the corresponding lithium and sodium halide salts.

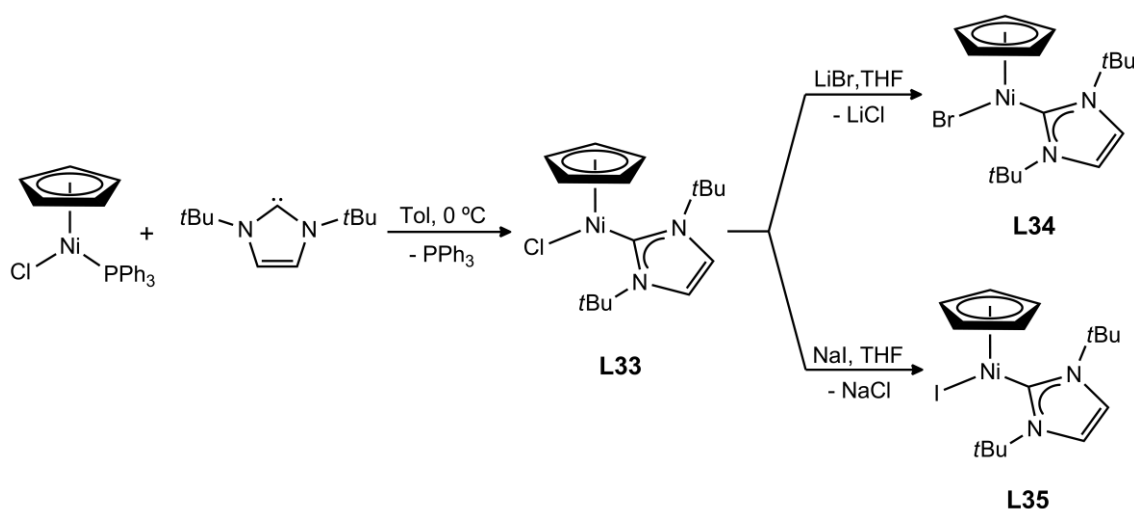


Figure 2.33 Synthesis of compounds **L33-L35** with chelating Cp-NHC ligands.

In the structural study of this family of complexes, it was found that they exhibited spin equilibria phenomena, which was the reason for the large paramagnetic contact shifts observed in VT-¹H NMR experiments. The experimental results combined with DFT calculations led to the conclusion that the energy gap between the involved singlet ($S = 0$) and triplet states ($S = 1$) is influenced not only by the halide electronic effects (the more electronegative the halogen atom the smaller the energy difference is between the two states), but also by the steric effects. In fact, the increase of the bond lengths between the metal center and the ligands by 3 to 12 %, when going from the singlet to the triplet state, allows the spin equilibria to shift toward the high spin state.⁸⁶

Chapter 2

2.1.5 Objectives of the present work

Driven by the previous above mentioned work on the $[\text{Ni}(\eta^5\text{-C}_5\text{H}_5)(t\text{Bu}_2\text{Im})\text{X}]$ system we decided to continue the study, now aiming at the synthesis of bulkier complexes of the type $[\text{Ni}(\eta^5\text{-C}_5\text{Me}_5)(t\text{Bu}_2\text{Im})\text{X}]$, X = Cl, Br and I, in an attempt to decrease the singlet-triplet energy gap through the expected enlargement of the Ni–ligands distances.

Therefore, Chapter 2 describes:

- the syntheses and isolation of new $[\text{NiCp}^*(\text{nNHC})\text{X}]$ complexes, with X = Cl, Br, I, and nNHC = normal N-heterocyclic carbene ($t\text{Bu}_2\text{Im}$);
- the synthesis and isolation of a new unexpected $[\text{NiCp}^*(\text{aNHC})\text{Cl}]$ compound, in which aNHC = abnormal N-heterocyclic carbene;
- characterization of these new complexes by single-crystal X-ray diffraction, ^1H and ^{13}C NMR spectroscopies and by magnetic susceptibility measurements in solid state and in solution;
- structural comparison of these compounds both in solid state and in solution;
- study of possible dynamic processes and spin equilibria of $[\text{NiCp}^*(\text{nNHC})\text{X}]$ (X = Cl, Br, I) complexes and comparison with $[\text{NiCp}(\text{nNHC})\text{X}]$ (X = Cl, Br, I) compounds already reported by our group.⁸⁶

2.2 RESULTS AND DISCUSSION

2.2.1 Pentamethylcyclopentadienyl Nickel complexes

2.2.1.1 Synthesis of new $[\text{Ni}(\eta^5\text{-C}_5\text{Me}_5)(\text{NHC})\text{X}]$ compounds

In this work, the chosen NHC was 1,3-bis(*tert*-butyl)imidazol-2-ylidene (*t*Bu₂Im) (**2.3**, Figure 2.34), in order to compare the aimed $[\text{Ni}(\eta^5\text{-C}_5\text{Me}_5)(\text{tBu}_2\text{Im})\text{X}]$ with the respective Cp analogous $[\text{Ni}(\eta^5\text{-C}_5\text{H}_5)(\text{tBu}_2\text{Im})\text{X}]$ complexes, which were previously synthesized and characterized in our group.⁸⁶ This carbene was prepared by deprotonation of the corresponding imidazolium salt with potassium *tert*-butoxide (KO*t*Bu) in THF, according to the procedure described in the literature.⁴⁰ The pure product was obtained by filtration and evaporation of the reaction solvent as an off-white crystalline solid.

Unlike $[\text{Ni}(\eta^5\text{-C}_5\text{H}_5)(\text{NHC})\text{X}]$, the $[\text{Ni}(\eta^5\text{-C}_5\text{Me}_5)(\text{NHC})\text{X}]$ compounds are less common, being the work developed by Chetcuti *et al.*⁷⁸ one of the first to report the syntheses of these complexes using a different approach to that used by Abernethy. Attempts to prepare the complexes $[\text{Ni}(\eta^5\text{-C}_5\text{H}_5)(\text{tBu}_2\text{Im})\text{X}]$ (X = Cl, I) by following the latter method also failed in our group, which prompted us to develop other alternative methods (see Figure 2.33), different from those used by Chetcuti and co-workers.⁸⁶ In fact, the failure of Abernethy's method is observed for carbenes containing very bulky R substituents, such as cyclohexyl or *tert*-butyl, because these groups protect the acidic proton of the imidazolium carbon, preventing the C–H σ -bond metathesis to occur.⁷⁷

Similarly, in the reaction of $[\text{Ni}(\eta^5\text{-C}_5\text{Me}_5)(\text{acac})]$ (**2.1**) (prepared by the addition of $[\text{Ni}(\text{acac})_2]$ to $\text{Li}(\eta^5\text{-C}_5\text{Me}_5)$ in THF) with the imidazolium salt $[\text{tBu}_2\text{ImH}]\text{Cl}$ (**2.2**) in THF at reflux, for 3h, did not allow the formation of the intended product. Only the starting material was recovered along with traces of unidentified products. Therefore, in this work the syntheses of the Ni(II) compounds were achieved by using an alternative method, where the *t*Bu₂Im (**2.3**) was used instead of the salt (Figure 2.34), an approach related but not identical to that used previously by us for the NiCp analogous.⁸⁶

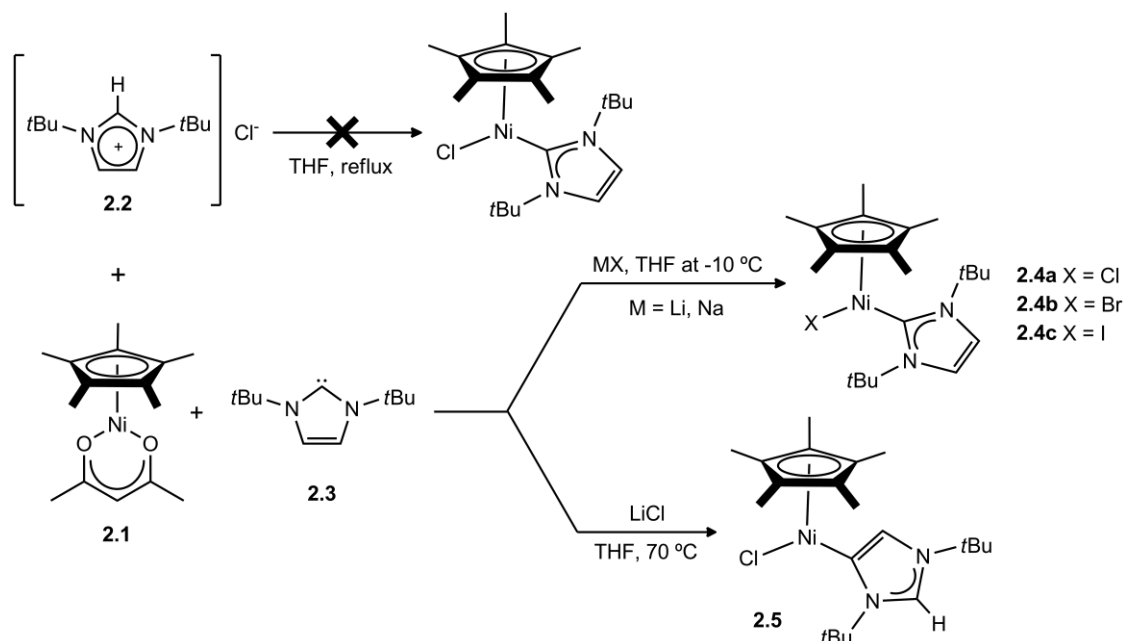


Figure 2.34 Synthetic route of compounds **2.4a-c** and **2.5**.

$[\text{Ni}(\eta^5\text{-C}_5\text{Me}_5)(\text{tBu}_2\text{Im})\text{X}]$, X = Cl, Br and I (**2.4a-2.4c**) were prepared by reaction of 1 equiv. of $[\text{Ni}(\eta^5\text{-C}_5\text{Me}_5)(\text{acac})]$ (**2.1**) with 1 equiv. of the tBu_2Im ligand (**2.3**) and an excess of the halogen source (6 equiv. of LiCl or LiBr or NaI), in THF, at -10 °C. In compounds **2.4a** and **2.4b**, the color of the solution changed almost instantaneously after the addition of the LiX (X = Cl and Br) from red to purple, whilst in compound **2.4c** from red to brown. The reaction mixtures were left at *ca.* -10 °C, for 2 hours. The workup consisted in the complete evaporation of the solvent followed by the multiple extractions of the solid residues with toluene until the solvent was colorless. The crystallization at -20 °C afforded the desired products, as a purple solid for **2.4a**, and dichroic crystals for **2.4b** (purple/red) and **2.4c** (red/green), which were structurally characterized by NMR spectroscopy and single crystal X-ray diffraction. The same conditions were used in the preparation attempts of the nickel-fluoride analogue, using KF. In the latter case, the color of the reaction did not change, being verified by NMR spectroscopy that the reaction did not occur.

By studying the reaction conditions, namely changing the reaction temperature, it was found that two different Ni(II) products can be obtained: one bearing a normal N-heterocyclic carbene (nNHC) and another one containing an abnormal NHC (aNHC). While the nNHC coordinates to a metal center through the C2 carbon, the aNHC coordinates via C4 or C5 carbons (Figure 2.35). This type of coordination was first reported by Crabtree and co-workers in 2011,⁸⁷ for a cationic iridium compound

containing a coordinated aNHC to Ir. Studies showed that the location of the carbene center at C4 or C5 makes the aNHCs less thermodynamically stable and more electron-donating than their nNHCs analogous.⁸⁸

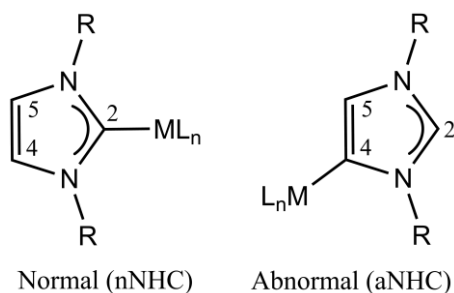


Figure 2.35 Normal NHC with coordination through the C2 carbon to the metal center and abnormal NHC with coordination to the metal through the C4 carbon.

Table 2.1 summarizes all the attempts to vary the reaction temperature in order to prepare compounds **2.4a-c** and their abnormal analogous.

Table 2.1 Variation of the reaction conditions in order to obtain compounds **2.4a-c** and their abnormal analogous.

Halogen source	Temperature (°C)	Time (h)	Final product	Yield (%)
LiCl	ca. -10	2	Compound 2.4a (Purple solid)	88
LiCl	ca. 70	Overnight	Compound 2.5 (pink crystals)	59
LiBr	ca. -10	2	Compound 2.4b (purple/red crystals)	73
LiBr	ca. 25	Overnight	Mixture: compound 2.4b (mostly) and Ni(II) complex with a(NHC)	—
LiBr	ca. 70	Overnight	Unidentified products (NMR)	—
NaI	ca. -10	2	Compound 2.4c (red/green crystals)	53
NaI	ca. 70	Overnight	Unidentified products (NMR)	—
KF	ca. -10	2	No reaction	—

Therefore, complex **2.5** was prepared using the same starting materials as compound **2.4a**, but instead of using low temperature, the reaction was left overnight at

Chapter 2

ca. 70 °C, in THF. In this reaction, the color changed from purple (when LiCl was added) to red, meaning that compound **2.4a** is formed in a first reaction step, being subsequently transformed into complex **2.5** by heating the reaction mixture. After evaporation of the solvent, the red/brown residue was extracted with toluene, concentrated, and cooled to -20 °C to afford pink crystals suitable for X-ray diffraction.

All compounds (**2.4a-c** and **2.5**) were characterized by NMR spectroscopy, elemental analysis and, for **2.4b-c** and **2.5**, by single crystal X-ray diffraction.

Further studies varying the solvent and temperature are required to evaluate whether the syntheses of the Br and I derivatives of the [NiCp*(aNHC)X] can be performed by this method.

2.2.1.2 X-ray diffraction studies

Crystals of compounds **2.4b-c** and **2.5** suitable for X-ray structure determination were crystallized in the monoclinic crystal system, in the $P2_1/c$ space group, for **2.4b-c**, and $P2_1$, for **2.5**. The molecular structures of these compounds (Figure 2.36) showed a nickel atom bonded to a η^5 -Cp* group, a NHC moiety, and a halide ligand in a piano stool geometry with the Cp* being the seat and the other ligands the legs. The molecular structures of **2.4b-c** and **2.5** are shown in Figure 2.36 and the selected bond distances and angles are listed in Table 2.2. Compound **2.4b** has two independent molecules in the asymmetric unit, which are labelled as molecule 1 and 2.

Considering that the Cp* centroid occupies a single coordination position, the nickel lies at the center of a trigonal plane formed by the ring centroid, the halide, and the carbene carbon atom of the NHC ligand, in which the sum of the three bond angles L-Ni-L is equal 360°. However, the angles about the Ni atom are deviated from the expected 120° angles of a trigonal structure (Table 2.2). Therefore, sometimes the geometry of this type of compounds is referred to as distorted square planar by considering the Cp* C1-C2 atoms occupying a single coordination site and the remaining vertices being defined by the atoms C3, C_{carbene} and the X. This is not just a matter of convenience, since the interaction between the metal and the Cp* is more intense along the L-Ni-L' plane.

The Ni-C_{carbene} bond lengths are not significantly different from each other: 1.947(3) Å for **2.4b** and 1.920(2) Å for **2.4c**. Similarly, small changes are also observed in the Ni-Cp*_{centroid}: 1.832(1) Å for **2.4b** and 1.8079(8) Å for **2.4c**.

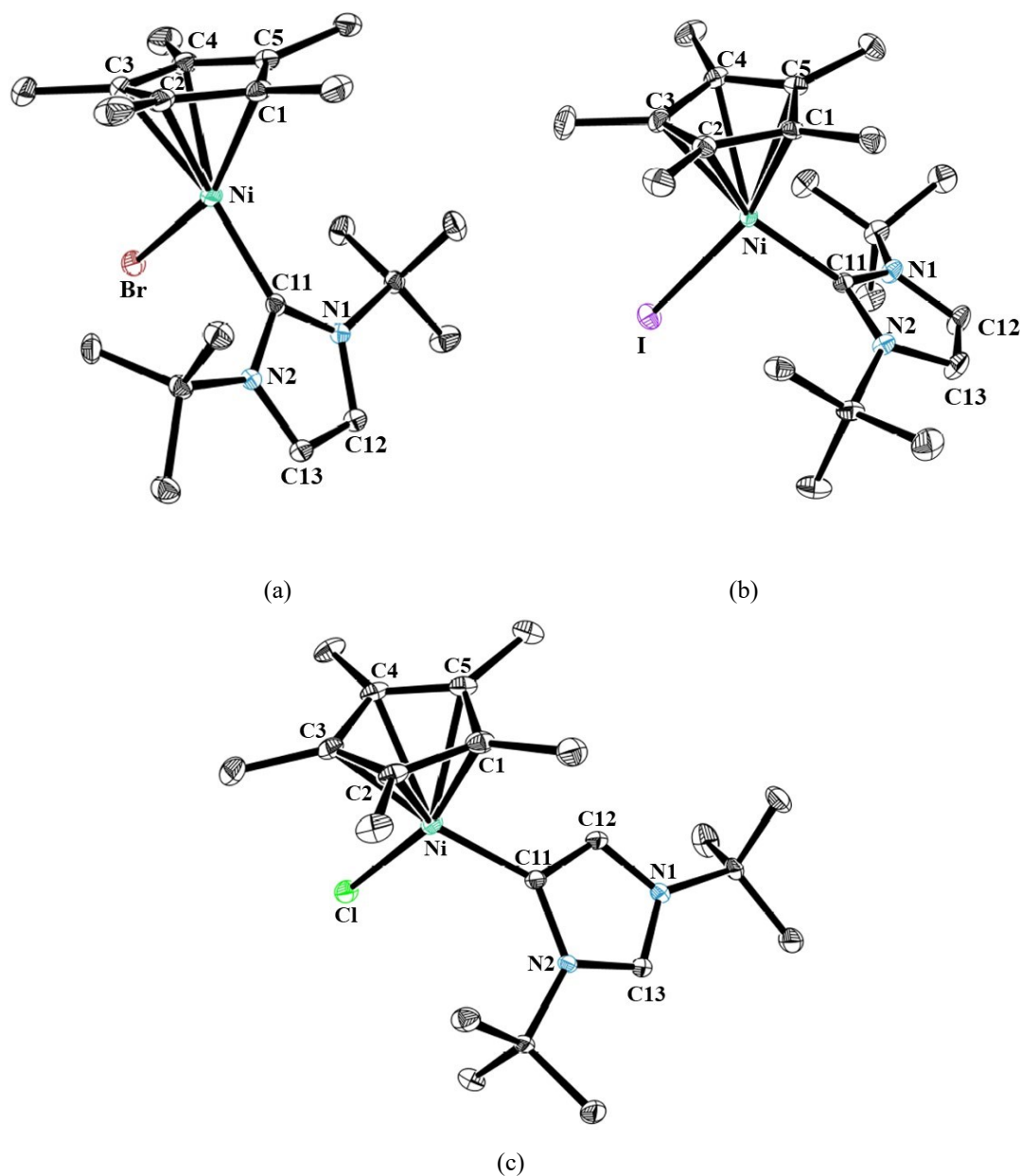


Figure 2.36 ORTEP-3 diagram for complexes (a) **2.4b** (b) **2.4c** and (c) **2.5** with ellipsoids drawn at 30 % probability level. All hydrogen atoms were omitted for clarity.

Although the differences in bond lengths are very subtle, there seems to be a slight decrease of the Ni-Cp* and Ni-NHC bonds when the volume of the halogen atom decreases, meaning that the electronic influence overcomes the stereochemical one.

Chapter 2

Table 2.2 Selected bond distances (Å) and bond angles (°), dihedral angles α and β for complexes **2.4b-c** and **2.5**.

Complex	2.4b		2.4c	2.5
	molecule #1	molecule #2		
<i>Distances (Å)</i>				
Ni-C1	2.136(3)	2.124(2)	2.140(2)	2.065(3)
Ni -C2	2.227(3)	2.218(3)	2.218(2)	2.172(2)
Ni -C3	2.177(3)	2.177(4)	2.142(3)	2.151(2)
Ni-C4	2.196(3)	2.179(3)	2.226(2)	2.222(2)
Ni-C5	2.238(3)	2.228(2)	2.159(2)	2.194(3)
C1-C2	1.445(5)	1.438(5)	1.405(3)	1.427(5)
C2-C3	1.389(5)	1.391(4)	1.433(3)	1.409(4)
C3-C4	1.448(4)	1.451(5)	1.432(4)	1.457(4)
C4-C5	1.384(5)	1.391(5)	1.394(3)	1.385(5)
C5-C1	1.445(4)	1.455(4)	1.472(3)	1.467(3)
Ni-X	2.3778(6)	2.3637(4)	2.5261(4)	2.2187(7)
Ni-C _{carbene}	1.947(2)	1.945(3)	1.920(2)	1.911(3)
Ni-Cp* _{centroid}	1.832(1)	1.819(1)	1.8079(8)	1.788(1)
<i>Angles (°)</i>				
X-Ni-C _{carbene}	89.74(8)	90.32(8)	96.51(6)	98.88(8)
C _c -Ni-Cp* _{cg}	145.37(10)	145.35(8)	132.44(7)	132.33(11)
Cp* _{cg} -Ni-X	124.89(5)	124.32(4)	131.04(4)	128.07(5)
C1-C2-C3	106.3(3)	106.7(3)	106.7(2)	106.6(2)
C2-C3-C4	109.3(3)	109.3(3)	109.4(2)	108.8(2)
C3-C4-C5	108.3(3)	108.3(3)	107.2(2)	108.3(2)
C4-C5-C1	107.1(3)	106.8(3)	108.1(2)	107.1(2)
C5-C1-C2	108.2(3)	108.3(3)	107.9(2)	108.4(2)
Dihedral α ^a	90.25(11)	90.23(11)	88.94(7)	85.21(9)
Dihedral β ^b	87.22(10)	89.82(9)	88.02(8)	66.23(9)

^a α = dihedral angle formed between the Cp* plane and the plane defined by atoms (Ni, X, C_{carbene});

^b β = dihedral angle formed between planes defined by atoms (C_{carbene}, N1, C12, C13, N2) and (Ni, X, C_{carbene}).

Also, these bonds are comparable to related analogous of the type [Ni(η^5 -C₅H₅)(NHC)X] (X = Cl, Br and I) reported by our research group,⁸⁶ indicating that the methyl substituents in the cyclopentadienyl ring have little influence on the coordination sphere of these compounds (**2.4b-c**). However, the carbene ¹³C NMR resonances in

compounds **2.4b** and **2.4c** appear at 176.81 and 170.36 ppm, respectively (in toluene-*d*₈). These resonances are considerably downfield shifted when compared to their corresponding Cp analogous (156.6 and 164.2 ppm, respectively, in toluene-*d*₈), likely indicating the increase of π -backdonation from the more electron-rich nickel atoms to the Cp* complexes.

Despite not having the X-ray structure of compound **2.4a**, the Ni-C_{carbene} bond length should be shorter for **2.5** because it is a stronger donor ligand and exhibits a smaller steric profile.

As mentioned before, the Cp* ligands are coordinated to the metal center with η^5 hapticities, being almost perpendicular to the Ni-X-C_{carbene} plane, as seen in Table 2.2 by the calculation of the dihedral angles α , which are reasonably close to 90°. Consistent with these observations, compounds **2.4a-c** and **2.5** exhibit a formal count of 18 valence electrons. Similarly, the dihedral angle β is close to 90° for compounds **2.4b-c**, indicating that also the NHC ligands are perpendicular to the Ni-X-C_{carbene} plane probably due to the steric hindrance between the *tert*-butyl on the NHC and the methyl substituents of the Cp*. The coordination of the aNHC allowed the *tert*-butyl to be farther away from the Cp*, displaying an angle β of 66.23(9)°, which is a reflex of a less constrained geometry.

The molecular structures also revealed that the distances between the carbon atoms of the pentacyclopentadienyl ligand are not equal. As mentioned in the introduction, there are no pure η^5 -Cp ligands with five equivalent M-C bonds. Therefore, according to the classification of Andersen *et al.*, compounds **2.4b** and **2.4c** present a Cp* with diene distortions, where two nonadjacent C-C bonds are shorter, having lengths less than 1.40 Å, than the other three remaining bonds (Figure 2.37). Also, one carbon atom is on the Ni-X-C_{carbene} plane.

As for compound **2.5** it presents an ene-allyl distortion, in which there are two adjacent C-C bonds (1.409(4) and 1.427(5) Å) shorter than the adjacent ones (1.457(4) and 1.467(3) Å), but larger than the opposite one (1.385(5) Å) (Figure 2.38).

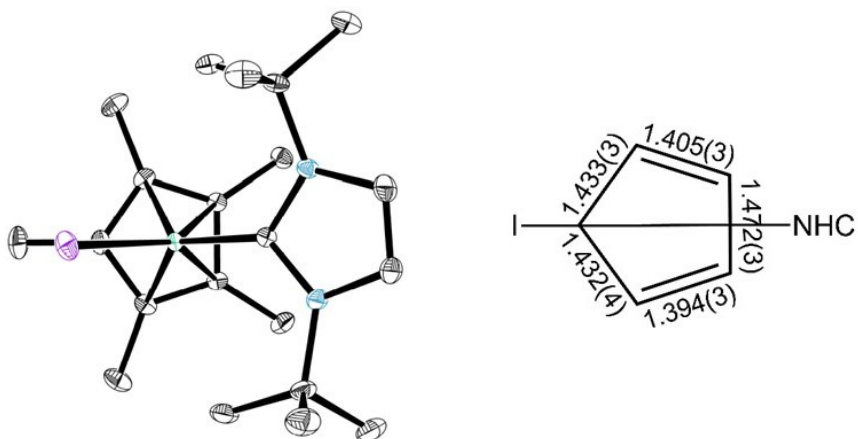
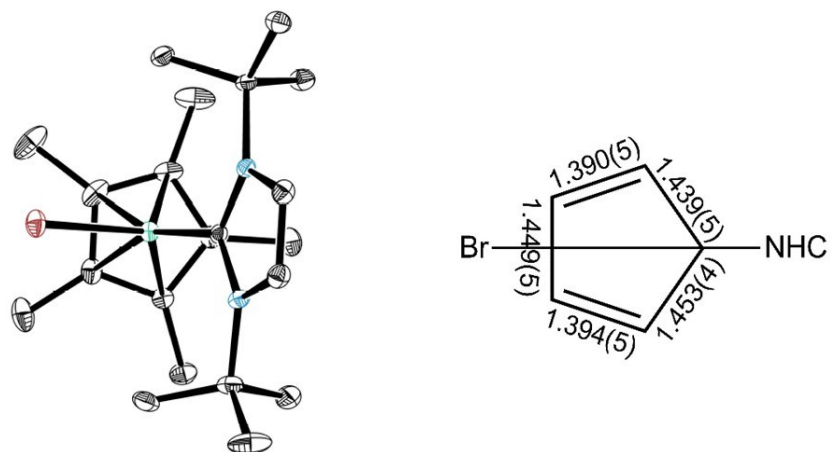


Figure 2.37 Molecular structures of 2.4b (top) and 2.4c (bottom) revealing the diene distortions.

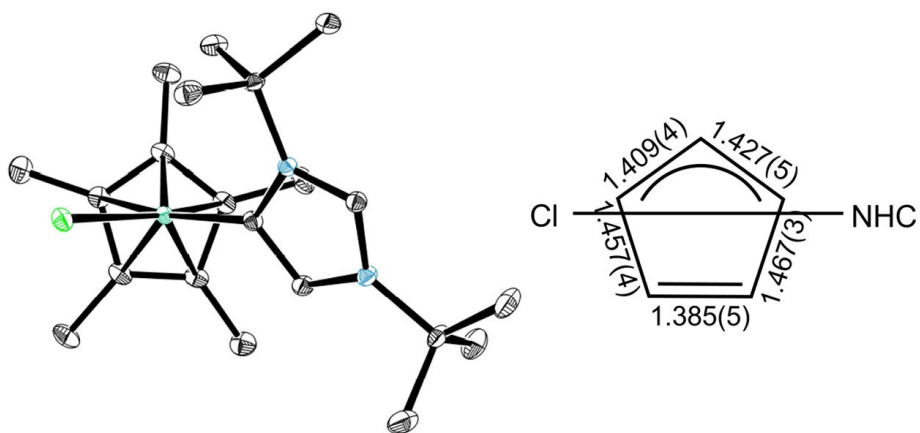


Figure 2.38 Molecular structure of 2.5 revealing the ene-allyl distortion.

2.2.1.3 Nuclear Magnetic Resonance (NMR) studies

The ^1H and ^{13}C NMR spectra of compounds **2.4a-c**, at room temperature, are straightforward with only three singlets corresponding to the $\text{HC}=\text{CH}$ protons of the NHC, the 15 protons of the Cp^* ligand and the 18 protons of the *tert*-butyl groups bonded to the nitrogen atoms in the NHC. The NMR spectrum of compound **2.5** is very different, presenting two singlet resonances for the *tert*-butyl groups, owing to a less symmetrical stereochemical environment.

The ^1H and ^{13}C NMR chemical shifts of the resonances of compounds **2.4a-c** are shown in Table 2.3.

Table 2.3 Chemical shifts (ppm) of ^1H NMR resonances of compounds **2.4a-c**, at room temperature, in toluene- d_8 .

Complex	$\text{HC}=\text{CH}$	$\text{NC}(\text{CH}_3)_3$	$\text{C}_5(\text{CH}_3)_5$
2.4a	6.66	2.06	1.82
2.4b	6.67	2.03	1.76
2.4c	6.65	1.96	1.60

The ^1H NMR spectra at room temperature revealed an effective mirror plane of symmetry present in solution for all the studied compounds **2.4a-c**, due to the observation of a single resonance for the *t*Bu₂ and $\text{HC}=\text{CH}$ protons. This plane contains the halogen, nickel, NHC carbene carbon atom and the Cp^* _{centroid} (Figure 2.39). The existence of a single and sharp $\text{C}_5(\text{CH}_3)_5$ resonance for the Cp^* shows that this ligand is rotating rapidly about the Ni- Cp^* _{centroid} even at $-80\text{ }^\circ\text{C}$.

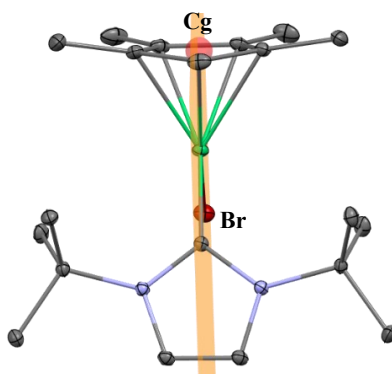


Figure 2.39 Symmetry plane containing the halogen, nickel, NHC carbene carbon atom and the Cp^* _{centroid} (Cg) on compound **2.4b**.

Chapter 2

Similar to the behavior observed for the NiCp analogous,⁸⁶ VT-¹H NMR experiments performed for complexes **2.4a-c**, in toluene-*d*₈, in a temperature range from -80 to +110 °C, revealed the presence of paramagnetic shifts for all the complexes, which are enhanced with an increase in temperature.

At -80 °C, the ¹H NMR spectrum of compound **2.4a** shows resonances of the C₅(CH₃)₅ (1.50 ppm), *t*Bu (1.89 ppm) and HC=CH (6.51 ppm) in the range of the expected values for a diamagnetic compound. However, as the temperature increases, the resonances undergo shifts to lower fields. At +80 °C, the resonances appear at 2.89, 2.20 and 6.88 ppm for C₅(CH₃)₅, *t*Bu₂ and HC=CH groups, respectively (Figure 2.40).

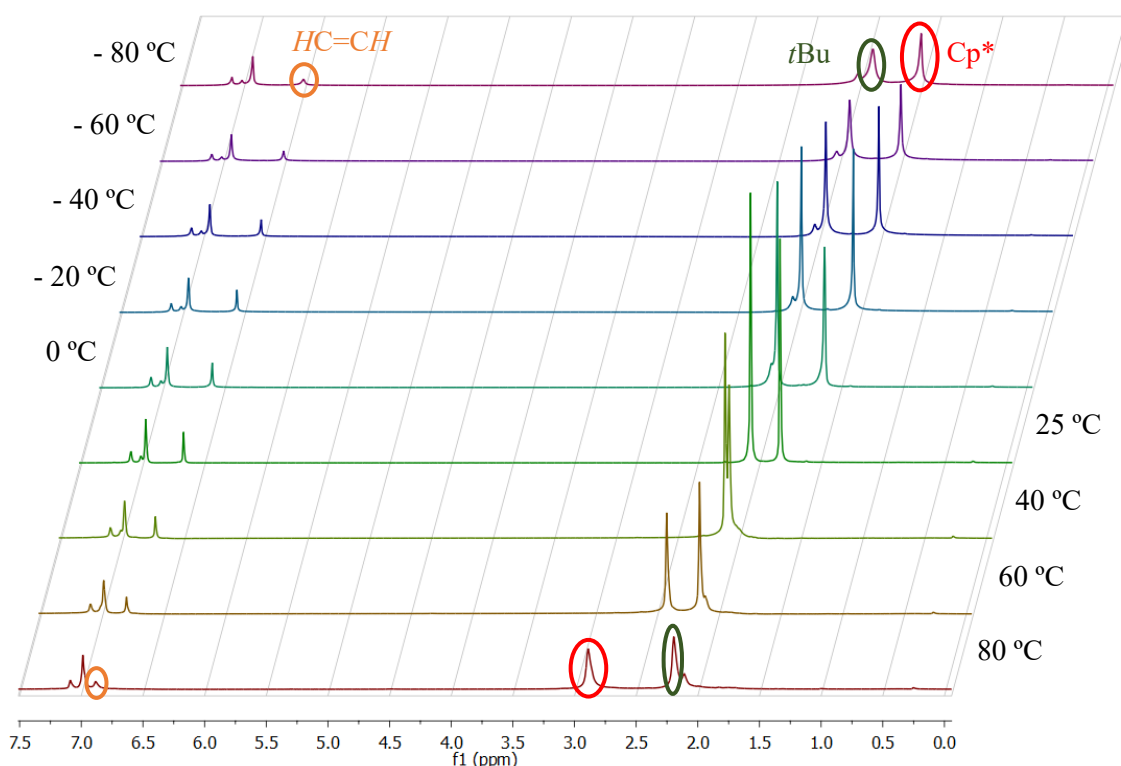


Figure 2.40 Stacking of VT- ¹H NMR spectra for compound **2.4a**, in toluene-*d*₈.

At +90 °C, small resonances at the baseline start to appear, meaning that the compound is decomposing (Figure 2.41). By raising the temperature to +110 °C, the number and intensity of these resonances increase, being impossible to understand the spectra and assign the resonances. After decreasing the temperature to +25 °C, the spectrum remains the same as at +110 °C, the solution exhibiting a change in color from purple to brown.

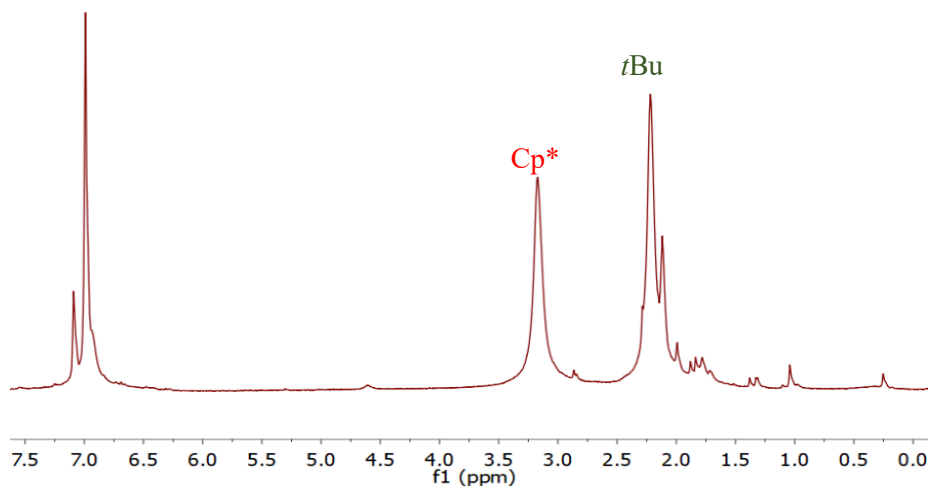


Figure 2.41 ^1H NMR spectrum for compound **2.4a** at +90 °C.

Compound **2.4b** exhibits a similar behavior to the previous complex, in which the $\text{C}_5(\text{CH}_3)_5$ resonance is downfield shifted from 1.49 ppm, at -80 °C, to 2.78 ppm, at +80 °C, and those of $t\text{Bu}_2$ and $\text{HC}=\text{CH}$ groups from 1.87 to 2.15 ppm and 6.54 to 6.88 ppm, respectively (Figure 2.42).

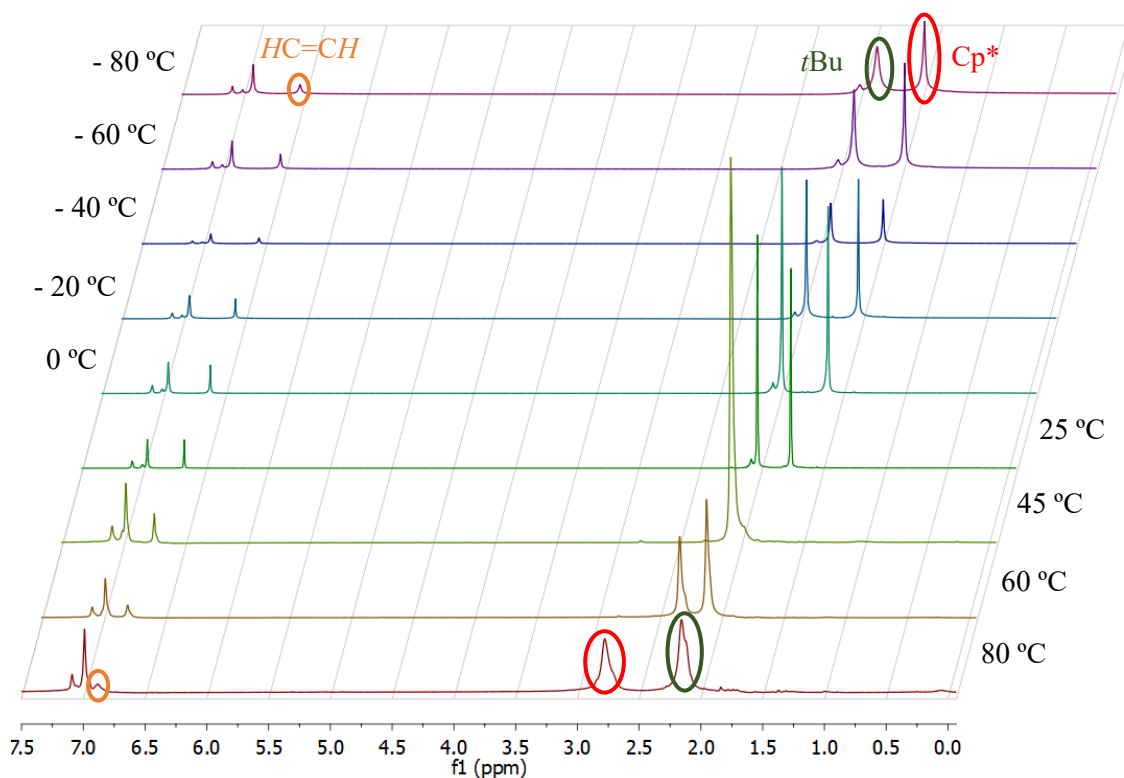


Figure 2.42 Stacking of VT- ^1H NMR spectra for compound **2.4b**, in toluene- d_8 .

Chapter 2

At +90 °C there are small signals of degradation (Figure 2.43). By raising the temperature to +110 °C, the spectrum is unrecognizable due to extensive degradation, and by decreasing the temperature to +25 °C it remains the same. The color of the solution in the NMR tube once again changed from purple to brown.

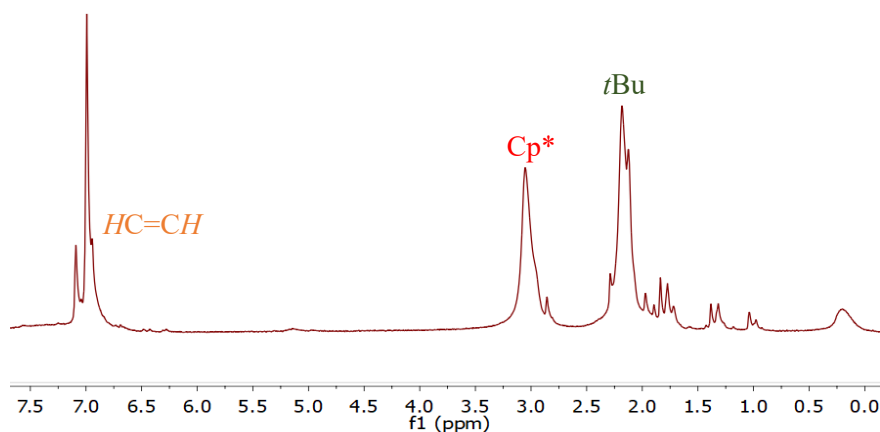


Figure 2.43 ¹H NMR spectrum for compound **2.4b** at +90 °C.

Like in the previous complexes, compound **2.4c** shows downfield shifts of the resonances with increasing temperature. Therefore, varying from -80 to +80 °C, shifts from 1.49 to 2.04 ppm for the C₅(CH₃)₅ ligand, from 1.83 to 2.04 ppm for tBu₂ and from 6.44 to 6.81 ppm for HC=CH, are observed (Figure 2.44).

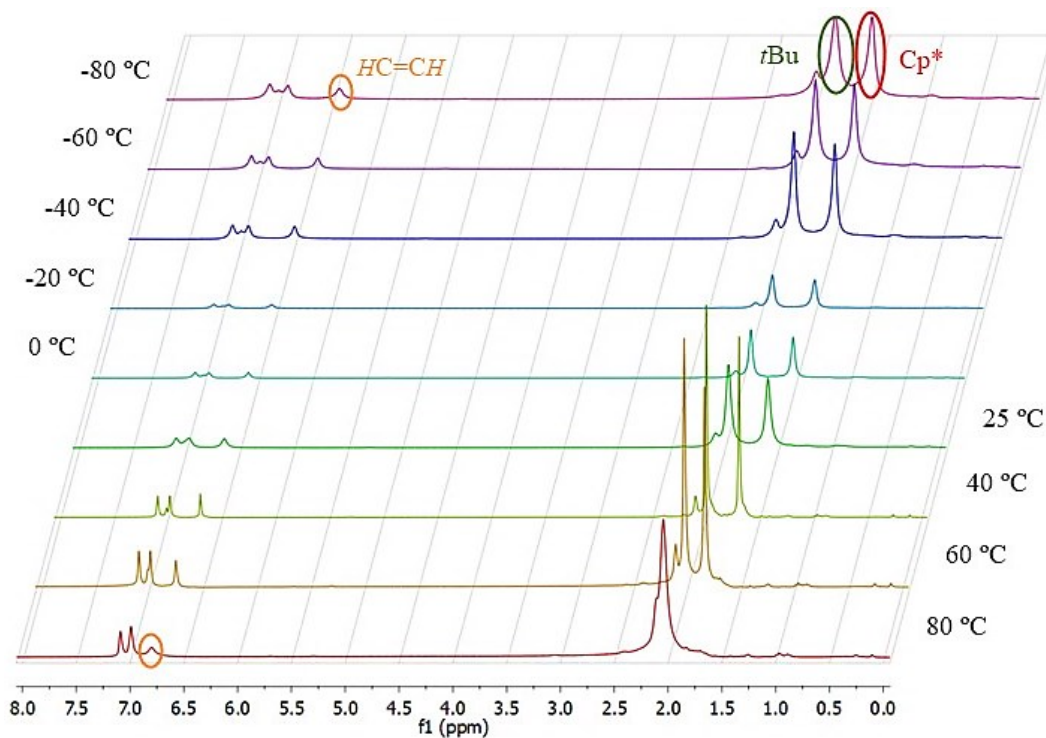


Figure 2.44 Stacking of VT-¹H NMR spectra for compound **2.4c**, in toluene-*d*₈.

At +90 °C, this complex, as the remaining ones, starts to decompose, its color turning to brown in the end (Figure 2.45).

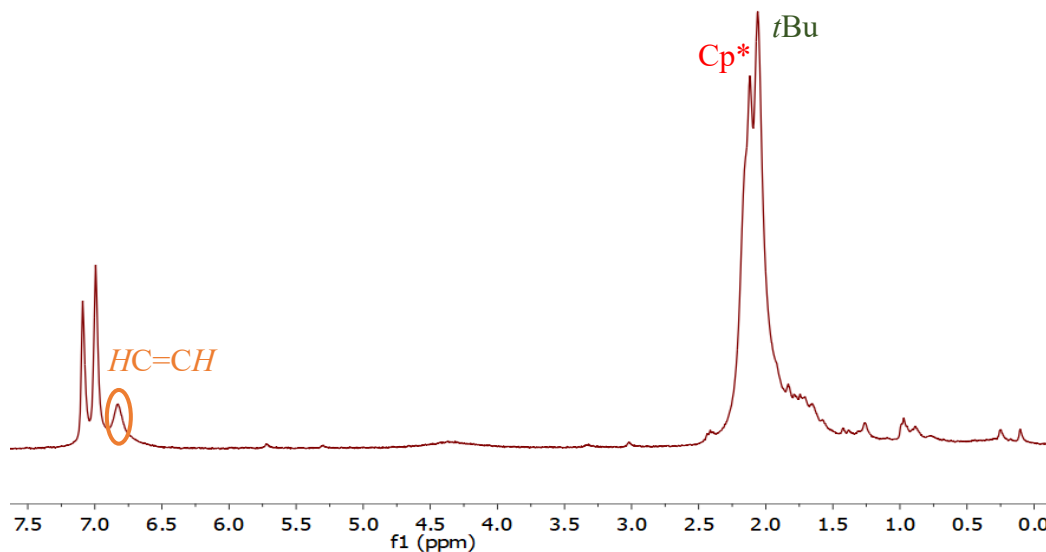


Figure 2.45 ^1H NMR spectrum for compound **2.4c** at +90 °C.

As for compound **2.5**, due to the lack of time, it was not possible to perform VT- ^1H NMR experiments. This study will be carried out in the near future as it would be interesting to analyze the differences in both nickel complexes (bearing nNHC or aNHC).

2.2.1.4 Spin Equilibrium

Figure 2.46 shows the variation of the chemical shifts of the different resonances ($t\text{Bu}$, $\text{C}_5(\text{CH}_3)_5$ and $\text{HC}=\text{CH}$) of compounds **2.4a-c**, in toluene- d_8 , with temperature variation. The chemical shifts variations with temperature are significant and, in general, non-linear suggesting that a spin equilibrium between the singlet ground state $S = 0$ (diamagnetic) and a triplet excited state $S = 1$ (paramagnetic) may be occurring. As the temperature increases all the resonances shift to lower fields, that of the $\text{C}_5(\text{CH}_3)_5$ group being the more pronounced one, since the methyl protons are at the distance of three bonds from the metal, whereas the remaining groups are at the distance of four bonds.

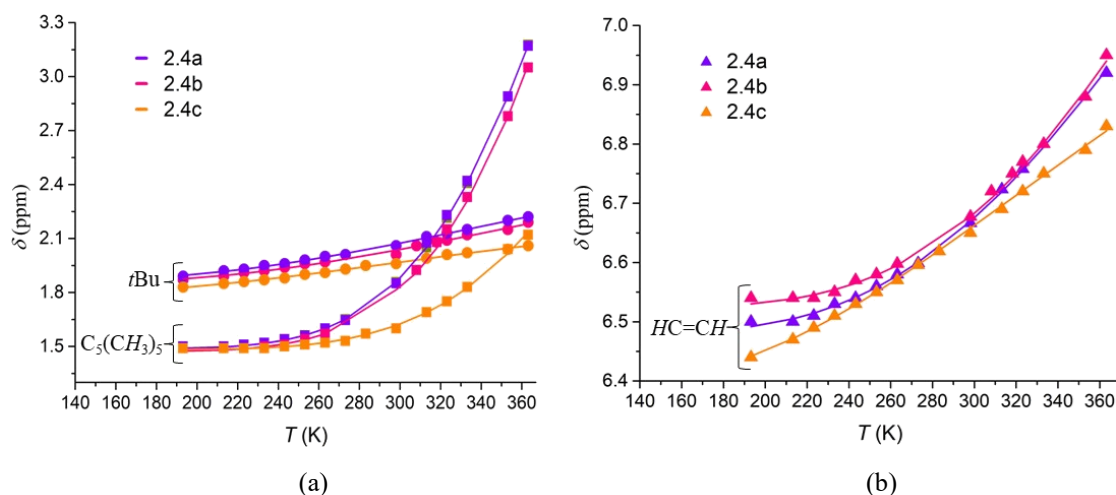


Figure 2.46 δ vs. T plots for the ^1H NMR resonances of compounds **2.4a-c** (a) for $t\text{Bu}$ and $\text{C}_5(\text{CH}_3)_5$ and (b) for $\text{HC}=\text{CH}$ resonances. The solid lines represent the best fits to the experimental data using the Equation 2.1.

The ^1H NMR chemical shifts of the three complexes can be modelled utilizing a Boltzmann distribution of spin states, according to the Eaton-Horrocks equation:^{19b,89}

$$\delta = \delta_{\text{ls}} + \frac{C}{T[1 + e^{(\Delta H - T\Delta S)/RT}]} \quad (2.1)$$

where δ is the experimental chemical shift, δ_{ls} is the calculated shift for the diamagnetic (low spin) species, ΔH and ΔS are the variations in enthalpy and entropy associated with the spin transition, respectively, T is the temperature and C is a constant related to the molar magnetic susceptibility of the high spin species. This equation considers that the spin equilibrium between the singlet and triplet states follows a Boltzmann distribution (the respective equilibrium constant being given by $k = \exp(-\Delta G/RT)$), and that the chemical shifts of the diamagnetic species are independent of temperature, while the behavior of the paramagnetic species corresponds to Curie's Law. It also assumes that the paramagnetic shifts result only from *contact shifts*, resulting from the isotropic interaction between nuclear spin and spin electron density of that nucleus (through bonds), disregarding the *pseudo-contact shifts*, which result from the anisotropic dipole interaction between electron spin and nuclear spin (through space).^{89,90}

The thermodynamic parameters for the singlet-triplet equilibrium, $\text{S} \rightleftharpoons \text{T}$, obtained from the non-linear least-squares fitting of the experimental δ values to the δ values calculated from Equation 2.1, using the software Solver[®], are presented in Table 2.4, as well as the calculated values of k and the effective magnetic moment μ_{eff} .

According to Equation 2.2, the μ_{eff} in solution can be calculated from k , provided that the magnetic moment of the triplet state species (μ_T) is known:^{18c}

$$\mu_{eff}^2 = \mu_T^2 \times x_T + \mu_S^2 \times x_S = \mu_T^2 (1 + 1/k)^{-1} \quad (2.2)$$

where x_T and x_S are the molar fractions of paramagnetic triplet ($S = 1$) and diamagnetic singlet ($S = 0$) species, respectively, and μ_S the magnetic moment of the singlet state species ($\mu_S = 0$).

Considering just the spin-only magnetic moment (neglecting the orbital angular momenta from each of the electrons), the magnetic moment of the species in the triplet state can be given by $\mu_T^2 = n(n + 2) = 2.828 \mu_B$ (see below Equation 2.3), in which n is the number of unpaired electrons ($n = 2$ in a Ni(II) triplet state).

Table 2.4 Thermodynamic parameters of the spin transition obtained from the fits of the ¹H NMR resonances for complexes **2.4a-c**.

Complex	Resonance	ΔH^o (kcal.mol ⁻¹)	ΔS^o (cal.mol ⁻¹ .K ⁻¹)	ΔG^o_{298} (kcal.mol ⁻¹)	k_{298}	μ_{eff} (μ_B)	x_T (%)
2.4a	<i>t</i> Bu	2.54	0.3	2.45	0.016	0.35	2
	C ₅ (CH ₃) ₅	6.83	17.0	1.76	0.051	0.62	5
	HC=CH	4.14	9.0	1.45	0.087	0.80	8
2.4b	<i>t</i> Bu	2.64	0.1	2.60	0.012	0.31	1
	C ₅ (CH ₃) ₅	7.90	21.1	1.61	0.066	0.70	6
	HC=CH	4.60	9.2	1.84	0.045	0.59	4
2.4c	<i>t</i> Bu	2.14	0.1	2.11	0.028	0.47	3
	C ₅ (CH ₃) ₅	7.36	18.9	1.74	0.053	0.63	5
	HC=CH	2.42	2.2	1.77	0.050	0.62	5

The quality of the fit can be estimated from the optimized values of the proton resonances. A reasonable fit can lead to:

- different values for δ_{ls} , regarding the protons of the different groups (in the range of 1.83, 1.49 and 6.47 for *t*Bu, C₅(CH₃)₅ and HC=CH, respectively, for all the three compounds **2.4a-c**), but within the range of the corresponding protons in the free ligand.

Chapter 2

- the same values of ΔH and ΔS , obtained from the ^1H resonances variation, for all the three different groups within the same complex.

The first condition is observed for the 3 compounds. However, with respect to the second condition, as the three values obtained for ΔH and ΔS are not in agreement in none of the complexes, one can assume that Equation 2.1 used in these fits is very likely not adequate to conveniently describe this spin-equilibrium process. As mentioned above, the use of Equation 2.1 is only appropriate if the paramagnetic shifts are attributed exclusively to *contact shifts* (through bonds), while the *pseudo-contact shifts* (through space) are negligible, which may not be the case for this Cp*Ni complexes. In fact, the latter contribution may be significant for spin delocalizations in aromatic π molecular orbitals of Ni(II) complexes.^{90b}

2.2.1.5 Magnetic properties

The effective magnetic moment, μ_{eff} , was measured in benzene solution by the Evans method,⁹¹ and in solid state by means of SQUID magnetometry, at the Solid-State Group laboratory of C²TN-IST, both at room temperature (Table 2.5).

Table 2.5 Effective magnetic moments μ_{eff} (μ_B) measured in benzene solution (Evans method) and in solid state (SQUID magnetometry), at r.t. for complexes **2.4a-c**.

Complex	μ_{eff} (μ_B)	
	solution	solid state
2.4a	1.6	2.02
2.4b	1.5	1.97
2.4c	1.1	1.64

The μ_{eff} can be calculated from the spin quantum number S and the Landé g factor according to the Equation 2.3:

$$\mu_{eff} = \sqrt{g^2 S(S+1)} \quad (2.3)$$

Considering the spin-only contribution and $g = 2$, the theoretical value of μ_{eff} for a high spin state, $S = 1$, is $2.828 \mu_B$. The lower μ_{eff} experimental values obtained in solution, especially for compound **2.4c**, compared to the calculated spin-only value, indicates that for all three compounds, the $S = 1$ state is less populated than the $S = 0$ state, at room temperature (Table 2.6). Consequently, the values of ΔG° are positive for all complexes **2.4a-c**.

Table 2.6 k , ΔG and x_T calculated from the μ_{eff} obtained in solution (Evans method) and in solid state (SQUID magnetometry), at r.t. for complexes **2.4a-c**.

Complex	solution			solid state		
	k_{298}	ΔG°_{298} (kcal.mol ⁻¹)	x_T (%)	k_{298}	ΔG°_{298} (kcal.mol ⁻¹)	x_T (%)
2.4a	0.47	0.45	32	1.04	0.025	51
2.4b	0.39	0.56	28	0.94	0.035	49
2.4c	0.18	1.02	15	0.51	0.40	34

It can be observed from Tables 2.5 and 2.6 that, in solution and in solid state, there is a relatively good agreement between the corresponding values of k , ΔG and x_T . Nevertheless, when comparing these results with those obtained by VT-¹H NMR spectroscopy based on the Eaton-Horrock equation, the calculated x_T is much lower (by around one order of magnitude) than the values shown in Table 2.6. As mentioned before, Equation 2.1 seems to be inadequate for these compounds since the *pseudo-contact shifts* are neglected. Regarding the magnetic studies, it could also be envisaged that a paramagnetic impurity could be present in all the complexes. However, the clear NMR spectra and the good elemental analysis obtained for all the compounds, the crystals of **2.4b-c**, which confirmed to be the right products, as well as the crystallinity of compound **2.4b**, do not corroborate this hypothesis.

The magnetic behavior of **2.4a-c** in solid state is shown in the $\chi_M T$ vs. T plot of Figure 2.47, in the temperature range of 2-300 K, where χ_M is the molar magnetic susceptibility per formula unit.

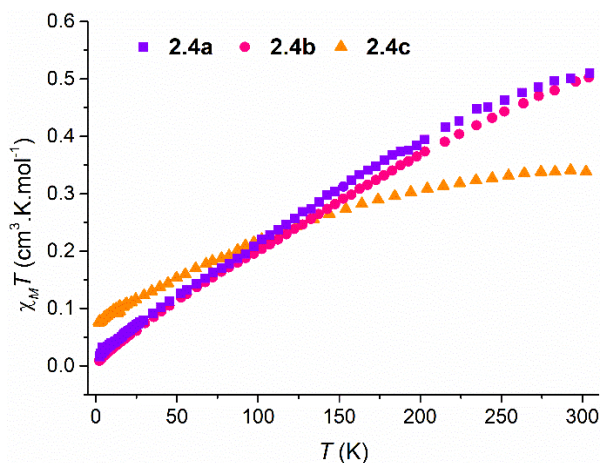


Figure 2.47 $\chi_M T$ vs. T plot for compound **2.4a-c**.

At room temperature, the $\chi_M T$ values are 0.51, 0.49 and 0.34 $\text{cm}^3 \cdot \text{K} \cdot \text{mol}^{-1}$ for complexes **2.4a-c**, respectively, reaching the values of 0.016, 0.009 and 0.077 $\text{cm}^3 \cdot \text{K} \cdot \text{mol}^{-1}$ upon cooling, at 2 K. The $\chi_M T$ of complexes **2.4a-b** increase with increasing temperature, indicating that the percentage of the population of the paramagnetic species in the triplet state is increasing. Therefore, by raising the temperature above 300 K, it would be possible to reach a spin equilibrium between the two states to a theoretical maximum χT value of 75 % (since $S = 1$ has three $M_s = 0, \pm 1$ spin states), which corresponds to equipartition of energy. However, in these complexes, this observation is precluded because of their degradation above +90 °C. Opposite to **2.4a-b**, the $\chi_M T$ values for compound **2.4c** tend to stabilize above *ca.* 200 K, indicating that the concentration of the paramagnetic species tends to a limit.

As mentioned in the introduction, the HOMO-LUMO energy difference (Δ) depends on the electronic properties of the ligands. Moving through the halogen periodic table group, the π -donor character of the halogen increases, simultaneously becoming less electronegative, which also results in an increase in their σ -donor character. By comparing these three compounds, we observe that the spin transition is favored by smaller and more electronegative halogen atoms, as observed for other nickel systems.^{19b,86,92} The decrease in the electronegativity of the halogen, as its volume increases, also translates into a greater covalent character of the Ni–X bond. This means that in the iodine complex the electron cloud associated with that bond is more delocalized than in the chlorine compound, resulting in less repulsion between the electrons, and leading to smaller pairing energies. So basically, the spin pairing in low spin species will have a lower energy cost in complexes containing larger and less electronegative halogen atoms, which

could explain the stabilization of the singlet state in these compounds, namely in complex **2.4c** when compared to the remaining compounds **2.4a-b**.

On the other hand, a spin transition could also be envisaged (Figure 2.48), where the $\chi_M T$ vs. T plot would be more abrupt in a short range of temperatures or, alternatively, the $\chi_M T$ increase would be gradual, as in the present case. In the range of temperature studied (2-300 K), owing to the decomposition of the complexes beyond *ca.* +90 °C, it remains unknown whether by extending this study to higher temperatures it would be possible to detect it.

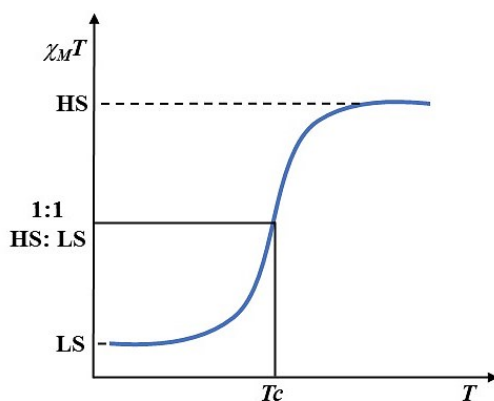


Figure 2.48 Schematic drawing of the plot $\chi_M T$ vs. T in a molecule exhibiting a spin transition process.

Despite the developed work, much remains to be done in order to clearly understand the phenomena behind the magnetic behavior of these three complexes. Therefore, in addition to the experimental work, DFT calculations are of fundamental importance to complement this study, because it is an important tool not only to support the studies developed, but also to enable the design of molecules with optimized properties. Also, single crystal X-ray diffraction measurements at different temperatures would be useful in order to correlate the structural differences with the observed magnetic behavior. As the three X-ray structures were measured at 150 K, it can be observed that all the $\chi_M T$ vs. T plots display similar $\chi_M T$ values, being unlikely to detect any significant differences in distances and angles in all the three structures. Unfortunately, due to lack of time, it was not possible to carry out these complementary studies within the duration of this thesis.

2.2.2 Conclusions

The work developed throughout this chapter allowed to draw some conclusions:

- The complexes $[\text{Ni}(\eta^5\text{-C}_5\text{Me}_5)(t\text{Bu}_2\text{Im})\text{X}]$ ($\text{X} = \text{Cl}, \text{Br}, \text{I}$) **2.4a-c** were synthesized in moderate to high yields (53-88 %) by using a new method, derived from that used by Chetcuti and co-workers, using the isolated NHC ligand instead of the corresponding imidazolium salt.
- By increasing the reaction temperature, this method allowed the occurrence of an intramolecular isomerization of the NHC ligand, leading to the isolation of a new Ni(II) compound containing the Cp* and an abnormal N-heterocyclic carbene ligand $[\text{NiCp}^*\{\text{a}(t\text{Bu}_2\text{Im})\}\text{Cl}]$ **2.5**, with a yield of 59 %, which was characterized by single crystal X-ray diffraction, elemental analysis and NMR spectroscopy.
- With exception of **2.4a**, all the other compounds (**2.4b-c** and **2.5**) afforded crystals suitable for X-ray diffraction; all compounds exhibit η^5 coordination mode of the Cp* ligand to the nickel atom with a diene type distortion for **2.4b** and **2.4c**, whereas **2.5** presents an ene-allyl type distortion.
- The analysis of the paramagnetic shifts observed in the resonances of complexes **2.4a-c**, in VT- ^1H NMR spectroscopy studies, point to the presence of spin equilibrium processes between the diamagnetic singlet ground state ($S = 0$) and the thermally accessible paramagnetic triplet state ($S = 1$) of the complexes, but do not lead to conclusive values of ΔH and ΔS for these processes, probably because the Eaton-Horrocks equation is not adequate for this type of complexes, since the thermodynamic parameters did not converge to the same values.
- The results obtained for the magnetic susceptibilities in solution, by the Evans method, and in solid state, by SQUID magnetometry, show that the triplet state is populated at room temperature, as a consequence of a thermal spin equilibrium process between the singlet and triplet states for complexes **2.4a-c**.

- These studies proved that the energy difference between $S = 0$ and $S = 1$ states in these complexes is indeed influenced by steric and electronic effects, as previously stated. The use of a Cp* ligand instead of a Cp slightly increases the distances between the ligands and the metal center, which consequently is reflected on the magnetic behavior. Also, the less electronegative halogen atom increases the energy gap between the two states, being complex **2.4c** the less well-behaved magnetically as seen in the $\chi_M T$ vs. T plot.

2.3 EXPERIMENTAL SECTION

2.3.1 General considerations

All operations dealing with air- and/or moisture-sensitive materials were carried out under inert atmosphere using a dual vacuum/nitrogen line, glovebox and standard Schlenk techniques. All solvents used were pre-dried with 4 Å molecular sieves and purified by refluxing over a suitable drying agent followed by distillation under nitrogen. THF-*d*₈ and toluene were dried over sodium/benzophenone. Solvents and solutions were transferred using a positive pressure of nitrogen through stainless steel cannulas and mixtures were filtered in a similar way using modified cannulas that could be fitted with glass fiber filter disks. The deuterated solvents used in the preparation of the NMR samples (toluene-*d*₈ and C₆D₆) were dried with molecular sieves (4 Å), degassed with three freeze-pump-thaw cycles and stored under inert atmosphere in J. Young ampoules. The salts LiCl, LiBr and NaI were dried under vacuum at 100 °C for several hours and stored under a nitrogen atmosphere. The imidazolium salts were prepared using the method developed by Arduengo⁹³ and deprotonated with KO*t*Bu, at room temperature, to generate the respective carbenes.⁴⁸ The compound [NiCp*(acac)] was synthesized according to the literature⁹⁴ from the reaction of [Ni(acac)₂] with LiCp*. The remaining reagents were used as received from commercial sources, namely pentamethylcyclopentadiene (Alfa Aesar).

2.3.2 Characterization techniques

2.3.2.1 Nuclear Magnetic Resonance

NMR spectra were recorded on Bruker "AVANCE III" 300 MHz (¹H, 299.995 MHz; ¹³C, 75.4296 MHz) or 400 MHz (¹H, 400.130 MHz; ¹³C, 100.613 MHz) spectrometers. The spectra were referenced internally using the residual proton resonances (¹H) and the solvent carbon (¹³C) resonances of the corresponding solvents to tetramethylsilane (δ = 0). All chemical shifts are quoted in δ (ppm) with the singlet multiplicity abbreviated as s. The samples were dissolved in degassed and dried C₆D₆ or

toluene-*d*₈ prepared inside a glovebox and transferred to J. Young NMR tubes. The deuterated solvents were dried over activated 4 Å molecular sieves and degassed by the freeze-pump-thaw technique. The magnetic susceptibility measurements in solution were carried out by the Evans method⁹¹ using a 3 % solution of hexamethyldisiloxane in C₆D₆ as reference.

2.3.2.2 Single crystal X-ray diffraction

Crystals suitable for X-ray diffraction were selected under an inert atmosphere, covered with polyfluoroether oil, and mounted on a nylon loop. The crystallographic data were collected using graphite monochromated Mo-K α radiation ($\lambda = 0.71073$ Å) on a Bruker AXS-KAPPA APEX II diffractometer equipped with an Oxford Cryosystem open-flow nitrogen cryostat, at 150 K. Cell parameters were retrieved using Bruker SMART software and refined using Bruker SAINT⁹⁵ on all observed reflections. Absorption corrections were applied using SADABS.⁹⁶ Structure solution and refinement were performed using direct methods with the programs SIR2014⁹⁷ and SHELXL⁹⁸ included in the package of programs WINGX-Version 2014.1.⁹⁹ All non-hydrogen atoms were refined anisotropically and the hydrogen atoms were inserted in idealized positions and refined as riding on the parent carbon atom. All the structures refined to a perfect convergence. The graphic presentations were generated using ORTEP-3,¹⁰⁰ where ellipsoids were drawn with a 30 % probability, and the hydrogen atoms were omitted for clarity. The most relevant crystallographic data for each compound is presented along the thesis text, while the experimental details are presented in Appendix II, Table II.3.

2.3.2.3 Elemental analysis

The elemental analysis were performed in a Fisons Instrument Mod EA-108, at *Laboratório de Análises of Instituto Superior Técnico (IST)*. All samples were prepared in sealed glass ampoules, under inert atmosphere and quickly weighed and mounted in air prior to combustion. Two independent determinations for each compound were executed.

2.3.2.4 Magnetic measurements

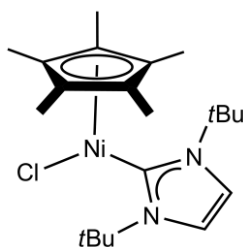
All samples (10-20 mg) used in the magnetic measurements were transferred to the sample holder in a glovebox, due to their air sensitivity. The magnetic measurements were performed using a 6.5 T S700X SQUID (Cryogenic Ltd.) magnetometer. The magnetic susceptibility was measured as a function of temperature under a static magnetic field of 500 G for **2.4a** and 1000 G for **2.4b-c** in the temperature range of 2-300 K. The diamagnetism correction for the experimental data was estimated using the Pascal constants as -2.55×10^{-4} , -2.80×10^{-4} and -2.66×10^{-4} emu mol⁻¹ for compounds **2.4a**, **2.4b** and **2.4c**, respectively.¹⁰¹

2.3.3 Synthetic procedures

2.3.3.1 General procedure for the syntheses of [Ni(η^5 -C₅Me₅)(tBu₂Im)X]

A solution of tBu₂Im (0.28g, 1.5mmol) in THF (20 mL) was added dropwise under nitrogen to a Schlenk tube containing a red solution of [NiCp*(acac)] (0.450g, 1.5 mmol) in the same solvent (20 mL), at -10 °C. After 5 minutes stirring at the same temperature, an excess of alkali halide salt (6 mmol) was added and the reaction mixture stirred for 2 hours in a cold bath at -10 °C. After warming to room temperature, the solvent was evaporated to dryness under vacuum and the crude was extracted at least three times with toluene.

2.3.3.1.1 Synthesis of [Ni(η^5 -C₅Me₅)(tBu₂Im)Cl] (**2.4a**)



Experimental Section

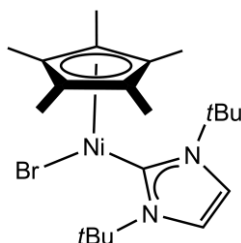
The general procedure described above was applied. After adding the LiCl salt, the color of the reaction changed from red to purple. Extraction of the crude with toluene, concentration of the solvent and storage at -20 °C gave the pure product as a purple solid. Yield: 0.54 g (88 %).

Anal. Calc. for $C_{21}H_{35}N_2NiCl$, obtained (calculated): C 61.59 (61.74), H 8.46 (8.64), N 7.01 (6.86)

1H NMR (400 MHz, toluene- d_8): δ 6.66 (s, 2H, HC=CH), 2.06 (s, 18, C(CH₃)₃), 1.82 (s, 15, C₅(CH₃)₅).

^{13}C NMR (100 MHz, toluene- d_8): δ 179.75 (NCN), 119.66 (HC=CH), 104.89 (C₅(CH₃)₅), 59.30 (C(CH₃)₃), 32.40 (C(CH₃)₃), 9.69 (C₅(CH₃)₅).

2.3.3.1.2 Synthesis of [Ni(η^5 -C₅Me₅)(tBu₂Im)Br] (2.4b)



The general procedure described above was applied. After adding the LiBr salt, the color of the reaction changed from red to purple. Extraction of the crude with toluene, concentration of the solvent and storage at -20 °C gave the pure product as dichroic purple/red crystals.

Yield: 0.495 g (73 %).

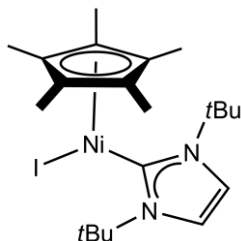
Anal. Calc. for $C_{21}H_{35}N_2NiBr$, obtained (calculated): C .55.96 (55.74), H 8.02 (7.80), N 6.35. (6.19).

1H NMR (300 MHz, toluene- d_8): δ 6.67 (s, 2H, HC=CH), 2.03 (s, 18, C(CH₃)₃), 1.76 (s, 15, C₅(CH₃)₅).

Chapter 2

^{13}C NMR (75 MHz, toluene- d_8): δ 176.81 (NCN), 120.14 (HC=CH), 104.95 ($\text{C}_5(\text{CH}_3)_5$), 59.41 ($\text{C}(\text{CH}_3)_3$), 32.70 ($\text{C}(\text{CH}_3)_3$), 10.26 ($\text{C}_5(\text{CH}_3)_5$).

2.3.3.1.3 Synthesis of $[\text{Ni}(\eta^5\text{-C}_5\text{Me}_5)(\text{tBu}_2\text{Im})\text{I}]$ (2.4c)



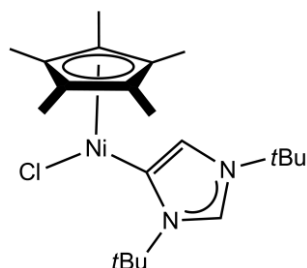
The general procedure described above was applied. After adding the NaI salt, the color of the reaction changed from red to brown. Extraction of the crude with toluene, concentration of the solvent and storage at $-20\text{ }^\circ\text{C}$ gave the pure product as dichroic red/green crystals.

Yield: 0.4 g (53 %).

Anal. Calc. for $\text{C}_{21}\text{H}_{35}\text{N}_2\text{NiI}$, obtained (calculated): C 49.98 (50.39), H 6.95 (7.05), N 5.69 (5.60).

^1H NMR (300 MHz, toluene- d_8): δ 6.65 (s, 2H, HC=CH), 1.96 (s, 18, $\text{C}(\text{CH}_3)_3$), 1.60 (s, 15, $\text{C}_5(\text{CH}_3)_5$).

^{13}C NMR (75 MHz, toluene- d_8): δ 170.36 (NCN), 120.73 (HC=CH), 104.34 ($\text{C}_5(\text{CH}_3)_5$), 59.59 ($\text{C}(\text{CH}_3)_3$), 33.09 ($\text{C}(\text{CH}_3)_3$), 11.4 ($\text{C}_5(\text{CH}_3)_5$).

2.3.3.2 Synthesis of $[\text{Ni}(\eta^5\text{-C}_5\text{Me}_5)\{\text{a}(\text{tBu}_2\text{Im})\}\text{Cl}]$ (2.5)

A solution of *t*Bu₂Im (0.28g, 1.5mmol) in THF (20 mL) was added dropwise under nitrogen to a Schlenk tube containing a red solution of [NiCp*(*acac*)] (0.450g, 1.5mmol) in the same solvent (20 mL) at room temperature. After 5 minutes stirring, an excess of LiCl (0.254g, 6 mmol) was added (the color changed instantly from red to purple). The reaction mixture was left stirring overnight at *ca.* 70 °C. After cooling to room temperature, the color of the reaction mixture changed to red, the solvent was evaporated to dryness under vacuum and the brown crude was extracted with toluene. Concentration of the solvent and storage at -20 °C gave the pure product as pink crystals.

Yield: 0.363 g (59 %).

Anal. Calc. for C₂₁H₃₅N₂NiCl, obtained (calculated): C 61.42 (61.74), H 8.85 (8.64), N 6.51 (6.86)

¹H NMR (300 MHz, THF-*d*₈): δ 8.32 (s, 1H, H13), 6.87 (s, 1H, H12), 2.06 (s, 9H, C(CH₃)₃), 1.55 (s, 9H, C(CH₃)₃), 1.40 (s, 15H, C₅(CH₃)₅)

¹³C NMR (75 MHz, THF-*d*₈): δ 139.77 (C 11), 130.97 (C13), 123.28 (C12), 99.84 (C(CH₃)₃), 59.55 (C(CH₃)₃), 57.18 (C(CH₃)₃), 31.67 (C(CH₃)₃), 29.85 (C(CH₃)₃), 10.25 (C₅(CH₃)₅).

2.4 REFERENCES

- 1 Kealy, T. J.; Pauson, P. L. *Nature*, **1951**, *168*, 1039.
- 2 O'Connor, J. M.; Casey, C. P. *Chem. Rev.* **1987**, *87*, 307
- 3 Chetwynd-Talbot, J.; Grebenik, P.; Perutz, R. N.; Powell, M. H. A. *Z. Inorg. Chem.* **1983**, *22*, 1675.
- 4 Bochmann, M. *Organometallics 2 – Complexes with transition metal-carbon π -bonds*, Oxford Chemistry Primers, Oxford University Press, 1st Ed., Oxford, **1994**.
- 5 (a) Wilkinson, G.; Pauson, P. L.; Birmingham, J. M.; Cotton, F. A.; Woodward, R. B. *J. Am. Chem. Soc.* **1953**, *75*, 1011; (b) Fischer, E. O.; Jira, R. *Naturforschung*, **1953**, *8B*, 217.
- 6 Abernethy, C. D.; Clyburne, J. A. C.; Cowley, A. H.; Jones, R. A. *J. Am. Chem. Soc.* **1999**, *121*, 2329.
- 7 Ohta, H.; Miyoshi, N.; Sakata, Y.; Okamoto, Y.; Hayashi, M.; Watanabe, Y. *Tetrahedron Lett.* **2015**, *56*, 2910.
- 8 Crabtree, R. H. *The Organometallic Chemistry of the Transition Metals*, John Wiley & Sons, 7th Edition, New York, **2019**.
- 9 Veiros, L. F. *J. Organomet. Chem.* **1999**, *587*, 221.
- 10 Calhorda, M. J.; Veiros, L. F. *Coord. Chem. Rev.* **1999**, *37*, 185.
- 11 Holland, P. L.; Smith, M. E.; Andersen, R. A.; Bergman, R. G. *J. Am. Chem. Soc.* **1997**, *119*, 12815.
- 12 Mohammed M. R.; Abdullahn M. A. *Recent Progress in Organometallic Chemistry*, London: IntechOpen, **2017**.
- 13 Salzer, A.; Werner, H.; *Angew. Chem.* **1972**, *84*, 949.
- 14 Smith, M. E.; Andersen, R. A. *J. Am. Chem. Soc.* **1996**, *118*, 11119.
- 15 Bunel, E. E.; Valle, L.; Manriquez, J. M. *Organometallics* **1985**, *4*, 1680.
- 16 (a) Shatruk, M.; Dragulescu-Andrasi, A.; Chambers, K. E.; Stoian, S. A.; Bominaar, E. L.; Achim, C.; Dunbar, K. R. *J. Am. Chem. Soc.* **2007**, *129*, 6104; (b) Ksenofontov, V.; Gaspar, A. B.; Gütllich, P. *Pressure effect studies on spin crossover and valence tautomeric systems*. In: P. Gütllich, H. A. Goodwin (Eds.), *Spin Crossover in Transition Metal Compounds III*. Topics in Current Chemistry, Vol. 235. Springer Berlin, Heidelberg, **2004**, pp. 23-64; (c) Graaf, C.; Sousa, C. *Chem. Eur. J.* **2010**, *16*, 4550.

- 17 Cambi, L.; Szegő, L. *Ber. Dtsch. Chem. Ges. B*, **1931**, *64*, 2591.
- 18 (a) Kläui, W.; Eberspach, W.; Gütlich, P. *Inorg. Chem.* **1987**, *26*, 3977; (b) Al-Obaidi, A. H. R.; Jensen, K. B.; McGarvey, J. J.; Toftlund, H.; Jensen, B.; Bell, S. E. J.; Carroll, J. G. *Inorg. Chem.* **1996**, *35*, 5055; (c) Pulliam, C. R.; Thoden, J. B.; Stacy, A. M.; Spencer, B.; Englert, M. H.; Dahl, L. F. *J. Am. Chem. Soc.* **1991**, *113*, 7398; (d) Tayagaki, T.; Galet, A.; Molnár, G.; Muñoz M. C.; Zwick, A.; Tanaka, K.; Real, J.-A.; Bousseksou, A. *J. Phys. Chem. B*, **2005**, *109*, 14859; (e) Gütlich, P.; Hauser, A.; Spiering, H. *Angew. Chem. Int. Ed. Engl.* **1994**, *33*, 2024; (f) Gorrell, B.; Parkin, G. *Inorg. Chem.* **1990**, *29*, 2452; (g) Weber, B.; Carbonera, C.; Desplances, C.; Létard, J-F. *Eur. J. Inorg. Chem.* **2008**, 1589; (h) Guo, Y.; Yang, X-L.; Wei, R-J.; Zheng, L-S.; Tao, J. *Inorg. Chem.* **2015**, *54*, 7670; (i) Zhu, Y-Y.; Li, H-O.; Ding, Z-Y.; Lü, X-J.; Zhao, L.; Meng, Y-S.; Liu, Tao, Gao, S. *Inorg. Chem. Front.* **2016**, *3*, 1624; (j) Nakaya, M.; Ohtani, R.; Shin, J. W.; Nakamura, M.; Lindoy, L. F.; Hayami, S. *Dalton Trans.* **2018**, *47*, 13809; (k) Boniolo, M.; Shylin, S. I.; Chernev, P.; Cheah, M. H.; Heizmann, P. A.; Huang, P.; Salhi, N.; Hossain, K.; Thapper, A.; Lundberg, M.; Messinger, J. *Chem. Commun.* **2020**, *56*, 2703; (l) Ossinger, S.; Näther, C.; Buchholz, A.; Schmidtman, M.; Mangelsen, S.; Beckhaus, R.; Plass, W.; Tuczek, F. *Inorg. Chem.* **2020**, *59*, 7966.
- 19 (a) Chetcuti, M. J. *Nickel–Carbon π -Bonded Complexes*. In: G. Wilkinson, F.G.A. Stone, E.W. Abel (Eds.), *Comprehensive Organometallic Chemistry II*; Vol. 9, Pergamon Press, Oxford, **1995**, pp. 107–191; (b) Pignolet, L. H.; Horrocks Jr, W. D. *J. Am. Chem. Soc.* **1969**, *91*, 3976.
- 20 (a) Ohtsu, H.; Tanaka, K. *Inorg. Chem.* **2004**, *43*, 3024; (b) Szacilowski, K. T.; Xie, P.; Malkhasian, A. Y. S.; Heeg, M. J.; Udugala-Ganehenege, M. Y.; Wenger, L. E.; Endicott, J. F. *Inorg. Chem.* **2005**, *44*, 6019; (c) Shokurov, A. V.; Kutsybala, D. S.; Kroitor, A. P.; Dmitrienko, A. A.; Martynov, A. G.; Enakieva, Y. Y.; Tsvadze, A. Y.; Selektor, S. L.; Gorbunova, Y. G. *Molecules*, **2021**, *26*, 4155; (d) Qamar, O. A.; Cong, C.; Ma, H. *Dalton Trans.* **2020**, *49*, 17106; (e) Ma, H.; Petersen, J. L.; Young Jr, V. G.; Yee, G. T.; Jensen, M. P. *J. Am. Chem. Soc.* **2011**, *133*, 5644.
- 21 Frydendahl, H.; Toftlund, H.; Becher, J.; Dutton, J. C.; Murray, K. S.; Taylor, L. F.; Anderson, O. P.; Tiekink, E. R. T. *Inorg. Chem.* **1995**, *34*, 4467.
- 22 Doering, W. E.; Roth, W. R. *Tetrahedron*, **1964**, *19*, 751.
- 23 Doering, W. E.; Roth, W. R. *Angew. Chem., Int. Ed. Engl.* **1963**, *2*, 115.

Chapter 2

- 24 Mutterties, E. L. *Inorg. Chem.* **1965**, 4, 769.
- 25 Bennett, M. J., Jr.; Cotton, F. A.; Davison, A.; Faller, J. W.; Lippard, S. J.; Morehouse, S. W. *J. Am. Chem. Soc.* **1966**, 88, 4371.
- 26 (a) Calderon, J. L.; Cotton, F. A.; DeBoer, B. G.; Takats, J. *J. Am. Chem. Soc.* **1970**, 92, 3801; (b) Calderon, J. L.; Cotton, F. A.; Takats, J. *J. Am. Chem. Soc.* **1971**, 93, 3587; (c) Cotton, F. A.; Musco, A.; Yagupski, G. *J. Am. Chem. Soc.* **1967**, 89, 6136; (d) Cotton, F. A.; Legzdins, P. *J. Am. Chem. Soc.* **1968**, 90, 6232; (e) Calderon, J. L.; Cotton, F. A.; Legzdins, P. *J. Am. Chem. Soc.* **1969**, 91, 2528; (f) Cotton, F. A.; Rusholme, G. A. *J. Am. Chem. Soc.* **1972**, 94, 402; (g) Hunt, M. M.; Kita, W. G.; Mann, B. E.; McCleverty, J. A. *J. Chem. Soc., Dalton Trans.* **1978**, 467.
- 27 Shriver, D. F.; Atkins, P. W.; Langford, C. H. *Inorganic Chemistry*, 2nd Ed., Oxford University Press, Oxford, **1998**.
- 28 (a) Green, M. L. H.; Michaelidou, D. N.; Mountford, P.; Suárez, A. G.; Wong, L.-L. *J. Chem. Soc., Dalton Trans.* **1993**, 1593; (b) Antonelli, D. M.; Gomes, P. T.; Green, M. L. H.; Martins, A. M.; Mountford, P. *J. Chem. Soc., Dalton Trans.* **1997**, 2435.
- 29 (a) Erker, G.; Nolte, R.; Tainturier, G.; Rheingold, A. *Organometallics* **1989**, 8, 454; (b) Waugh, J. S.; Loehlin, J. H.; Cotton, F. A.; Shoemaker, D. P. *J. Chem. Phys.* **1959**, 31, 1434.
- 30 Okuda, J. *J. Organomet. Chem.* **1988**, 353, C1-C4.
- 31 Jolly, P.W.; Wilke, G. *The Organic Chemistry of Nickel*, Academic Press, Vol. I, Cap. VI, New York, **1974**.
- 32 Pasynkiewicz, S.; Pietrzykowski, A. *Coord. Chem. Rev.* **2002**, 231, 199.
- 33 (a) Kuhn, H.; Winter, M. *J. Organomet. Chem.* **1983**, 256, C5. (b) Kuhn, H.; Winter, M. *J. Organomet. Chem.* **1983**, 243, C83. (c) Kuhn, H.; Winter, M. *J. Organomet. Chem.* **1983**, 243, C42. (d) Bellis, V. M.; Kuhn, N.; Winter, M. *Inorg. Chim. Acta*, **1985**, 104, L11. (e) Kuhn, H.; Winter, M. *Chem.-Ztg.* **1983**, 107, 14; (f) Salzer, A., Court, T. L.; Werner, H. *J. Organomet. Chem.* **1973**, 54, 325.
- 34 Kuhn, H.; Winter, M. *J. Organomet. Chem.* **1986**, 301, C9.
- 35 (a) Jutzi, P. *Comments Inorg. Chem.* **1987**, 6, 123; (b) Jutzi, P.; Reumann, G. *J. Chem. Soc., Dalton Trans.* **2000**, 2237.
- 36 Arduengo, A. J.; Dias, H. V. R.; Dixon, D. A.; Harlow, R. L.; Klooster, W. T.; Koetzle, T. F. *J. Am. Chem. Soc.* **1994**, 116, 6812.
- 37 Díez-González, S.; Nolan, S. P. *Coord. Chem. Rev.* **2007**, 251, 874.

- 38 Bourissou, D.; Guerret, O.; Gabbaï, F. P.; Bertrand, G. *Chem. Rev.* **2000**, *100*, 39.
- 39 Irikura, K. K.; Goddard, W. A.; Beauchamp, J. L. *J. Am. Chem. Soc.* **1992**, *114*, 48.
- 40 Arduengo, A. J.; Dias, H. V. R.; Harlow, R. L.; Kline, M. *J. Am. Chem. Soc.* **1992**, *114*, 5530.
- 41 Fischer, E. O.; Maasböl, A. *Angew. Chem., Int. Ed. Engl.* **1964**, *3*, 580.
- 42 Boehme, C.; Frenking, G.; *Organometallics* **1998**, *17*, 5801.
- 43 Schrock, R. R. *J. Am. Chem. Soc.* **1974**, *96*, 6796.
- 44 Wanzlick, H. W.; Schönherr, H. J. *Angew. Chem., Int. Ed. Engl.* **1968**, *7*, 141.
- 45 Öfele, K. J. *Organomet. Chem.* **1968**, *12*, P42.
- 46 Hopkinson, M. N.; Richter, C.; Schedler, M.; Glorius, F. *Nature*, **2014**, *510*, 485.
- 47 Schönherr, H. J.; Wanzlick, H. W. *Chem. Ber.* **1970**, *103*, 1037.
- 48 Arduengo, A. J.; Harlow, R. L.; Kline, M. A.; *J. Am. Chem. Soc.* **1991**, *113*, 361.
- 49 Jahnke, M. C.; Hahn, F. E. *Introduction to N-Heterocyclic Carbenes: Synthesis and Stereoelectronic Parameters* (Ch. 1). In: S. Díez-González (Ed.), *N-Heterocyclic Carbenes: From Laboratory Curiosities to Efficient Synthetic Tools*, 2nd Ed., RSC, **2016**.
- 50 (a) Arduengo, A. J.; Goerlich, J. R.; Marshall, W. J. *J. Am. Chem. Soc.* **1995**, *117*, 11027; (b) Arduengo, A. J.; Goerlich, J. R.; Marshall, W. J. *Liebigs Ann.* **1997**, 365; (c) Enders, D.; Breuer, K.; Raabe, G.; Runsink, J.; Teles, J. H.; Melder, J. P.; Ebel, K.; Brode, S. *Angew. Chem.* **1995**, *107*, 1119; (d) Hahn, F. E.; Wittenbecher, L.; Boese, R.; Bläser, D. *Chem. Eur. J.* **1999**, *5*, 1931; (e) Lavallo, V.; Canac, Y.; Präsang, C.; Donnadieu, B.; Bertrand, G. *Angew. Chem. Int. Edn.* **2005**, *44*, 5705; (f) Aldeco-Perez, E.; Rosenthal, J.; Donnadieu, B.; Parameswaran, P.; Frenking, F.; Bertrand, G. *Science* **2009**, *326*, 556; (g) Schuster, O.; Yang, L.; Raubenheimer, H. G.; Albrecht, M. *Chem. Rev.* **2009**, *109*, 3445.
- 51 Herrmann, W. A.; Kocher, C. *Angew. Chem., Int. Ed. Engl.* **1997**, *36*, 2162.
- 52 Arduengo, A. J.; Gamper, S. F.; Callabrese, J. C.; Davidson, F. *J. Am. Chem. Soc.* **1994**, *116*, 4391.
- 53 Nemcsok, D.; Wichmann, K.; Frenking, G. *Organometallics* **2004**, *23*, 3640.
- 54 (a) Termaten, A. T.; Schakel, M.; Ehlers, A. W.; Lutz, M.; Spek, A. L.; Lammertsma, K. *Chem. Eur. J.* **2003**, *9*, 3577; (b) Garrison, J. C.; Simons, R. S.; Kofron, W. G.; Tessier, C. A.; Youngs, W. J. *Chem. Commun.* **2001**, 1780; (c) Abernethy, C. D.; Codd, G. M.; Spicer, M. D.; Taylor, M. K. *J. Am. Chem. Soc.* **2003**, *125*, 1128; (d) Hu, X.; Castro-Rodriguez, I.; Olsen, K.; Meyer, K. *Organometallics*

Chapter 2

- 2004, 23, 755; (e) Cavallo, L.; Correa, A.; Costabile, C.; Jacobsen, H. *J. Organomet. Chem.* **2005**, 690, 5407. (f) Hu, X.; Tang, Y.; Gantzel, P.; Meyer, K. *Organometallics* **2003**, 22, 612. (g) Hu, X.; Meyer, K. *J. Organomet. Chem.* **2005**, 690, 5474.; (h) Vogler, A.; Kunkely, H. *Coord. Chem. Rev.* **2004**, 248, 273.
- 55 Herrmann, W. A.; Runte, O.; Artus, G. *J. Organomet. Chem.* **1995**, 501, C1.
- 56 Green, J. C.; Scurr, R. G.; Arnold, P. L.; Cloke, F. G. N. *Chem. Commun.* **1997**, 1963.
- 57 Herrmann, W. A. *Angew. Chem. Int. Ed. Engl.* **2002**, 41, 1290.
- 58 Tolman, C. A. *Chem. Rev.* **1977**, 77, 313.
- 59 Chianese, A. R.; Li, X.; Janzen, M. C.; Faller, J. W.; Crabtree, R. H. *Organometallics* **2003**, 22, 1663.
- 60 Kelly, R. A.; Clavier, H.; Giudice, S.; Scott, N. M.; Stevens, E. D.; Bordner, J.; Samardjiev, I.; Hoff, C. D.; Cavallo, L.; Nolan, S. P. *Organometallics* **2008**, 27, 202.
- 61 Wolf, S.; Plenio, H. *J. Organomet. Chem.* **2009**, 694, 1487.
- 62 Schaub, T.; Radius, U. *Chem. Eur. J.* **2005**, 11, 5024.
- 63 Dorta, R.; Stevens, E. D.; Scott, N. M.; Costabile, C.; Cavallo, L.; Hoff, C. D.; Nolan, S. P. *J. Am. Chem. Soc.* **2005**, 127, 2485.
- 64 Köcher, C.; Herrmann, W. A. *J. Organomet. Chem.* **1997**, 532, 261.
- 65 Huang, J. K.; Stevens, E. D.; Nolan, S. P. *Organometallics* **2000**, 19, 1194.
- 66 Chianese, A. R.; Kovacevic, A.; Zeglis, B. M.; Faller, J. W.; Crabtree, R. H. *Organometallics* **2004**, 23, 2461.
- 67 Rahman, M. M.; Liu, H.-Y.; Eriks, K.; Prock, A.; Giering, W. P. *Organometallics* **1989**, 8, 1.
- 68 Huang, J. K.; Schanz, H. J.; Stevens, E. D.; Nolan, S. P. *Organometallics* **1999**, 18, 2370.
- 69 Dorta, R.; Stevens, E. D.; Hoff, C. D.; Nolan, S. P. *J. Am. Chem. Soc.* **2003**, 125, 10490.
- 70 Perrin, L.; Clot, E.; Eisenstein, O.; Loch, J.; Crabtree, R. H. *Inorg. Chem.* **2001**, 40, 5806.
- 71 Magill, A. M.; Cavell, K. J.; Yates, B. F. *J. Am. Chem. Soc.* **2004**, 126, 8717.
- 72 Cavallo, L.; Correa, A.; Costabile, C.; Jacobsen, H. *J. Organomet. Chem.* **2005**, 690, 5407.
- 73 Hillier, A. C.; Sommer, W. J.; Yong, B. S.; Petersen, J. L.; Cavallo, L.; Nolan, S.

- 73 Hillier, A. C.; Sommer, W. J.; Yong, B. S.; Petersen, J. L.; Cavallo, L.; Nolan, S. *P. Organometallics* **2003**, *22*, 4322.
- 74 Regitz, M. *Angew. Chem., Int. Ed. Engl.* **1996**, *35*, 725.
- 75 Banach, Ł.; Guńka, P.A.; Zachara, J.; Buchowicz, W. *Coord. Chem. Rev.* **2019**, *389*, 19.
- 76 Abernethy, C. D.; Cowley, A. H. Jones, R. A. *J. Organomet. Chem.* **2000**, *596*, 3.
- 77 Kelly, R. A.; Scott, N. M.; Díez-González, S.; Stevens, E. D.; Nolan, S. P. *Organometallics* **2005**, *24*, 3442.
- 78 Ritleng, V.; Barth, C.; Brenner, R.; Milosevic, S.; Chetcuti, M. J. *Organometallics* **2008**, *27*, 4223.
- 79 Oertel, A. M.; Ritleng, V.; Chetcuti, M. J. *Organometallics* **2012**, *31*, 2829.
- 80 Ritleng, V.; Oertel, A. M.; Chetcuti, M. J. *Dalton Trans.* **2010**, *39*, 8153.
- 81 Junquera, L. B.; Fernández, F. E.; Puerta, M. C.; Valerga, P. *Eur. J. Inorg. Chem.* **2017**, 2547.
- 82 Fischer, P.; Linder, T.; Radius, U. *Anorg. Allg. Chem.* **2012**, *638*, 1491.
- 83 Sun, H.-M.; Hu, D.-M.; Wang, Y.-S.; Shen, Q.; Zhang, Y. *J. Organomet. Chem.* **2007**, *692*, 903.
- 84 Postigo, L.; Royo, B. *Adv. Synth. Catal.* **2012**, *354*, 2613.
- 85 Postigo, L.; Lopes, R.; Royo, B. *Dalton Trans.* **2014**, *43*, 853.
- 86 Silva, L. A. C. *Complexos alílicos, ciclopentadienílicos e indenílicos de níquel(II) estabilizados por carbenos N-heterocíclicos*, PhD Thesis, IST – Universidade Técnica de Lisboa, **2007**.
- 87 Gründemann, S.; Kovacevic, A.; Albrecht, M.; Faller, J. W.; Crabtree R. H. *Chem. Commun.* **2001**, 2274.
- 88 (a) Sini, G.; Eisenstein, O.; Crabtree, R. H. *Inorg. Chem.* **2002**, *41*, 602; (b) Tonner, R.; Heydenrych G.; Frenking, G. *Chem. Asian J.* **2007**, *2*, 1555; (c) Denk, K.; Sirsch, P.; Herrmann, W. A. *J. Organomet. Chem.* **2002**, *649*, 219; (d) Bazinet, P.; Yap, G. P. A.; Richeson, D. S. *J. Am. Chem. Soc.* **2003**, *125*, 13314; (e) Mayr, M.; Wurst, K.; Ongania, K.-H.; Buchmeiser, M. R. *Chem. – Eur. J.* **2004**, *10*, 1256; (f) Chianese, A. R.; Kovacevic, A.; Zeglis, B. M.; Faller, J. W.; Crabtree, R. H. *Organometallics* **2004**, *23*, 2461.
- 89 (a) Eaton, D. R.; Phillips, W. D.; Caldwell, D. J. *J. Am. Chem. Soc.* **1963**, *1*, 397; (b) Eaton, D. R.; Phillips, W. D. *Adv. Magn. Reson.* **1965**, *1*, 103.

Chapter 2

- 90 (a) Eaton, D. R. *J. Chem. Phys.* **1965**, *43*, 392; (b) McGarvey, B. R. *Inorg. Chem.* **1995**, *34*, 6000; (c) Engelhardt, G.; Feuerstein, M.; Sieger, P.; Markgraber, D.; Stucky, G.; Srdanov, V. *Chem. Commun.* **1996**, 729; (d) Cremer, P.; Burger, P. *J. Am. Chem. Soc.* **2003**, *125*, 7664.
- 91 (a) Evans, D. F. *J. Chem. Soc.* **1959**, 2003; (b) Kur, S. K. *J. Magn. Reson.* **1989**, *82*, 169.
- 92 Sacconi, L. *J. Chem. Soc. (A)*, **1970**, 248.
- 93 Arduengo, A. J., World Patent WO9114678 5, Oct 3, **1991**.
- 94 Bunel, E. E.; Valle, L.; Manriquez, J. M. *Organometallics* **1985**, *4*, 1680.
- 95 *SAINTE Software for the CCD Detector System*, Version 7.03, Bruker AXS Inc., Madison, WI, USA, **2004**.
- 96 Sheldrick, G. M. *SADABS, Program for Empirical Absorption Correction*, Univ. of Göttingen, German, **1996**.
- 97 Burla, M. C.; Caliandro, R.; Carrozzini, B.; Cascarano, G. L.; Cuocci, C.; Giacovazzo, C.; Mallamo, M.; Mazzone, A.; Polidori, G. Crystal structure determination and refinement via SIR2014, *J. Appl. Cryst.* **2015**, *48*, 306.
- 98 (a) Sheldrick, G. M. Crystal structure refinement with *SHELXL*, *Acta Crystallogr.* **2015**, *71*, 3; (b) Hübschle, C. B.; Sheldrick, G. M.; Dittrich, B. ShelXle: a Qt graphical user interface for SHELXL, *J. Appl. Crystallogr.* **2011**, *44*, 1281.
- 99 (a) Farrugia, L. J. WinGX suite for small-molecule single-crystal crystallography, *J. Appl. Crystallogr.* **1999**, *32*, 837; (b) Farrugia, L. J. WinGX and ORTEP for Windows: an update, *J. Appl. Crystallogr.* **2012**, *45*, 849.
- 100 (a) Burnett, M. N.; Johnson, C. K. *ORTEP-III: Oak Ridge Thermal Ellipsoid Plot Program for Crystal Structure Illustration*, Oak Ridge National Laboratory, **1996**, 6895; (b) Farrugia, L. J. ORTEP-3 for Windows—A Version of It ORTEP-III with a Graphical User Interface (GUI), *J. Appl. Crystallogr.* **1997**, *30*, 565.
- 101 Carlin, R. L. *Magnetochemistry*, Springer, Berlin, **1986**.

CHAPTER 3

**General Conclusions
and
Future Perspectives**

3.1 GENERAL CONCLUSIONS

The aim of this work was the preparation and full characterization of new metal complexes of cobalt and nickel aiming at the study of their unique magnetic properties. This thesis was divided into two Chapters according to the type of metal complexes studied.

Chapter 1 described the study of the Single-Ion Magnet behavior of homoleptic Co(II) compounds bearing two 2-iminopyrrolyl ligands. With this purpose in mind, modifications in the pyrrolyl ligand backbone were performed to evaluate the influence of ligand bulkiness, asymmetry and electronic donor ability on the magnetic properties of this family of complexes, in which it was observed a significant enhancement of the SIM behavior. In order to coordinate these chelating ligands to the cobalt center the deprotonation of their neutral ligand precursors with a strong base, NaH, was first required, a procedure generally performed *in situ*, followed by reaction with CoCl₂, obtaining the intended products, in moderate yields. Each of the synthesized complexes was crystalized in an appropriate solvent at -20 °C, resulting in crystals suitable for X-ray diffraction. The latter technique was an essential tool not only for the correlation between chemical structure and magnetic behavior, but also as a basis and starting point for the theoretical calculations, which were of key importance in this work. All the bis(2-iminopyrrolyl) Co(II) complexes synthesized displayed Single-Ion Magnet behaviors with high values of the magnetic anisotropy, D , and energy barriers for spin reversal, U_{eff} , higher than most of the tetracoordinated Co(II)-based SIMs reported in the literature.

From these studies it can be concluded that changes in the geometry of the complexes, especially from distorted tetrahedral to distorted trigonal pyramidal geometry, enhances the SIM behavior, not only by improving the values of D , but also by displaying slow relaxation of the magnetization at zero DC field. Two of these complexes exhibit considerably high values of U_{eff} 85 and 135(8) cm⁻¹ which, to the best of our knowledge, correspond to the third and second largest values, respectively, for the spin-reversal energy barrier so far reported for a tetrahedral Co(II)-N₄ complex under zero field, which is rare in Co(II) compounds.

Chapter 2 described the study of the spin equilibria existing in nickel complexes of the type [Ni(η^5 -C₅Me₅)(*t*Bu₂Im)X], with X = Cl, Br and I. The compounds of this family were synthesized using a new synthetic route, despite the attempts to follow the procedure

Chapter 3

used by Chetcuti and co-workers. This new method employed the isolated 1,3-bis(*tert*-butyl)imidazol-2-ylidene, *t*Bu₂Im (via the reaction of the corresponding imidazolium chloride salt with KO*t*Bu in THF, followed by evaporation of the solvent to dryness), and its reaction with [NiCp*(*acac*)], in the presence of an excess of the halogen source (LiCl, LiBr and NaI) in THF, at *ca.* -10 °C (**2.4a-c**), to afford the desired complexes. The reaction temperature is crucial, as the formation of a new and unexpected nickel(II) complex stabilized by an abnormal NHC, **2.5c**, occurs by isomerization of the initially coordinated normal *t*Bu₂Im ligand when increasing the temperature to 70 °C. All these compounds were characterized by NMR and, for **2.4b-c** and **2.5**, by single crystal X-ray diffraction, showing diene and ene-allyl type distortions for complexes **2.4b-c** and **2.5**, respectively. The study of the magnetic properties of complexes **2.4a-c** was carried out in solution by VT ¹H-NMR and using the Evans method, and in solid state by DC magnetic measurements. The results revealed that there is in fact a thermal spin equilibrium process between the singlet and triplet states for all the compounds studied. These conclusions corroborate the premise that steric and electronic factors affect the energy gap between the *S* = 0 and *S* = 1 states, since an enhancement of the paramagnetism is obtained when replacing a Cp by a bulkier Cp* group (due to a slightly increase in the distances between the ligands and the metal center) and when changing the halogen atom from less electronegative iodine atom toward the more electronegative bromine and chlorine (the latter effect owing to a decrease of the energy gap between the two states).

3.2 FUTURE PERSPECTIVES

Since the molecular system described in chapter 1 is very promising due to the exhibited high values of magnetic anisotropy and spin-reversal energy barrier, we should consider in the future to further expand this study to other 3*d* transition metals such as iron. Unfortunately, despite synthesizing a few homoleptic Fe(II) compounds bearing 2-iminopyrrolyl ligands, the magnetic properties could not be studied due to lack of time. Since the geometry is an important feature to bear in mind when designing new SIMs, theoretical calculations are of great importance to predict the symmetry of the compounds in order to enhance this behavior.

Regarding Chapter 2, since improved magnetic properties were obtained by replacing the Cp for a Cp* group (which increased the bond lengths between the metal center and the ligands), it would be interesting in the future to try new approaches such as the use of bulkier carbene ligands, like the 1,3-bis(adamant-1-yl)imidazol-2-ylidene, or even replacing the Cp* with bulkier groups (for instance, pentabenzylcyclopentadiene). It would be also important to prepare nickel compounds of the type $[\text{NiCp}^*\{\text{a}(t\text{Bu}_2\text{Im})\}\text{X}]$ (X = Br and I) by changing the reaction temperature, in order to study their magnetic properties and compare them with the studied $[\text{NiCp}^*\{\text{n}(t\text{Bu}_2\text{Im})\}\text{X}]$ compounds.

APPENDIX I

Magnetometers

11. Superconducting Quantum Interference Device (SQUID) - Cryogenic Ltd.

The SQUID magnetometer is the most sensitive magnetometer available, demonstrating a field resolution at the 10^{-17} T level.¹ Developed in 1962, a direct-current (DC) SQUID consists of two Josephson junctions formed into a superconducting ring (Figure I.1). A Josephson junction is made by sandwiching a thin layer of a nonsuperconducting material between two layers of superconducting material. The devices are named after Brian Josephson,² who predicted that pairs of superconducting electrons could "tunnel" right through the non-superconducting barrier from one superconductor to another, where the junction acts as a weak superconductor. From the Ginzburg-Landau theory³ it can be derived, that a DC current flows through such a junction in absence of neither an external voltage nor magnetic field, being this called direct-current (DC) Josephson effect. As for the alternating-current (AC) effect, a voltage is maintained across the junction causing the amplitude of the supercurrent to oscillate in time.

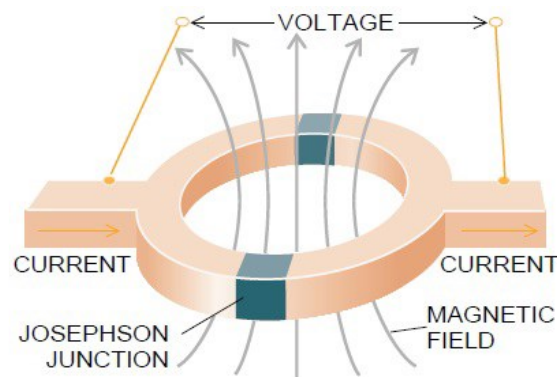


Figure I.1 The direct-current (DC) SQUID consisting of two Josephson junctions arranged on a superconducting ring.⁴

The SQUID magnetometers usually detect the change of magnetic flux, created by mechanically moving of the sample through superconducting pick-up coils. This movement induces a current that is detected in the SQUID, producing an output voltage proportional to the magnetization of the sample. The great sensitivity of the SQUID devices is associated with measuring changes in magnetic field related to one magnetic flux quantum: $\Phi_0 = \frac{2\pi\hbar}{2e} \approx 2,0678 \times 10^{-15} \text{ T} \cdot \text{m}^2$ (\hbar is the reduced Planck constant and

Appendix I

e is the elementary charge). Therefore, the SQUID in essence is a flux-to-voltage transducer, converting tiny changes in magnetic flux into a voltage. To reliably suppress the influence of all kinds of external magnetic fields, the pick-up coils are made as second order gradiometer. Figure I.2 shows the scheme of a general detection system and a single scan, where the maximum of the voltage signal, V_{SQUID} , corresponds to the sample centered in between the double coil of the pick-up gradiometer and the view of the cryostat.⁵

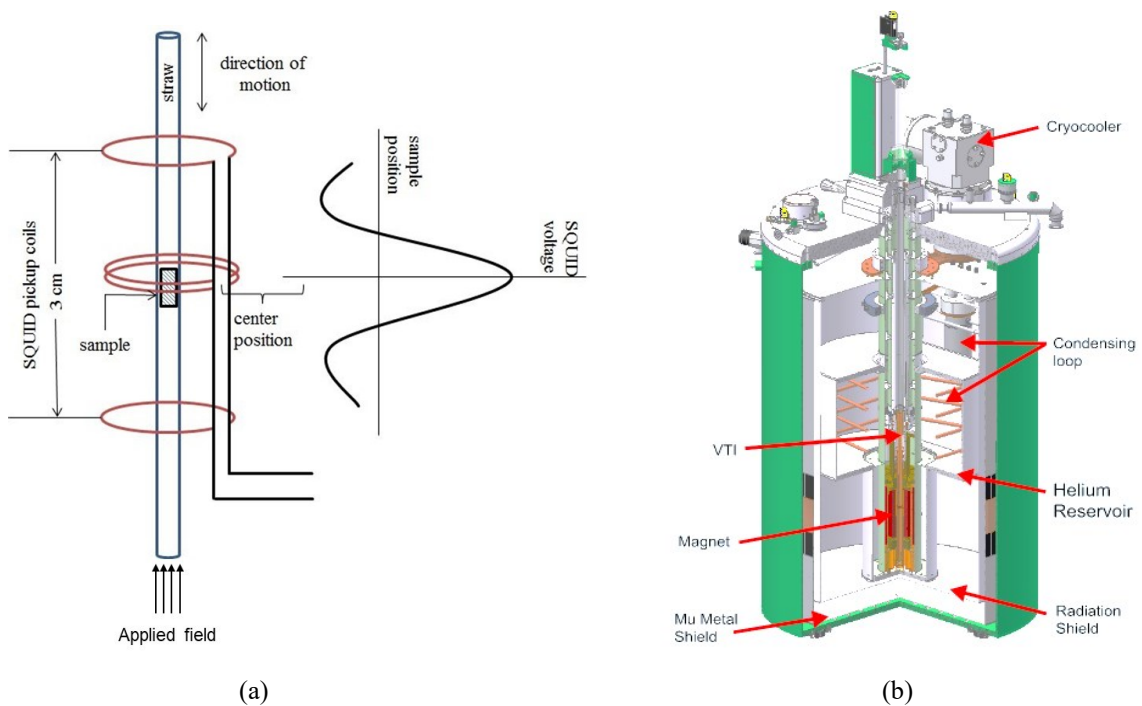


Figure I.2 (a) Schematic setup of a SQUID magnetometer with 2nd order gradiometer (left). The centering SQUID response V_{SQUID} versus sample position (right) (adapted from Ref.6) and (b) three quarter section view of the standard cryostat and insert.⁵

The S700X SQUID magnetometer from Cryogenic Ltd. (Figure I.3), used in this work, is one of the most sensitive instruments to perform magnetic measurements as a function of the magnetic field and temperature with a resolution down to 10^{-11} Am². It allows the performance of both static (DC magnetization) and dynamic (AC susceptibility) measurements in a wide range of temperatures (1.5-400 K) and magnetic fields, up to 7 T.⁵



Figure I.3 SQUID (Cryogenic Ltd.) facility available at C²TN.

Additionally, this equipment can perform measurements at temperatures down to 0.3 K by using a different probe, the Helium-3 Insert, that allows the sample to achieve as shown in Figure I.4.



Figure I.4 ³He insert.⁵

Although the S700X magnetometer is also equipped with AC coils to perform AC susceptibility measurements, the frequency range is only from 10⁻² to 500 Hz, slightly narrow to study our compounds. Therefore, those measurements have been performed by using different magnetic facilities (see next sections).

I2. MagLab 2000 – Oxford Instruments

MagLab 2000 is a multipurpose characterization system capable to perform DC extraction, AC susceptibility and specific heat measurements under fields up to 12 T, due to the existence of several interchangeable probes.

The equipment used in this work (Figure I.5) comprises a Variable Temperature Insert (VTI), operating in the range 1.5-400 K in either DC extraction or AC susceptibility. It consists of two main parts, the coil set and the extraction head (Figure I.6).⁷



Figure I.5 MagLab 2000 (Oxford Instruments) facility available at C²TN-IST.

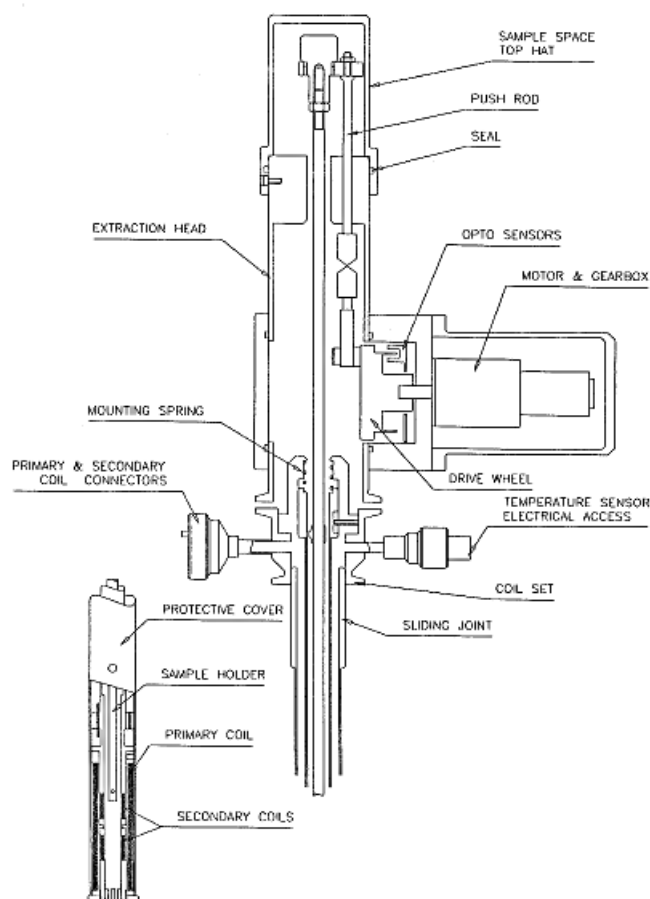


Figure I.6 Magnetic properties probe of the MagLab 2000 multipurpose characterization system (Oxford Instruments).⁷

The sensitivity of this probe for DC extraction is only up to 10^{-5} emu (10^{-8} Am²), significantly lower than the SQUID. For these reasons static DC measurements with small

samples are usually performed in the latter. On the other hand, the MagLab system offers great advantage in $M(B)$ measurements for dynamic studies, since it allows ramping the field in non-persistent mode, and getting faster sweeping rates, up to 90 Oe.s^{-1} , when compared with SQUID, which only works in persistent mode attaining only a maximum of 20 Oe.s^{-1} sweeping rate.

Another advantage of this facility is the aforementioned possibility to perform AC susceptibility measurements within a large range of frequencies (10-10000 Hz) with a considerable high sensitivity (10^{-11} Am^2). Consequently, MagLab is frequently used to perform the AC susceptibility measurements either as a function of frequency or temperature and even magnetic field.⁸

I3. Vibrating Sample Magnetometer (VSM) - Cryogenic Ltd.

VSM systems are used to measure the magnetic properties of materials as a function of magnetic field, temperature, and time. The instrument and technique were originally developed in the 1950s by Foner,⁹ in which a magnetic material is vibrated within a uniform magnetic field H , inducing an AC signal in suitably placed sensing coils. The upward motion of the magnetic sample causes an increase in flux through the upper pick-up coils and a decrease in flux through the lower pick-up coils. The reverse is true for downwards motion of the sample. Therefore, the overall signal induced when the sample is vibrating is proportional to the magnetic moment of the sample which can be recorded as a function of applied field, temperature and time (Figure I.7).¹⁰

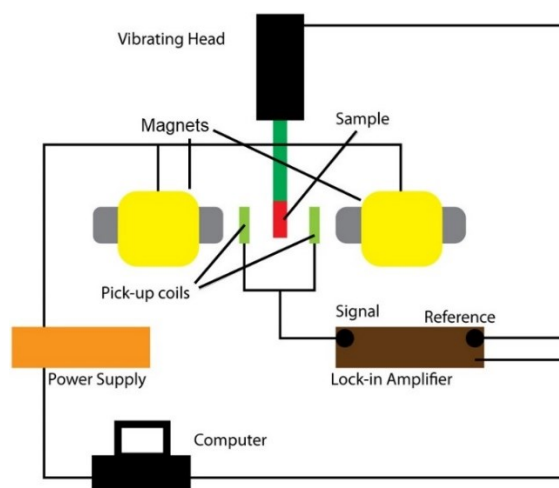


Figure I.7 Schematic diagram of a general VSM.

Appendix I

In this type of systems, the pickup coils are designed to maximize the induced signal, in order to improve the sensibility and to reduce the noise, especially associated with fluctuations of the applied magnetic field. The signal processing, using a lock-in amplifier, enables high signal-to-noise ratios to be obtained, and the vibrator provides the sinusoidal vertical motion of the sample within the pickup coils necessary for the VSM.

The VSM Magnetometer Facility used in this work allows DC magnetization and AC magnetic susceptibility measurements operating within a temperature range of 1.6-375 K and under fields up to 14 T (Figure I.8).



Figure I.8 VSM (Cryogenic Ltd.) facility available at C²TN-IST.

The DC probe sensitivity is of 10^{-6} emu (10^{-9} Am²), which may be insufficient to characterize properly materials with low magnetic moments or having very small sample volumes, as it is the case of nanoscale magnets. The AC susceptibility can be measured with a sensitivity of 10^{-7} emu/Gauss, in the frequency range 1 Hz-20 kHz.¹¹

References

- 1 Kleiner, R.; Koelle, D.; Ludwig, F.; Clarke, J. *Proc. IEEE* **2004**, *92*, 1534.
- 2 Josephson, B. D. *Phys. Lett.* **1962**, *1*, 251.
- 3 Ginzburg, V. L.; Landau, L. D. *Zh. Eksp. Teor. Fiz.* **1950**, *20*, 1064.
- 4 Clarke, J. SQUIDS. *Scientific American.* **1994**, 46.
- 5 S700X SQUID Magnetometer Manual, Cryogenic limited.

- 6 Yildirim, O. *Effect of microstructure on the magnetic properties of transition metal implanted TiO₂ films*, PhD Thesis, Technische Universität Dresden, **2016**.
- 7 *MagLab 2000*, Oxford Instruments (UK) Ltd, Oxford, UK, **1997**.
- 8 Pereira, L. C. J. Low Temperature and High Fields Laboratory, C²TN. [Online] **2022**.
http://www.ctn.tecnico.ulisboa.pt/facilities/uk_syst_maglab2000.htm.
- 9 Foner, S. *Rev. Sci. Instrum.* **1959**, *30*, 548.
- 10 *VSM & ACS measurement Option User Manual*, Cryogenic Limited, **2019**.
- 11 Pereira, L. C. J. Low Temperature and High Fields Laboratory. C²TN. [Online] **2022**.
<https://c2tn.tecnico.ulisboa.pt/index.php/the-center/infrastructures-services/infrastructures-own-available-in-campus/32-infrastructure/es/306-lthmfl-vsm-magnetometer-laboratory>.

APPENDIX II

Crystallographic data

Chapter 1

Table II.1 Crystallographic data and refinement details of complexes 1.4d-f.

	1.4d	1.4e	1.4f
Formula	C ₅₀ H ₆₆ CoN ₄	C ₆₄ H ₈₆ CoN ₄	C ₄₂ H ₄₂ CoN ₄
<i>M</i>	781.99	970.29	661.72
λ (Å)	0.71073	0.71073	0.71073
<i>T</i> (K)	150(2)	150(2)	150(2)
Crystal system	Monoclinic	Monoclinic	Triclinic
Space group	<i>P</i> 21/ <i>c</i>	<i>P</i> 21/ <i>c</i>	<i>P</i> -1
<i>a</i> (Å)	12.2261(5)	12.9181(10)	11.8079(8)
<i>b</i> (Å)	12.9194(5)	23.922(2)	11.9156(8)
<i>c</i> (Å)	26.3835(13)	18.3733(14)	11.9156(8)
α (Å)	90	90	69.540(4)
β (Å)	92.773(2)	96.868(3)	65.731(3)
γ (Å)	90	90	80.103(4)
<i>V</i> (Å ³)	4162.5(3)	5637.2(8)	1703.4(2)
<i>Z</i>	4	4	2
ρ_{calc} (g.cm ⁻³)	1.248	1.143	1.290
μ (mm ⁻¹)	0.452	0.346	0.540
Crystal size	0.150×0.080×0.080	0.200×0.140×0.100	0.200×0.140×0.100
Crystal color	Red	Red	Red
Crystal description	Prism	Prism	Plate
θ_{max} (°)	25.738	25.714	25.670
Total data	19742	31313	25160
Unique data	7905	10672	6402
<i>R</i> _{int}	0.0695	0.1894	0.0690
<i>R</i> [<i>I</i> > 2σ(<i>I</i>)]	0.0541	0.0720	0.0435
<i>R</i> _w	0.1107	0.1365	0.0920
Goodness of fit	1.022	0.934	0.997
ρ_{min}	-0.397	-0.381	-0.452
ρ_{max}	0.599	0.653	0.410

Appendix II

Table II.2 Crystallographic data and refinement details of complexes **1.4g-i**.

	1.4g	1.4h	1.4i
Formula	C ₉₂ H ₈₆ Co ₂ F ₂₄ N ₈	C ₅₀ H ₆₀ CoN ₄ O ₅	C ₄₆ H ₅₀ CoN ₄
<i>M</i>	1867.46	855.95	717.83
λ (Å)	0.71073	0.71073	0.71073
<i>T</i> (K)	150(2)	150(2)	150(2)
Crystal system	Monoclinic	Monoclinic	Monoclinic
Space group	<i>P</i> 21/ <i>c</i>	<i>P</i> 21/ <i>c</i>	<i>P</i> 21/ <i>c</i>
<i>a</i> (Å)	16.3544(7)	14.5176(10)	10.0141(5)
<i>b</i> (Å)	30.4234(12)	11.6635(9)	17.8450(11)
<i>c</i> (Å)	17.0224(7)	28.041(2)	22.1492(14)
α (Å)	90	90	90
β (Å)	93.854(3)	102.059(4)	95.304(2)
γ (Å)	90	90	90
<i>V</i> (Å ³)	8450.5(6)	4643.3(6)	95.304(2)
<i>Z</i>	4	4	4
ρ_{calc} (g.cm ⁻³)	1.468	1.224	1.210
μ (mm ⁻¹)	0.498	0.419	0.472
Crystal size	0.150×0.150×0.050	0.150×0.080×0.080	0.150×0.080×0.060
Crystal color	Green	Red	Purple
Crystal description	Prism	Plate	Prism
θ_{max} (°)	25.752	25.739	28.307
Total data	50683	29460	162540
Unique data	15967	8807	9797
<i>R</i> _{int}	0.1206	0.1899	0.0630
<i>R</i> [<i>I</i> > 2σ(<i>I</i>)]	0.0616	0.0754	0.0285
<i>R</i> _w	0.1344	0.1503	0.0586
Goodness of fit	1.001	0.978	0.857
ρ_{min}	-0.591	-0.359	0.239
ρ_{max}	1.167	0.739	-0.253

Chapter 2

Table II.3 Crystallographic data and refinement of complexes 2.4b-c and 2.5.

	2.4b	2.4c	2.5
Formula	C ₂₁ H ₃₅ N ₂ NiBr	C ₂₁ H ₃₅ N ₂ NiI	C ₂₁ H ₃₅ N ₂ NiCl
<i>M</i>	914.29	501.12	409.67
λ (Å)	0.71073	0.71073	0.71073
<i>T</i> (K)	150(2)	150(2)	150(2)
Crystal system	Monoclinic	Triclinic	Monoclinic
Space group	<i>P</i> 2 ₁ / <i>c</i>	<i>P</i> 2 ₁ / <i>c</i>	<i>P</i> 2 ₁
<i>a</i> (Å)	17.7551(19)	8.7747(3)	9.3248(11)
<i>b</i> (Å)	15.0046(17)	15.5691(7)	12.0972(14)
<i>c</i> (Å)	17.7551(19)	16.5251(8)	10.1585(12)
α (Å)	90	90	90
β (Å)	112.97	96.465(2)	109.072(4)
γ (Å)	90	90	90
<i>V</i> (Å ³)	4355.2(8)	2243.21(17)	1083.0(2)
<i>Z</i>	8	4	2
ρ_{calc} (g·cm ⁻³)	1.394	1.484	1.256
μ (mm ⁻¹)	2.733	2.247	1.025
Crystal size	0.250×0.180×0.050	0.100×0.100×0.100	0.100×0.080×0.040
Crystal color	Purple	Red	Pink
Crystal description	Needle	Block	Block
θ_{max} (°)	28.518	28.300	28.284
Total data	164461	102750	23633
Unique data	9180	5549	5356
<i>R</i> _{int}	0.0652	0.0335	0.0323
<i>R</i> [<i>I</i> > 2σ(<i>I</i>)]	0.0399	0.0257	0.0254
<i>R</i> _w	0.0921	0.0632	0.0527
Goodness of fit	1.014	1.047	1.022
ρ_{min}	-0.446	-0.636	-0.208
ρ_{max}	0.448	0.751	0.235

APPENDIX III

Fitting parameters of the generalized Debye model

Fitting parameters of the generalized Debye model

Table III.1 Fitting parameters of the generalized Debye model for complex **1.4a**, from 5.5 to 14 K, under an applied DC field of 3000 Oe.

<i>T</i> (K)	χ_T (cm⁻³/mol)	χ_S (cm⁻³/mol)	τ (s)	α
5.5	5.47(9)	0.290(5)	$2.70(8) \times 10^{-3}$	0.114(6)
6	4.98(6)	0.284(6)	$1.86(4) \times 10^{-3}$	0.091(5)
6.5	4.64(3)	0.276(4)	$1.30(1) \times 10^{-3}$	0.083(3)
7	4.24(2)	0.263(4)	$9.44(6) \times 10^{-4}$	0.080(3)
7.5	3.95(1)	0.256(3)	$6.67(3) \times 10^{-4}$	0.071(2)
8	3.64(1)	0.257(6)	$4.84(3) \times 10^{-4}$	0.058(4)
8.5	3.48(1)	0.250(7)	$3.64(2) \times 10^{-4}$	0.057(4)
9	3.24(1)	0.242(8)	$2.73(2) \times 10^{-4}$	0.055(4)
9.5	3.097(8)	0.228(6)	$2.06(9) \times 10^{-4}$	0.056(3)
10	2.925(8)	0.225(7)	$1.561(8) \times 10^{-4}$	0.052(4)
10.5	2.795(8)	0.212(9)	$1.159(7) \times 10^{-4}$	0.057(4)
11	2.666(6)	0.21(1)	$8.62(5) \times 10^{-5}$	0.054(4)
11.5	2.577(6)	0.18(1)	$6.24(5) \times 10^{-5}$	0.065(5)
12	2.471(6)	0.17(2)	$4.58(6) \times 10^{-5}$	0.070(6)
12.5	2.368(8)	0.21(5)	$3.4(1) \times 10^{-5}$	0.06(1)
13	2.287(5)	0.19(2)	$2.16(1) \times 10^{-5}$	0.091(4)
13.5	2.190(3)	0.17(4)	$1.589(9) \times 10^{-5}$	0.070(4)
14	2.106(4)	0.15(2)	$1.20(1) \times 10^{-5}$	0.037(6)

Table III.2 Fitting parameters of the generalized Debye model for complex **1.4b**, from 7 to 15 K, under an applied DC field of 1000 Oe.

<i>T</i> (K)	χ_T (cm⁻³/mol)	χ_S (cm⁻³/mol)	τ (s)	α
7	0.299(3)	$3.438(3) \times 10^{-2}$	$3.63(4) \times 10^{-3}$	0.135(6)
8	0.252(8)	$3.22(1) \times 10^{-2}$	$1.66(1) \times 10^{-3}$	0.081(2)
8.5	0.247(4)	$3.14(8) \times 10^{-2}$	$1.21(3) \times 10^{-3}$	0.078(1)
9	0.230(4)	$3.49(6) \times 10^{-2}$	$7.85(2) \times 10^{-4}$	0.029(1)
10	0.195(3)	$3.13(2) \times 10^{-2}$	$1.697(5) \times 10^{-4}$	0.023(2)
11	0.185(9)	$2.51(1) \times 10^{-2}$	$6.251(1) \times 10^{-5}$	0.060(7)
13	0.161(1)	$3.59(7) \times 10^{-2}$	$1.273(9) \times 10^{-5}$	0.012(2)
14	0.1447(7)	$3.46(1) \times 10^{-2}$	$7.236(8) \times 10^{-6}$	0.008(2)
15	0.1339(3)	$3.33(1) \times 10^{-2}$	$4.873(5) \times 10^{-6}$	0.027(1)

Appendix III

Table III.3 Fitting parameters of the generalized Debye model for complex **1.4c**, from 5 to 10 K, without the application of a DC field.

T (K)	χ_T (cm ⁻³ /mol)	χ_S (cm ⁻³ /mol)	τ (s)	α
5	6.2(1)	1.01(7)	$4.1(3) \times 10^{-4}$	0.59(1)
6	5.2(1)	1.05(7)	$4.2(3) \times 10^{-4}$	0.54(2)
7	4.20(7)	1.11(5)	$2.9(2) \times 10^{-4}$	0.42(2)
8	3.52(4)	1.19(4)	$1.86(7) \times 10^{-4}$	0.26(2)
9	3.03(1)	1.04(3)	$8.5(2) \times 10^{-5}$	0.17(1)
10	2.687(9)	0.69(7)	$2.9(2) \times 10^{-5}$	0.14(2)

Table III.4 Fitting parameters of the generalized Debye model for complex **1.4c**, from 5 to 12 K, under an applied DC field of 800 Oe.

T (K)	χ_T (cm ⁻³ /mol)	χ_S (cm ⁻³ /mol)	τ (s)	α
5	5.1(1)	0.334(1)	$8.22(3) \times 10^{-3}$	0.115(4)
5.5	5.42(7)	0.335(1)	$5.59(1) \times 10^{-3}$	0.076(2)
6	4.53(3)	0.314(1)	$3.12(3) \times 10^{-3}$	0.042(2)
6.5	3.898(6)	0.326(9)	$1.76(4) \times 10^{-3}$	0.014(5)
7	3.88(1)	0.310(2)	$1.29(6) \times 10^{-3}$	0.011(2)
7.5	3.699(8)	0.302(2)	$8.45(3) \times 10^{-4}$	0.013(2)
8	3.411(5)	0.296(1)	$5.15(1) \times 10^{-4}$	0.008(1)
8.3	3.309(7)	0.293(4)	$3.71(1) \times 10^{-4}$	0.014(2)
8.5	3.261(5)	0.285(3)	$3.02(7) \times 10^{-4}$	0.018(1)
9	3.061(4)	0.261(3)	$1.661(4) \times 10^{-4}$	0.031(2)
9.3	2.934(3)	0.246(3)	$1.138(2) \times 10^{-4}$	0.029(1)
9.5	2.849(2)	0.249(3)	$8.88(2) \times 10^{-5}$	0.0249(1)
10	2.691(1)	0.202(6)	$4.80(1) \times 10^{-5}$	0.040(2)
11	2.473(1)	0.18(2)	$1.53(2) \times 10^{-5}$	0.026(3)
12	2.272(3)	0.16(4)	$5.3(1) \times 10^{-6}$	0.038(2)

Fitting parameters of the generalized Debye model

Table III.5 Fitting parameters of the generalized Debye model for complex **1.4d**, from 7 to 11 K, without the application of a DC field.

T (K)	χ_T (cm ⁻³ /mol)	χ_S (cm ⁻³ /mol)	τ (s)	α
7	0.291(2)	0.071(9)	$3.279(6) \times 10^{-4}$	0.376(6)
8	0.260(1)	0.079(6)	$2.790(4) \times 10^{-4}$	0.266(5)
9	0.231(4)	0.072(4)	$1.228(7) \times 10^{-4}$	0.191(3)
10	0.207(2)	0.064(6)	$3.619(3) \times 10^{-5}$	0.151(4)
11	0.188(2)	0.028(2)	$9.633(2) \times 10^{-6}$	0.196(5)

Table III.6 Fitting parameters of the generalized Debye model for complex **1.4d**, from 5.5 to 10.5 K, under an applied DC field of 800 Oe.

T (K)	χ_T (cm ⁻³ /mol)	χ_S (cm ⁻³ /mol)	τ (s)	α
5.5	0.330(4)	0.0264(4)	$8.6(2) \times 10^{-3}$	0.052(7)
6.5	0.311(5)	0.0206(5)	$6.1(1) \times 10^{-3}$	0.123(8)
7.5	0.2889(5)	0.020(7)	$2.420(8) \times 10^{-3}$	0.010(1)
8.5	0.2615(2)	0.0165(5)	$8.67(1) \times 10^{-4}$	0.0799(5)
9	0.2313(1)	0.0149(6)	$4.555(4) \times 10^{-4}$	0.0601(5)
9.5	0.23	0.01	2.18×10^{-4}	0.12
10	0.2108(6)	0.0010(6)	$1.234(7) \times 10^{-4}$	0.0735(4)
10.5	0.1997(5)	0.0164(1)	$6.159(4) \times 10^{-5}$	0.085(4)

Appendix III

Table III.7 Fitting parameters of the generalized Debye model for complex **1.4e**, from 6 to 13.5 K, without the application of a DC field.

T (K)	χ_T (cm ³ .mol)	χ_S (cm ³ .mol)	τ (s)	α
6	0.328(1)	0.03515(9)	$2.96(3) \times 10^{-3}$	0.299(2)
6.5	0.291(1)	0.0338(1)	$1.82(1) \times 10^{-3}$	0.270(2)
7	0.2652(8)	0.0327(1)	$1.220(9) \times 10^{-3}$	0.230(2)
7.5	0.240(2)	0.0322(4)	$8.2(1) \times 10^{-4}$	0.183(5)
8	0.228(2)	0.0301(7)	$5.7(1) \times 10^{-4}$	0.165(8)
8.5	0.210(2)	0.0288(7)	$4.03(6) \times 10^{-4}$	0.136(8)
9	0.1978(8)	0.0283(5)	$2.87(3) \times 10^{-4}$	0.106(5)
9.5	0.1867(7)	0.0267(5)	$2.06(2) \times 10^{-4}$	0.093(59)
10	0.1757(4)	0.0256(4)	$1.434(7) \times 10^{-4}$	0.075(3)
10.5	0.1638(4)	0.0257(5)	$9.96(6) \times 10^{-5}$	0.040(4)
11	0.1587(2)	0.0238(4)	$7.01(3) \times 10^{-5}$	0.045(3)
11.5	0.1514(1)	0.0232(4)	$4.84(2) \times 10^{-5}$	0.029(3)
12	0.1454(1)	0.0224(6)	$3.35(2) \times 10^{-5}$	0.024(3)
12.5	0.13946(9)	0.0240(8)	$2.38(2) \times 10^{-5}$	0.0087(3)
13	0.13478(7)	0.025(1)	$1.69(2) \times 10^{-5}$	0.006(3)
13.5	0.13057(5)	0.025(1)	$1.20(2) \times 10^{-5}$	0.011(3)

Fitting parameters of the generalized Debye model

Table III.8 Fitting parameters of the generalized Debye model for complex **1.4e**, from 5.5 to 13.5 K, under an applied DC field of 1200 Oe.

T (K)	χ_T (cm ³ .mol)	χ_S (cm ³ .mol)	τ (s)	α
5.5	0.350(3)	0.0223(1)	$4.67(9) \times 10^{-3}$	0.367(2)
6	0.322(2)	0.0217(1)	$3.02(3) \times 10^{-3}$	0.331(1)
6.5	0.297(2)	0.0222(2)	$1.96(3) \times 10^{-3}$	0.282(3)
7	0.273(2)	0.0217(3)	$1.27(2) \times 10^{-3}$	0.245(4)
7.5	0.244(1)	0.0227(4)	$7.8(1) \times 10^{-4}$	0.181(4)
8	0.223(1)	0.0217(4)	$5.48(5) \times 10^{-4}$	0.156(4)
8.5	0.2054(7)	0.0214(3)	$3.74(2) \times 10^{-4}$	0.123(3)
9	0.1944(4)	0.0209(2)	$2.68(1) \times 10^{-4}$	0.103(2)
9.5	0.1814(4)	0.0214(3)	$1.823(7) \times 10^{-4}$	0.069(3)
10	0.1720(3)	0.0199(3)	$1.249(4) \times 10^{-4}$	0.062(2)
10.5	0.1642(3)	0.0199(4)	$8.29(4) \times 10^{-5}$	0.051(3)
11	0.1568(2)	0.0188(5)	$5.39(3) \times 10^{-5}$	0.049(3)
11.5	0.1507(2)	0.0195(7)	$3.55(3) \times 10^{-5}$	0.0479(3)
12	0.14442(7)	0.0200(6)	$2.31(2) \times 10^{-5}$	0.043(2)
12.5	0.1385(1)	0.021(2)	$1.56(3) \times 10^{-5}$	0.032(5)
13.5	0.12975(4)	0.018(3)	$6.7(2) \times 10^{-6}$	0.050(4)

Appendix III

Table III.9 Fitting parameters of the generalized Debye model for complex **1.4f**, from 6 to 12 K, under an applied DC field of 2000 Oe.

T (K)	χ_T (cm ⁻³ /mol)	χ_S (cm ⁻³ /mol)	τ (s)	α
6	4.3(1)	0.361(3)	$5.0(2) \times 10^{-3}$	0.047(6)
7	3.92(2)	0.354(1)	$2.06(1) \times 10^{-3}$	0.029(2)
8	3.26(2)	0.365(6)	$8.23(8) \times 10^{-4}$	0.010(5)
8.5	3.07(1)	0.372(5)	$5.30(3) \times 10^{-4}$	0.009(3)
9	2.85(1)	0.359(7)	$3.15(2) \times 10^{-4}$	0.014(4)
9.5	2.71(1)	0.362(9)	$1.88(1) \times 10^{-4}$	0.025(5)
10	2.579(8)	0.35(1)	$1.092(8) \times 10^{-4}$	0.033(5)
10.5	2.496(6)	0.30(2)	$6.20(6) \times 10^{-5}$	0.062(6)
11	2.368(6)	0.22(3)	$3.38(7) \times 10^{-5}$	0.074(8)
12	2.168(6)	0.10(1)	$1.180(7) \times 10^{-5}$	0.058(5)

Table III.10 Fitting parameters of the generalized Debye model for complex **1.4g**, from 3.5 to 20 K, under an applied DC field of 1000 Oe.

T (K)	χ_T (cm ⁻³ /mol)	χ_S (cm ⁻³ /mol)	τ (s)	α
3.5	0.880(2)	0.039(3)	$3.94(9) \times 10^{-3}$	0.341(4)
4.5	0.577(3)	0.040(9)	$8.66(9) \times 10^{-4}$	0.211(4)
5.5	0.428(2)	0.040(7)	$3.02(3) \times 10^{-4}$	0.062(5)
6.5	0.363(3)	0.041(2)	$1.29(2) \times 10^{-4}$	0.049(1)
7.5	0.313(2)	0.041(2)	$7.73(1) \times 10^{-5}$	5.00×10^{-16}
8.5	0.280(4)	0.035(5)	$5.147(2) \times 10^{-5}$	1.59×10^{-16}
9	0.250(8)	0.039(1)	$3.026(4) \times 10^{-5}$	1.64×10^{-16}
10	0.237(4)	0.039(1)	$1.988(2) \times 10^{-5}$	4.50×10^{-16}
11	0.211(6)	0.039(3)	$1.276(3) \times 10^{-5}$	7.50×10^{-16}
12	0.197(3)	0.040(3)	$8.92(2) \times 10^{-6}$	2.68×10^{-15}
13	0.178(4)	0.044(7)	$6.82(4) \times 10^{-6}$	2.57×10^{-15}
14	0.166(4)	0.042(1)	$5.58(5) \times 10^{-6}$	2.09×10^{-15}
15	0.158(4)	0.039(2)	$4.418(7) \times 10^{-6}$	1.46×10^{-15}
16	0.15(1)	0.042(5)	$4.00(2) \times 10^{-6}$	4.57×10^{-15}
18	0.139(8)	0.039(6)	$2.98(2) \times 10^{-6}$	4.20×10^{-15}
20	0.121(5)	0.038(6)	$2.34(2) \times 10^{-6}$	3.30×10^{-15}

Fitting parameters of the generalized Debye model

Table III.11 Fitting parameters of the generalized Debye model for complex **1.4h**, from 6 to 14 K, under an applied DC field 1500 Oe.

<i>T</i> (K)	χ_T (cm ⁻³ /mol)	χ_S (cm ⁻³ /mol)	τ (s)	α
6	5.14(3)	0.387(6)	$1.080(8) \times 10^{-3}$	0.005(1)
7	4.69(2)	0.376(8)	$5.66(5) \times 10^{-4}$	0.002(2)
8	4.10(1)	0.316(7)	$3.10(2) \times 10^{-4}$	0.042(3)
8.5	3.80(2)	0.30(1)	$2.32(2) \times 10^{-4}$	0.041(5)
9	3.66(1)	0.29(1)	$1.81(1) \times 10^{-4}$	0.052(4)
9.5	3.40(1)	0.28(1)	$1.380(8) \times 10^{-4}$	0.046(4)
10	3.28(1)	0.25(1)	$1.068(8) \times 10^{-4}$	0.060(5)
10.5	3.069(9)	0.284(2)	$8.36(6) \times 10^{-5}$	0.037(5)
11	2.978(9)	0.23(2)	$6.37(7) \times 10^{-5}$	0.052(6)
12	2.706(5)	0.153(3)	$3.53(5) \times 10^{-5}$	0.047(6)
13	2.493(2)	0.24(3)	$2.05(4) \times 10^{-5}$	0.009(5)
14	2.348(7)	0.15(3)	$9.9(2) \times 10^{-6}$	0.023(3)

Appendix III

Table III.12 Fitting parameters of the generalized Debye model for complex **1.4i**, from 7.5 to 17.5 K, without the application of a DC field.

T (K)	χ_T (cm ⁻³ /mol)	χ_S (cm ⁻³ /mol)	τ (s)	α
7.5	0.280(8)	0.068(2)	$8.99(7) \times 10^{-4}$	0.275(2)
8	0.265(7)	0.063(2)	$7.15(6) \times 10^{-4}$	0.255(2)
8.5	0.248(3)	0.061(8)	$5.6(2) \times 10^{-4}$	0.22(1)
9	0.228(2)	0.058(8)	$4.22(9) \times 10^{-4}$	0.19(1)
9.5	0.214(3)	0.058(1)	$3.35(1) \times 10^{-4}$	0.131(2)
10	0.208(7)	0.052(4)	$2.81(2) \times 10^{-4}$	0.155(5)
10.5	0.2196(5)	0.054(4)	$2.33(2) \times 10^{-4}$	0.109(4)
11	0.193(5)	0.046(4)	$1.91(1) \times 10^{-4}$	0.146(1)
11.5	0.187(7)	0.043(6)	$1.56(1) \times 10^{-4}$	0.153(6)
12	0.177(5)	0.042(5)	$1.258(9) \times 10^{-4}$	0.127(5)
12.5	0.168(1)	0.040(4)	$1.015(7) \times 10^{-4}$	0.108(5)
13	0.159(4)	0.039(7)	$8.28(7) \times 10^{-5}$	0.078(6)
13.5	0.153(5)	0.0387(9)	$6.82(8) \times 10^{-5}$	0.063(7)
14	0.148(3)	0.036(7)	$5.48(5) \times 10^{-5}$	0.063(5)
14.5	0.143(2)	0.034(6)	$4.44(3) \times 10^{-5}$	0.054(4)
15	0.137(2)	0.033(7)	$3.58(3) \times 10^{-5}$	0.034(4)
15.5	0.133(1)	0.031(7)	$2.86(2) \times 10^{-5}$	0.034(3)
16	0.129(9)	0.032(8)	$2.32(2) \times 10^{-5}$	0.019(4)
16.5	0.125(7)	0.031(9)	$1.85(2) \times 10^{-5}$	0.013(3)
17	0.121(7)	0.028(1)	$1.43(3) \times 10^{-5}$	0.013(4)
17.5.	0.118(7)	0.030(2)	$1.17(3) \times 10^{-5}$	0.007(5)

Fitting parameters of the generalized Debye model

Table III.13 Fitting parameters of the generalized Debye model for complex **1.4i**, from 6 to 17.5 K, under an applied DC field 1200 Oe.

T (K)	χ_T (cm ³ /mol)	χ_S (cm ³ /mol)	τ (s)	α
6	0.318(5)	0.017(6)	$5.7(1) \times 10^{-3}$	0.031(3)
6.5	0.296(3)	0.017(7)	$3.73(4) \times 10^{-3}$	0.015(2)
7	0.288(3)	0.017(1)	$2.70(4) \times 10^{-3}$	0.031(3)
7.5	0.263(2)	0.016(2)	$1.84(2) \times 10^{-3}$	0.028(3)
8	0.239(1)	0.016(2)	$1.26(1) \times 10^{-3}$	0.007(3)
8.5	0.229(8)	0.016(2)	$9.57(5) \times 10^{-4}$	0.015(3)
9	0.221(4)	0.016(1)	$7.42(2) \times 10^{-4}$	0.017(2)
9.5	0.206(5)	0.016(2)	$5.55(2) \times 10^{-4}$	0.005(2)
10	0.197(4)	0.016(2)	$4.36(2) \times 10^{-4}$	0.002(2)
10.5	0.191(4)	0.016(2)	$3.52(1) \times 10^{-4}$	0.011(2)
11	0.182(3)	0.016(1)	$2.789(7) \times 10^{-4}$	0.009(2)
11.5	0.173(2)	0.0158(2)	$2.194(5) \times 10^{-4}$	0.005(2)
12	0.166(3)	0.016(2)	$1.746(5) \times 10^{-4}$	0.004(2)
12.5	0.162(2)	0.015(2)	$1.3902(4) \times 10^{-4}$	0.009(2)
13	0.155(2)	0.015(2)	$1.080(2) \times 10^{-4}$	0.004(2)
13.5	0.1501(1)	0.0143(2)	$8.39(1) \times 10^{-5}$	0.014(1)
14	0.1447(1)	0.0141(3)	$6.38(2) \times 10^{-5}$	0.011(2)
14.5	0.1394(8)	0.0147(3)	$4.795(6) \times 10^{-5}$	0.0103(9)
15	0.1352(1)	0.0139(5)	$3.60(2) \times 10^{-5}$	0.012(3)
15.5	0.1310(9)	0.0143(2)	$2.68(2) \times 10^{-5}$	0.015(3)
16	0.1270(8)	0.0164(9)	$2.05(2) \times 10^{-5}$	0.010(3)
16.5	0.1235(6)	0.0176(2)	$1.54(2) \times 10^{-5}$	0.012(3)
17	0.1203(5)	0.0152(2)	$1.14(2) \times 10^{-5}$	0.021(4)
17.5	0.1178(4)	0.0228(2)	$9.3(2) \times 10^{-6}$	0.011(3)